

# Coupled Hydraulic, Thermal and Chemical Simulations for Geothermal Installations

Yodha Y. Nusiaputra



This document is licensed under the Creative Commons Attribution 4.0 International License (CC BY 4.0): <https://creativecommons.org/licenses/by/4.0/deed.de>

# Coupled Hydraulic, Thermal and Chemical Simulations for Geothermal Installations

Zur Erlangung des akademischen Grades eines  
DOKTORS DER NATURWISSENSCHAFTEN

von der Fakultät

Bauingenieur-, Geo- und Umweltwissenschaften  
des Karlsruher Instituts für Technologie (KIT)

genehmigte

DISSERTATION

von

Yodha Yudhistra Nusiaputra, M.Sc.

aus Surakarta, Indonesien

Tag der mündlichen

Prüfung: 17. Februar 2017

Referent: Prof. Dr. Thomas Kohl

Korreferent: Prof. Dr. Thomas Schulenberg

Karlsruhe 2017

---

## ABSTRACT

---

Geothermal installations (e.g. wellbore and power block) cost is a major factor determining the economic feasibility of binary geothermal power plant project. The purpose of this research was to study various technical factors to optimize their design and operation, aims at significant cost efficiency. The first part of the thesis was devoted to modeling and optimization of modular Organic Rankine Cycles. Modularization technique was devised to utilize various wellhead temperatures (120 - 170°C), mass flow rates and ambient temperatures (-10 - 40°C). A multiple-input and multiple-output control strategy was developed using steady-state optimization to maximize plant performance during off-design. Dynamic simulations were also performed to test the optimal control strategy for both 60 kWel Gross-Schönebeck ORC and 1,000 kWel conceptual modular ORC at insular operation condition.

The objective of the second part of the thesis was the development of thermohydro-chemical (THC) wellbore flow simulator, WellboreKit, to simulate pressure, temperature and mineral deposition of multiphase flow under different condition. The properties of multicomponent fluid mixtures were computed by using gEOSkit, an equation of state solver assembled for two-phase, multisalt (Na-Ca-K-Mg-Cl-HCO<sub>3</sub>) and multigas (CO<sub>2</sub>-N<sub>2</sub>-CH<sub>4</sub>-H<sub>2</sub>S) geothermal fluids. gEOSkit is based on extended Duan-Sun fugacity-activity approach to partition liquid-like (aqueous) and gas-like (non-aqueous) phases. Improved gas activity coefficient has been accomplished through the extension of neutral interaction between dissolved gasses.

The two-phase flow was modeled by using a heterogeneous equilibrium model. Elmer FEM, a finite element solver, was used to solve the mass, energy, momentum and species transport conservation equations. The flow pattern has been determined by physically-based mechanistic flow model. To solve the geochemistry reaction, PHREEQC was coupled to Elmer using Python as a wrapper. An operator splitting algorithm has been applied to solve the problem sequentially. The simulation results show the impact of operation parameters (e.g. flow rate, injection temperature) and constitutive correlations like the slip correlation; scaling-corrosion related wall-friction model, and reaction kinetics to barite, calcite, and amorphous silica thickness. This tool allows slow-transient analyses that predicting wellbore system dynamics such as time-varying flow rate, temperature, pressure, fluid composition, and tendency to mineral deposition.

---

## KURZFASSUNG

---

Geothermische Anlagen (z. B. Bohrloch und Energieblock) Kosten sind ein wichtiger Faktor, der die ökonomische Durchführbarkeit eines binären geothermischen Kraftwerksprojekts bestimmt. Der Zweck dieser Forschung war es, verschiedene technische Faktoren zu untersuchen, um ihre Konstruktion und ihren Betrieb zu optimieren, zielt auf eine beträchtliche Kosteneffizienz. Der erste Teil der Arbeit widmete sich der Modellierung und Optimierung modularer organischer Rankine cycle. Modularisierungstechnik wurde entwickelt, um verschiedene Bohrlochkopftemperaturen (120 - 170 °C), Massendurchflüsse und Umgebungstemperaturen (-10 - 40 °C) zu nutzen. Eine Steuerungsstrategie mit mehreren Eingängen und mehreren Ausgängen wurde unter Verwendung einer stationären Optimierung entwickelt, um die Anlagenleistung während des Off-Designs zu maximieren. Dynamische Simulationen wurden ebenfalls durchgeführt, um die optimale Steuerstrategie für 60 kWel Gross-Schönebeck ORC und 1.000 kWel konzeptionelle modulare ORC im Inselbetrieb zu testen.

Das Ziel des zweiten Teils der Arbeit war die Entwicklung des thermohydrochemischen (THC) Bohrlochströmungssimulators WellboreKit zur Simulation von Druck, Temperatur und Mineralablagerung von Mehrphasenströmung unter verschiedenen Bedingungen. Die Eigenschaften von Mehrkomponenten-Fluidgemischen wurden unter Verwendung von gEOSkit, einer Zustandsgleichungslöser für zweiphasige, multisalt (Na-Ca-K-Mg-Cl-HCO<sub>3</sub>) und multigas (CO<sub>2</sub>-N<sub>2</sub>-CH<sub>4</sub>-H<sub>2</sub>S) geothermische Flüssigkeiten, berechnet. gEOSkit basiert auf einem erweiterten Duan-Sun Fugazitäts-Ansatz für die Trennung von flüssigen (wässrigen) und gasähnlichen (nicht-wässrigen) Phasen. Durch die Erweiterung der neutralen Wechselwirkung zwischen gelösten Gasen wurde eine verbesserte Gasaktivität erreicht.

Die Zweiphasenströmung wurde unter Verwendung eines heterogenen Gleichgewichtsmodells modelliert. Elmer FEM, ein Finite-Elemente-Löser, wurde verwendet, um die Masse-, Energie-, Momentum- und Spezies-Transport-Konservierungsgleichungen zu lösen. Das Strömungsmuster wurde durch ein physikalisch basiertes mechanistisches Strömungsmodell bestimmt. Um die Geochemistry-Reaktion zu lösen, wurde PHREEQC an Elmer unter Verwendung von Python als Hülle gekoppelt. Ein Operatoraufteilungsalgorithmus wurde angewandt, um das Problem sequentiell zu lösen. Die Simulationsergebnisse zeigen

die Auswirkungen von Betriebsparametern (z. B. Strömungsrate, Einspritztemperatur) und konstitutive Korrelationen wie die Schlupfkorrelation, dem Wandreibungmodell unter Betracht der Korrosion und Ausfällung, und Reaktionskinetik auf die Baryt-, Calcit- und amorphe Siliciumdioxid-Dicke. Dieses Tool ermöglicht langsame Transientenanalysen, die die Dynamik des Bohrlochsystems vorhersagen, wie z. B. zeitvariable Strömungsgeschwindigkeit, Temperatur, Druck, Fluidzusammensetzung und Tendenz zur Mineralablagerung.

---

## ACKNOWLEDGEMENT

---

I would like to thank Prof. Thomas Kohl and Prof. Thomas Schulenberg for the support encouragement. Helmholtz Centre Potsdam GFZ (German Research Centre for Geosciences) is greatly thanked in providing for the period 1 October 2010 - 31 March 2014, which is funded by BMBF (Grant 03G0753A 'Sustainability concepts for exploration of geothermal reservoir in Indonesia'). I express my thanks to IKET (Institute for Nuclear and Energy Technologies) of Karlsruhe Institute of Technology (KIT), EnBW Energie Baden-Württemberg, and the Helmholtz funding program for the further funding support, with special thanks to Dr.-Ing. Dietmar Kuhn. I also appreciate and express thanks to the PT PLN (Persero) for agreeing and supporting my study leave.

Dr. Alain Dimier of EIFER (European Institute for Energy Research) is acknowledged for allowing me to develop the wellbore simulator in Etumos, his Elmer-PHREEQC coupling platform, and the fruitful discussions on the codes. Without his support, I would not finish the second part of the thesis. Stephanie Frick of GFZ Potsdam and Hans-Joachim Wiemer of IKET are thanked for supporting the ORC power-plant modeling and optimization. Dr.-Ing. Henning Francke is acknowledged for the water-salt-gas equation of state foundations. I also thank Dr.-Ing. Elisabeth Schröder for the geothermal fluid properties discussions. My modeling on the mineral scaling in wellbores could not have been accomplished without any discussions with Fabian Nitschke through his geochemistry knowledge. Dr. Kemal Erbas, Dr. Makky S Jaya, Prof. David Bruhn, Prof. Ernst Huenges, Dr. Roman Zorn, Prof. Frank Schilling, and Prof. Jochen Kolb are thanked for general supports on the study. All colleagues in Section 4.1 (Reservoir Technologies) of Helmholtz Centre Potsdam GFZ and Geothermic Division, Applied Geosciences KIT are be grateful for the wonderful years during my work in Germany.

Finally, I would like to express my profound and infinite appreciation to my beloved wife Hijraini Nainggolan, my daughter Luisa Azzahra, my parents, and Indonesian families in Karlsruhe who spent their valuable time with me on this long journey.

---

# CONTENTS

---

|          |  |    |
|----------|--|----|
| <b>1</b> | <b>Introduction</b>  | 1  |
| 1.1      | Motivation   | 3  |
| 1.2      | Thesis structure   | 8  |
| <b>2</b> | <b>Basics</b>  | 10 |
| 2.1      | Geothermal working fluids  | 10 |
| 2.2      | Conservation equations   | 12 |
| 2.3      | Heat transfer and pressure drop  | 14 |
| 2.4      | Geochemical reactions  | 21 |
| 2.4.1    | Dissolution and precipitation of minerals                                      | 21 |
| 2.4.2    | Kinetics of geochemical reactions  | 23 |
| 2.5      | Equation of state for geothermal fluids  | 24 |
| 2.5.1    | Fugacity-activity phase partitioning   | 24 |
| 2.5.2    | Apparent molar properties  | 26 |
| <b>3</b> | <b>Modular geothermal Organic Rankine Cycles</b>                               | 27 |
| 3.1      | Empirical correlations for optimal turbine inlet temperature and pressure      | 27 |
| 3.1.1    | Introduction   | 28 |
| 3.1.3    | Thermodynamic modelling  | 29 |
| 3.1.5    | Results and discussion   | 32 |
| 3.1.6    | Conclusions  | 37 |
| 3.2      | Steady-state optimization of the Organic Rankine Cycles                        | 38 |
| 3.2.1    | Three-zone heat exchanger model  | 38 |
| 3.2.2    | Rotating component model   | 43 |
| 3.2.3    | Reverse modeling based on manufacturer's data: 60 kWel<br>Gross-Schönebeck ORC | 44 |
| 3.2.4    | Multivariable control strategy optimization                                    | 57 |
| 3.3      | Dynamic characteristics of the Organic Rankine Cycles                          | 59 |
| 3.3.1    | Thermodynamics modeling in Modelica/Dymola/TIL                                 | 59 |
| 3.3.3    | Retrofitting control strategies for 60 kWel Groß-Schönebeck ORC                | 63 |
| 3.3.4    | Dynamic of load change: 1,000 kWel modular ORC simulation                      | 66 |

|          |  |     |
|----------|--|-----|
| <b>4</b> | <b>Thermal-economic modularization of small, Organic Rankine Cycle power plants for mid-enthalpy geothermal fields</b> | 78  |
| 4.1      | Introduction   | 78  |
| 4.2      | System description and methodology   | 80  |
| 4.3      | Component modelling  | 82  |
| 4.3.1    | Heat exchangers  | 82  |
| 4.3.2    | Feed pump  | 86  |
| 4.3.3    | Turbine  | 86  |
| 4.4      | Results  | 88  |
| 4.4.1    | Component sizing for normal-design: thermodynamic optimization   | 89  |
| 4.4.2    | Off-design mapping   | 92  |
| 4.4.3    | Annual simulation and thermo-economic selection  | 95  |
| 4.5      | Conclusions  | 99  |
| <b>5</b> | <b>gEOSkit - An equation of state assembled for two-phase multicomponent geothermal fluids</b>                         | 100 |
| 5.1      | Introduction   | 100 |
| 5.2      | Chemical characterization of geothermal fluids   | 103 |
| 5.3      | Evaluation of the vapor-liquid equilibrium   | 104 |
| 5.3.1    | Theoretical background   | 104 |
| 5.3.2    | Solver algorithm   | 108 |
| 5.3.3    | VLE validation   | 111 |
| 5.4      | Thermophysical properties  | 115 |
| 5.4.1    | Isobaric heat capacity and enthalpy  | 115 |
| 5.4.2    | Density  | 119 |
| 5.4.3    | Viscosity  | 120 |
| 5.5      | Conclusions  | 121 |
| <b>6</b> | <b>Thermohydro-chemical modelling of geothermal well flow with two-phase multicomponent fluids</b>                     | 123 |
| 6.1      | Introduction   | 123 |
| 6.2      | The two-phase one-dimensional wellbore problem   | 125 |
| 6.2.1    | Heat transfer models   | 128 |
| 6.2.2    | Pressure drop models   | 130 |

|          |  |            |
|----------|--|------------|
| 6.2.3    | Geochemical reaction models .....  | 131        |
| 6.2.4    | Thermodynamics .....   | 132        |
| 6.3      | Numerical approach .....   | 133        |
| 6.3.1    | Technical description of Elmer-PHREEQC coupling .....                          | 133        |
| 6.3.2    | Model validation .....   | 134        |
| 6.4      | Geothermal fluid production/injection example .....                            | 135        |
| 6.4.1    | Impact of chemical composition .....   | 139        |
| 6.4.2    | Impact of slip correlation .....   | 141        |
| 6.4.3    | Impact of wall friction .....  | 142        |
| 6.4.4    | Impact of reaction kinetic .....   | 143        |
| 6.4.5    | Impact of operation parameter .....  | 145        |
| 6.5      | Conclusions .....  | 148        |
| <b>7</b> | <b>Summary and conclusions</b> .....   | <b>149</b> |
| 7.1      | Major results .....  | 150        |
| 7.2      | Further improvement and direction .....  | 152        |
| <b>A</b> | <b>ORC dynamic simulation model</b> .....                                      | <b>153</b> |
| <b>B</b> | <b>gEOSkit correlation formulae</b> .....                                      | <b>154</b> |
| <b>C</b> | <b>Technical description of WellboreKit: Elmer-PHREEQC coupling</b> .....      | <b>159</b> |
| C.1      | State of the Elmer-PHREEQC coupling at the beginning of the thesis: Etumos ... | 160        |
| C.2      | WellboreKit coupling interfaces .....  | 160        |
| C.2.1    | Overview of the wellbore simulator routines .....                              | 161        |
| C.2.2    | Detailed description of the solver .....                                       | 161        |
| C.2.3    | Detailed description of function classes .....                                 | 163        |
| C.3      | WellboreKit features .....   | 165        |
| <b>D</b> | <b>WellboreKit transient terms</b> .....                                       | <b>167</b> |
| <b>E</b> | <b>Partial validation of WellboreKit</b> .....                                 | <b>170</b> |
|          | <b>References</b> .....  | <b>172</b> |

---

## ABBREVIATIONS AND ACRONYMS

---

|          |   |
|----------|---|
| AD       | absolute deviation                                  |
| AARD     | average absolute relative deviation                 |
| CMA-ES   | covariance matrix algorithm - evolutionary strategy |
| CMTD     | corrected mean temperature difference               |
| CRF      | capital recovery factor                             |
| CWTD     | corrected weighted temperature difference           |
| DP       | design point  |
| DPM      | distributed parameters model                        |
| EGS      | enhanced geothermal system                          |
| EOS      | equation of state                                   |
| FEM      | finite element model                                |
| GrSk     | Groß Schönebeck                                     |
| GrSk60   | Groß Schönebeck 60 kWel                             |
| GWP      | global warming potential                            |
| HX       | heat exchangers                                     |
| IAP      | ion activity product                                |
| ITD      | initial temperature difference                      |
| LMTD     | logarithmic mean temperature difference             |
| MCF      | mean cash flow                                      |
| MIMO     | multiple-input multiple-output                      |
| mORC1000 | modular ORC 1,000 kWel                              |
| NCG      | non-condensable gas                                 |
| NTU      | number of transfer units                            |
| ODP      | ozone depletion potential                           |
| ORC      | organic Rankine cycle                               |
| PR       | Peng-Robinson                                       |
| SEM      | stream evolution model                              |
| SIC      | specific investment cost                            |
| SoWat    | Sodium chloride-Water                               |

|      |  |
|------|--|
| TDS  | total dissolved solids                       |
| TEMA | Tubular Exchangers Manufacturers Association |
| THC  | thermal-hydraulic-chemical                   |
| TIL  | TLK-Ift-Library                              |
| TIP  | turbine inlet pressure                       |
| TIT  | turbine inlet temperature                    |
| TITP | turbine inlet temperature and pressure       |
| TVD  | true vertical depth                          |
| UML  | unified modeling language                    |
| VLE  | vapor-liquid equilibrium                     |

---

## NOMENCLATURE

---

### Latin symbols

|           |  |
|-----------|--|
| $E_a$     | activation energy, kJ/mol  |
| $a$       | activity, mol/kg   |
| $A$       | area, m <sup>2</sup>   |
| $B$       | baffle spacing, m  |
| $Bo$      | boiling number   |
| $C_a$     | clearance, m   |
| $U$       | component matrices of species, overall heat transfer coefficient |
| $Z$       | compressibility  |
| $C$       | concentration, mol/kgw; cost                                     |
| $c$       | constant, coefficient  |
| $\rho$    | density, kg/m <sup>3</sup>                                       |
| $d$       | diameter, m  |
| $D$       | diffusivity  |
| $r$       | discount rate; ratio; radius, m                                  |
| $r_{kin}$ | reaction rate  |
| $E$       | emissivity   |
| $H$       | enthalpy, J  |
| $Hg$      | Hagen number   |
| $K$       | equilibrium constant; gain; solubility, mol/kgw                  |
| $F$       | factor   |
| $f$       | friction factor, function  |
| $R$       | gas constant, 8.314 J/(K-mol); resistance                        |
| $y$       | gas mole fraction  |
| $g$       | gravity, m <sup>2</sup> /s                                       |
| $q$       | heat flux, W/m <sup>2</sup>                                      |
| $Q$       | Heat, W  |
| $T_i$     | integral time constant   |
| $u$       | internal energy  |
| $h_{LG}$  | latent heat, J/kg  |
| $L$       | length, m  |
| $m$       | mass   |
| $G$       | mass flux, kg/m <sup>2</sup> -s                                  |
| $w$       | mass fraction  |

|           |   |
|-----------|---|
| $M$       | molar mass, kg/mol                                      |
| $I$       | momentum, kg-m/s  |
| $N$       | number  |
| $Nu$      | Nusselt number  |
| $C_L$     | pitch factor  |
| $P$       | Power, W  |
| $Pr$      | Prandtl number  |
| $p$       | pressure, bar or MPa; probability                       |
| $k$       | rate constant   |
| $r_{kin}$ | reaction rate, mol/kgw/s                                |
| $e$       | relative roughness, error                               |
| $Re$      | Reynolds number   |
| $n$       | rotational speed, Hz                                    |
| $b$       | set point weight; molality, mol/kgw                     |
| $S$       | source term; reactive surface area, m <sup>2</sup> /kgw |
| $h$       | specific enthalpy, J/kg; height, m                      |
| $s$       | specific entropy, J/(kg-K)                              |
| $c_p$     | specific heat capacity, J/(kg-K)                        |
| $T$       | temperature, °C or Kelvin                               |
| $t$       | time, s   |
| $P_t$     | tube pitch, m   |
| $X_{tt}$  | turbulent-turbulent Lockhart-Martinelli parameter       |
| $x$       | vapor quality   |
| $v$       | velocity, m/s   |
| $V$       | volume, m <sup>3</sup>                                  |
| $W$       | work, W; width, m                                       |
| $z$       | axial distance, m                                       |

## Greek symbols

|               |   |
|---------------|---|
| $\gamma$      | activity coefficient  |
| $\sigma$      | Boltzmann constant, $1.38064852 \cdot 10^{-23} \text{ m}^2\text{-kg}/(\text{s}^2\text{-K})$ |
| $\beta$       | corrugation angle   |
| $\Delta$      | difference  |
| $\mu$         | dynamic viscosity, Pa-s; chemical potential; nozzle opening                                 |
| $\eta$        | efficiency  |
| $\emptyset$   | enlargement factor  |
| $\phi$        | fugacity coefficient  |
| $\zeta$       | gas-electrolyte interaction parameter   |
| $\alpha$      | heat transfer coefficient, $\text{W}/(\text{m}^2\text{-K})$                                 |
| $\theta$      | inclination angle   |
| $\pi$         | pressure ratio  |
| $\lambda$     | thermal conductivity, $\text{W}/(\text{m}^2\text{-K})$ ; gas-ion parameter                  |
| $\varepsilon$ | void fraction   |

## Subscripts and superscripts

|        |                             |
|--------|-----------------------------|
| $\phi$ | apparent                    |
| $AQ$   | aqueous                     |
| $a$    | aqueous; air; annulus       |
| $B$    | boiling                     |
| $c$    | casing                      |
| $cem$  | cement                      |
| $cd$   | condensation                |
| $crit$ | critical                    |
| $e$    | earth                       |
| $ev$   | evaporation                 |
| $F$    | fan                         |
| $F$    | friction; forced convection |
| $j$    | gas                         |
| $G$    | gas                         |
| $g$    | geothermal fluid            |
| $H$    | heterogeneous; hydrogen ion |
| $h$    | hydraulic                   |
| $inj$  | injection                   |

|            |                         |
|------------|-------------------------|
| <i>i</i>   | inner; species; salt    |
| <i>is</i>  | isentropic              |
| <i>L</i>   | liquid                  |
| <i>m</i>   | mineral; master species |
| <i>nu</i>  | neutral                 |
| <i>NA</i>  | non-aqueous             |
| <i>o</i>   | outer                   |
| <i>k</i>   | phase                   |
| <i>pp</i>  | pinch-point             |
| <i>P</i>   | pump                    |
| <i>r</i>   | reaction                |
| <i>sat</i> | saturation              |
| <i>s</i>   | solid; shell-side       |
| <i>t</i>   | tube; time              |
| <i>T</i>   | turbine                 |
| $\phi^2$   | two phase               |
| <i>V</i>   | vapor                   |
| <i>w</i>   | wall                    |
| <i>wb</i>  | wellbore                |
| <i>wf</i>  | working fluid           |
| <i>y</i>   | year                    |

# 1

## INTRODUCTION

Geothermal power development would constitute one of the alternative ways to mitigate the global warming for the conservation of global scale environment due to the carbon dioxide gas emission of very low content from the power plants. Geothermal power plants provide base-load electricity with no fuel cost. Thus, providing “infinite” source of energy once it has been tapped from beneath the earth. Currently, the total globally installed capacity amounts to about 12 GWe, in 24 countries, with a total production of 76 TWh/yr. So far, practically all power plants use hydrothermal resources. Geothermal power generation started in 1904 in Larderello, Italy. In earlier days, reservoirs with dry steam have been tapped, later also those with steam/water mixtures. Such high-temperature fields ( $> 200$  °C in less than 2 km depth) are mostly located in volcanic areas and are correspondingly rare [Rybach, 2014]. Only a few of them are dry steam dominated with the average power plant size is about 50 MWe. While, the majority is of the low to mid-enthalpy type.

The distribution of geothermal energy as a function of the resources temperature and the potential have been evaluated recently by [Stefansson, 2005]. More than 70% of the geothermal resources available in the world are water dominated fields, at temperatures under 150 °C and pressure below 15 bars. From a general correlation between the existing geothermal high-temperature resources and the number of volcanoes, the total expected geothermal potential has been estimated being about 200 GWe worldwide.

In 2050, geothermal electricity generation could reach 1,400 TWh per year, i.e. around 3.5% of global electricity production [IEA, 2011]. With advanced technology such as binary power plants, it is now possible to convert heat from fluid with lower temperatures (100–190 °C) to power. But the conversion efficiency is correspondingly low (a few percentage points only) and the plant size is also limited (only a few MWe). Figure 1. 1 shows a global comparison between geothermal and the other generation technologies, regarding Levelized cost of energy and Levelized cost of avoided energy. One can observe that conventional geothermal provides the lowest LCOE (3.7 to 8.5 cents US\$/kWh).

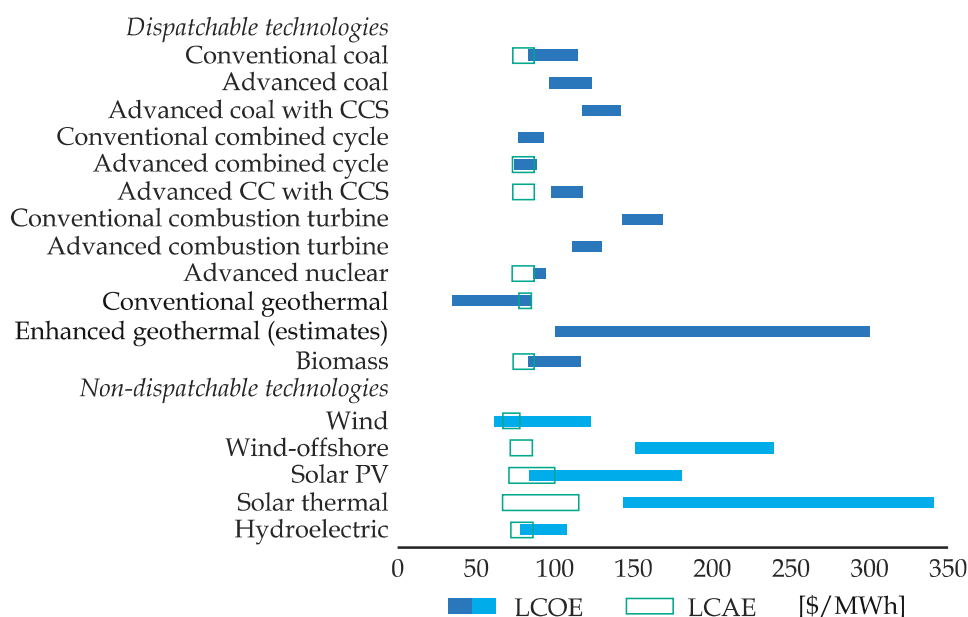


Figure 1. 1: Levelized and avoided cost of power generation technologies (adapted from EIA [2015] and Huenges [2014]).

The binary cycle technology with Organic Rankine Cycle (ORC) seems to be the most efficient and convenient solution for water-dominant resources with a temperature lower than 190 °C thus increasing the number of reservoirs that can be used. In these plants, the thermal energy of the fluid is transferred through a heat exchanger to a binary conversion cycle in which a secondary fluid (usually a refrigerant, a hydrocarbon or a mixture) works in a closed cycle. Electricity generation using low-temperature heat sources is characterized by relatively low conversion efficiencies (about 8-10%), but the binary power plants have a low environmental impact due to the “confinement” of the geothermal fluid and the almost total reinjection [DiPippo, 2008].

Indonesia’s estimated conventional hydrothermal geothermal resource base is considered to be among the largest in the world. The Government of Indonesia plans to achieve around 6,000 MW of installed geothermal power capacity by 2020, a more than a fourfold increase of the end-2012 capacity of 1,335 [Ashat and Adriansyah, 2012]. This aggressive plan will require strong government support to realize. Additional coal-fired power plants will most likely meet any shortfall in the expansion of geothermal power generation capacity. Indonesia has a plenty of untapped geothermal resources, and the remarkable reduction effect of the CO<sub>2</sub> emission can be expected if the geothermal power is used as alternative energy of fossil fuel.



Figure 1. 2: The distribution of geothermal areas in Indonesia [dena, 2012]: 276 geothermal areas and 29 GWel of potential geothermal resources. Circular dashed lines is the symbol for non-volcanic geothermal.

Based on a study of [Fauzi, 2015] the geothermal resource potential of Indonesia is revised down to be approximately 24,000 MWe, some 5,000 MWe less than the 2013 national estimate. It is interesting to note that about 8,000 MWe out of 24,000 MWe resources are classified as non-electrical-grade ( $< 100$  C) to mid-enthalpy (150 to 190 C) resources as defined by Sanyal [2005]. Thus, suitable for binary cycle technology. Albeit the capacity of the mid-enthalpy systems are only approximately one-third of the total potential, they are spread, well distributed as well as in the non-volcanic geothermal, see Figure 1. 2. In Indonesia itself, one study from [Hochstein and Sudarman, 2008] confirms that since the 1960s to 2000s, 130 out of 200 wells (or around 65%) are identified as low to mid-enthalpy wells, suitable for binary cycle technology.

## 1.1 MOTIVATION

As described in the section above, binary cycle technology seems to be a most convenient method to convert widely-spread, mid-enthalpy geothermal potential to electrical power. The key element for a large diffusion of this type of small size geothermal plants is standardization that delivers low costs. Nevertheless, a “standardization” of this energy conversion technology is really difficult, due to the number of different types of the available reservoir, e.g. temperature, pressure, chemical composition [Franco and Vaccaro, 2012].

Figure 1. 3 depicts cost structure of subcritical binary power plants which are adapted from Borealis GeoPower [2016], Sabo [2013], Verkis consulting [2014],

Astolfi et al. [2014], and Chatenay et al., [2014]. The auxiliary cost comprises exploration, management, indirect cost and piping. It can be observed that the factors controlling the overall costs and commercial feasibility of geothermal binary power systems are mainly dependent on the technical system installations: power block and the wellbore. These installations allocate approximately 65 - 80% of the total investment costs.

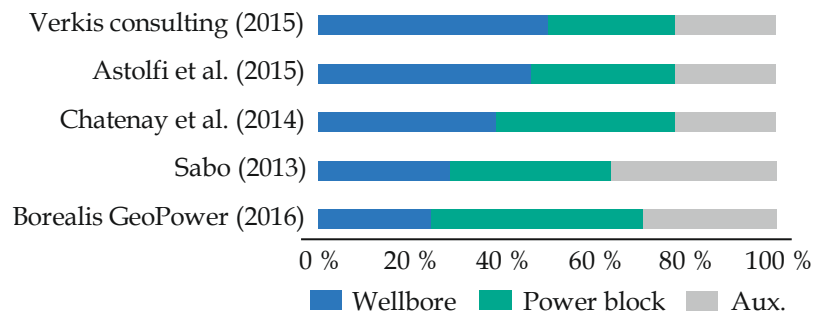


Figure 1. 3: Cost structure of binary geothermal power plants

Backed by this background, the main focus of this research was to enhance the overall economics of geothermal binary cycles as a means of optimum wellbore design and operation. Just as important though by using the wellbore to deliver heat to standardized energy conversion machinery. With this in mind, the overall motivation of this thesis are twofold:

1. To enhance the economics of geothermally fueled Organic Rankine Cycle using modularity and advanced control strategy
2. To gain understanding of thermohydro-chemical (THC) behavior of fluid flow in geothermal wellbores by development of a numerical tool

Proper design of the facilities and their reliable operation require a thermohydro-chemical simulation model. Backed by these motivations, the study was carried out in two parts: modular organic Rankine cycles and reactive wellbore simulator. Figure 1. 4 shows the scheme of the system.

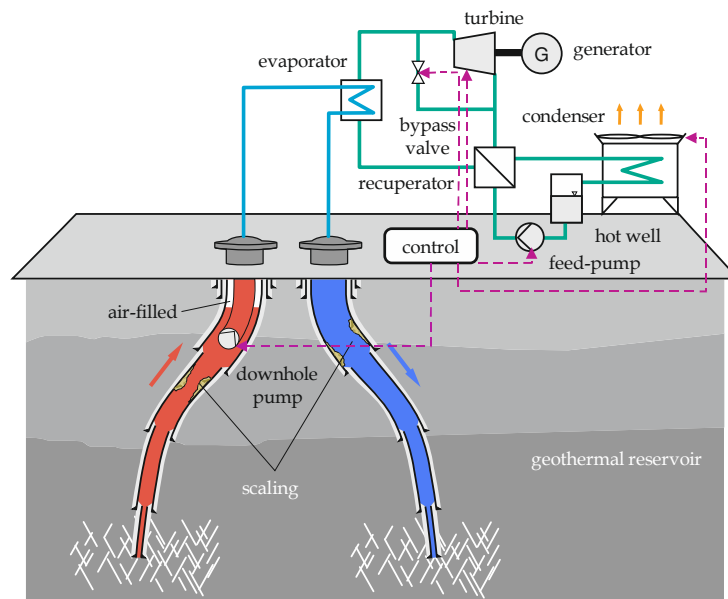


Figure 1. 4: Geothermal installations scheme: Modular with advanced-controlled power block and wellbores.

### *Modular Organic Rankine Cycles*

Modular design is an attempt to fuse the advantages of standardization with those of optimized operation. To demonstrate the cost saving potential by using modular infrastructure, comparison of non-modular and modular scenarios is illustrated in the following, adapted from Dahlgren [2013].

Assume that a firm is planning the future expansion of a power plant that has to satisfy increasing but uncertain demand. As above, the demand increases with probability  $p$  or it stays the same with probability,  $1 - p$ . Demanding that the two scenarios have the same total cost,  $I_{small} = I_{big}$ , and rearranging reveals how much more one is willing to pay for capacity  $nx$  spread out over  $n$  separate investments; that is,  $nK_{small}$  rather than incurring all the cost,  $K_{big}$ , at once. The cost of a big (non-modular) and a small (modular) investment for each increment is denoted by  $K_{big}$  and  $K_{small}$ , respectively. With a constant discount rate  $r$ . As can be seen in Figure 1. 5a, the ratio  $nK_{small}/K_{big}$  increases almost linearly in  $n$ , number of modular increment. For instance, with  $r/p = 0.2$  as in Figure 1. 5a, considering 10 years of demand increase the total investment cost  $10 \cdot K_{small}$  of the modular strategy is allowed to be over twice that of the one-off investment cost  $K_{big}$  yet still produce an equivalent present value of the total cost.

Mass-produced modular technology that is manufactured to stock can significantly reduce the lead time to deploy a new investment. We next examine how shorter lead times can be beneficial in term of total investment costs.

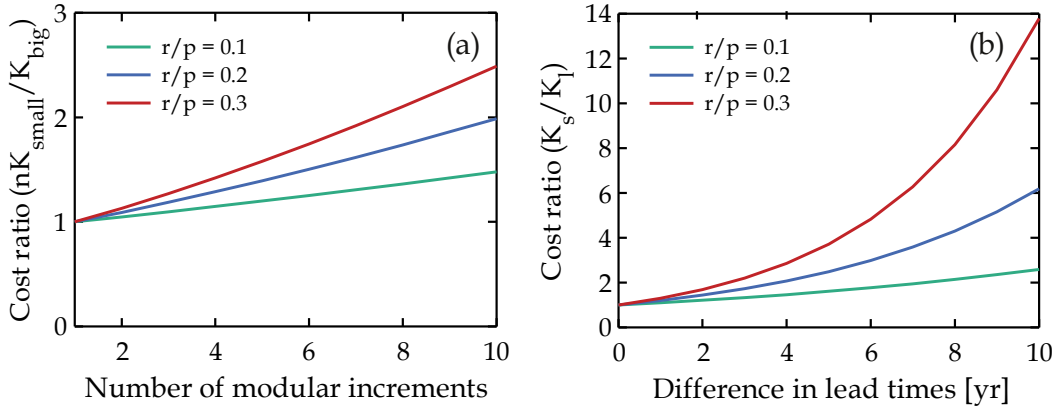


Figure 1. 5: Small modular powerplant cost advantages: discounted total capital cost (a) and lead time (b) reduction. Modified from Dahlgren et al. [2013].

A difference in lead time of only a few years can for reasonable values of  $\rho$  compensate for significant increases in capital cost. The effect is illustrated in Figure 1. 5b. For example, at  $r/p = 0.2$  a difference in lead time of 4 years can make up for a factor of 2 increase in the cost of the short lead time technology. Assuming that  $p = 20\%$  and  $r = 5\%$ , if the lead time for construction decreases by 3 years, this can lead to potential cost savings of 45–50%.

The attractiveness of the shorter lead time scenario is obviously compounded at greater values of  $r/p$ . The reasons are the same as in the preceding section; increasing the discount rate,  $r$ , lowers the present value of future costs and decreasing the probability  $p$  of a demand increase has the consequence of further deferring these costs in the future.

In addition to potential cost-saving, modular powerplant offers higher flexibility, e.g. to function efficiently at various resource and ambient temperatures, load demand, and adapt to wellhead temperature changes during power production.

*Reactive wellbore simulator*

With the high cost of drilling wells, there is a lot of interest in reviewing how wellbores could be used more productively. Thus, wellbore simulation is of great importance for a variety of geothermal production-operation calculations, including well drilling and completion, stimulation, controlling mineral scaling, and analyzing pressure-transient test data. The availability of reliable downhole pressure data during hydraulic tests is of crucial importance for interpreting the behavior of the underground system. Especially in the case of enhanced geothermal system (EGS), the high pressure and temperature conditions make downhole measurements rather a challenge and expensive. Downhole pressure/temperature can be measured with  $p - T$  tools either at a constant depth for the whole duration of operations as a log within a limited period. As experiences at Soultz have shown, data gaps or even incorrect measurements over extended periods occur [Mégel *et al.*, 2005].

Wellbore simulation can also be used to determine if idle production wells could be flowed back to the system or be converted to injection wells. It has been used for modeling marginal recharge effects on production wells and the potential change in performance if the marginal recharge zone is isolated. Another application of wellbore simulation is characterizing active wells. As the reservoir pressure decreases, less productive wells might choke as they may not be able to overcome system pressure anymore or brine production from new wells may also add strain to an injection system. In each case, wellbore simulation can be used to generate a set of deliverability curves for the wells which can then be used to decide how the wells can be managed [Alvarez and Fra-Olahem, 2011]. Various wellbore issues such as scaling and the effect on production should be modeled for mitigation.

Scaling on wellbore casing reduces thermal water flow-rate which lower the well productivity or injectivity. To recover the productivity/injectivity, power producers have to remove the scales by well workover descaling which costs about 100 K to 500 K USD [Valdez *et al.*, 2009] depending on the mineral scales location. Thus, a reactive wellbore simulation is of great importance to predict precipitation amount with regard to time, which leads to the maintenance cost of wells. It is expected to result in a trade-off between well productivity and maintenance cost, optimizing the overall plant operation.

## 1.2 THESIS STRUCTURE

This thesis comprises two main parts, namely modular geothermal ORC and reactive wellbore simulator. The first part consists of two studies, as well as the second part. Three studies are published in or submitted to international journals. One study is issued in international conference proceedings.

In Chapter 2, the basic physical phenomena in specific studies are described and the governing and constitutive equations are summarized. In the subsequent four Chapters, specific studies are presented, as outlined below. Finally, discussion and concluding remarks are reported in Chapter 7.

### *Part I. Modeling and Optimization of Modular Geothermal Organic Rankine Cycles (ORC)*

#### *Control-strategy optimization of modular ORC*

In Chapter 3, I developed Multiple Input Multiple Output (MIMO) control strategies for geothermally fueled ORC, which correlates three measured parameters to control three operating parameters controlled by the turbine, pump, and condenser fans. The objective of the first study of the thesis is to model the small-scale geothermal ORC, to validate the heat transfer model with commercial code results, and implement it to develop modular geothermal ORC. Additionally, dynamic characteristic analysis and optimization of the power plants is also carried out.

#### *Modularization technique for geothermal ORC*

In the study presented in Chapter 4, a method to standardize ORC for various wellhead temperatures (120–170 °C), mass flow rates and ambient temperatures (–10–40 °C) has been devised. Thermal-economic criteria are determined to optimize ORC plant dimensions for such applications. The multiple-input-multiple-output (MIMO) control strategy was implemented, to maximize net power production at off-design conditions.

## *Part II. Thermohydro-Chemical Geothermal Wellbore Simulator*

### *Two-phase multicomponent geothermal fluid properties*

gEOSkit, an Equation of State (EOS) solver for geothermal fluids using pressure and enthalpy as independent variables, has been developed, as described in Chapter 5. By using a combination with speciation solvers, the aim is to provide an efficient tool for two-phase geochemical transport simulation in wellbores. An improved gas activity coefficients based on the extension of neutral interactions for the dissolved gasses is developed. The solver is established in the object-oriented scheme to facilitate extension of other salt and gas components. The validity of the solver presented here is evaluated using the experimental data from literature and online field-measurements.

### *Numerical modeling of two-phase deep geothermal wellbores*

WellboreKit, a model for calculating thermal, hydraulic, and chemical (THC) behavior during (de-)pressurization of a two-phase (aqueous and non-aqueous) multicomponent geothermal fluid in the deep wellbore, is presented (see Chapter 6). It is a reactive wellbore simulator established in collaboration with European Institute for Energy Research (EIFER). The code is developed in coupled Elmer-Python-PHREEQC open-source platform and can simulate transient mass flow, pressure, temperature, and chemical species concentration and saturation profile. A sequential coupling between transport and (de-)compression with heat transfer of geothermal fluid-rock formation is implemented by using operator splitting method.

# 2

## BASICS

The purpose of this chapter is to explain briefly the concepts of fluid that works in geothermal energy conversion systems and the relevant terms that will be mentioned to frequently in this thesis. First, the criteria of a geothermal reservoir and secondary fluids are discussed. Then modeling method of the fluid thermohydro-chemical (THC) state changes, i.e. pressure, enthalpy, temperature, species concentration and saturation for geothermal technical installations are presented.

### 2.1 GEOTHERMAL WORKING FLUIDS

Fluid works in geothermal energy conversion systems comprise of the reservoir as primary fluid and, in the case of a binary cycle, secondary fluid. High-enthalpy geothermal reservoirs are normally hosted in fractured volcanic rock and can be both in the area and in thickness. Low to mid-enthalpy geothermal reservoirs are regarded as deep formation water [Bozau *et al.*, 2015]. The reservoir fluid is as a water-salt-gas mixture. Conventional hydrothermal reservoir fluid thermophysical properties can be viewed as pure water. Increasing development of enhanced geothermal system (EGS) reservoirs which typically are located at greater depth, is most likely expected to results in the presence of non-negligible salt and gas.

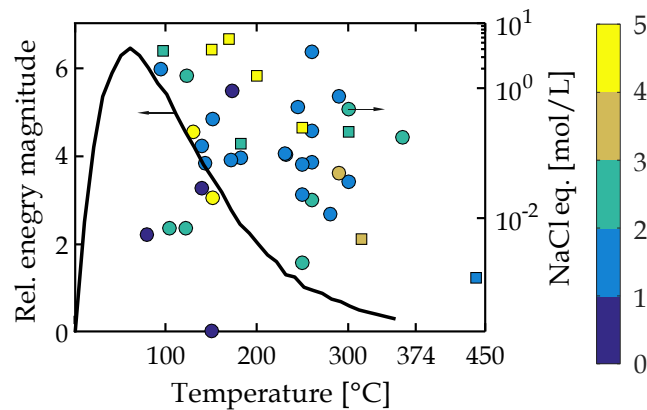


Figure 2. 1: Approximated worldwide distribution and salinity of geothermal resources adapted from Stefansson [2005]: Salinities of various geothermal resources (filled circles - hydrothermal system; filled squares - enhanced geothermal system) as a function of depth (1 - 5 km as scaled on the color bar).

Figure 2. 1 shows the distribution of geothermal energy magnitude (in relative unit) as a function of the reservoir temperature. It can be seen that the low temperature resources, having temperatures of 130 °C or lower comprises 68% of the total geothermal energy considered, whereas the remaining 32% of the total are resources with temperature higher than 130 °C [Stefansson, 2005]. The salinity (TDS) of those resources are varying and independent of the reservoir temperature, ranging from almost zero to 10 mol/L NaCl equivalent.

The salt and gas component as impurities can contain up to around 30 different species'. Thus, it is regarded as multicomponent fluids. However, relationship between depth or temperature and salinity is not clear. The thermophysical properties and saturation index of minerals are mainly affected by major electrolytes, e.g. Na-Ca-K-Mg-Cl and major gases, e.g. CO<sub>2</sub>-H<sub>2</sub>S-N<sub>2</sub>-CH<sub>4</sub>. The rest of the chemical species' is only affect in speciation process.

Second, the secondary working fluid for the binary cycle. This fluid is used to extract heat from low to mid-enthalpy reservoir fluid to produce heat and electricity. After Vetter [2013] the binary working fluid should among other things meet the following criteria:

- Low critical pressure and temperature (compared to water)
- Low specific volume
- High thermal conductivity
- Non-corrosive, toxic or flammable and stable

Also, low ozone depletion potential (ODP) and a low greenhouse warming potential (GWP) are important requirements for the suitability of the working fluid. Figure 2. 2 shows the wet vapor areas of different organic media in the  $T - s$  diagram. The two-phase region of water is also included for comparison.

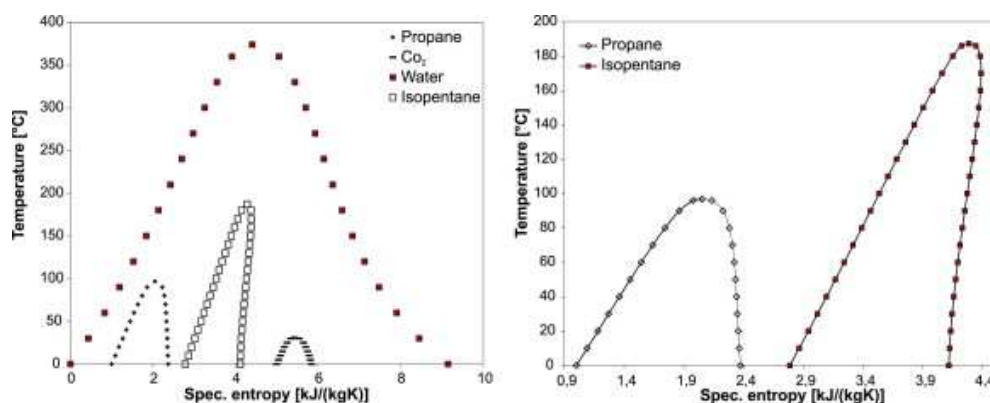


Figure 2. 2: Two-phase regions of some organic fluids and water from Vetter [2013].

Based on gradient of the vapor line, secondary working fluid can be classified as dry (retrograde) and wet fluids. Water with a negative dew line slope is a wet fluid, but many organic media are retrograde which have a dew line with at minimum a limited positive slope (like isopentane, Figure 2. 2). In wet media, the vapor need to be superheated, to prevent the development of droplets at the turbine outlet. For retrograde fluids, no superheating is required since the expansion of in the two-phase region is thermodynamically not possible. Conversely, the vapor cannot expand to condensing temperature because the expansion occurs in dry vapor region. Thus, a larger part of the supplied heat cannot be used. As a result, in cycles with retrograde fluids, an added recuperator is often used to increase the thermal efficiency. In the recuperator, a part of the rejected heat is used to preheat the working fluid.

The section hereunder describes basics to model the geothermal working fluid state changes in geothermal technical systems.

## 2.2 CONSERVATION EQUATIONS

In this thesis, mass, energy, and momentum balances have been programmed in Distributed Parameters Model, Finite Element solver Elmer [Råback *et al.*, 2016] and have been implemented in Finite Volume solver TIL/Dymola [Richter, 2008]. These tools are used in next specific studies on advanced control strategy, modularization, and reactive wellbore simulator. For reactive wellbore simulation, the chemical reactions modeled include aqueous complexation, adsorption, and precipitation-dissolution of minerals, both in equilibrium and kinetic approach via PHREEQC [Parkhurst and Appelo, 1999] and gas exsolution-dissolution via gEOSkit, an equation of state for two-phase multicomponent geothermal fluid, see Chapter 5.

### *Mass*

From the continuity condition, the change of mass with regard to time in a control volume is equal to stream (advection) of mass and mass source. Thus, the mass balance of fluid flow is expressed as

$$\frac{\partial \rho}{\partial t} = -\frac{\partial}{\partial z}(\rho v) + S, \quad (2.1)$$

here  $z$  is axial distance along the flow path,  $\rho$  is the liquid density,  $v$  the velocity and  $S$  the external source/sink term. Note that the first term represents the change of mass of liquid, the second the advective transport of liquid and the third is the fluid mass source.

When chemical reactions occur, the species masses are not conserved anymore, only the total mass. Therefore, we use the mathematical formulation for reactive transport developed by Saaltink et al. [1998]. According to this formulation, the mass balance of solute transport is written as

$$\begin{aligned} U_a \frac{\partial}{\partial t} (\rho_l w_{H_2O} C_a) + U_d \frac{\partial}{\partial t} (\rho_s C_d) + U_m \frac{\partial}{\partial t} (\rho_s C_m) \\ = U_a \left( -\frac{\partial}{\partial z} (\rho_l w_{H_2O} v_a C_a) + D_a \frac{\partial^2}{\partial z^2} (\rho_l w_{H_2O} C_a) + S \right), \end{aligned} \quad (2.2)$$

where subscripts  $a, d, m$  refers to aqueous species, adsorbed species and minerals, and  $l, s$  refers to liquid and solid phase, respectively.  $w_{H_2O}$  is the water mass fraction (kg of water/kg of solution),  $S$  the external source/sink mass solute term,  $C$  represent the concentrations of the species and  $U$  are the component matrices for all species, which can be computed from the stoichiometric coefficient of the chemical reactions. This matrices relate the total concentration of the component with the concentration of every species, for instance, the component Ca has species Ca (aq) and  $\text{CaCO}_3$ .

### Energy

According to the first principal of thermodynamics, the transient description of the energy state of an open system is obtained from a balance of internal, kinetic, and potential energies. Neglecting the temporal storage of potential energy, the time-dependent change in the internal and kinetic energy is calculated from the convection-induced change in the internal and kinetic energy as well as the heat transferred and the work by pressure and gravitational forces:

$$\frac{\partial}{\partial t} \left( \rho u + \frac{\rho v^2}{2} \right) = -\frac{\partial}{\partial z} \left[ v \left( \rho u + \frac{\rho v^2}{2} \right) \right] + \dot{q} \frac{P}{A} + \dot{W} \frac{P}{A} - \frac{\partial}{\partial z} (vp) + \rho v g \sin(\theta), \quad (2.3)$$

where  $u$  internal energy,  $\dot{q}$  heat flux,  $\dot{w}$  work flux, e.g. pumping work,  $P$  wetted perimeter, and  $A$  cross-sectional area. From the integration of mass and energy balances, we can calculate thermodynamic state in a one-dimensional balance space.

The energy balance is associated with each problem and related to a state variable using constitutive laws which will be described in the following chapter. For a complete description of the fluid flow, the calculation of the pressure drop is necessary, which results from the momentum balance.

### *Momentum*

Corresponding to Newton law of mechanic, the time-dependent change of momentum of bodies is equal to the sum of all the bodies acting forces. The momentum is defined as the product of mass and velocity. A fluid mass  $dm$  flowing with velocity  $v$  gives momentum  $I = v \cdot dm$ .

The time-dependent change of impulse of fluid flows in a control volume with the constant cross-sectional area can be obtained by summing the momentum change of charge and discharge flow, the gravitational force, and the frictional force. The dynamic momentum balance can thus formulate as

$$\frac{\partial}{\partial t}(\rho v) = -\frac{\partial}{\partial z}(\rho v^2) + \rho g \sin(\theta) - \frac{\partial p}{\partial z} + \left(\frac{\partial p}{\partial z}\right)_F \quad (2.4)$$

This formulation of momentum balance allows the description of fast pressure dynamics. The time derivative of the momentum of the control volume  $\partial(\rho v)/\partial t$  is assumed to be zero which is reasonable as long as fast dynamic processes, e.g. sound propagation, are not considered [Casella and Leva, 2006].

## 2.3 HEAT TRANSFER AND PRESSURE DROP

In the one-dimensional simulation, to close the energy and momentum equations, constitutive relations are required. The equations describe heat transfer and pressure drop phenomena by using empirical correlations derived from experimental data. Albeit their empirical characteristic which limits the range of validity, some correlations are generic and thus useful to describe the physical phenomena occurred in the modeled systems. Other constitutive relations, i.e. fluid-rock heat transfer, annulus heat transfer will be described in the individual study within this thesis.

Calculation of heat transfer coefficient of fluid in forced convection single-phase flow and two-phase flow, such as that occurring during boiling, should be distinguished depending on the flow cross-sectional area. Additionally, each must be defined differently between laminar and turbulent flow. Turbulent flow is mainly found for applications in this thesis. Detailed correlations used in the individual study are described here. Nevertheless, two-phase heat transfer of flow through tube bundle is explicitly defined in Chapter 4.

### Single-phase heat transfer in tube/plate channel

The basic equation describes turbulent forced convection by means of the non-dimensional relationship inspired from well-known Dittus-Boelter [1930] equation as

$$Nu = c \cdot Re^m Pr^n \quad (2.5)$$

where the influence of temperature-dependent viscosity is neglected. Parameters  $m$ ,  $n$ , and  $c$  depends on plate pattern and geometrical parameter. The exponents  $m$  and  $n$  are set according to recommendations for corrugated plate heat exchangers.  $m$  is associated mainly on flow regime (laminar or turbulent) and ranges between 0.5 to 0.8,  $n$  is commonly 0.33.

The constant  $c$  can be defined from scientific literatures (see Table 2. 1), or identified with experimental data later on. This is done by minimizing the difference between predicted and measured values for a set of working points.

| Description  | References                | Equations   |
|--|---------------------------|---|
| Tube channel.<br>$0.7 \leq Pr \leq 16,700$<br>$Re \gtrsim 10,000$<br>$L/d \gtrsim 10$                                    | [Sieder and Tate, 1936]   | $Nu = 0.027Re^{0.8}Pr^{0.33}$   |
| Plate channel: Extending the Leveque theory.<br>The range of validity is not explicitly given in the original reference. | VDI [Martin, 1996]        | $Nu = c_q Pr^{1/3} (\mu/\mu_w)^{1/6} [2Hg \cdot \sin(2\beta)]^q$<br>$\xi Re^2 = 2 \frac{\rho \Delta p d_h^3}{\mu^2 L} = 2Hg$<br>, with constants $c_q = 0.122$ is geometric parameter, $q = 0.374$ is based on experiment data, and $\xi$ is derived from the pressure drop correlation (see eq. (2. 13)) |
| Pure water flow in plate channel<br>$30 \leq \beta \leq 60$<br>$Re \geq 1,000$<br>$1 \leq \phi \leq 1.5$                 | [Muley and Manglik, 1999] | $Nu = [0.2668 - 0.006967\beta + 7.244 \times 10^{-5}\beta^2] \times [20.78 - 50.94\phi + 41.16\phi^2 - 10.51\phi^3] \times Re^{[0.728+0.0543\sin(\pi\theta/45+3.7)]} Pr^{1/3} (\mu/\mu_w)^{0.14}$<br>for $Re \geq 1000$   |

Table 2. 1: Heat transfer correlations for fluid flowing in tube or plate channel.

For organic fluid flow in plate channel, VDI correlation [Martin, 1996] is preferred in this study, because this correlation has a wider applicability due to the possibility of adjusting to experimental data [Claesson, 2004].

### *Single-phase heat transfer of flow through tube bundle*

The heat transfer coefficient of single-phase fluid flowing through tube bundle may be expressed by simplified Delaware [Serth, 2007], as

$$\alpha = 0.5(1 + B/d_s)(0.08Re_s^{0.6821} + 0.7Re_s^{0.1772}) \cdot (\lambda/d_{eff})Pr^{0.33} \quad (2.6)$$

with Reynolds number  $Re_s = \dot{m} \cdot d_{eff}/(A_s\mu)$ , flow effective diameter  $d_{eff} = 4C_L P_t^2 - \pi d_o^2/\pi d_o$ , and flow effective cross-sectional area  $A_s = d_s C_a B/P_t$ . Other geometric variables,  $C_L$ ,  $C_a$ ,  $B$ , and  $P_t$  are defined as pitch factor (1.0 for square, 0.86 for triangular), clearance, baffle spacing, and tube pitch respectively.

### *Evaporation heat transfer in plate channel*

Organic fluid two-phase heat transfer in chevron corrugation plate channel is modeled using correlations available in the literature. The literature covering two-phase flows in plate heat exchanger is still limited, and most of them are for refrigeration applications which have saturation temperature range  $-25 \leq T_{sat} \leq 20$  °C, compared to ORC applications  $80 \leq T_{sat} \leq 200$  °C. In the refrigeration applications, those few correlations lead to very high discrepancies in the prediction of the heat transfer coefficient. Garcia-Cascales et al. [2007] compared 4 boiling heat transfer correlations and 5 condensation heat transfer correlations and showed that the predicted coefficients can vary in a ratio as high as 1 to 7. In the model used in this study, the evaporation heat transfer coefficient is estimated with an expression of the Hsieh [2002] correlation below

$$\alpha_{ev} = \alpha_L (c \cdot Bo^{0.5}), \quad (2.7)$$

where  $Bo = \dot{q}/(G \cdot h_{LG})$  is the boiling number and  $\alpha_L$  is the all-liquid non-boiling heat transfer coefficient (see eq. (2.5)). The correlation was developed with a 60° chevron angle and results coefficient  $c$  of 88. The heat transfer coefficient is assumed to be constant during the whole evaporation process. This is selected because the Boiling number constant can be easily adjusted later with experimental data. The evaporation heat transfer is quality-dependent. However, in this model, an average heat transfer coefficient is considered by integration with regard to quality.

### Condensation heat transfer in tube channel

The condensation of the organic fluid takes place in horizontal or slightly inclined pipes, which are circulated vertically by cooling air. Thus, the condenser is a cross-flow heat exchanger.

For the calculation of the heat transfer on the ORC side during the simulation and the design of the condenser, the correlations from Dobson-Chato [1998] and Yu-Koyama [1998] are used. These correlations are not part of the TIL library but have been implemented in the existing models thanks to an object-oriented approach. For smooth inner tube, the Dobson-Chato [1998] is implemented,

$$Nu = 0.023 Re_L^{0.8} Pr_L^{0.4} \left[ 1 + \frac{2.22}{X_{tt}^{0.89}} \right]. \quad (2.8)$$

For the microfinned tube, Yu-Koyama [1998] correlation is used, as written in the following.

$$\begin{aligned} Nu &= (Nu_F^2 + Nu_B^2)^{0.5} \\ Nu_F &= 0.152 (\emptyset_v / X_{tt}) Re_L^{0.68} (0.3 + 0.1 Pr_L^{1.1}) \\ \emptyset_v &= 1.1 + 1.3 \{ G^{0.35} X_{tt}^{0.35} / [g d_i \rho_V (\rho_L - \rho_V)]^{0.75} \} \\ Re_L &= G(1-x) d_i / \mu_L \\ Nu_B &= 0.725 H(\varepsilon) [Ga \cdot Pr_L / (Ph_L \mu_A)]^{0.25} \\ Ga &= g \rho_L^2 d_i^3 / \mu_L^2 \\ H(\varepsilon) &= \varepsilon + \{10(1-\varepsilon)^{0.1} - 8.0\} (\varepsilon)^{0.5} [1 - (\varepsilon)^{0.5}] \\ \varepsilon^{-1} &= 1 + [(1-x) \rho_V / (x \rho_L)] \{0.4 \\ &\quad + 0.6 [x(\rho_L / \rho_V) + 0.4(1-x)]^{0.5} / [x + 0.4(1-x)]^{0.5} \}, \end{aligned} \quad (2.9)$$

where  $X_{tt}$  turbulent liquid - turbulent gas Lockhart-Martinelli factor,  $d_i$  mean inner diameter,  $Ph_L = c_{p,L}(T_s - T_w) / h_{LG}$ .  $T_s$  and  $T_w$  are defined as saturation and tube wall temperature and  $h_{LG}$  latent enthalpy.

The pressure drop due to the friction of fluid flow can be distinguished into single-phase and two-phase for each flow area type. In the following, we presented pressure drop correlations for both phases. The constitutive relations described in this section is applied to close the momentum equations.

Two approaches are used to calculate two-phase pressure drop: By using one-fluid assumption and two-phase multiplier applied to equation below

$$\left(\frac{\partial p}{\partial z}\right)_F = f_k \frac{G^2}{2d_h \rho}, \quad (2.10)$$

where  $f_k$  is friction factor phase  $k$ . For one-fluid approach, the mass-flux and the density are assumed as effective two-phase mixture. By implementing the two-phase multiplier approach, the single-phase (liquid or gas) mass flux and density are used.

#### *Single phase pressure drop in tube channel*

Application of single-phase flow through tube channel in this study includes geofluid flow in the evaporator, condensers, and wellbores. To compute single-phase Darcy friction factor in tube channel Fang [2011] correlation is used.

$$f = 1.613 \left[ \ln \left( 0.234(e/d_i)^{1.1007} - \frac{60.525}{Re^{1.1105}} + \frac{56.291}{Re^{1.0712}} \right) \right]^{-2} \quad (2.11)$$

where  $Re$ ,  $e$ ,  $d_i$  are Reynolds number, relative roughness, and inner diameter, respectively. For low Reynolds number or laminar flow, we use theoretically maximum friction factor for laminar flow

$$f = 64/Re. \quad (2.12)$$

As mentioned before, for the one-fluid assumption, eqs. (2.11) - (2.12) are applied to predict two-phase pressure drop using two-phase mixture Reynolds number  $Re_m$ .

### *Single phase pressure drop in plate channel*

The pressure loss in plate heat exchangers depends on the chevron angle  $\theta$ , which describes the rotation of the panels to the main flow direction. In the range  $0^\circ$  to  $90^\circ$  applied VDI Heat Atlas [2010] correlation for the friction factor.

$$\begin{aligned}
 f_0 &= \frac{c_0}{Re} \text{ for } Re < 2,000 \text{ (laminar)} \\
 f_0 &= (1.8 \log Re - 1.5)^{-2} \text{ for } Re \geq 2,000 \text{ (turbulent)} \\
 f_{1,0} &= \frac{c_1}{Re} + c_2, Re < 2,000 \\
 f_{1,0} &= \frac{c_3}{Re^n}, Re \geq 2,000 \\
 f_1(Re) &= c_4 \cdot f_{1,0}(Re) \\
 \frac{1}{\sqrt{f}} &= \frac{\cos\theta}{\sqrt{c_5 \cdot \tan\theta + c_6 \cdot \sin\theta + f_0(Re)/\cos\theta}} + \frac{1 - \cos\theta}{\sqrt{f_1(Re)}}
 \end{aligned} \tag{2.13}$$

where  $c_0 = 64$ ,  $c_1 = 597$ ,  $c_2 = 3.85$ ,  $c_3 = 39$ . The  $f_0$  and  $f_1$  denote friction factor at chevron angles of  $0^\circ$  and  $90^\circ$ . Constants  $c_4$ ,  $c_5$ , and  $c_6$  are adjusted by experimental data with the typical value of 3.8, 0.18, 0.36, respectively.

### *Single phase pressure drop of air flow through finned tube bundle*

For single-phase through the finned tube bundle flow channel, Haaf [1988] correlation for air passing finned-tube is employed. The equation is quasi-similar with eq. (2.10) formula and can be written as

$$\Delta p_a = N_t \cdot c \cdot Re^{-1/3} \left( \frac{d_{eq}}{P_t} \right)^{0.6} \cdot \left( \frac{P_t}{d_{eq}} \right) \left( \frac{G_a^2}{2 \rho} \right), \tag{2.14}$$

with the coefficient  $c$  of 10.5. For standard design purpose, the GPSA [2004] correlation was used for its simplicity. It uses specific correlations that are different from that one of eqs. (2.14). The air (fin-side) static pressure drop is derived using power regression from GPSA chart for fan static pressure as follows

$$\Delta p_a = (1.1245 \cdot 10^{-10}) \cdot G_a^{1.8}, \tag{2.15}$$

where  $G_a$  is air mass flux (kg/m<sup>2</sup>-s). The regression has R<sup>2</sup> value of 0.99. Approximation fan total pressure (PF, in Pa) using inlet air density if using forced draft fan or outlet air density if using induced draft fan, can be calculated as

$$PF = \Delta p_a + \left[ \frac{\dot{V}}{12.7 \left( \frac{\pi d_F^2}{4} \right)} \right]^2 \frac{\rho}{\rho_{(21^\circ\text{C})}}, \quad (2.16)$$

with  $\dot{V}$  is air volumetric flow (m<sup>3</sup>/s), and  $\rho_{(21^\circ\text{C})}$  is air density at 21 °C.

#### *Two-phase pressure drop in tube channel*

In this study, it is desirable to express the two-phase frictional pressure gradient in tube channel, versus the total mass flux in a dimensionless form like the Darcy friction factor versus the Reynolds number, especially for wellbore simulation. The two-phase Darcy friction factor can be predicted using the Fang [2011] correlation eq. (2.11) implementing one-fluid, heterogeneous two-phase mixture.

#### *Evaporation pressure drop in tube bundle*

Once a phase change occurs in the heat exchangers, the transport of thermal energy depends on the thermodynamic states of all the present phases. For the boiling on tube bundle, one may use two-phase multiplier to extend single-phase pressure drop friction factor  $f_{\phi^2} = c_{\phi^2} f_{sp}$  in eqs. (2.11) and (2.12). To model boiling organic fluid, two-phase multiplier from Grant [1977] is used,

$$\begin{aligned} c_{\phi^2} &= 1 + \left[ Y \left( \frac{\rho_L f_G}{\rho_G f_L} - 1 \right) \right] \\ Y &= x + 0.15\sqrt{x} \text{ for } x \\ Y &= x + 0.15\sqrt{x} - 0.16x^{400}, \end{aligned} \quad (2.17)$$

with subscripts  $L, G$  denote liquid and gas phase, respectively. The two-phase multiplier is based on liquid phase. Thus, to compute two-phase pressure gradient, liquid mass flux and density are employed into eq. (2.10).

*Evaporation pressure drop in plate channel*

For boiling organic fluid in plate flow channel, the two-phase Darcy friction factor from Hsieh-Lin [2002] is implemented.

$$f_{\phi^2} = c \cdot Re_{eq}^{-1.25} , \quad (2.18)$$

with coefficient  $c$  of 61,000, equivalent Reynolds number  $Re_{eq}$  is defined by using equivalent mass flux (as a function of quality and density, see Hsieh-Lin [2002]) and the pressure gradient is calculated by eq. (2.10).

## 2.4 GEOCHEMICAL REACTIONS

A geochemical system comprises a set of atomic elements. The basic components of this systems are the chemical species that are defined as any chemical entity distinctive from the rest due to its elemental composition and by the phase at which it is existing. For example, CO<sub>2</sub> gas is different species than dissolved CO<sub>2</sub>. Not all the species are needed to describe the composition of an aqueous system [Saaltink *et al.*, 1998]. The reactions taking place in the system can be presented as linear combinations of the different species with its stoichiometric coefficient in the reaction. Hence, there is a division of chemical species (secondary species) that can be expressed as a linear combination of the remaining species (primary species). In this way, the primary species can fully describe the chemical system and the rest of the species are related to them. This approach leads to a significant reduction of the number of variables and the computational cost. Most hydro-chemical processes in groundwater are nearly fast and can be effectively considered as equilibrium reactions [Garcia, 2009]. Therefore, all the reference chemical reactions in this thesis (see Chapter 6) will be imposed as such. Different reactions like aqueous complexation, dissolution and precipitation of minerals will be take into account.

### 2.4.1 Dissolution and precipitation of minerals

Under equilibrium conditions, dissolution/precipitation reactions can be described by the law of mass action. Any form of equilibria in water can be described by the law of mass action which formulates that for a generalized reaction type  $aA + bB + \dots \leftrightarrow cC + dD + \dots$ , the distribution at equilibrium of the species at the left and right side of the reaction is given by

$$K = \prod_i^{I_{aq}} a_i^{c_i} \prod_m^{M_{aq}} a_m^{-c_m} = \frac{\{C\}^c \{D\}^d \dots}{\{A\}^a \{B\}^b \dots} , \quad (2.19)$$

$K$  is the equilibrium constant while the bracketed quantities denote effective concentration or activity of the species. Main consideration is that the law of mass action is only valid for the activity of ions, which is the measured total concentration corrected for the effects of electrostatic shielding and for the presence of aqueous complexes [Appelo and Postma, 2005]. This law applies to any type of reaction including mineral dissolution in water, establishment of complexes between dissolved species. For mineral dissolution the activity of a solid phase is taken as 1, which means the equilibrium constant is left as  $\{C\}^c \{D\}^d \dots$ , which is defined later to be dependent on temperature and pressure. The equilibrium condition only provides a correlation between the variables involved in the aforementioned equation. This equation does not include the concentration of the solid phase and therefore the amount of dissolved/precipitated mineral cannot be computed.

In order to calculate amount of dissolved/precipitated minerals, the saturation index (SI) has to first be known. This index indicates dissolution or precipitation of minerals by comparing ion activity product (IAP) with the equilibrium constant,  $SI = IAP/K$ . If  $SI = 1$  represents equilibrium;  $SI > 1$  represents supersaturation;  $SI < 1$  represents subsaturation. IAP is calculated using actual activities of species, which are computed using Debye-Hückel [1923] equation for low ionic strength and Pitzer [1973] equation for high ionic strength. When SI exceed 1, the concentration change of aqueous species before and after reaction can be interpreted as amount of precipitated minerals.

Determination of the equilibrium constant should take temperature into account although it is usually specified at conditions of 25°C and 1 atm. These standard conditions do not always apply to reservoir fluid where temperatures are higher and also disposed to variations. Equilibrium constants  $K$  is temperature dependent and defined as [Appelo and Postma, 2005]

$$\frac{d(\ln K)}{dT} = \frac{\Delta H_r}{RT^2} , \quad (2.20)$$

where  $\Delta H_r$  is the reaction enthalpy, heat gained or lost by the system ( $\Delta H_r$  is exothermic if negative, and endothermic if positive). This equation reveals that  $K$  increases with temperature for positive  $\Delta H_r^0$  and  $K$  decreases with temperature for negative  $\Delta H_r^0$ , where  $\Delta H_r^0$  is at a standard state analogous to  $\Delta G_r^0$ . For

minerals which have non-linear relationship between  $\log K$  value and temperature, the equilibrium constants  $K$  is modeled by

$$\log(K) = c_1 + c_2T + \frac{c_3}{T} + c_4\log(T) + \frac{c_5}{T^2} , \quad (2. 21)$$

with constants  $c_{1-5}$  are defined in the databases based on best-fit on experimental data.

Pressures usually do not affect the solubility of solids. However, it does affect the solubility of gasses which will be discussed in Chapter 2.5.1 regarding vapor-liquid equilibrium. For some minerals, nevertheless, pressure can have a significant effect on its solubility, i.e. anhydrite, gypsum [Appelo *et al.*, 2014], and can be written as

$$\log K = \log K_{p=1} - \frac{\Delta V_r(p-1)}{(2.303 \cdot 10^5)RT} , \quad (2. 22)$$

where  $\Delta V_r$  is the volume change of the reaction ( $\text{m}^3$ ),  $p$  is pressure (bar),  $T$  is temperature (K).

#### 2.4.2 Kinetics of geochemical reactions

Mineral concentration in a fluid during dissolution is followed as a function of time. In the beginning, the mineral concentration will increase sharply with time but eventually the rate of increase drops until equilibrium between mineral and water is achieved. At this (saturation) point the mineral stops precipitated. The reaction of a mineral can be followed by observing at its concentration as a function of time. The reaction rate  $r$  (in mol/kgw/s) is expressed in terms of the change in concentration of any of the reacting components with respect to time

$$r_{kin} = \pm k \cdot S \left| 1 - \left( \frac{IAP}{K} \right)^p \right|^q , \quad (2. 23)$$

with temperature-dependent rate constant (mol/m<sup>2</sup>/s)  $k$ ,  $S$  surface area (m<sup>2</sup>/kgw), saturation index (SI)  $IAP/K$ . This rate equation can be derived from transition-state (linear) theory, where the coefficient  $p$  and  $q$  are related to the rate law used. Often,  $p$  and  $q$  equal to 1. Alex law [Alekseyev *et al.*, 1997] defines  $p = 0.184$ ,  $q = 4.04$ . Also, Nonlinear Burton-Cabrera-Frank (BCT) law with  $p = 1$ ,  $q = 2$  [Burton *et al.*, 1951]. An advantage of this formulation is that the rate equation applies for both under saturation and supersaturation, and the rate is zero at

equilibrium. The rate is constant over a large region when the geochemical reaction is far from equilibrium ( $IAP/K < 0.1$ ), and the rate approaches zero once  $IAP/K$  approaches 1.0 (equilibrium). Nevertheless, the uncertainties involved with reaction rates are often considerable, which is one of the main reasons to use the assumption of chemical equilibrium.

## 2.5 EQUATION OF STATE FOR GEOTHERMAL FLUIDS

The equation of state of geothermal fluids can be derived from two main functions: vapor-liquid equilibrium and aqueous/non-aqueous (two-phase) properties. Vapor-liquid equilibrium (VLE) describes dissolution and exsolution of gasses, including water evaporation.

### 2.5.1 Fugacity-activity phase partitioning

Given the importance of the water-salt-gas systems in geochemistry and petroleum (geothermal) engineering, in the following, Springer et al. [2012] described briefly various computational models have been developed to represent the properties of such systems. These models are can be classified into two:

1.  $\phi$ - $\phi$  models, in which a homogeneous equation of state is used to compute the properties of both the liquid and gas phases.
2.  $\gamma$ - $\phi$  models, in which an activity coefficient formulation is used to compute the behavior of aqueous solutions while an equation of state provides the fugacity coefficients of components in the gas phase.

The  $\phi$ - $\phi$  approaches have been constructed either by incorporating electrolyte-specific terms into nonelectrolyte equations of state or by combining a classical equation of state with an excess Gibbs energy model for electrolytes. The  $\phi$ - $\phi$  approaches have been shown to be most appropriate for high-temperature systems (i.e., above ca. 300 °C), in which electrolytes exist primarily in the form of ion pairs [Duan and Sun, 2003; Anderko and Pitzer, 1993]. Meanwhile, the existing  $\gamma$ - $\phi$  models are focused primarily on reproducing the solubility of CO<sub>2</sub> in water and aqueous solutions of selected salts. In particular, Duan and Sun [Duan and Sun, 2003; Duan and Mao, 2006] developed gases solubility models using the well-known Pitzer [1973] activity coefficient formulation for the aqueous phase, which are merged and extended in this thesis.

The  $\phi$ - $\phi$  and  $\gamma$ - $\phi$  approaches have their advantages and disadvantages. In principle, the  $\phi$ - $\phi$  approach is more appropriate for systems that transition from the subcritical to supercritical range because it can handle the vapor-liquid critical behavior, at least within the limitations of classical equations of state. Also, it can

reproduce volumetric properties simultaneously with phase equilibria. However, it is much more computationally intensive because the solution of phase equilibrium conditions must be accompanied by solving the equation of state in each phase. The  $\gamma$ - $\varphi$  methods, while much less computationally intensive, impose a division of the phase space into gas-like and liquid-like regions even when such a division is not physically rigorous. However, the  $\gamma$ - $\varphi$  methods are much more amenable to integration with speciation and chemical equilibrium calculations react [Springer *et al.*, 2012], which is one of the ultimate objective of Chapter 5. Therefore, the  $\gamma$ - $\varphi$  approach is more appropriate for this study.

$$\begin{aligned} \mu_j^L &= \mu_j^V \\ \mu_j^{L(0)} + RT \cdot \ln a_j p + RT \ln \gamma_j &= \mu_j^{V(0)} + RT \cdot \ln y_j p + RT \cdot \ln \phi_j, \end{aligned} \quad (2.24)$$

we obtain,

$$\ln \frac{y_j p}{K_j} = \frac{\mu_j^{L(0)} - \mu_j^{V(0)}}{RT} - \ln \phi_j + \ln \gamma_j. \quad (2.25)$$

The standard chemical potential of gas  $j$  in liquid phase  $\mu_j^{L(0)}$  is the chemical potential in hypothetically ideal solution of unit molality [Denbigh, 1971]. The vapor phase standard chemical potential  $\mu_j^{V(0)}$  is the hypothetically ideal gas chemical potential when the pressure is equal to 1 bar. In the parameterization,  $\mu_j^{V(0)}$  as a reference number, can be set to any number because only the difference between  $\mu_j^{L(0)}$  and  $\mu_j^{V(0)}$  is important. Here we set it to zero for convenience.

The activity coefficients in eq. (2.25)  $\gamma_j$  are obtained from an expression for the excess Gibbs energy, which is expressed as a sum of three contributions

$$\frac{G^{ex}}{RT} = \frac{G_{LR}^{ex}}{RT} + \frac{G_{II}^{ex}}{RT} + \frac{G_{SR}^{ex}}{RT}, \quad (2.26)$$

where  $G_{LR}^{ex}$  represents the contribution of long-range electrostatic interactions,  $G_{II}^{ex}$  accounts for specific ionic (ion-ion and ion-molecule) interactions, and  $G_{SR}^{ex}$  is a short-range contribution resulting from intermolecular interactions. Based on Duan-Sun model, the long-range and ion-ion, ion-molecule interaction contribution is calculated from a virial expansion of excess Gibbs energy [Pitzer and Mayorga, 1973] expressed in terms of molalities

$$(\ln y_j)_{LR,II} = \sum_c 2\lambda_{j-c}b_c + \sum_a 2\lambda_{j-a}b_a + \sum_c \sum_a \zeta_{j-a-c}b_c b_a , \quad (2.27)$$

where  $\lambda$  and  $\zeta$  are second-order (gas-ion) and third-order (gas-electrolyte) interaction parameters, respectively. Extension to Duan-Sun (DS) model is proposed by adding the short contribution term to take into account of dissolved gas interactions. It is derived by analyzing and regressing experimental data of salt-gas-water mixtures which are described in Chapter 5. Thus the activity coefficient of gas  $j$  can be expressed as

$$\ln y_j = (\ln y_j)_{LR,II} + \sum_{j'} \chi_{j-j'} b_{j'} , \quad (2.28)$$

with  $\chi_{j-j'}$  binary interaction of dissolved gases, derived based on best-fit to measurement data in literatures.

## 2.5.2 Apparent molar properties

An apparent molar property of a component in a solution shows an intensive quantity of the component that is derived from the corresponding property of the solution using mole-weighted sum, see eq. (2.29). The objective is to detach the contribution of each component to the non-ideality of the mixture.

$$\psi^{AQ} = w_{\text{H}_2\text{O}}^{AQ} \cdot \psi_{\text{H}_2\text{O}}^{AQ} + \sum_{N_i} \frac{w_i^{AQ}}{M_i} \cdot \psi_i^\phi + \sum_{N_j} \frac{w_j^{AQ}}{M_j} \cdot \psi_j^\phi , \quad (2.29)$$

where  $\psi$  i.e. enthalpy, heat capacity, or density;  $i$  and  $j$  are salt and gas component, respectively. Apparent molar properties are functions of the temperature and the composition, e.g. total molality,  $\psi^\phi = f(T, \sum b)$ . For ideal solution, an apparent molar property is similar to the corresponding partial molar property.

To describe electrolyte solution properties, apparent molar properties that are used in this thesis are apparent molar volume (density), apparent molar heat capacity, and apparent molar enthalpy. For transport property, i.e. viscosity the apparent property is expressed as the ratio between the viscosity of the aqueous solution and pure water.

# 3

## MODULAR GEOTHERMAL ORGANIC RANKINE CYCLES

Chapter 3.1 is published as

Nusiaputra, Y. Y., Qadri, F., Kuhn, D., Abdurrachim, H., *Empirical Correlations for Optimal Turbine Inlet Temperature and Pressure for Geothermal Sub- and Supercritical Organic Rankine Cycles* in World Geothermal Congress 2015, Melbourne

### 3.1 EMPIRICAL CORRELATIONS FOR OPTIMAL TURBINE INLET TEMPERATURE AND PRESSURE

#### ABSTRACT

Geothermal ORCs are classified as low temperature power-plant which has relatively low thermal efficiency. Hence, it is important to design such systems on its optimum operating condition, e.g. turbine inlet temperature and pressure (TITP) to maximize the energy recovery. In the present study, empirical correlations are developed to calculate the optimal TITP of sub- and supercritical ORC for geothermal applications, i.e. hybrid (flash-binary) power-plant and medium-enthalpy wells. In geothermal ORCs, injection temperature parameter is an important design prerequisite due restriction to mineral scaling. Therefore, the ratio of hot brine temperature (or equivalently, the heat input) to critical temperature of the working fluids and the injection temperature, are used to correlate the optimal TITP. The correlations are derived from the optimal TITP data of 6 typical working fluids at maximum specific net-power resulted from GeSi (Geothermal Simulation, an in-house program). In order to evaluate the accuracy, the correlations are tested by using the simulation results of other 15 pure working fluids at brine temperature of 120 °C – 180 °C and injection temperature of 70 °C – 160 °C. The prediction of the optimal TITP using the correlations is within 5% error. These correlations are very convenient for pre-design in fast and robust manner, especially to predict performance of new working fluids in specific working conditions. As a case study, hybrid power-plant application in Indonesia is used. With average brine temperature of 453.15 K (180 °C) it is found, for n-pentane, the optimal turbine inlet temperature/pressure is 434.15 K (161 °C) / 1.9 MPa, which yields thermal efficiency of 15.5 %.

### 3.1.1 Introduction

Binary cycles (Organic Rankine Cycles) are commonly used to utilize low-grade temperature heat from brine in geothermal power. Basically ORC is the same as ordinary Rankine cycle but organic Rankine cycle used an organic fluid as working fluid instead of water. The organic fluid has a lower evaporation temperature than water, which is suitable for heat recovery at low temperatures. These plants are classified as low temperature power-plant which has relatively low thermal efficiency. Hence, it is important to design such systems on its optimum operating condition, e.g. turbine inlet temperature and pressure (TITP) to maximize the energy recovery.

ORC should be operated at optimum condition to optimize the utilization of low-grade heat from the brine. Several studies have been carried out to determine the optimum conditions of the cycle. Wei [2007] founded in his research that the maximum power can be obtained by utilizing the waste heat as much as possible. Then He [2012] also conducted a study to determine the optimum evaporator temperature for sub-critical cycle. The condition of fluid at turbine inlet is assumed always at saturated vapor for dry fluids. The optimum point is determined by optimizing curve area on the  $T - s$  diagram that performed iteratively in EES (Engineering Equation Solver). Vetter et al. [2013] have also developed a simulation program to determine the optimum conditions of cycle numerically by varying the pressure and temperature at turbine inlet. Net power for any variations in temperature and pressure have been compared and they selected the greatest net power as optimum conditions.

Reduced pressure parameters ( $p_r = p/p_{crit}$ ) and reduced temperature parameter ( $T_r = T/T_{crit}$ ) are commonly used to express general relation like in General Compressibility Diagram ( $Z$  vs.  $p_r$ ) that is applicable for a variety of gases. Based on the condition, it is also expected a correlation between the optimum conditions of ORC (optimum temperature,  $T_1$  and pressure,  $p_1$  at turbine inlet) and brine temperature ( $T_g$ ). So in this study will be investigated the correlation between the dimensionless parameter  $p/p_{crit}$ ,  $T_1/T_{crit}$  and  $T_g/T_{crit}$ . By using the correlation, the optimum temperature ( $T_1$ ) and the optimum pressure ( $p_1$ ) at turbine inlet can be determined easily based on brine temperature ( $T_g$ ) and critical state of working fluid ( $T_{crit}$  and  $P_{crit}$ ).

### 3.1.2 Thermodynamic modeling

Figure 3. 1 showed a simple scheme of organic Rankine cycle that consists of evaporator, turbine, condenser and pump. Geothermal fluid provides the heat source for the process. The heat is extracted in the heat exchanger using working fluid. Selection of the working fluid depends on its thermo-physical properties. After Wei et al., [2007] the working fluid should inter alia meet the following criteria:

- Low critical pressure and temperature (compared to water)
- Low specific volume
- High thermal conductivity
- Non corrosive, toxic or flammable and stable

In addition, low ozone depletion potential (ODP) and a low greenhouse warming potential (GWP) are important requirements for the suitability of the working fluid. Depending on the gradient of the vapor line, a distinction is made between dry (retrograde) and wet fluids. Water as a wet fluid has a negative dew line slope, but many organic media are retrograde e they have a dew line with at least a partial positive slope as butane in Figure 3. 1.

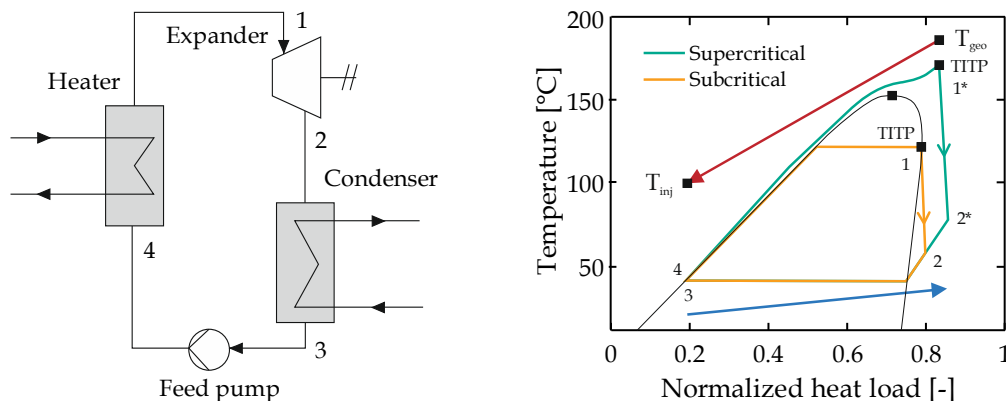


Figure 3. 1: Scheme for sub-critical and super-critical cycle for n-butane in T-s diagram.

Type of cycle depends on the pressure of working fluid in evaporator when the heat is given. If the fluid pressure is smaller than critical pressure ( $p_1 < p_{crit}$ ) while heat is given, then the working fluid will undergo evaporation from the liquid phase to a vapor while it passed through two phases region which makes a process called sub-critical cycle (cycle by the dashed lines in Figure 3. 1: 1-2-3-4-1). The super-critical cycle (cycle: 1\*-2\*-3-4-1\* in Figure 3. 1), the pressure of work-

ing fluid is above critical pressure ( $p_1^* > p_{crit}$ ) while heat is given, so that the working fluid does not pass through two phase region, but beyond the critical point directly.

The first and second laws of thermodynamics can be applied to determine the performance of organic Rankine cycle. The amount of work produced and heat added to the system can be determined by using energy balance. The following is a calculation of organic Rankine cycle for each component.

- Process 1-2: process of isentropic expansion in turbine. The maximum power that can be produced by the turbine is

$$\dot{W}_T = \dot{m}(h_1 - h_2) \quad (3.1)$$

- Process 2-3: process of isobaric cooling in condenser. The rate of heat rejected from condenser is

$$\dot{Q}_{out} = \dot{m}(h_2 - h_3) \quad (3.2)$$

- Process 3-4: process of isentropic compression in pump. Power required by pump to raise the pressure of working fluid is

$$\dot{W}_P = \dot{m}(h_4 - h_3) \quad (3.3)$$

- Process 4-1: process of isobaric heating in evaporator. Heat rate received on evaporator is

$$\dot{Q}_{in} = \dot{m}(h_1 - h_4) \quad (3.4)$$

- Cycle net power output ( $P_{net}$ )

$$P_{net} = \dot{W}_t - \dot{W}_p \quad (3.5)$$

- Thermal efficiency

$$\eta_I = \frac{P_{net}}{\dot{Q}_{in}} = \frac{\dot{W}_t - \dot{W}_p}{\dot{Q}_{in}} \quad (3.6)$$

All the above processes are ideal processes, which are considered no losses. In the actual condition, these losses always occur and cannot be avoided. The losses led to increase the entropy in compression and expansion process. Because of the entropy increasing in compression and expansion process, so the isentropic efficiency of pump and the isentropic efficiency of turbine can be determined by eq. (3. 7) and eq. (3. 8).

$$\eta_P = \frac{h_{4s} - h_3}{h_4 - h_3} \cong \frac{v_3(p_4 - p_3)}{h_4 - h_3} \quad (3. 7)$$

$$\eta_T = \frac{h_1 - h_2}{h_1 - h_{2, is}} \quad (3. 8)$$

In order to compare different working fluids this paper focuses on the specific net power output of the thermodynamic cycle. This is the relevant variable for geothermal application and waste heat utilization. If the energy is extracted from a closed loop (e.g. combined heat and power systems) or from a valuable energy source, one has to compare the efficiency of the processes. Furthermore, the net power output considering the electricity demands of the cycle pump and condenser is taken into account to evaluate the thermodynamic systems. The net power output of the cycle is the product of thermal efficiency and the heat supplied to the organic fluid

$$P_{net} = \eta_I \dot{Q}_{in} \quad (3. 9)$$

Where  $P_{net}$ ,  $\eta_I$ ,  $\dot{Q}_{in}$  are net power output, thermal efficiency, and heat input, respectively. As it can be seen by the formula above, the net power output is dependent on two factors that affect each other. The heat input to the cycle is not a fixed value, but, like thermal efficiency, depends on live vapor parameters and cycle design. This is because of the sensitive heat source and the varying exit temperature of the geothermal fluid. In order to objectively compare various cycle designs with different workings fluids, an index number is used. This is the specific net power output the net power output that can be achieved with 1 kg/s geothermal fluid mass flow rate under given conditions

$$P_{net, spec} = \frac{P_{net}}{\dot{m}_{geo}} [\text{kWs/kg}] \quad (3. 10)$$

### 3.1.4 Results and discussion

Table 3. 1 shows the default parameters of the simulation of the ORCs using six typical working fluids. Pressure losses in the heat exchangers, pipes, or mechanical losses were not included in the calculations. The brine temperatures and injection temperatures are standard value for state-of-the art of medium-enthalpy geothermal application worldwide.

| <b>ORC process parameters</b>                |              |
|--|--------------|
| condensation temperature                     | 40 °C        |
| pump efficiency                              | 0.75         |
| turbine efficiency                           | 0.8          |
| minimal temperature difference in the heater | 5 K          |
| <b>geothermal fluid parameters</b>           |              |
| mass flow rate                               | 1 kg/s       |
| pressure                                     | 1.4 MPa      |
| wellhead temperature                         | 120 - 180 °C |
| injection temperature                        | 70 - 160 °C  |

Table 3. 1: Power-plant simulation parameters.

By varying temperature and pressure at turbine inlet (TITP), the maximum possible specific net power output was evaluated. The brine temperature and injection temperature is kept constant with 1 kg/s of brine mass flow rate. Simulations were carried out to calculate 174 working conditions with variation in brine temperature of 120 – 180 °C and injection temperature of 70 – 160 °C. The minimum temperature difference between brine temperature and injection temperature was 20 °C, which is economically sound for practical application.

#### *The empirical correlation for optimum TITP*

Temperature and pressure at turbine inlet are the main parameter to determine the optimum conditions of cycle. Based on the optimum conditions of each working fluid that are obtained from simulation, the relationship can be investigated from characteristics of working fluid at turbin inlet: vapor temperature ( $T_1$ ), vapor pressure ( $p_1$ ), critical temperature ( $T_{crit}$ ), critical pressure ( $p_{crit}$ ) and brine temperature ( $T_g$ ). The results of investigation shows that at optimum conditions, a dimensionless parameter  $T_1/T_{crit}$  and  $T_g/T_{crit}$  for all working fluid is spread on a particular line as shown in Figure 3. 2. With a quadratic equation approach, the

relationship of  $T_1$ ,  $T_g$  and  $T_{crit}$  can be written in the form of the following correlation

$$f = \sum_{i=1}^{10} c_{uv} \left( \frac{T_g}{T_{crit}} \right)_n^u T_{inj,n}^v \quad (3.11)$$

where  $f = \left( \frac{T_1, opt}{T_{crit}} \right)$  for TIT,  $f = \left( \frac{p_1, opt}{p_{crit}} \right)$  for TIP, and the coefficients with  $u = 0,1,2,3$  and  $v = 0,1,2,3$ , are listed in Table 3. 2 as following.

| $i$ | coefficient | TIT       | TIP       | $i$ | coefficient | TIT       | TIP       |
|-----|-------------|-----------|-----------|-----|-------------|-----------|-----------|
| 1   | $c_{00}$    | 0.9506    | 0.6863    | 6   | $c_{02}$    | -8.00E-03 | -1.98E-02 |
| 2   | $c_{10}$    | 0.1239    | 0.5541    | 7   | $c_{03}$    | 1.23E-03  | 2.11E-03  |
| 3   | $c_{20}$    | 1.22E-02  | 0.1196    | 8   | $c_{11}$    | -8.66E-03 | -1.29E-02 |
| 4   | $c_{30}$    | -7.57E-03 | -2.91E-02 | 9   | $c_{21}$    | -2.80E-03 | -1.75E-03 |
| 5   | $c_{01}$    | 2.67E-02  | 9.97E-02  | 10  | $c_{12}$    | 1.95E-03  | 5.94E-03  |

Table 3. 2: Optimum turbine inlet temperature and pressure (TITP) correlation coefficients.

The empirical correlation above was using normalized value of input variables, which are normalized ratio of brine to critical temperature and normalized injection temperature. Therefore, each variable should be transformed to normalized value using

$$\left( \frac{T_g}{T_{crit}} \right)_n = \left( \frac{T_g}{T_{crit}} - 1.006 \right) / 9.263E - 2 ,$$

and

$$T_{inj,n} = (T_{inj} - 372.1) / 22.01 .$$

The correlation was derived from 174 simulation results (blue dots) with variation in brine temperature of 120 - 180 °C and injection temperature of 70 - 160 °C. It was observed that they have consistent trend in relation with ratio of brine temperature to critical temperature and injection temperature. Hence, they are fitted using third order polynomial function with respect to these two parameters. The fitting result has R-squared of 0.9794 and RMSE (Root Mean Squared Error) of 0.01732 as can be seen in Figure Figure 3. 2.

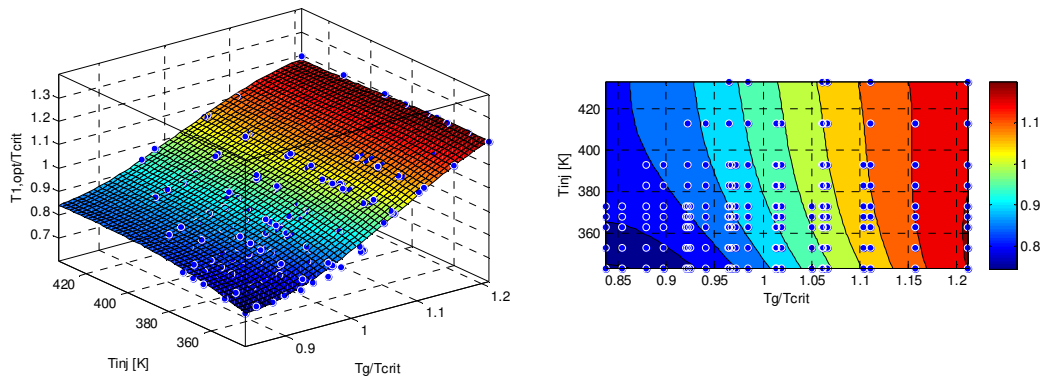


Figure 3. 2: Fitting result of optimum turbine inlet temperature (TIT): surface fit (a); contour of the fitting (b).

For the optimum turbine inlet pressure, similar trends are observed. Using third order polynomial, the data are fitted results empirical correlation for TIP with R-squared of 0.9821 and RMSE of 0.07639. The surface fitting results can be seen in Figure 3. 3.

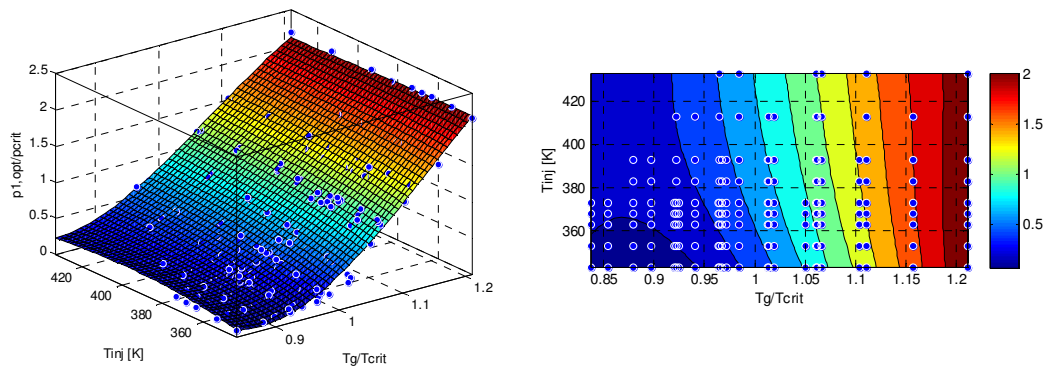


Figure 3. 3: Fitting result of optimum turbine inlet temperature (TIP): surface fit (a); contour of the fitting (b).

The correlation surface seems has quite good agreement with symmetrical trend. However, validation compared to simulation results were carried out in section 3.2 to prove the empirical results.

*Comparison with simulation results*

As mentioned earlier that there is a certain correlation between the optimum conditions (vapor temperature and pressure at turbine inlet), critical state of the working fluid (critical temperature and critical pressure) and brine temperature. These correlations can be used to predict optimum temperature and pressure at turbine inlet. However, the correlation must be tested to others working fluid to prove whether these correlations are generally accepted. Fifteen organic working fluids with critical temperature near brine temperature were selected. The results of verification for all the selected working fluid can be seen in Table 3. 3. The comparison of optimum temperature and pressure at turbine inlet was obtained from correlation and simulation at random  $T_g = 120 - 180$  °C and  $T_{inj} = 70 - 160$  °C. It shows that all optimum points of cycle (optimum temperature and pressure at turbine inlet) have quite good agreement. There are some inaccuracies in TIP prediction which results a maximum relative error of 25.64%. Nonetheless, the specific net power-output predictions are still in accuracy within 2%.

| Working fluid | $T_{geo}$ | $T_{inj}$ | TIT [K] |      |        | TIP [MPa] |      |        | Spec. net power [kW] |       |        |
|---------------|-----------|-----------|---------|------|--------|-----------|------|--------|----------------------|-------|--------|
|               |           |           | Corr.   | Sim. | RD     | Corr.     | Sim. | RD     | Corr.                | Sim.  | RD     |
| propane       | 175       | 99        | 445     | 443  | 0.40%  | 9.3       | 8.7  | 6.84%  | 40.75                | 40.82 | -0.18% |
| R124          | 180       | 158       | 453     | 448  | 1.14%  | 6.38      | 6.1  | 4.56%  | 13.24                | 13.07 | 1.31%  |
| isobutene     | 152       | 115       | 410     | 420  | -2.44% | 3.26      | 3.14 | 3.83%  | 20.6                 | 20.79 | -0.93% |
| butene        | 134       | 86        | 371     | 373  | -0.52% | 1.72      | 1.75 | -1.75% | 20.56                | 20.83 | -1.32% |
| trans-butene  | 141       | 92        | 381     | 381  | 0.07%  | 1.77      | 1.7  | 4.06%  | 23.74                | 23.37 | 1.60%  |
| R114          | 151       | 102       | 403     | 401  | 0.68%  | 2.41      | 2.35 | 2.55%  | 25.71                | 25.56 | 0.59%  |
| R236ea        | 139       | 106       | 393     | 394  | -0.04% | 2.37      | 2.37 | -0.09% | 16.24                | 16.3  | -0.39% |
| cis-butene    | 161       | 121       | 418     | 427  | -2.11% | 3         | 2.73 | 9.85%  | 24.74                | 24.59 | 0.64%  |
| R21           | 180       | 132       | 440     | 448  | -1.77% | 4.05      | 3.22 | 25.64% | 34.46                | 34.17 | 0.85%  |
| neopentane    | 182       | 158       | 452     | 450  | 0.43%  | 3.58      | 3.75 | -4.48% | 14.93                | 15.12 | -1.24% |
| R125          | 122       | 74        | 390     | 390  | -0.10% | 6.52      | 6.69 | -2.61% | 15.29                | 15.43 | -0.93% |
| R11           | 180       | 136       | 437     | 445  | -1.94% | 2.49      | 2.15 | 15.92% | 32.15                | 31.6  | 1.74%  |
| R245ca        | 165       | 140       | 424     | 425  | -0.10% | 2.59      | 2.61 | -0.86% | 15.82                | 15.9  | -0.53% |
| R123          | 158       | 121       | 410     | 409  | 0.31%  | 1.66      | 1.57 | 5.67%  | 22.85                | 22.51 | 1.50%  |
| R141b         | 180       | 155       | 439     | 445  | -1.18% | 2.23      | 2.25 | -0.71% | 18.57                | 18.68 | -0.59% |

Table 3. 3 Comparison between correlation and simulation results.

When the optimum point of each working fluid is plotted with surface of the empirical correlation, it would seem that all the optimum point scattered around correlation line, especially the area around  $T_g/T_{crit} = 1$  as shown in Figure 3. 4.

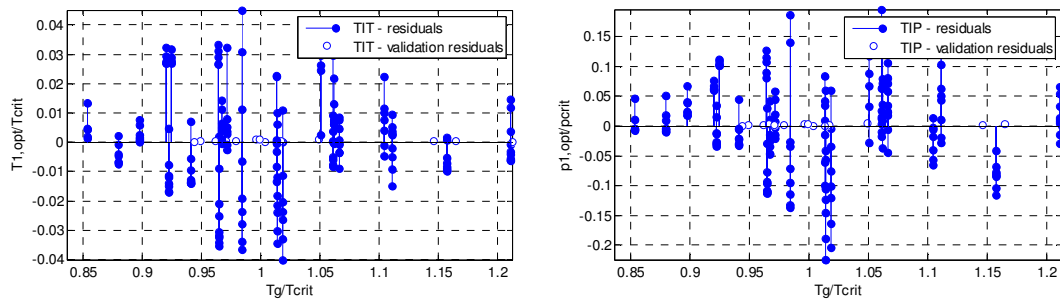


Figure 3. 4: Residuals of 174 data and validation data from different 15 working fluids: TIT (a); TIP (b).

After Vetter et al. [2013], it is concluded that a higher net power output is obtained from the working fluid with critical temperature close to brine temperature ( $T_g/T_{crit} = 1$ ).

Based on the results of verification, it can be concluded that correlation in eqs. (3.11) - (3.12) can be used to predict the optimum temperature and pressure at turbine inlet. But, for more accurate results need to be checked a few points around prediction point with simulation programs to ensure that the prediction point was correct.

#### *Choice of working fluids: practical application*

Hybrid power-plant application in Indonesia example was for practical application. The working conditions are taken from the literature for Lahendong, North Sulawesi field [Bambang, 2006]. The brine temperature out from the flash power-plant is 453.15 K (180 °C). The minimum injection temperature is 160 °C to avoid scaling. The mass flow rate of brine is measured as 11.44 kg/s. Five working fluid candidates are taken such as isobutane, butane, pentane, isopentane, and propane. The results are shown in Table 3. 4 below.

As can be inferred from Table 3. 4, pentane results the best net power output with subcritical-process in the cycle. It can be observed that for hybrid power-plant application, supercritical cycle does not convey real benefit since the injection temperature is limited. The plant with higher efficiency will have better net power output.

| No. | Working fluid | Opt. TIT [K] | Opt. TIP [MPa] | $P_{net}$ [kW] | Efficiency | Type          |
|-----|---------------|--------------|----------------|----------------|------------|---------------|
| 1   | pentane       | 441          | 2.07           | 157.7          | 15.80%     | subcritical   |
| 2   | isopentane    | 443          | 2.43           | 154.2          | 15.40%     | subcritical   |
| 3   | butane        | 452          | 4.69           | 149.6          | 15.00%     | supercritical |
| 4   | isobutane     | 454          | 5.58           | 141.1          | 14.10%     | supercritical |
| 5   | propane       | 439          | 9.33           | 121.2          | 12.10%     | supercritical |

Table 3. 4: Results of empirical correlation: Lahendong case study.

### 3.1.5 Conclusions

Based on the simulation results and discussion, it can be concluded some of the following:

1. Simulation for six typical organic working fluids with 1 kg/s mass flow rate at brine temperatures of 120 – 180 °C and injection temperature of 70 – 160 °C has been carried out to derive empirical correlation for optimum turbine inlet temperature and pressure (TITP).
2. It has been obtained correlation to predict the optimum temperature ( $T_1$ ) and pressure ( $p_1$ ) at turbine inlet. The correlation has been tested on 15 organic working fluids. It was obtained that all the optimum point spread around correlation line with relative error for optimum TIT, TIP, and specific net power output within 2.5%, 26%, and 2%.
3. For brine temperature 453.15 K (180 °C), the optimum condition of cycle with pentane as working fluid is obtained at turbine inlet temperature,  $T_1 = 434.15$  K (161 °C) and pressure  $p_1 = 1.9$  MPa, with thermal efficiency of 15.8%.
4. The empirical correlations obtained can be used for rough estimation of TITP and specific net power output. Within typical value ranges, it valid regardless of pinch-point, condensation temperature, and regeneration option. This correlation is very useful in pre-design stage to predict the optimum temperature and pressure at turbine inlet for organic Rankine cycle.

### 3.2 STEADY-STATE OPTIMIZATION OF THE ORGANIC RANKINE CYCLES

In this subchapter, a detailed overview of the development of the steady-state ORC model is given. Emphasis is established on component sizing with implications for the dynamic simulation presented in subchapter 3.3, in particular, to optimize performance during off-design condition, which is the key point of modularization presented in Chapter 4.

#### 3.2.1 Three-zone heat exchanger model

Heat exchanger (HX) models can be classified according to the discretization detail used by different types of models, such as distributed parameters and discretized/stream evolution models or DPM and SEM, respectively. The model proposed here belongs to the first type (DPM), a three zone heat exchanger model, see Figure 3. 5. Three-zone model assume a global heat transfer coefficient for the whole heat exchanger that can be dependent on variables, such as air flow rate and evaporator global heat flux. Calculations of the HX uses the NTU or LMTD solutions found for single-phase HXs.

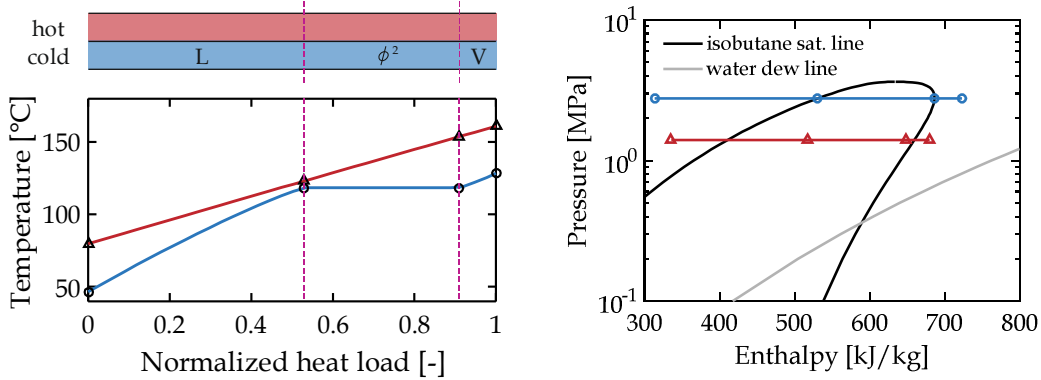


Figure 3. 5: Three zone heat exchanger partitioning of water/isobutane (evaporator).

By using logarithmic mean temperature difference (LMTD) approach, governing equation for each HX zone can be defined as

$$A_k = \frac{\dot{Q}_k}{U_k \cdot CMTD_k}, \quad (3.13)$$

where zone index  $k = L, \phi^2, V$  indicate liquid, two-phase, and vapor zone, respectively. The heat flow  $\dot{Q}_k$  is calculated through energy balance as describe in

eqs. (3. 2) and (3. 4). The local heat transfer coefficient of each zone  $U_k$  defined by eq. (4. 4) in the following Chapter 4. For two-phase zone, the heat transfer coefficient is computed as an average over the quality range by integration

$$\bar{\alpha}_{\phi^2} = \int_0^1 \alpha_{\phi^2} dx , \quad (3. 14)$$

where  $\alpha_{\phi^2}$  is two-phase heat transfer coefficient varies with vapor quality. The corrected mean temperature difference (CMTD) of each zone is defined by

$$CMTD_i = \frac{(T_{sec,in} - T_{pri,out}) - (T_{pri,out} - T_{sec,in})}{\ln((T_{sec,in} - T_{pri,out}) / (T_{pri,out} - T_{sec,in}))} . \quad (3. 15)$$

As closing equation, the total heat transfer area can be expressed as sum of the three zones area

$$A = A_L + A_{\phi^2} + A_V = \frac{\dot{Q}}{U \cdot WTD} , \quad (3. 16)$$

where, weighted average temperature difference (WTD) is determined as

$$WTD = \frac{\dot{Q}_L \cdot CMTD_L + \dot{Q}_{\phi^2} \cdot CMTD_{\phi^2} + \dot{Q}_V \cdot CMTD_V}{\dot{Q}} , \quad (3. 17)$$

The total pressure drop of the primary and secondary fluids is sum of pressure drop across the three zones and can be written as

$$\Delta p = \Delta p_L + \Delta p_{\phi^2} + \Delta p_V, \quad (3. 18)$$

with the correlations to compute single- and two-phase pressure drop are described in chapter 2 (eqs. (2. 11) - (2. 13)).

The governing equations can be used for two modes: sizing and simulation. The sizing mode was used for dimensioning the HX at the design point. Meanwhile, the simulation mode was used to examine the off-design behavior, i.e. mass flow, temperature boundary change.

### *Code-to-code comparison*

A code-to-code comparison is performed applying the three zone HX (3Z-HX) model, which is used within the present thesis, and the related best estimate heat exchangers code ASPEN Plus: Exchanger Design and Rating (EDR), which is developed based on HTFS and B-JAC. The aim of this code-to-code comparison is primarily the validation of the physical models described above.

A horizontal, single-pass, shell-and-tube TEMA-E evaporator for tropical climate application has been designed at optimized modular design point (see Chapter 4 for a detailed description). Such evaporator HX worked with the working-fluid flowing through the shell and the geothermal fluid flowing through the tubes in the opposite direction, so the HX worked in counter-current mode. At the design point, geothermal fluid enters the HX at 161 °C and 1.4 MPa. Meanwhile, isobutane enters at 45.07 °C and 2.58 MPa. Both present model and EDR models use same internal geometrical information from the designed evaporator HX.

Due to its modularity, the evaporator was expected to work at the off-design condition, to maximize performance under other geothermal and ambient temperature, i.e. 120 - 170 °C and (-10) - 40 °C, respectively. Several simulations were carried out with isobutane (R-600a) on six levels of geothermal fluid mass flow rate (8.92 - 21.98 kg/s) and six levels of evaporation pressure (1.64 - 2.9 MPa), therefore, 36 points of working conditions were tested. The comparison of important parameters between present model and ASPEN Plus EDR is shown in Figure 3. 6a to Figure 3. 6f.

In the first test, the geothermal fluid outlet temperature is the variable examined to evaluate the agreement between the present model and ASPEN Plus EDR. The comparison between the present model results and EDR values are displayed in Figure 3. 6a, where, shaded zone corresponds to  $\pm 2$  °C differences between present model and ASPEN Plus EDR results. A good agreement is observed between the present model and most of the EDR values. Another parameter used to prove the accuracy of the model is the isobutane temperature at the outlet of the evaporator. Figure 3. 6b shows the comparison between present model and EDR values. In this case, shaded zone corresponds to  $\pm 2$  °C difference.

A good correlation between present model and EDR is encountered again. The difference is always lower than  $\pm 4\%$  relative error in the heat load tests studied. The comparison between the experimental results and the calculated values obtained with the model are displayed in the following Figure 3. 6c that shows the measured and modeled heating capacity of the evaporator HX. The heating capacity has been compared according to the geothermal fluid and isobutane flow. In this figure, the shaded zone corresponds to  $\pm 4\%$  relative error.

Also, the heat transfer coefficient comparison results in a great agreement between the present model and EDR calculations. It is remarkable that the error of present model results is always under  $\pm 2\%$  relative error, with the heat transfer coefficient results from EDR.

Equation (3. 17) computes the weighted temperature difference (WTD) of evaporator HX in the present model, which is compared with EDR results in Figure 3. 6e. In this figure, the compact line corresponds to 100% accuracy and shaded zone corresponds to  $\pm 0.5$  °C. This means, in most cases, the difference between present model and EDR results is lower than 0.5 °C.

It has been verified that the calculated isobutane outlet pressure which corresponds to pressure drop, presented in eq. (3. 18), differ from EDR values by no more than 0.1 MPa. This large deviation shows the fact that the refrigerant is flowing through the shell, and the correlation chosen can be introducing additional errors to the calculations.

From the comparison, it is possible to say that the accuracy is good for all parameters, i.e. heating capacity and fluid outlet temperature, except for pressure drop. It can be concluded that the three-zone HX code is reliable to predict heat transfer behavior quite accurately compared to SEM used by ASPEN Plus: EDR. Hence, reducing computational cost for ORC system optimization. By further applying off-design correlations of turbine and pump on the computation, the off-design operation could be optimized. This optimization, however, will later be introduced in Chapter 4.

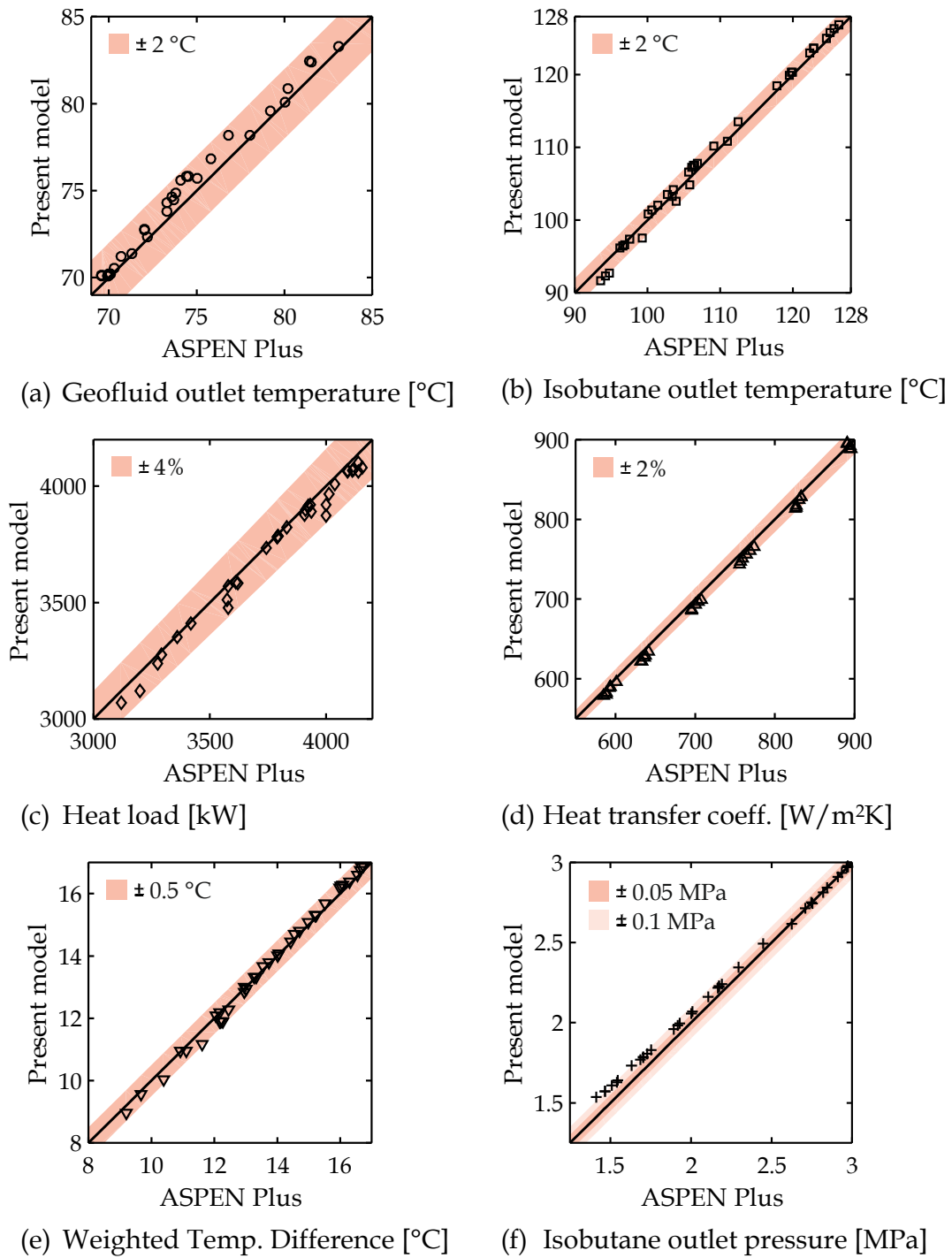


Figure 3. 6: Comparison between the model presented here (three-zone DPM) with Aspen Plus EDR results.

### 3.2.2 Rotating component model

The rotating component is assumed as a quasi-steady component which is evolving fast compared to thermal inertia in the heat exchangers, thus has little dynamic variability. This means parameters are simultaneously changed and the time the derivative term is considered as zero.

For a turbine with given stage pitch diameter and turbine rotational speed, the isentropic efficiency is a function of volumetric flow rate of working fluid and enthalpy drop through the turbine [Ghasemi *et al.*, 2013]. The isentropic efficiency of the turbines is obtained from manufacturer data (specification or process diagram). For radial turbines, the maximum (design-point) value is ranging from approximately 70 to 88% [Dixon, 2002]. However, as discussed in the following, deviations of operating condition from this maximum adversely affects the performance of the turbine. This deviation can be expressed as a function of spouting velocity ( $u/c_0$ ) and ratio of volumetric flow rate ( $r_{VT}$ ). For the considered turbine in this study, the dependence of  $\eta_T$  on these parameters is written as for  $\eta_T = \eta_{T,DP} \times F_{u/c_0} \times F_{\dot{V}}$  the application.

$$u/c_0 = 0.7(\Delta h_{is}/\Delta h_{is,DP})^{0.5}$$

$$F_{u/c_0} = \sum_{i=0}^5 c_i (u/c_0)^i, \quad (3.19)$$

where  $c_0 = -0.0014$ ,  $c_1 = 2.5106$ ,  $c_2 = -1.7379$ ,  $c_3 = 1.2346$ ,  $c_4 = -1.3781$ , and correction factor with regard to volumetric flow rate can be written as

$$r_{VT} = \dot{V}_T/\dot{V}_{T,DP}$$

$$F_{\dot{V}} = \sum_{i=0}^5 c_i r_{VT}^i, \quad (3.20)$$

where  $c_0 = 0.038$ ,  $c_1 = 2.588$ ,  $c_2 = -2.533$ ,  $c_3 = 1.117$ ,  $c_4 = -0.21$ .

The pump is modeled by the quadratic relationship between volumetric flow rate and pressure increase with efficiency change about volumetric flow rate and rotational speed. Both of turbine and pump relationships are described in Chapter 4.

### 3.2.3 Reverse modeling based on manufacturer's data: 60 kWel Gross-Schönebeck ORC

The 60 kWel Groß-Schönebeck (GrSk) organic Rankine cycle is the focus test rig for the ORC models developed in this thesis. It is an on-site laboratory, owned by GeoForschungsZentrum (GFZ) Potsdam that has not been commissioned until this thesis is written. Nevertheless, the experiments are needed to be performed later for validation and fitting purposes. One of the final goals of this thesis is to create dynamic models of the 60 kWel GrSk. ORC that can be easily reconfigured once the experiment can be done. As such, there are some aspects of the modeling that use some geometrical assumptions that were not yet confirmed by any data. These assumptions are reported in the following modeling descriptions and have been accounted for in all simulation attempts.

Figure 3. 7 shows a photograph and a schematic drawing of the developed experimental apparatus. The developed ORC consists of heat exchangers, i.e., a pre-heater, evaporator, and condensers that heat or cool the working fluid, as well as a turbine, a pump, and a storage tank. A shell-and-plate type heat exchanger was used for the evaporator since it must contain working fluid in both liquid and vapor states simultaneously to produce saturated vapor. The level of the liquid state working fluid in the evaporator was controlled by using a float-type level sensor and a circulation pump. It maintains the liquid level of the evaporator at a constant from its base by adjusting the working fluid flow rate from the storage tank. A shell-and-plate type heat exchanger was used for the preheater, considering the easiness of its connectivity to the evaporator. Air-cooled, finned-tube heat exchangers were used for the condensers, considering general design in case of fresh-water scarcity for cooling purposes.



Figure 3. 7: The 60 kWel Groß-Schönebeck ORC system comprises the preheater, evaporator, turbine, air-cooled condensers, hot well, and feed pump. The additional auxiliary component includes lubricant cooler. Courtesy of Durr-Cyplan [2011].

The GrSk4 well was planned to be used to produce hot-brine, the heat source, in parallel with three-stage ORCs. The shell-and-plate heat exchangers, i.e. preheater and evaporator were supplied by Vahterus. The finned-tube condensers were supplied by GEA Küba. The centrifugal pump, which comprises an impeller and is of the vertical type, was supplied by GRUNDFOS (model CR5-12A). The pump used magnetic bearing and was connected with an inverter which adjusted its rotational speed by converting the frequency. The turbine was designed and manufactured by E&P Turbo. The generator is hermetically mounted in the same casing with the turbine. The storage tank was designed in a cylindrical shape with a volume of 80 L, and was manufactured by the integrator. At the time it was installed, all the components including the instrumentation were integrated by Cyplan, which is now bought by Dürr and so-called Dürr-Cyplan. A small lubricant cooler is attached to cool n-butane which lubricates turbo-generator. However, it is not modeled due to its low exergy flow.

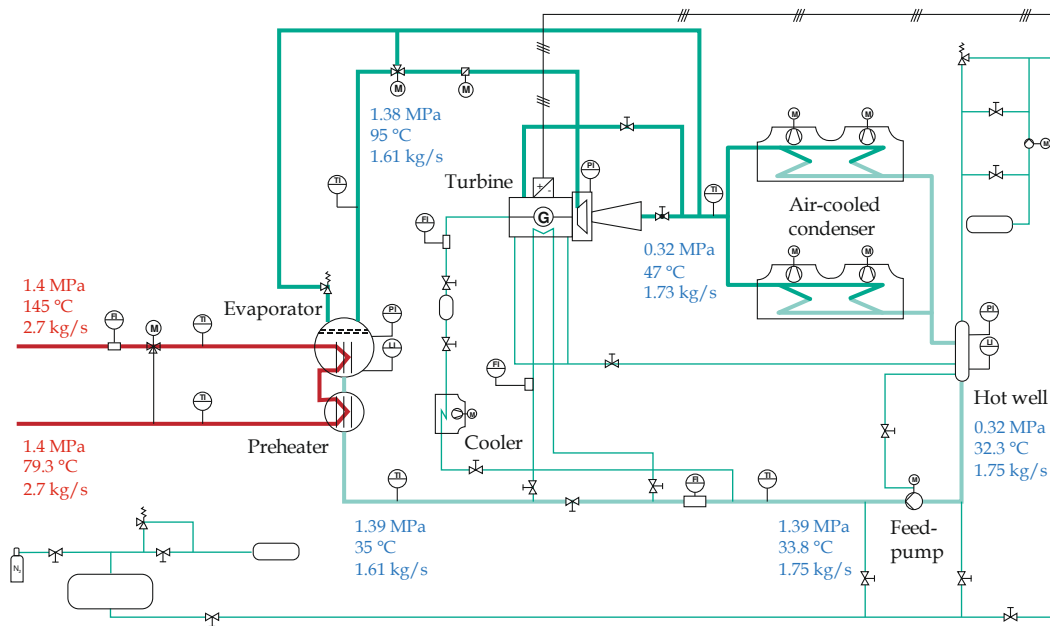


Figure 3. 8: 60 kWel Groß-Schönebeck ORC piping, instrumentation, and a components diagram. The tank outside the loop is filled with nitrogen that is used for purging in the start-up process. The current configuration uses air-cooling for the heat rejection. Courtesy of Dürr-Cyplan [2011].

The complete configuration of these components is shown in Figure 3. 8. The brine and n-butane circuits are represented by bold lines, signifying the heat source and working fluid, respectively.

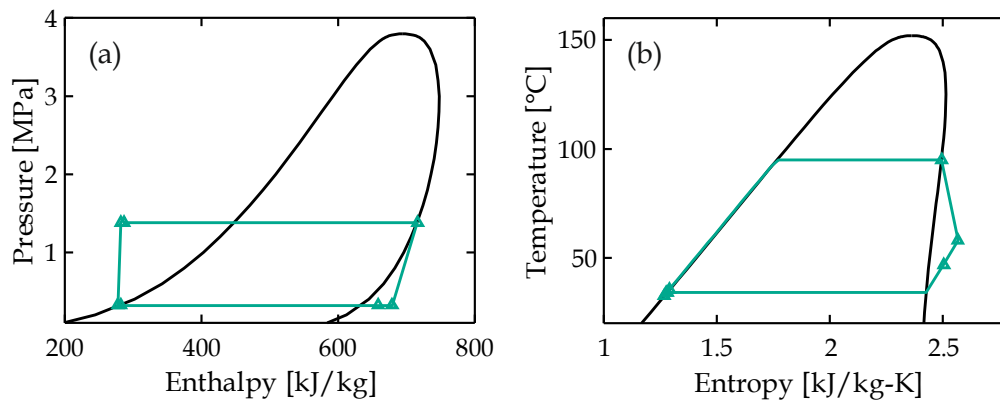


Figure 3. 9: (a)  $p - h$  and (b)  $T - s$  diagram of the 60 kWel GrSk. system.

Figure 3. 9 shows the  $p - h$  and  $T - s$  diagram of the designed cycle at the design point. All the component size modeled later are based on these property values. The thermodynamic cycle design process can be briefly described as follows. As the basis of the cycle design, condensation pressure was considered first and set to the saturation value, i.e., 0.32 MPa, of the working fluid at 34 °C. The condensation temperature was determined to be 14 °C higher than the atmospheric temperature in autumn. Cycle efficiency increases as the pressure ratio between the turbine inlet and its outlet rises. However, the turbine was limited regarding increasing the pressure ratio. A radial type of turbine whose pressure ratio between its inlet and outlet is 4.31 was given. Although, the inlet  $pT$  and flow-rate is hypothetically not at the design point (the analysis is described in the next section). Therefore, the evaporation pressure, which is considered to be the same as the turbine inlet pressure, was set to 1.38 MPa in consideration of the condensation pressure and the pressure ratio at the turbine inlet and outlet, which is 4.31 (1.38/0.32). The evaporation temperature was set to the saturation value, which is 95 °C, of the n-butane at the evaporation pressure. The ORC was designed to keep the turbine inlet temperature at saturated vapor condition (without superheating) to maximize performance.

The typical Rankine cycle, which uses water as its working fluid, requires a superheater to avoid any decrease in quality during the expansion process in the turbine. On the other hand, the present ORC, which uses isobutane, does not need a superheater, because saturated vapor curve in the temperature versus entropy ( $T - s$ ) diagram for n-butane has a positive slope, as shown in Figure 3. 9b, and liquid droplets are not formed during the expansion process, in contrast to water. A superheated approach for dry fluid such as isobutane is not appropriate and would even cause a decrease in ORC efficiency due to the limited temperature

difference between the hot and cold sides. The mass flow rate was set to 1.61 kg/s to generate 60 kW theoretically, by designing the nozzle throat area of the turbine under the above condition.

At the design point (DP), the Grassmann diagram in Figure 3. 10 describes the exergy flow entering and leaving the power plant and the losses. The total exergy input to the system is estimated to be 212.24 kW, which arrives from tapping a part of the flow from the production well, and produces a power output of 58.76 kW. The condenser consists of two air-cooled condensers which have exergy losses of 12.58 kW (5.9 %). This equipment consumes 4.8 kW or 2.2 % of the total exergy, which is not plotted on the diagram. The preheater-evaporator loss is 36.85 kW (17.36 %), and the turbine loss is 33.21 kW (15.6 %), represent two major losses in the system. The exergy waste of the brine being sent back to the reservoir is significantly large at 52.98 kW. This amount constitutes 24.96 % of the total input of exergy.

It can be observed that a large irreversibility took place due to the inefficiency of the turbine which was supposed to be used on its specific design point. The lower efficiency of rotating components denotes that the turbine and pump are operated far from the design point. Hence, emphasis should be laid on design-point optimization for operation in particular off-design conditions.

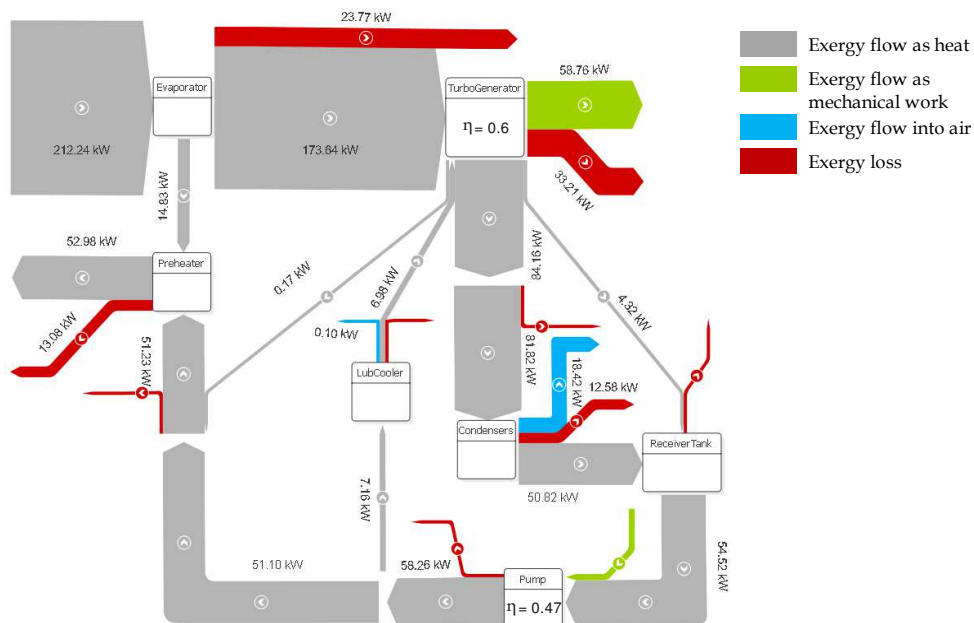


Figure 3. 10 Grassmann diagram for exergy flow and losses in 60 kW GrSk ORC.

To optimize the power conversion process, two major components are modeled in detail, e.g. heat exchangers and rotating components. There are several correlations available to characterize the behavior of the heat exchangers encountered in organic Rankine cycles so that the heat transferred and the pressure drop can be evaluated. The models can be more or less complex depending on the accuracy required. Geometrical info regarding HXs is required for this analysis. Nevertheless, this is not always available for heat exchangers due to confidentiality issues. Geometrical information is often missing, and only some reference values are occasionally found in catalogs for particular experimental conditions. To solve this issue, a three-zone HX model-based sizing is accomplished in this chapter to determine the detailed geometry of heat exchangers working in 60 kWel organic Rankine cycle. They comprise shell-and-plates HX either as preheater or evaporator and finned-tube HXs as the condensers.

### *Preheater-evaporator sizing*

The geometry of shell-and-plate heat exchangers is equivalent with the standard geometry of plate heat exchangers as can be seen in Figure 3. 11. A ratio of effective heat transfer area to the whole circular plate is assumed to be 0.7 [Hesselgreaves, 2001], and further new geometry parameters need to be assigned if deterministic heat transfer correlations are used. Both hot and cold fluids flow through the plate, and cold one goes through boiling process, the correlation is chosen for the heat transfer coefficient is the Hsieh-Lin [2002] correlation. This correlation is widely accepted by researchers to characterize pool and nucleate boiling in plate geometry. For the liquid phase flow Mungley-Manglik and VDI Martin [2010] correlation are used, which also will be used for the calculations of heat transfer for the fluid in the hot and cold side, respectively.

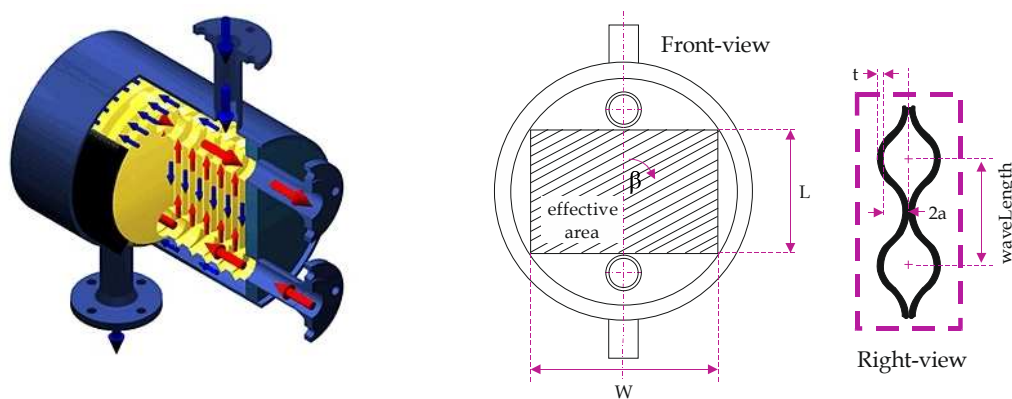


Figure 3. 11: Illustration of shell-and-plate heat exchangers (a) flow characteristics (adapted from Vahterus [2011]) and (b) dimension designation.

The design point of the preheater and evaporator are summarized in Table 3. 5. By determining width and chevron angle of the plate, three degrees of freedom are available when dimensioning a plate heat exchanger: the amplitude, the enlargement factor (corrugation pattern), and the total flow width. The total flow width is given by the plate width multiplied by the number of channels, which is related to some plates. Number of plates  $N_p$  can be computed as

$$N_p = 2(W_{tot}/W) + 1 . \quad (3. 21)$$

After calculating heat transfer area of each phase zone, the length  $L_k$  can be known, which is defined as

$$L_k = \frac{A_k}{\phi_e(N_p - 2)W} , \quad (3. 22)$$

where  $A_k$  is heat transfer area (subscript  $i$  denotes the phase zone),  $\phi_e$  is enlargement factor and  $W$  is plate width. Thus, proportional to the area in eq. (3. 16), the plate length can be computed as  $L = L_L + L_{\phi^2} + L_V$ .

|               | mass flow<br>$\dot{m}$ [kg/s] | pressure<br>$p_{in}$ [MPa] | inlet temp.<br>$T_{in}$ [°C] | outlet temp.<br>$T_{out}$ [°C] | heat load<br>$\dot{Q}$ [kW] |
|---------------|-------------------------------|----------------------------|------------------------------|--------------------------------|-----------------------------|
| PREHEATER     |                               |                            |                              |                                |                             |
| geofluid-side | 2.7                           | 1.5                        | 140                          | 100                            | -234                        |
| n-butane-side | 1.61                          | 1.39                       | 35                           | 95                             | 234                         |
| EVAPORATOR    |                               |                            |                              |                                |                             |
| geofluid-side | 2.7                           | 1.5                        | 100                          | 80                             | -459                        |
| n-butane-side | 1.61                          | 1.39                       | 95                           | 95                             | 459                         |

Table 3. 5: Operating condition parameters of preheater and evaporator.

The absolute deviation (AD) of the heat transfer area (thermal)  $AD_1$  and pressure drop (hydraulic)  $AD_2$  has been used as objective function and the constraint. Based on the manufacturer's data, the objective heat transfer area is 5.8 m<sup>2</sup> and 19.7 m<sup>2</sup> for preheater and evaporator, respectively. Likewise, the pressure drop is constrained around 128 mbar and 156 mbar. They can be written as

$$AD_1 = \left| \frac{A - A_{obj}}{A_{obj}} \right| , \text{ and} \quad (3. 23)$$

$$AD_2 = \left| \frac{\Delta p - \Delta p_{obj}}{\Delta p_{obj}} \right|,$$

where  $A$  and  $\Delta p$  are heat transfer area and pressure drop, respectively. One pass configuration is assumed for both plate HXs. An iterative scheme is required to fit the three degrees of freedom using Covariance Matrix Algorithm - Evolutionary Strategy (CMA-ES) from Hansen et al., [2006]. Minimum and maximum values of them are taken as follows:

- $1.2 \cdot 10^{-3} \leq a \leq 2.5 \cdot 10^{-3}$  m. Increasing pattern amplitude  $a$  increases cross-sectional area of the flow channel, thus decreases the Reynolds number.
- $1.1 \leq \phi_e \leq 1.5$ . Increasing enlargement factor  $\phi_e$  decreases the hydraulic diameter which increases the Reynolds number.
- $0.1 \leq W_{tot} \leq 4$  m (for preheater) and  $10 \leq W_{tot} \leq 15$  m (for evaporator). Increasing the total width  $W_{tot}$  decreases the Reynolds number. This leads to a lower pressure drop and to a higher required heat transfer area, since the heat transfer coefficient is also decreased.

Therefore, by imposing a heat transfer area and a pressure drop limitation, it is possible to define the corrugation pattern and total flow width of the plate heat exchanger. The fitting procedure can be described as

1. Process parameters from the heat and mass balance are determined and chevron angle  $\beta$ , pattern amplitude  $a$ , enlargement factor  $\phi_e$ , total width  $W_{tot}$  are estimated.
- 2. For each zone, use eqs. (3. 13) - (3. 16) to compute the required heat transfer area  $A_L, A_{\phi^2}, A_V$ .
3. Compute the length of each zone  $L_L, L_{\phi^2}, L_V$  using eq. (3. 22).
4. Compute the pressure drop of each zone using eq. (2. 10).
5. Evaluate absolute deviation of total heat transfer area  $AD_1$  and pressure drop  $AD_2$  with eq. (3. 23).
6. Step 2 - 5 are iterated until the absolute deviation of the area is minimized while maintaining absolute deviation of pressure drop below 10%.

The imposed and resulted geometrical parameters of the evaporator model are presented in Table 3. 6.

| PREHEATER ( $A = 5.8 \text{ m}^2$ )   |            |                   |         |
|---------------------------------------|------------|-------------------|---------|
| Parameter                             | Value      | Parameter         | Value   |
| number of plates                      | 17         | wall thickness    | 0.75 mm |
| length                                | 2.93 m     | pattern amplitude | 1.57 mm |
| width                                 | 0.25 m     | wave length       | 13 mm   |
| chevron angle, $\beta$                | $30^\circ$ | height            | 62 mm   |
| EVAPORATOR ( $A = 19.7 \text{ m}^2$ ) |            |                   |         |
| Parameter                             | Value      | Parameter         | Value   |
| number of plates                      | 131        | wall thickness    | 0.75 mm |
| length                                | 0.72 m     | pattern amplitude | 1.66 mm |
| width                                 | 0.42 m     | wave length       | 10 mm   |
| chevron angle, $\beta$                | $60^\circ$ | height            | 529 mm  |

Table 3. 6: Best fitted dimension of preheater and evaporator.

It can be seen that preheater and evaporator are assumed to have different chevron angles, which are chosen by minimizing the absolute deviation of pressure drop. The pressure drop is evaluated using Hsieh-Lin [2002] correlation for boiling and VDI Martin [2010] for single-phase.

### Condenser sizing

Since air condensers are well-known components in hydrocarbon processing applications, a method based on GPSA (Gas Processors and Suppliers Association) [Gas Processors Suppliers Association, 2004] standard is used to compute the condenser size and fan consumption. The inputs are the process parameters as tabulated in Table 3. 7. Special attention is paid to the fan power consumption since it can amount for a non-negligible share of the generated power. The fan consumption is computed as a function of the total pressure drop and volumetric flow rate.

|               | mass flow        | pressure       | inlet temp.   | outlet temp.   | heat load      |
|---------------|------------------|----------------|---------------|----------------|----------------|
|               | $\dot{m}$ [kg/s] | $p_{in}$ [MPa] | $T_{in}$ [°C] | $T_{out}$ [°C] | $\dot{Q}$ [kW] |
| n-butane-side | 0.805            | 0.32           | 47            | 3.2            | -307           |
| air-side      | variable         | 0.1            | 20            | variable       | 307            |

Table 3. 7: Operating conditions of one cell condenser.

The careful calculation has to be taken since the standard calculation of GPSA uses English units instead of SI units. Geometry ratio parameters were assumed: APF, AR, and APSF, which are total external area/ft of fin tube, area ratio of fin tube compared to the exterior area of 1 in. OD bare tube, external area of fin tube/sq ft of bundle face area. Width is defined as  $= F_a/L$ , and face area  $F_a = A_o/APSF$ . By those given parameters and calculated heat transfer area, other geometrical parameters can be calculated. Such as number of tubes can be computed as

$$N_t = \frac{A_o}{APF \cdot L}, \quad (3.24)$$

where  $A_o$  and  $L$  are total external area and condenser length, respectively. By using calculated face area  $F_a$ , the diameter of fans can be calculated as

$$d_F = \left( 4 \frac{0.4 \cdot F_a}{N_F \cdot \pi} \right)^{0.5}, \quad (3.25)$$

with  $N_F$  is number of fans. In order to approximate the brake power per fan, following relation is applied

$$P_F = \frac{\dot{V}_F \cdot \Delta p_a}{\eta_F}. \quad (3.26)$$

The total air pressure drop  $\Delta p_a$  calculation includes (1) air static pressure drop and (2) pressure drop about volumetric flow and fan area. The first term, air static pressure drop, is a quadratic function of air face mass velocity. Since the fan is not covered all the face area, the second term is applied.

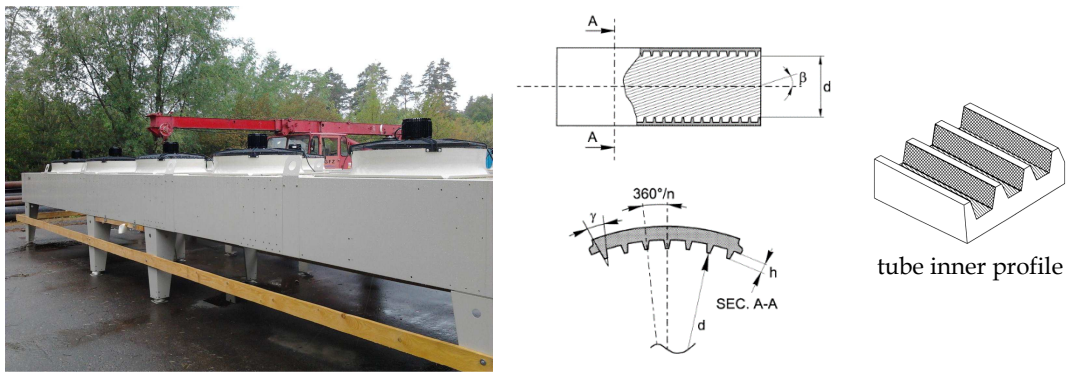


Figure 6. 1: Photograph and illustration of finned micro-tube heat exchangers [Cavallini, 2010] used in the 60 kWel GrSk ORC.

The sizing was conducted with basic assumptions of 5 forced-draft fans, 1 in. OD fin tube with 5/8 in. high fins, and 2.5 in. (triangular) tube pitch. The bundle layout is defined as 3 tube passes, 4 row of tubes, and 30 ft (9.14 m) long tubes. APF, AR, and APSF are fixed at 5.58 sq. ft/ft, 21.4, and 107.2, respectively. Again, an iterative sizing procedure is required.

1. Determine basic geometry and approximate overall heat transfer coefficient ( $26.7 \text{ W/m}^2\text{K}$ ) from GPSA standard.
2. Define air temperature rise, e.g. cooling-air outlet temperature.
3. Calculate CWTD, unit width, the number of tubes, tube-side pressure drop, tube-side film coefficient, air quantity, air face mass velocity, air-side film coefficient, and overall heat transfer coefficient.
4. Steps 2 - 4 are iterated until an agreement between manufacturer's data and the model result is fulfilled.
5. Calculate minimum fan diameter, air-side pressure drop, and fan power by using eqs. (3. 25) - (3. 26).

The sizing results are summarized in Table 3. 8 below.

| Parameter           | Unit              | Data   | Model  | Abs. Dev |
|---------------------|-------------------|--------|--------|----------|
| width               | m                 | 1.54   | 1.5    | 2.60%    |
| area (outer)        | m <sup>2</sup>    | 1,328  | 1,476  | 11.14%   |
| n-butane pr. drop   | mbar              | 14     | 26     | 85.71%   |
| fan diameter        | m                 | 1.35   | 1.18   | 12.59%   |
| Air volumetric flow | m <sup>3</sup> /h | 94,318 | 94,719 | 0.43%    |
| fan power per unit  | W                 | 480    | 472    | 1.67%    |

(a) Manufacturer's data

| Parameter                | Value  | Parameter                | Value   |
|--------------------------|--------|--------------------------|---------|
| tube length              | 9.14 m | fin thickness            | 0.15 mm |
| number of serial tubes   | 4      | fin pitch                | 2.54 mm |
| serial tube distance     | 55 mm  | tube inner diameter      | 22.1 mm |
| number of parallel tubes | 26     | tube wall thickness      | 1.65 mm |
| parallel tube distance   | 63.5   | number of parallel flows | 35      |

(b) Detailed air-cooled condenser geometry (1 cell or bay)

Table 3. 8: Best fitted dimension of one cell condenser.

### *Pump and turbine sizing*

Pump size was determined by using pump manufacturer's data (GRUNDFOSS). The performance curve for the turbine is not available. Thus, the turbine size was defined by assuming the design-point (DP) is equivalent to the plant's design-point (see evaporator outlet pressure, temperature, and mass flow rate in Table 3.9). Nonetheless, this assumption has to be tested later due to finding that the turbine is operated far from its manufactured DP.

| Parameter         | Value                                  | Parameter         | Value                   |
|-------------------|--|-------------------|-------------------------|
| TURBINE           |  | PUMP              |                         |
| inlet nozzle area | 1.52 X 10 <sup>-3</sup> m <sup>2</sup> | shut-off pressure | 2.66 MPa                |
| is. enthalpy drop | 66.7 kJ/kg                             | design vol. flow  | 0.034 m <sup>3</sup> /s |
| outlet vol. flow  | 1.86 m <sup>3</sup> /s                 |                   |                         |

Table 3.9: Assumed design-point parameters of turbine and pump.

By given shut-off pressure and design volumetric flow at 50 Hz, the quadratic character of the pump can be computed with eq. (4.12) described in Chapter 4. These size parameters are useful to be imposed as inputs to operation optimization and dynamic simulation performed in the next subchapter.

### *Experimental validation*

Due to the problem of well productivity, the Groß-Schönebeck 60 kWel ORC is not viable to be operated until this thesis is written. In this section, experimental validation procedures are prepared to validate the recent model, identify the model parameters, and analyze the differences. The parameter identification process is illustrated in the flow chart given in Figure 3.12 and Figure 3.13 for heat exchangers and turbine. The parameters of the model are identified by imposing some measurements as input variables and by minimizing a global error function accounting for the errors on the prediction of the main output variables

$$error = \sum_1^{N_{var}} \frac{1}{N_{var}} \left( \sqrt{\sum_1^{N_{test}} \left( \frac{x_{calc} - x_{meas}}{x_{meas}} \right)^2} \right), \quad (3.27)$$

where  $x$ ,  $N_{var}$ ,  $N_{test}$  denote the output variables, number of the the measured output variables, and number of the the test for each output variable, respectively.

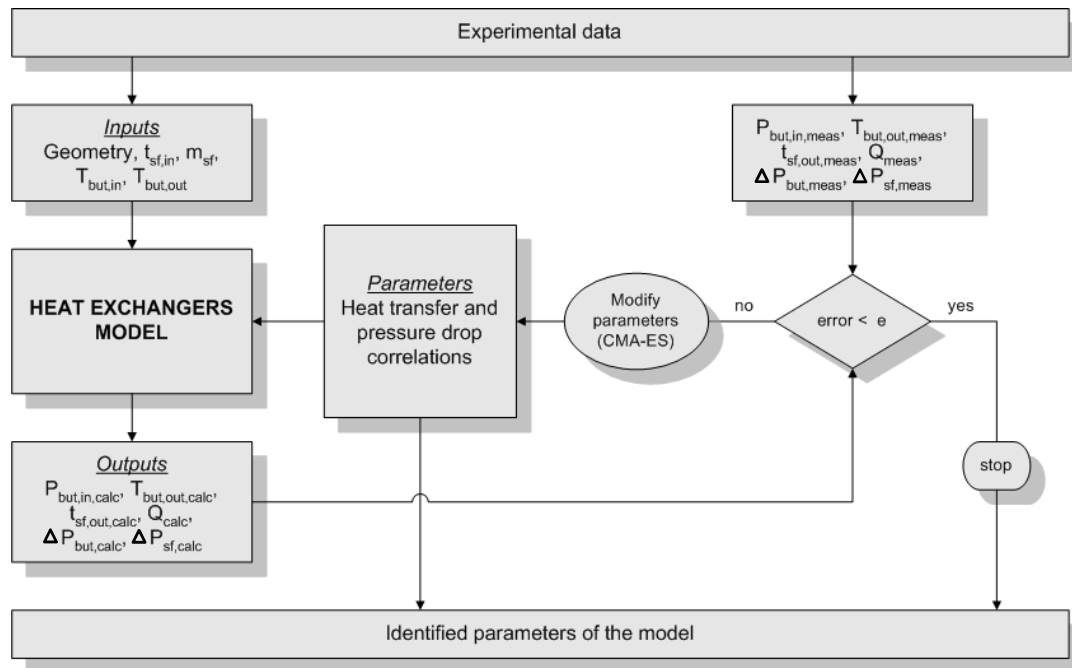


Figure 3. 12: Procedure for parameter identification process of HXs.

A comparison between measured and calculated values is of great importance to test the HX models describe before. Knowledge of the exact geometry of the HXs is required for an inverse study, e.g. evaluating heat transfer and pressure drop correlations. The input variables of the heat exchanger model are the geometry, the inlet temperature and the mass flow of the secondary fluid (geothermal). The model calculates the pressure drops of hot and cold sides, the heat load, and the outlet temperature. Imposing the mass flow rate as an input variable and the outlet pressure as an output variable is only a convention. In fact, the outlet pressure could be imposed as an input (in the experimental set-up, it is measured by the pressure transducer) and the mass flow rate will be predicted by the model.

The evaluation of heat transfer and pressure drop correlations are proceeded as the following. By implementing modified Wilson-plot method and Equal Reynolds number method [Muley and Manglik, 1999], single-phase and two-phase heat exchange coefficients  $c$ , see eqs. (2. 5) and (2. 7), respectively; and friction coefficient  $c$ , see eq. (2. 18). This is described by the simplified modeling approach that the identified correlations not only account for the heat exchange, but also for pressure drops and ambient heat losses (mainly in the evaporator which lower the coefficient  $c$ ) [Quoilin *et al.*, 2010].

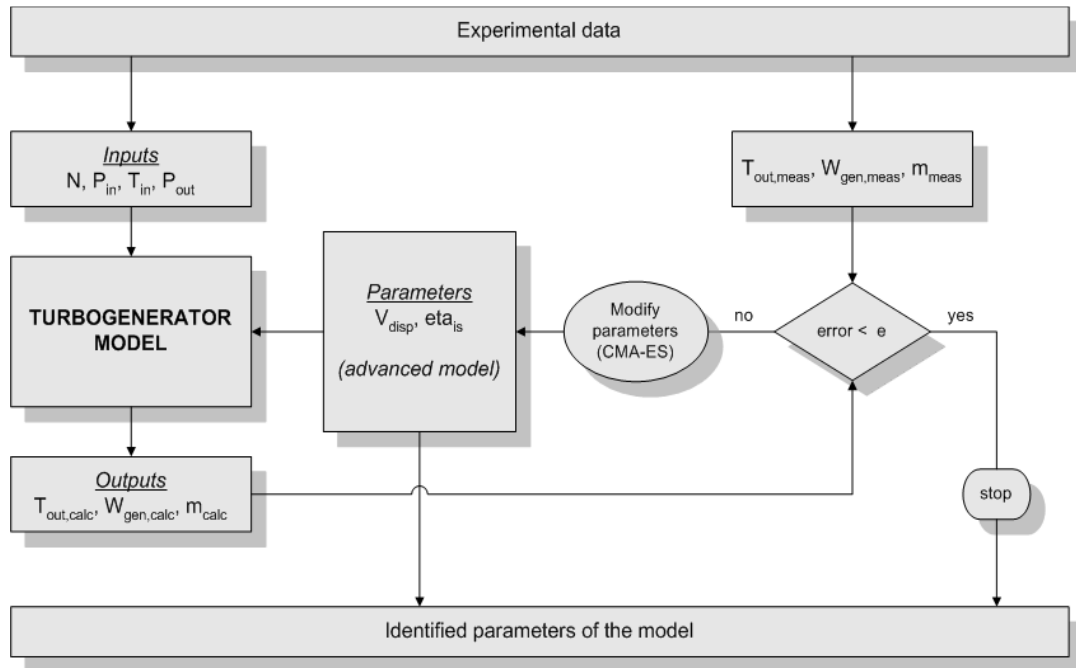


Figure 3. 13: Procedure for parameter identification process of turbine-generator.

For the turbine, the design-point outlet volumetric flow rate and isentropic efficiency can be fitted by using experimental data at varying operating conditions. The analysis will draw an important conclusion regarding the necessity of determining the proper design-point about off-design operation. The parameters of the turbine model are tuned to best fit the three model outputs (mass flow rate, outlet temperature, shaft power) to experimental data. The input variables of this calculation are the turbine rotational speed, the working fluid inlet pressure, the inlet temperature and the outlet pressure. The parameters of the turbine model are identified by minimizing an error objective function in eq. (3. 27) (using CMA-ES) defined as an average of the errors for each output.

The objective of the experimental work is to define actual design-point (DP) of the installed turbo-generator, i.e. DP outlet volumetric flow rate, DP isentropic efficiency (and DP isentropic enthalpy drop). Given these DP parameters, the behavior of the turbo-generator is described by an advanced model of isentropic efficiency correction factors, see eqs. (3. 19) and (3. 20). Also, the mass flow rate flowing through the turbine is governed by Stodola cone rule (see eq. (4. 13) in Chapter 4) dependent to pressure and density (or temperature) at the turbine inlet. It should be noted that this rule has coefficient  $C_T$  indicating equivalent flow area in square meters, which is also needed to be identified.

### 3.2.4 Multivariable control strategy optimization

Modular design prerequisites flexible power plant which can be established by means of the advanced control strategy. By using this, operation optimization on external environmental parameters is carried out. In this thesis, we developed a multivariable control strategy for geothermal ORC application. Optimum parameters like evaporating pressure and superheating (the difference between turbine inlet temperature and saturation temperature) can be obtained for given working conditions. Four inputs are necessary to determine this evaporating pressure and superheating: the geothermal fluid temperature, the condensation temperature, geothermal fluid flow-rate and the working fluid flow-rate. Nonetheless, it is important to base the control system on variables that are easily and constantly measurable. In the systems under consideration here, the geothermal fluid temperature is fixed, geothermal fluid flow rate and ambient temperature are two parameters that are fluctuating. Thus, the control strategy will be based on them.

Since subcooling in the condenser is fixed, condensation temperature and ambient temperature can be related, provided that the cooling air flow rate is known. The optimal evaporating pressure and superheating can, therefore, be correlated to the geothermal fluid flow-rate and to the ambient temperature, which will be dealt in more detail in the next subchapter 3.3.3. To determine this optimum over a broad range of working conditions, the model described previously is implemented in steady-state in Matlab. The optimum evaporating temperature is determined using the Covariance Matrix Algorithm - Evolutionary Strategy (CMA-ES) [Hansen, 2006] for working conditions varying in the following range:

$$\begin{aligned} 120^{\circ}C &\leq T_{geo} \leq 170^{\circ}C \\ 0.2 \cdot \dot{m}_{geo,DP} &\leq \dot{m}_{geo} \leq 1.2 \cdot \dot{m}_{geo,DP} \text{ at } T_{geo,DP} \\ -10^{\circ}C &\leq T_{amb} \leq 40^{\circ}C . \end{aligned} \tag{3.28}$$

To best match these optimum conditions, three degrees of freedom are utilized that are the turbine nozzle opening, the pump speed, and the condenser fan speed. It should be noted that the action of these three parameters has very different time constants. A modification of the pump flow rate changes the working conditions of the evaporator and therefore induces a variation in the evaporating temperature and the quantity of superheating, but with a delay due to the thermal and fluid dynamics of the heat exchanger. Conversely, a modification of the turbine nozzle induces a nearly instantaneous change in the evaporating pressure. Here,

the volumetric flow rate absorbed by the turbine is modified, while the mass flow rate is kept constant.

The evaporating pressure being a more critical working condition than the superheating, it is decided to control the evaporating pressure with the turbine nozzle and the superheating with the pump flow rate. Meanwhile, the condensation temperature is controlled by condenser fan flow-rate. PI controllers are used to maintaining the desired working conditions. The choice of PI controllers over PID controllers is justified by their satisfactory behavior in the simulations performed in Section 3.3 and by the higher sensitivity of PID controllers to measurement noise (Sylvain, 2011). The equation describes the control signal:

$$CS = K_p \left( b \cdot e + \frac{1}{T_i} \int e + track \cdot dt \right), \quad (3.29)$$

where  $e$  is the error between the present value and the set point, both scaled between 0 and 1,  $b$  is the set point weight on the proportional action,  $K_p$  is the proportional gain, and  $T_i$  is the integral time constant. The control signal saturates at 0 and at 1. The variable “track” is defined as the difference between CS and its saturated value, in order to avoid integral windup.  $K_p$ ,  $b$  and  $T_i$  are parameters to be tuned. This is done manually, with the aim of minimizing the stabilization time towards a steady-state of the system. Since the variable affects each other, it is called multiple input, multiple output (MIMO) control strategy as depicted in Figure 3.14.

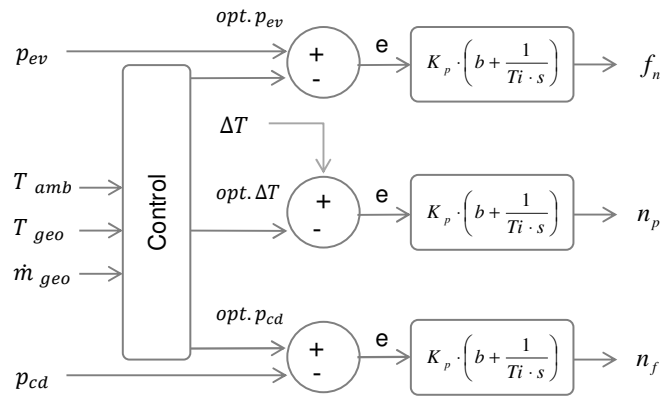


Figure 3.14: Multivariable (MIMO) control strategy: optimum evaporating temperature, superheating, and condensation temperature.

### 3.3 DYNAMIC CHARACTERISTICS OF THE ORGANIC RANKINE CYCLES

The system dynamics of the 60 kWel Groß-Schönebeck ORC (GrSk60) and a conceptual 1,000 kWel modularized-ORC (mORC1000) are investigated in this subchapter. Simulations of the dynamic response of the ORCs to changes in ambient air temperatures and electrical load from the grid on representative days for temperate and tropical climates are presented. A control-oriented model describing ORCs dynamic behavior has been constructed using mathematical models of heat exchangers and turbomachinery. Changes in electrical load cause movement of working fluid mass between the hot and cold sides of the ORC. Movement of geothermal fluid mass results in variations in working fluid mass flow rate, pressures, temperatures, and net power output. The ORC maintains a relatively stable net power output when operating under ambient and load fluctuations representative of an average day in a small isolated grid. The simulations highlight the potential for utilizing multivariable control strategy for ORC mass-flow rate control in low load, and the need for control of superheating conditions in high ambient temperature, for the sustained efficient operation of the ORC within varying operating condition.

#### 3.3.1 Thermodynamics modeling in Modelica/Dymola/TIL

The dynamic power-plant modeling effort in this thesis includes the following list of components:

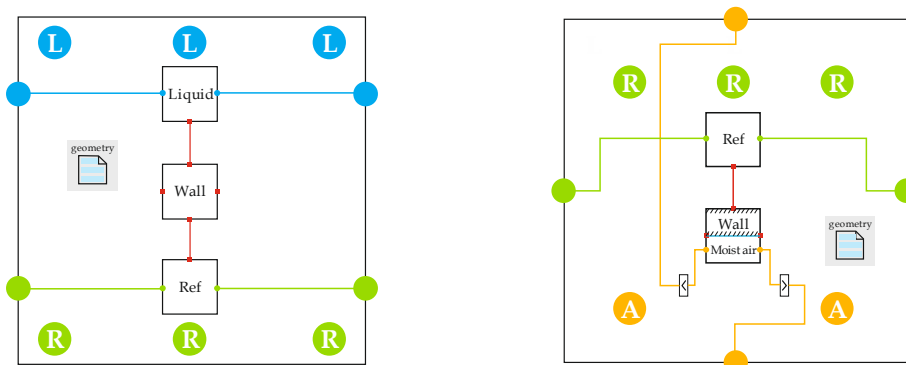
- Centrifugal pump
- Shell-and-plate heat exchanger (60 kWel GrSk)
- Shell-and-tube heat exchanger (1,000 kWel modular ORC)
- Fin-and-tube heat exchanger
- Expansion valve
- Receiver (hot-well)
- Assembled system model with initialization

The top level models should present variables that are interesting to design or field engineer. The models include configurations of the components with suitable parameters and boundary conditions that can be used to either validate the presented models or extend them to new or interesting scenarios. Variables such as total loop fluid mass, heat exchanger power, pump power required, and turbine power produced, are suitable for this. Likewise, simulation 'sensors' should be included in the top level model at the same physical locations as real sensors could be found in the physical cycle, for easy comparison and validation.

Finally, provisions should be allowed for the implementation of control systems. For reference, a diagram of the final top level Modelica model used for validation of the 60 kWel GrSk loop is included here in Appendix A. The working loop of the ORC is modeled as a closed loop thermodynamic system, which means that it contains a fixed mass of working fluid which is pumped around the cycle and expands, compresses and exchanges heat as it passes through the components.

### TIL Library

TIL library implemented in Dymola/Modelica is amenable to fulfill the modeling above requirements. The TIL consists of some smaller cell models, each with its connectors, and therefore inlet and outlet mass flow rates, specific enthalpies, and pressure. The fluid model is differentiated as VLE (two-phase) fluid (green), liquid (blue), and humid air (orange) as we can see in Figure 3. 15. A spatial discretization scheme is specified as a parameter, which dictates how the fluid state of each cell is represented, with the default being ‘centered’ which approximates the cell’s representative specific enthalpy equal to its average between inlet and outlet specific enthalpy. The TIL heat exchanger models can be connected directly to the turbomachinery models, though some parameters need to be tuned so that the models match each other. See Section 3.2 for further details of the used shell-and-plate HXs, finned tube HXs, shell-and-tube HXs, pump, and turbine. In Section 3.3.2, this model is finally used to investigate potential improvements to the GrSk60 power plant. The implementation of new correlations to the heat transfer models that go with the TIL is easy. Hence, once the experimental data is available, the heat transfer fitting and validation can be certainly carried out by the reverse engineer.



(a) Counter-flow heat exchangers model      (b) Cross-flow heat exchangers model

Figure 3. 15: TIL scheme of the heat exchanger model: counter-flow heat exchangers: shell-and-tube/plate heaters (a) and finned-tube condensers (b).

The heat exchangers and turbomachinery correlations described in the previous section was implemented in this library. The dynamic heat transfer behavior of TIL has been validated by Vetter [2014] using experimental data from Dwivedi et al. [2007] for plate HX and single-phase system. In his work, the behavior of outlet temperature by changing hot and cold sides mass flow was simulated and compared with measured results. From the comparison, there was good agreement between simulated and measured performances. Thus, confirming that HX model of TIL is qualitatively valid.

To close the cycle, another component which is receiver (hot well) is described by the following equation as mass storage

$$\frac{d\rho}{dt} = \frac{1}{V_{tank}} (\dot{m}_{in} - \dot{m}_{out}) , \quad (3.30)$$

where  $V_{tank}$  is volume of the tank. Valve is modeled by using correlation as

$$\dot{m} = (2\rho_{in}\Delta p)^{0.5} A_{eff} , \quad (3.31)$$

where  $A_{eff}$  is effective flow area.

#### *Horizontal shell-and-tube heat exchangers with shell-side evaporation*

One pass horizontal shell-and-tube evaporator offers pure counter-current heat exchange, easy to clean, and have been used in commercial geothermal binary (ORC) power plant, for instance, the one which is owned by ENEL [Ghasemi *et al.*, 2013]. Shell-and-tube heat exchangers library using modified tube-and-tube HX in TIL were developed. The following describes the approach to model forced flow shell-side boiling in a TEMA E-type shell and tube heat exchanger.

There are very few data available in the open literature for boiling two-phase flows on the shell side of real industrial shell and tube heat exchanger geometries. Many of the models and correlations for two-phase pressure drop multipliers and flow patterns are based on test data obtained from rectangular tube bundle test sections [Grant *et al.*, 1977]. The flow pattern occurs in this kind of two-phase flow are

- Spray flow, occurring at high mass flow qualities with liquid carried along by the gas as a spray.
- Bubbly flow, occurring at low mass flow qualities with gas distributed as discrete bubbles in the liquid.
- Intermittent flow, where intermittent slugs of liquid are propelled through the model by gas.

Geometry modification in a cross-flow heat exchanger (tube-and-tube) model has been carried out to model this shell-side evaporator. Each cell of this HX represents one control volume between baffles as can be observed in Figure 3. 16.

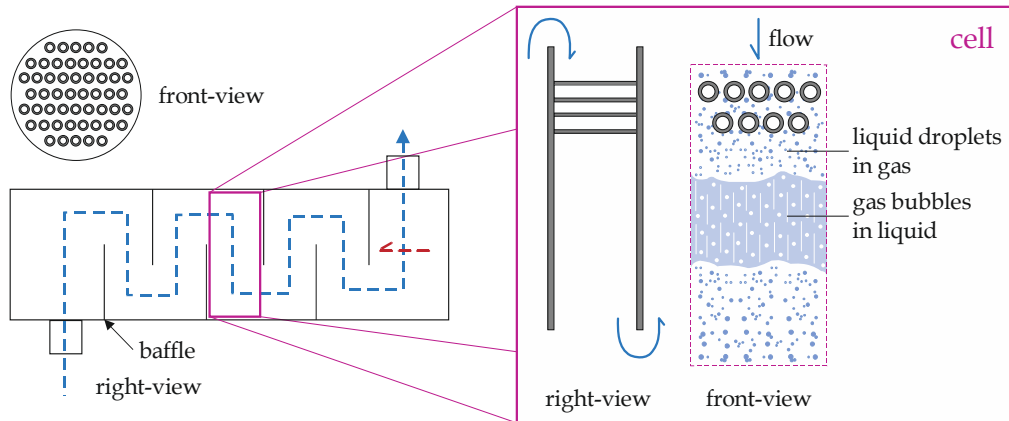


Figure 3. 16: Shell-and-tube HX with shell-side evaporation model.

The heat transfer and pressure drop have been implemented applying correlations describe in Chapter 2. For cell exhibiting two-phase zone, the heat transfer coefficient is computed as an average over the quality range by integration.

### 3.3.2 Retrofitting control strategies for 60 kWel Groß-Schönebeck ORC

To demonstrate how the model described previously can be used as an optimization tool, we conducted control strategy study for GrSk60. The models developed in this study were designed with an experimental facility in mind that could be used to validate the system of models. So the scope of the modeling was set according to the size, configuration, and components used in that test facility, which was designed and built by the GeoForschungsZentrum Potsdam and is known as the Groß-Schönebeck Insitu Laboratory. One of the facility installed at the testing laboratory is an Organic Rankine cycle with up to 60 kW of electrical power, delivered through a separate heating loop, and up to 320 kW of cooling power, drawn through a separate loop. A complete description of the laboratory setup is detailed in the previous section. A dynamic model has been assembled based on the dimensions emphasized in Section 3.2. The object diagram is shown in Figure A.1 (see Appendix A).

#### *Sudden small-load variation*

Operation in insular mode, especially for remote area application in archipelago country like Indonesia, required regulation to small load changes. The frequency change imposed by variation of load can be described by

$$\Delta f = \Delta P / K_n (1 - e^{-t/c_t}) \quad (3.32)$$

where  $t$  = time (s)  $c_t$  = time constant which is typically 5 - 10 seconds (Vuorinen, 2009)  $K_n$  = typically natural power gain of the network. Without frequency control, the frequency change will be  $1/K_n$  times the power difference. Typically, change in 10% drop in power produced will reduce the frequency by 3 - 5 Hz. The frequency then will be too low for most of the electrical equipment in the power system, and thus frequency control is needed to maintain the frequency in allowable limits.

A secondary control strategy is implemented by bypassing a part of the working fluid directly to the condenser, see Figure 3. 17. This strategy will allow a fast load reduction because of less mass flow through the turbine.

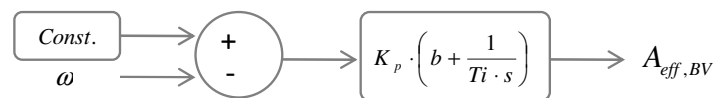


Figure 3. 17: Vapor bypass control strategy.

The input parameter on this control is grid frequency. The grid frequency is kept constant by changing the supplied power following the load demand. The PI parameters are summarized in Table 3. 10 below.

| Bypass valve |           |
|--------------|-----------|
| $K_p$        | $10^{-6}$ |
| $b$          | 1         |
| $T_i$        | 0.05 s    |

Table 3. 10 Vapor bypass control strategy PI parameters.

The assembled model was simulated to examine the control systems behavior. A base load of 41 kW oscillates. The power plant runs at the full-load and the vapor bypass valve actuating to change the supplied power of the turbine with load demand. The simulation results are depicted in Figure 3. 18.

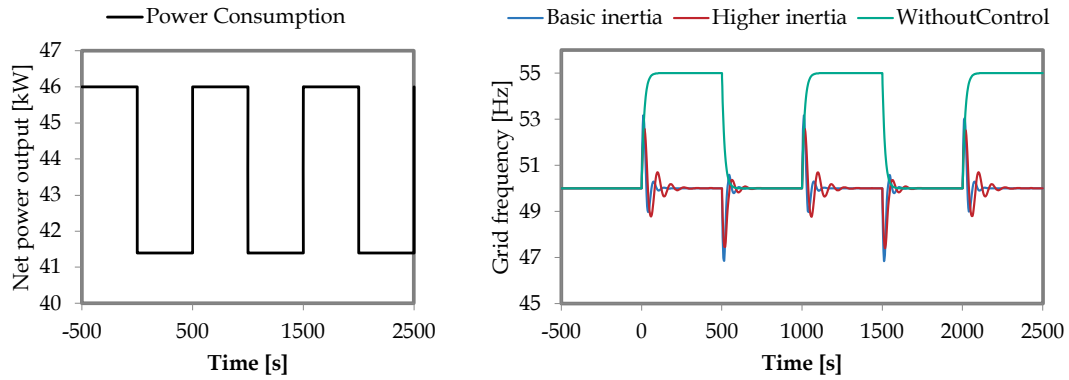


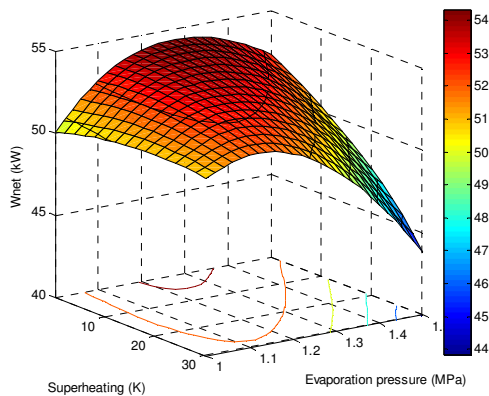
Figure 3. 18: Sudden 10% change of electrical load under three scenarios: without control, basic inertia, and higher inertia.

From the simulation, it can be identified, 10% of rapid load changes will change the frequency by  $\pm 2.5$  Hz. It is observed that bypassing a small fraction of the vapor will counterbalance the rapid load changes, keeps the frequency within 50 Hz. Increasing the inertia (e.g. flywheel system) also shows positive effects in reducing the peak frequency difference.

*Ambient temperature part-load*

As it is installed in a temperate climate, the GrSk test-bench exhibits a wide range of ambient temperature, e.g. from  $-5$  to  $35$  °C, during a year. A simultaneous multivariable control strategy optimization was carried out to find optimum evaporation pressure, superheating degree, and condensation pressure, see Figure 3. 19.

$T_{\text{ambient}} = 10$  °C



$T_{\text{ambient}} = 30$  °C

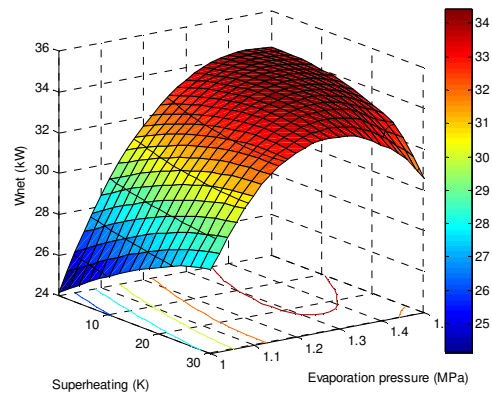


Figure 3. 19: The values of the net power output of plant are shown as functions of the two independent variables at an ambient temperature of (a)  $10$  °C and (b)  $30$  °C.

By implementing the MIMO control strategy on GrSk60, the net power output can be optimized as shown in Figure 3. 20.

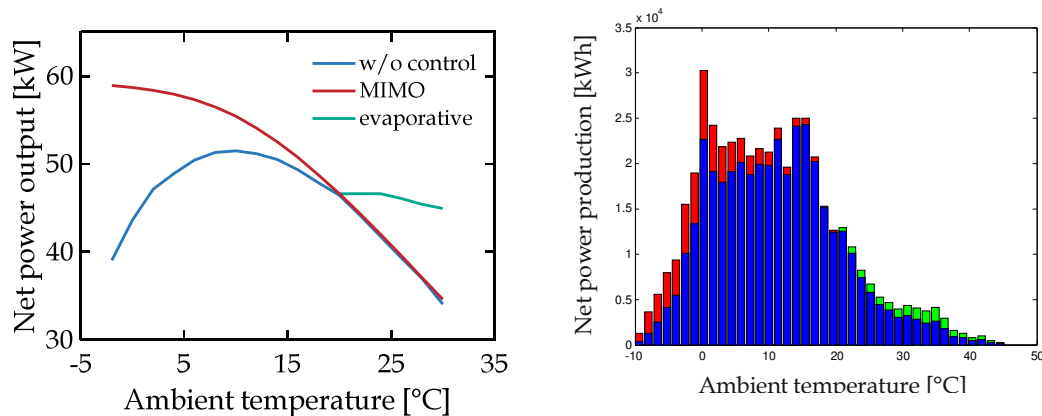


Figure 3. 20: (a) The optimum values of the objective function are compared with the without-control-case one. (b) The total electricity generation in the base-case operation and the optimal operation are compared. The optimal operation offers 14.7% increase in the total electricity generation.

As predicted, at high ambient temperatures, the ACC system should be at full capacity for the optimal operation, but at low ambient temperatures, the cooling capacity of the ACC system should be adjusted to obtain the optimal operation by reducing volume flow rate of the air (rotational speed of the fans). This cooling control, evaporation pressure ( $p_{ev}$ ) and superheating ( $\Delta T$ ) controls increase net power output by 34.2% in winter time and 14.7% yearly, and even more 18.1% yearly if evaporative-cooling is applied. Water consumption for evaporative-cooling is 0.043 – 0.188 kg/s of fresh water with water temperature equivalent to ambient temperature. For comparison, the design geothermal fluid mass flow is 2.7 kg/s.

From the simulation results, for temperate climate, it is advisable to design the ORC at 10 °C rather than 20 °C in the existing design. This design point shift would lead to increase net power output during low ambient temperature which is denser distributed in one year.

### 3.3.3 Dynamic of load change: 1,000 kWel modular ORC simulation

In the insular operation mode, in which the modular geothermal ORC serves as a single power generator, the load-following mode should be applied to the plant. Moreover, when other renewables such as solar and the wind come online, the grid has to adjust to these intermittent sources. The flexibility is thus needed from other generation sources (i.e. geothermal) on the grid during certain hours of the day. This section examined how the modular geothermal ORC may behave on rapid, wide range load change to stabilize the grid frequency.

The simulated model is shown in the object diagram in Figure A.2. This configuration represents the 1,000 kWel modular ORC (mORC1000). The system mainly equipped with one variable-nozzle turbine, two shell-and-tube evaporators and 17 bays of finned-tube condensers as described in the following. Variable-nozzle turbine (see Figure 3. 21) is used in the system to adjust the openings of its nozzles to ensure the required flow at throat area, which broadens the operating range of the turbine, and improves the matching relationship between the turbine and the other equipment. The guide vanes are moved in such a way that the flow area between the vanes changes, and work thus similarly to a turbine control valve in an axial turbine. But the difference is that the flow change in the radial turbine is not made by throttling the flow, but by changing the flow area for acceleration of the fluid [Valdimarsson, 2014].

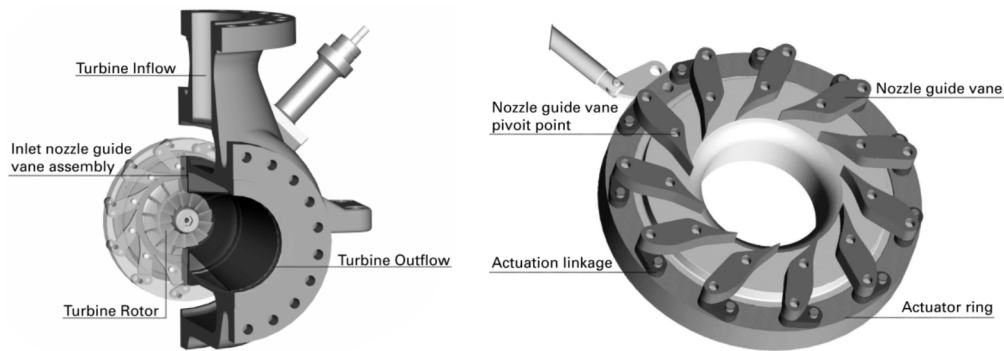


Figure 3. 21: Schematic of the variable IGV system of Atlas Copco. This variable IGV mechanism adjusts the flow area opening which avoids throttling process at the inlet [Valdimarsson, 2014].

Simulations have been run with the evaporator and recuperator model discretized with 25 cells; the condenser was discretized with 20 cells. Particularly for the evaporator and recuperator, this discretization were chosen to model each control volume between baffle. Also, to keep the acceptable execution time. The model parameters are listed in Table 3. 11.

| Parameter         | Value                | Parameter         | Value                                  |
|-------------------|----------------------|-------------------|--|
| EVAPORATOR        |                      | PUMP              |  |
| shell diameter    | 0.44 m               | shut-off pressure | 2.66 MPa                               |
| total tube length | 22 m                 | design vol. flow  | 0.034 m <sup>3</sup> /s                |
| RECUPERATOR       |                      | TURBINE           |  |
| shell diameter    | 0.54 m               | inlet nozzle area | 1.52 X 10 <sup>-3</sup> m <sup>2</sup> |
| total tube length | 14 m                 | is. enthalpy drop | 66.7 kJ/kg                             |
| CONDENSER         |                      | outlet vol. flow  | 1.86 m <sup>3</sup> /s                 |
| number of cells   | 17                   | CONTROL VALVE     |  |
| fan capacity      | 38 m <sup>3</sup> /s | design area       | 4.97 X 10 <sup>-2</sup> m <sup>2</sup> |

Table 3. 11: Size parameters of heat exchangers, rotating components and valve of mORC1000.

The most common control strategy is to define a constant evaporating temperature (or pressure) and superheating which is so called constant pressure. In this case, it is not possible to know a priori which constant evaporating temperature will be optimal for the process. This regulation strategy requires two

measurements: evaporation pressure and temperature at the evaporator outlet. The scheme is presented in Figure 3. 22. This regulation strategy requires two measurements:  $p_{ev,out}$  and  $T_{ev,out}$ . The  $T_{ev,out}$  and  $p_{ev,out}$  setpoints are 115 °C and 1.95 MPa, respectively.

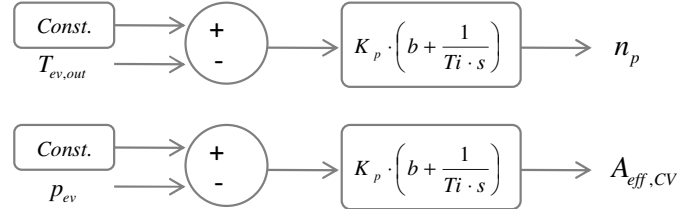


Figure 3. 22: Constant pressure control strategy: evaporating pressure and temperature after evaporator are measured and regulated by adjusting the control valve opening and the pump rotational speed.

A second traditional regulation strategy is tested to maintain thermal efficiency at varying working conditions. The pump rotational speed is selected to control the flow rate for a constant temperature at the turbine inlet as illustrated in Figure 3. 23. The TIT setpoint is 115 °C.

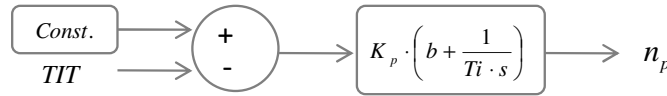


Figure 3. 23: Sliding pressure control strategy: temperature after evaporator are measured and regulated by adjusting and the pump rotational speed.

A third regulation strategy, which is developed in this thesis, is tested to obtain the best performance to varying working conditions, i.e., geothermal mass flow rate and ambient temperature fluctuations. This strategy corresponds to the MIMO control strategy depicted in section 3.2.4, Figure 3. 14. To determine this optimum over a broad range of working conditions, the model described in Section 3 is implemented in steady-state in Matlab. The optimum turbine inlet temperature (TIT), evaporation pressure ( $p_{ev}$ ), and condensation pressure ( $T_{cd}$ ) were de-termined using the CMAES (Covariance Matrix Algorithm - Evolutionary Strategy) for 36 working points at  $\dot{m}_{geo}$  and  $T_{amb}$  varying boundary conditions. The turbine inlet temperature is controlled by pump speed. It is determined by the evaporation pressure and superheating. While superheating is a function of geothermal fluid mass flow and ambient temperature. For geothermal fluid temperature of 161 °C, the multivariable regression from the optimization results are in the following

$$\Delta T_{ev,out} [^{\circ}C] = \max \left( (487.8 - 371.4 \cdot \log(\dot{m}_g) - 1.448 \cdot T_a + 26.51 \cdot \log^2(\dot{m}_g) + 0.9851 \cdot \log(\dot{m}_g) \cdot T_a), 0.1 \right), \quad (3.33)$$

$$TIT [^{\circ}C] = -4.5503 \cdot p_{ev}^2 + 45.579 \cdot p_{ev} + 29.287 + \Delta T_{ev,out},$$

with  $\dot{m}_g$ ,  $T_a$ , and  $p_{ev}$  are in kg/s, K, and MPa, respectively. Geothermal fluid mass flow  $\dot{m}_g$  is the only variable used to compute optimal evaporation pressure. The relationship can be written as

$$p_{ev} [MPa] = -0.0038 \cdot \dot{m}_g^2 + 0.1693 \cdot \dot{m}_g + 0.9073. \quad (3.34)$$

Condensation temperature  $T_{cd}$  setpoint is determined as function of geothermal fluid mass flow and ambient temperature  $T_a$  as

$$T_{cd} [^{\circ}C] = -255 + 0.4721 \cdot \dot{m}_g + 0.9532 \cdot T_a, \quad (3.35)$$

with variables in similar unit as eq. (3.3).  $K_p$ ,  $b$  and  $T_i$  are control parameters to be tuned. This is done manually, with the aim of minimizing the stabilization time towards a steady-state of the system. The following parameters (Table 3.12) are obtained.

|       | SLIDING. PR. | CONST PR. |      | MIMO |      |      |
|-------|--------------|-----------|------|------|------|------|
|       | Pump         | Pump      | CV   | Pump | IGV  | Fan  |
| $K_p$ | 5E-3         | 5E-3      | 1E-8 | 1E-3 | 1E-3 | 0.5  |
| $b$   | 1            | 1         | 1    | 1    | 1    | 1    |
| $T_i$ | 2 s          | 2 s       | 1 s  | 1 s  | 3 s  | 20 s |

Table 3.12: PI parameters for the three control strategies.

#### *Ramp up/down behavior*

Performance test of the three control strategies has been performed under the following ramp up/down conditions: the mass flow rate changes from 8.6 to 19.6 kg/s in 2, 1, and 0.5 hours which corresponds to  $1.5 \times 10^{-3}$  kg/s<sup>2</sup>,  $3 \times 10^{-3}$  kg/s<sup>2</sup>, and  $6 \times 10^{-3}$  kg/s<sup>2</sup> of mass acceleration respectively, see Figure 3.24. In the following, results of the transient simulation of the above-mentioned modular-system, mORC1000, are presented. The simulations were run under tropical climate design conditions, i.e. wellhead temperature of 161 °C and ambient temperature of 20°C (see Chapter 4.4).

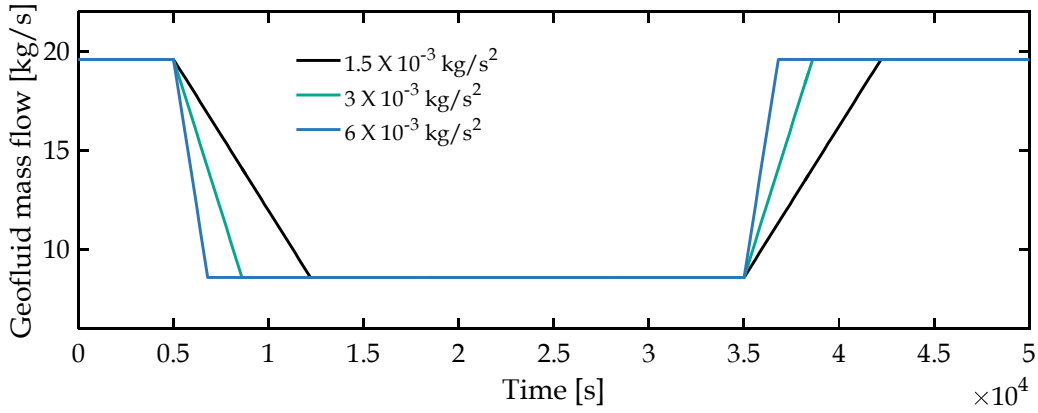


Figure 3. 24: Three ramp up/down scenarios to test the control strategies performance under dynamic load change.

Based on simulation results, it is interesting to find that the plant performance about  $m_{geo}$  is differ between ramp-up and ramp-down in load. This performance hysteresis is described and analyzed in the following section.

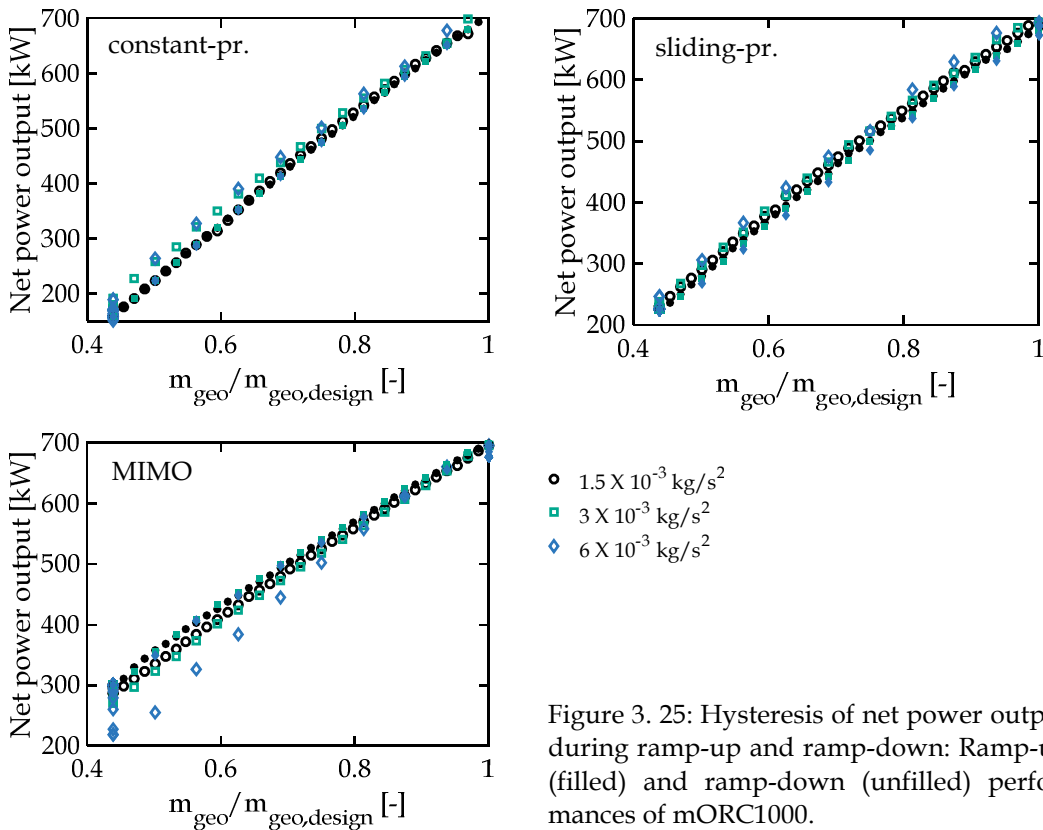


Figure 3. 25: Hysteresis of net power output during ramp-up and ramp-down: Ramp-up (filled) and ramp-down (unfilled) performances of mORC1000.

Figure 3. 25 shows net power output hysteresis of the system. The net power of the ORC is the power produced by the turbines subtracted by the parasitic work of the system. The parasitic work of the system which includes the work of the (feed and downhole) pumps and the fans of ACC. The peak net power output of the system is 700 kWel. This output is based on the assumption of well productivity index of 10 kg/s/bar with 1,500 m depth for the downhole pump calculation. It can be observed that MIMO has the best off-design performance followed by sliding pressure and constant pressure.

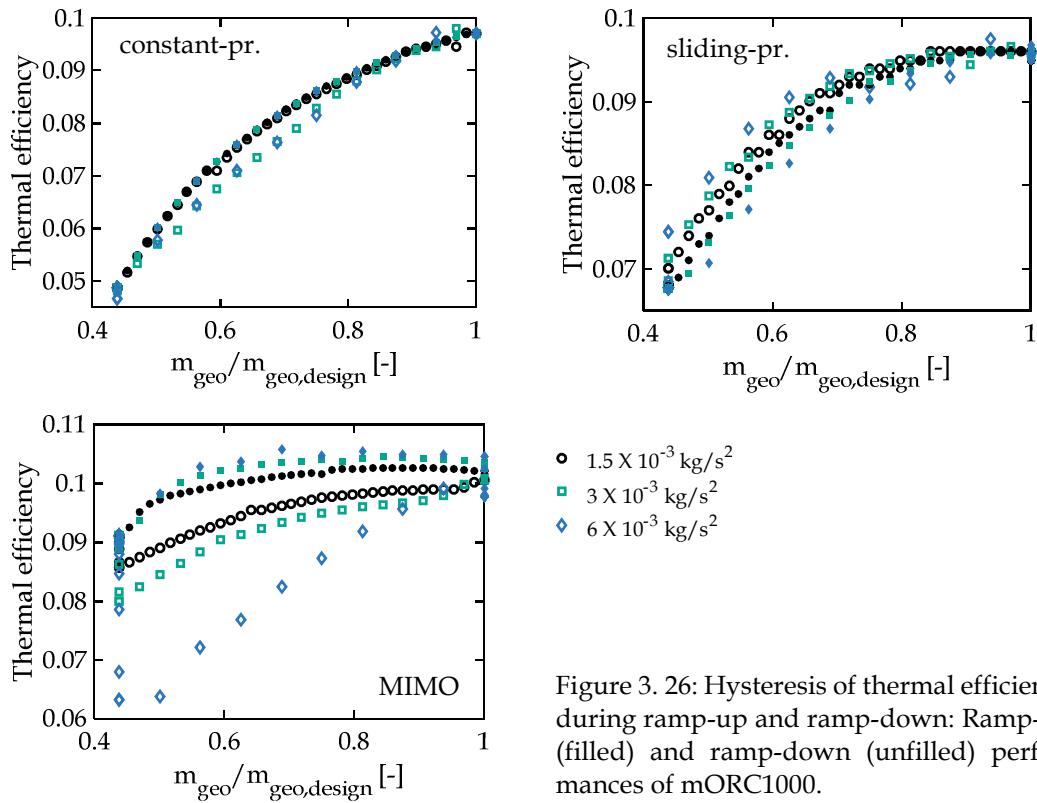


Figure 3. 26: Hysteresis of thermal efficiency during ramp-up and ramp-down: Ramp-up (filled) and ramp-down (unfilled) performances of mORC1000.

Hysteresis on thermal efficiency is also studied, and results are shown in Figure 3. 26. In general, MIMO shows benefit over the two traditional control strategies. Caution should be taken when utilizing MIMO control at ramp-down acceleration faster than  $3 \times 10^{-3} \text{ kg/s}^2$ . At this condition, the ORC with MIMO exhibits lower thermal efficiency at  $\dot{m}_{geo}/\dot{m}_{geo,design} < 0.8$ . Nonetheless, the performance is still better than constant pressure.

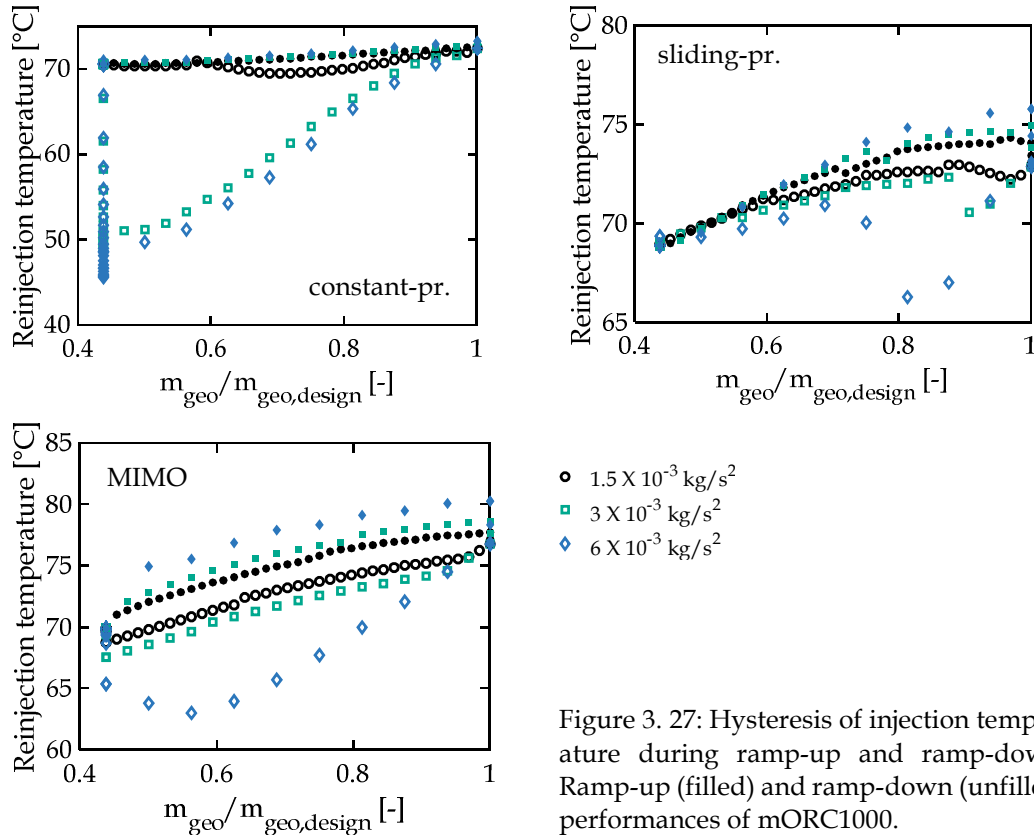


Figure 3. 27: Hysteresis of injection temperature during ramp-up and ramp-down: Ramp-up (filled) and ramp-down (unfilled) performances of mORC1000.

The injection temperature threshold was set at 70°C to avoid scaling at heat exchangers and injection wells [Manente *et al.*, 2013]. In correlation to thermal efficiency, the injection temperature also possesses strong hysteresis phenomena, see Figure 3. 27. Constant pressure control strategy shows very low injection temperature when operating at ramp-down acceleration faster than  $1.5 \times 10^{-3} \text{ kg/s}^2$ . The sliding pressure performs quite a stable injection temperature with significant drop from 0.7 to 1  $\dot{m}_{geo}/\dot{m}_{geo,design}$ . In general, the MIMO shows most stable and high injection temperature when operating at ramp up/down slower than  $6 \text{ kg/s}^2$ . It is to be noted though that it is not recommended to use the constant pressure for ramp-down acceleration higher than  $1.5 \text{ kg/s}^2$  since the injection temperature drop significantly due to mass accumulation on the hot-side.

The hysteresis analyses above have revealed that the MIMO shows an advantage over the other two traditional control strategies. Ramp-down typically increases the performance, especially if MIMO is applied. The opposite has been shown by ramp-down which deteriorates the performance of all three control strategies.

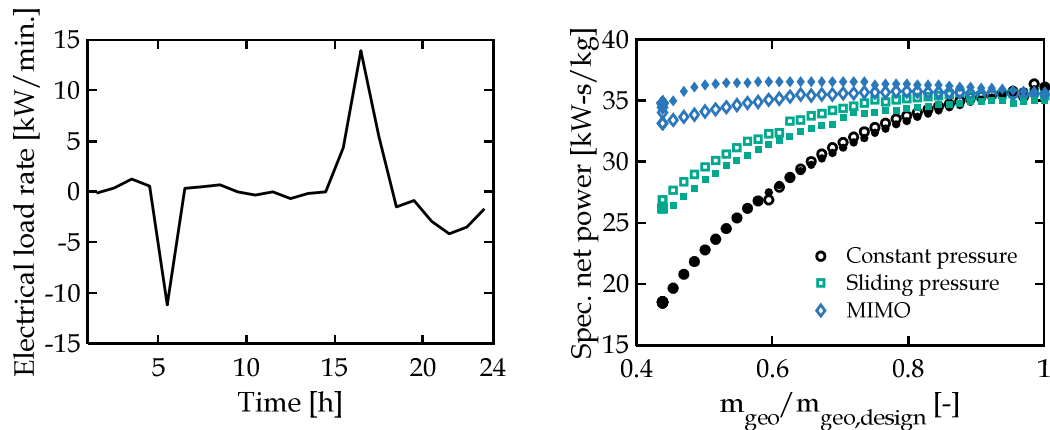


Figure 3. 28: (a) Typical electrical load rate for insular operation and (b) specific net power output at acceleration of  $1.5 \times 10^{-3} \text{ kg/s}^2$ .

To demonstrate the dynamic of load change, load speed diagram of Lembata Island, Indonesia, has been taken as reference (Figure 3. 30a). Maximum ramp-up rate is  $13.93 \text{ kW/min.}$  and maximum ramp-down is  $-11.15 \text{ kW/min.}$ , see Figure 3. 28a. Comparison of control strategies at  $1.5 \times 10^{-3} \text{ kg/s}^2$  or equivalent to  $\pm 14$  to  $\pm 17 \text{ kW/min}$  is depicted in Figure 3. 28b, in average, for four parallel mORC1000 units ( $4 \times 1,000 \text{ kWel}$ ). To equally quantify the performance, specific net power output is used here as a performance indicator. MIMO specific net power output is almost stable throughout the range of  $\dot{m}_{geo}/\dot{m}_{geo,design}$ , confirming reliability of the control strategy. In contrarily, the traditional ones exhibit a significant decrease on performance as  $\dot{m}_{geo}/\dot{m}_{geo,design}$  decreases, particularly when applying the constant pressure.

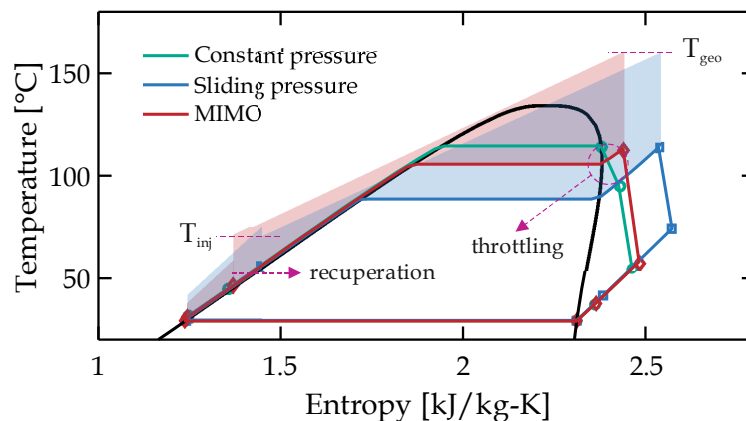


Figure 3. 29: T-s diagram of the three control strategies at  $0.5 \dot{m}_{geo}/\dot{m}_{geo,design}$  and ambient temperature of  $20 \text{ °C}$ : structural losses due to temperature difference in HXs and throttling in CV.

The above-described analyses show the benefit of multivariable (MIMO) control strategy over the traditional constant and sliding pressure control strategies. Finally, it is possible to illustrate the simulated processes in a  $T - s$  diagram of iso-butane (Figure 3. 29). The shown processes are representing the states at  $0.5 \dot{m}_{geo}/\dot{m}_{geo,design}$  and design ambient temperature of  $20^\circ\text{C}$ . This comparison shows that inefficiency occurs due to exergy losses in the control-valve (CV) and the evaporator. Throttling the flow in the control-valve before turbine inlet possess an exergy loss which deteriorate the performance when using the constant pressure. Likewise, temperature difference area (blue) of the sliding pressure is larger than of that MIMO (red) due to lower evaporation temperature and higher superheating. This behavior imposes the sliding pressure less efficient compared to MIMO. MIMO control strategy excludes those two sources of exergy losses in the operation.

#### *Application to insular operation*

To illustrate how it can be used in practice, the selected case study cover the typical insular application of Indonesia. The electrical load and ambient temperature applied to the mORC1000s ( $4 \times 1,000 \text{ kWel}$ ) is shown in Figure 3. 30a for the one simulated day. An ambient temperature fluctuation from  $17$  to  $23^\circ\text{C}$  (tropical climate) is shown. Specifically, Figure 3. 30b demonstrates a situation where each control strategy imposed different geothermal-fluid mass flow rate. These mORC1000 simulations are conducted to deliver a gross output of  $1,000 \text{ kWel}$  at design point conditions listed later in Chapter 4. The reduction of geofluid mass flow rate delivers more efficient cycle that maximizes well production capacity.

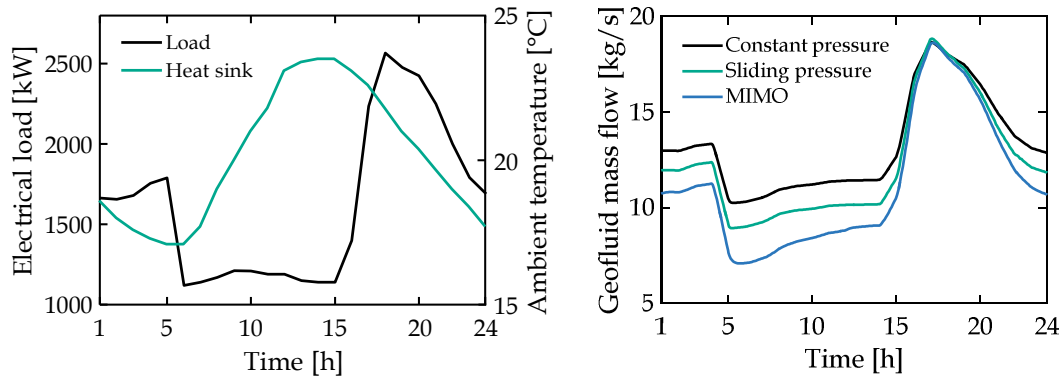


Figure 3. 30: 4 X mORC1000 simulations during one-day operation: typical electrical load and ambient temperature fluctuations in insular operation (a) and geothermal fluid mass flow rate imposed to fulfill the electrical load demand (b).

The dynamic phenomena in the mORC1000 during fluctuations in electrical load and ambient air temperatures used for cooling the system are presented for typical insular conditions in Indonesia. Simulations of 4 X mORC1000 operation on a typical insular load and ambient temperature of Indonesia are conducted with the heat input from the geothermal fluid capped at wellhead temperature of 161 °C. The mORC1000 produces a peak net power output of approximately 700 kW at 19:00 (peak load) as indicated by simulations for conditions on a typical insular operation in Indonesia, with an ambient temperature of 21 °C. This output is gradually decreased until 00:00 and remains relatively stable during the night (mid-load). Start from 06:00, the output is again ramped-down following the load (base-load). This production amount is steady until 17:00 when the plant is again ramped-up to peak-load.

During this one day operation, the isobutane mass flow rate of the MIMO is the lowest, followed by the sliding pressure and the constant pressure (Figure 3. 31a). Turbine inlet temperature (TIT) is lower for the constant pressure due to throttling, constant for the sliding pressure and higher for the MIMO (Figure 3. 31b). Likewise, the turbine inlet pressure (TIP) for the constant pressure and MIMO behave similarly, though the TIP of the sliding pressure is moving. Condensation temperature (or equivalently pressure) behavior is like the isobutane mass flow rate (Figure 3. 31d). Lower geothermal fluid and isobutane mass flow rate in MIMO is incurred due to the combined effect of higher evaporation pressure and the lower condensation pressure, which larger the pressure ratio in the turbine. The geothermal fluid mass flow rate imposed to the plant is at a minimum at 6:00 results from the particular combination of lowest ambient air temperature and lowest electrical load for the day. Geothermal fluid injection temperature out from the systems remains relatively stable at about the threshold value of 70°C for most of the day. The MIMO attains a maximum injection temperature of > 75 °C between 17:00 and 20:00 causing highest thermal efficiency at peak load operation (Figure 3. 31e).

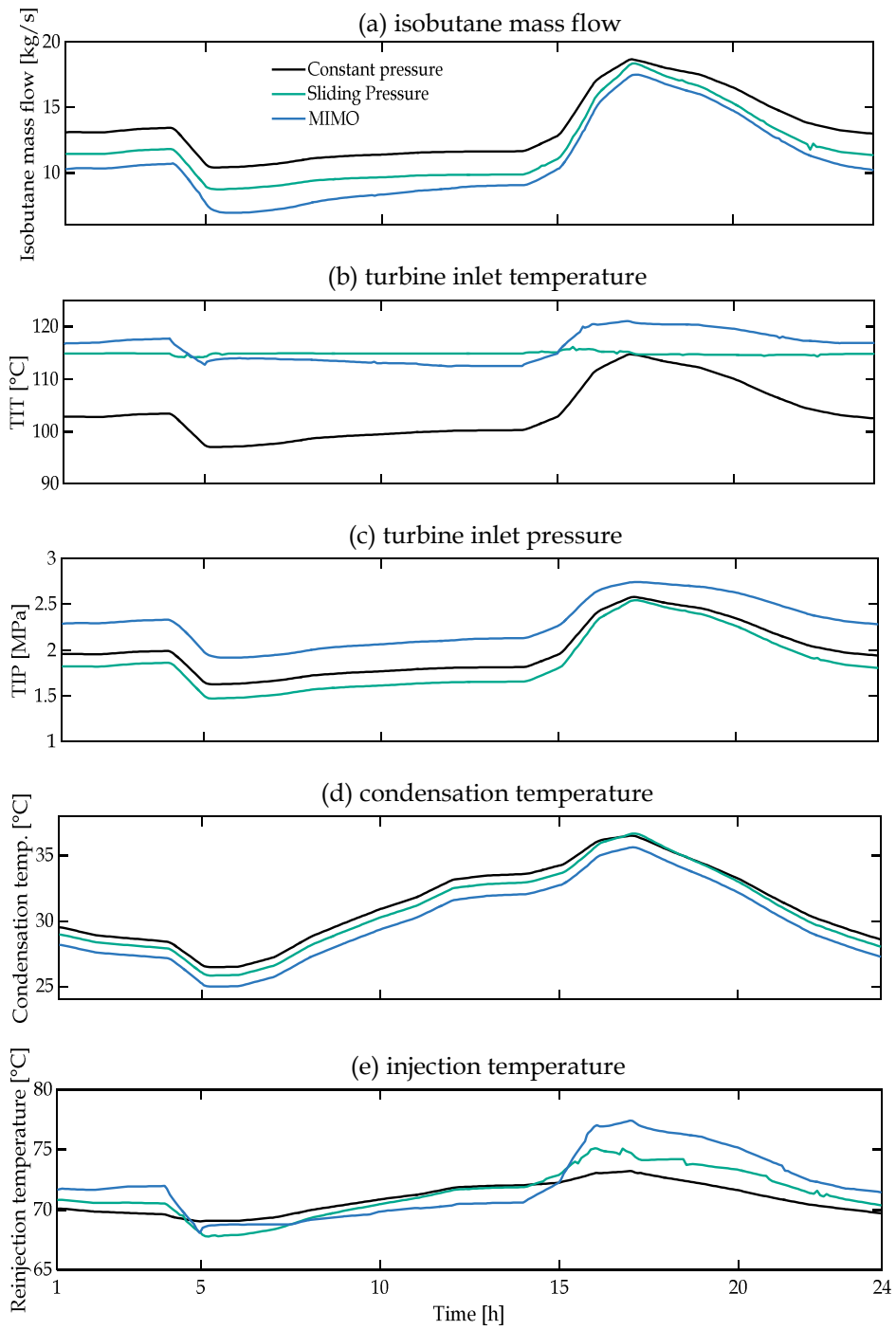


Figure 3. 31: Simulation results by changing electrical load and ambient temperature.

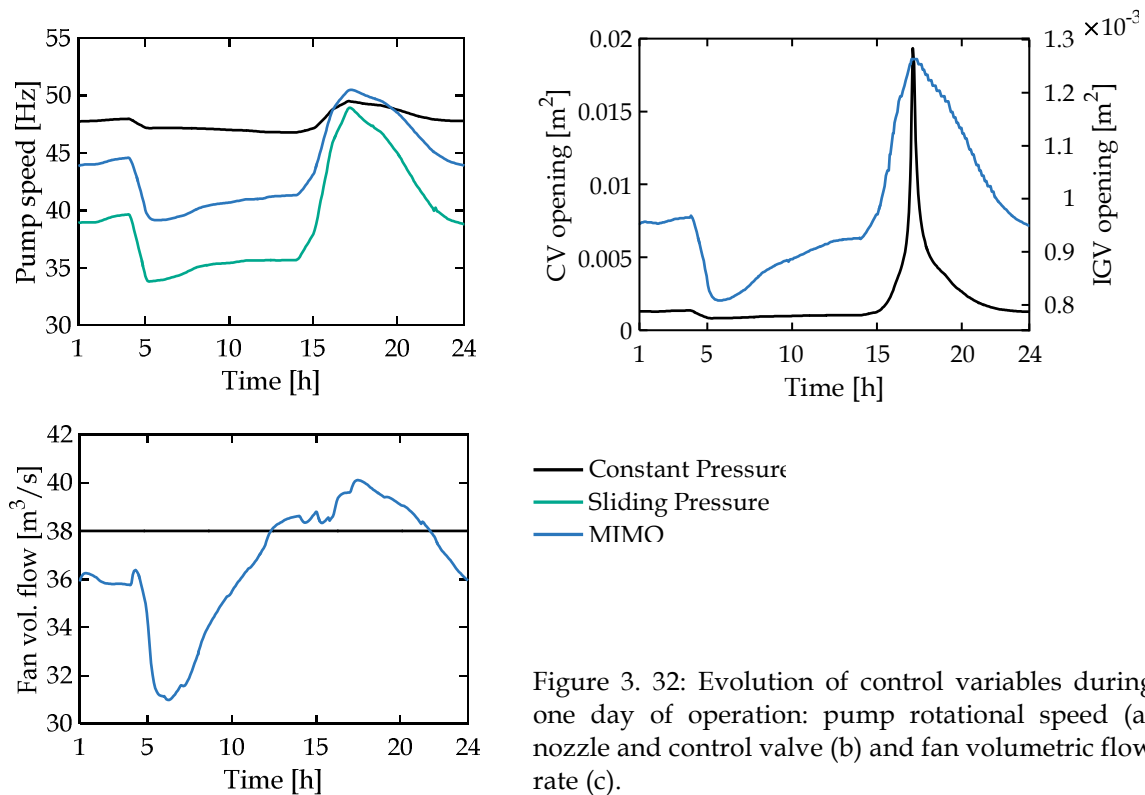


Figure 3. 32: Evolution of control variables during one day of operation: pump rotational speed (a) nozzle and control valve (b) and fan volumetric flow rate (c).

In MIMO application, changes in mass flow rate decrease the turbine inlet density due to higher turbine inlet temperature (Figure 3. 32a). Since pump speed governs the mass-flow rate in the mORC1000, the nozzle has to adapt by widening the flow area (Figure 3. 32b). The impact of the lower isobutane mass flow rate entering the condensers contributes to decreases in turbine outlet pressure, though the cooling air mass flow rate also decreases (Figure 3. 32c). The advantage is twofold: increase of turbine pressure ratio while reducing fan parasitic power.

The dynamic simulation of mORC1000 has been presented using zero and one-dimensional equations in component modeling. Selection of the steady-state set-point of three control strategies and the impact of changes in geothermal fluid mass flow rate on the cycle performance have been discussed. Dynamic characteristics of the mORC1000's have been analyzed using tropical climates ambient air temperature data. The fast ramp-down in load has been shown to result in isobutane mass moving from the cold-side of the ORC and accumulating on the hot-side, which ultimately results in decreases in turbine inlet pressure and net power output. The opposite has been shown to occur during fast ramp-up in electrical load.

# 4

## THERMAL-ECONOMIC MODULARIZATION OF SMALL, ORGANIC RANKINE CYCLE POWER PLANT FOR MID-ENTHALPY GEOTHERMAL FIELDS

published as

Nusiaputra, Y. Y., Wiemer, H-J., Kuhn, D., *Thermal-Economic Modularization of Small, Organic Rankine Cycle Power Plants for Mid-Enthalpy Geothermal Fields* in *Energies* 2014, 7, 4221-4240

### ABSTRACT

The costs of the surface infrastructure in mid-enthalpy geothermal power systems, especially in remote areas, could be reduced by using small, modular Organic Rankine Cycle (ORC) power plants. Thermal-economic criteria have been devised to standardize ORC plant dimensions for such applications. We designed a modular ORC to utilize various wellhead temperatures (120–170 °C), mass flow rates and ambient temperatures (–10–40 °C). A control strategy was developed using steady-state optimization, in order to maximize net power production at off-design conditions. Optimum component sizes were determined using specific investment cost (SIC) minimization and mean cashflow (MCF) maximization for three different climate scenarios. Minimizing SIC did not yield significant benefits, but MCF proved to be a much better optimization function.

### 4.1 INTRODUCTION

Rural areas worldwide, particularly in developing countries, often lie outside the reach of grid power supplies. In these regions, electricity tends to be supplied via diesel engines which require expensive fuel and are sources of atmospheric pollution. Some rural areas have mid-enthalpy geothermal resources under various geological conditions, whether these are shallow/deep, magmatic/amagmatic or identified/hidden. These kinds of resources comprise 70% of the world's total geothermal resources that are suitable for electricity generation [Stefansson, 2005]. A geothermally driven, decentralized power plant may, therefore, offer a viable and ecologically sound option for producing electricity in suitable rural and remote regions, such as the Chena Hot Springs in Alaska [Aneke *et al.*, 2011]. Nonetheless, certain requirements must be met. The plant must be capable of meeting

small, modulating electricity loads with continuous annual growth and as such it has to be flexible in terms of incremental capacity expansion and frequency control, and have a short construction period to advance energy production, and cash flow starts [Bäumer *et al.*, 1990]. It should be able to function efficiently at various different resource and ambient temperatures, and adapt to wellhead temperature changes during power production.

The subject presented in this paper is the development of a modular standardized power plant. Modularity and standardization are expected to lead to cost savings, due to reductions in plant engineering, assembly and installation time and maintenance. These are also expected to improve quality and reliability of the cycles. For example, Volkswagen has managed to save \$1.7 billion annually through effective product architecture and component commonality [Dahmus, 2001].

In this study, the subcritical Organic Rankine Cycle (ORC) system is used as a technology to convert mid-enthalpy geothermal energy into electricity. It is a well-proven technology that has been in commercial use since the beginning of the 1980s [Quoilin *et al.*, 2013]. Cycle simplicity and component availability are the main advantages with this technology, particularly in remote area applications. Supercritical ORCs were developed recently in order to achieve higher cycle efficiencies; however, they are not yet sufficiently reliable for widespread use in remote areas. The theoretical advantages of mixture working fluid ORCs have been demonstrated. Nonetheless, pure working fluid ORC power plants remain the most economical and proven technology [Quoilin *et al.*, 2013], though they still offer potential for technical improvement.

An example of potential improvements could include advances in component technology, such as turbines with variable nozzle-vanes [Valdimarsson, 2014], speed pumps and fans; these would allow the cycle to adapt to a wide range of operating conditions. A control strategy to operate a geothermal ORC system at various wellhead and ambient temperatures has been proposed in [Manente *et al.*, 2013]. However, the size of the ORC components was not optimized regarding the operation in a wide range of operating conditions.

Another study dealt with power plant sizing, taking into consideration wellhead temperature decline during operation, but the control was not optimized [Gabrielli, 2012]. The system is thereby a supercritical ORC with variable speed pump, constant turbine-nozzle and constant fan-speed. The authors of [Quoilin *et al.*, 2013] concluded that plant design should be based on the lowest temperature of the geothermal wellhead.

In this study, we propose a thermal-economic modularization technique for a subcritical geothermal ORC, which operate under variable wellhead and ambient temperatures, considering both sizing and control aspects. Off-design steady-state optimization was developed using Covariance Matrix Algorithm-Evolutionary Strategy (CMA-ES) to achieve the maximum net power output. Modularization was tested in three different climate types temperate, tropical, and dry, using two main functions: specific investment-cost (SIC) minimization and mean cash-flow (MCF) maximization.

## 4.2 SYSTEM DESCRIPTION AND METHODOLOGY

Figure 4. 1 shows the layout of the power system under investigation. The aim of this paper is to propose a methodology for sizing a standardized, modular geothermal ORC power-plant. Consequently, Figure 4. 1 does not describe the system in detail, but rather offers a generic layout. The system consists of six main components, namely evaporator, recuperator, condenser, fan, pump, and turbine. The recuperator helps maintain a high injection temperature; it increases thermal efficiency, and reduces the thermal condenser load. The heat exchangers are represented by a counter-flow shell/tube configuration, with working fluid flowing in the shell of the evaporators and in the tube of the air-cooled condensers. The pump is centrifugal with a variable speed drive. The turbine is equipped with nozzle-vanes, which are also controlled with an electric drive. Isobutane was used as a working fluid in the system. Working fluid selection is an essential and initial step of the ORC design process, but it is not the main concern of this work.

Isobutane was chosen because it has the highest energetic efficiency in medium well-head temperature range [Augustine, 2009], low global warming potential, low ozone depleting potential, and good market availability.

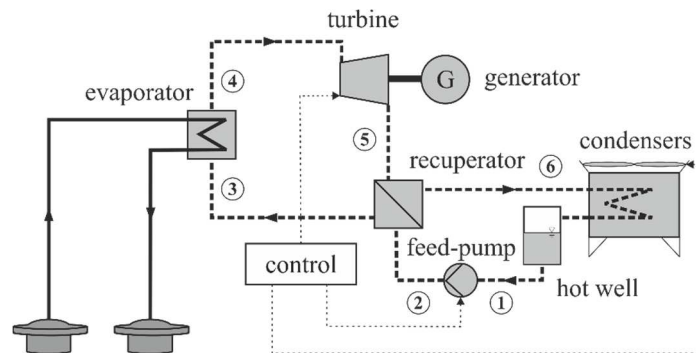


Figure 4. 1: Diagram of a recuperative small, modular geothermal Organic Rankine Cycle (ORC) with adaptive control.

The ORC system considered in this paper is subcritical vapor-cycle, in which heat from a geothermal geofluid is used to heat and evaporate Isobutane. The working fluid vapor then drives the turbine for power generation, and then gets condensed in the air-cooled condenser. The liquid Isobutane is collected in a hot-well and then pumped back to the evaporator to repeat the cycle.

The modular power-plant is designed to work at geothermal wellhead temperatures of 120–170 °C, which is considered a suitable temperature range for Isobutane and also represents typical mid-enthalpy geothermal fields. Currently, more than 150 geothermal binary units with an average capacity between 1 MW and 3 MW are installed world-wide [DiPippo, 2008]. The design capacity of the modular plant is defined as 1,000 kW<sub>e</sub>. The thermodynamic cycles of the system are shown in Figure 4. 2.

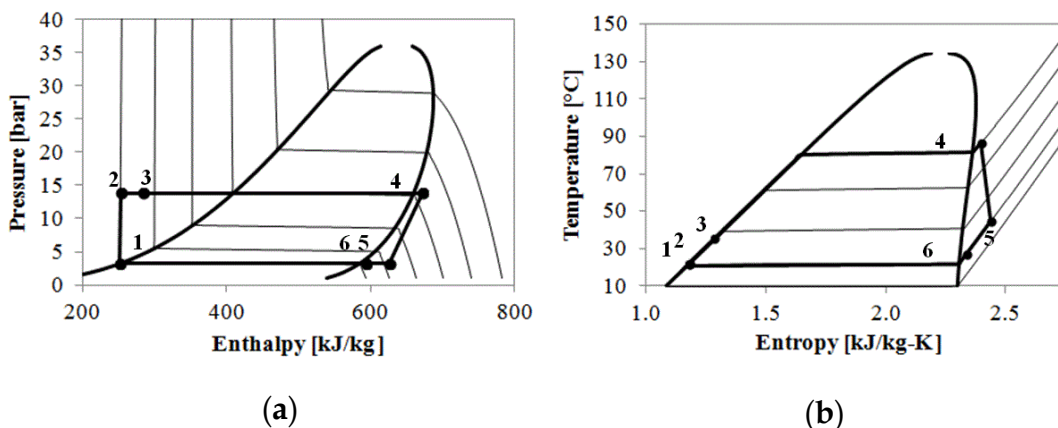


Figure 4. 2: (a)  $p - h$  diagram and (b)  $T - s$  diagram of the system for isobutane.

In order to maximize the amount of energy recovered from the geothermal heat and simultaneously consider the installation cost, component size must be optimized. Operation parameters of the ORC should consider the daily and annual course of ambient temperatures, and should be regularly adjusted in the event of changes in wellhead temperature and geofluid flow rate.

Consequently, a good design will include the following steps:

- ▶ 1. Thermodynamic optimization for a given design-point: normal (design) wellhead and ambient temperature. The components will then be sized using optimum thermodynamic parameters
2. Mapping the power plant net-power at operation points from the design conditions. This results from an optimal control strategy that maximizes the net power output.
3. Simulation of annual electricity production. Performance is then evaluated using constant exergy input for each off-design condition. The variation of the ambient temperature was examined for three different climate types.
4. Steps 1–3 are repeated for each design-point, and finally the optimal design-point is selected using thermo-economic criteria. Cost correlations of each component are implemented to evaluate the component sizes.

Each step is described in Section 4.4. The component modeling, which is the basis for all subsequent evaluation steps, will be addressed in the following section.

## 4.3 COMPONENT MODELING

### 4.3.1 Heat exchangers

The models were implemented in Matlab (The MathWorks, Natick, MA, USA) and the fluid properties computed using Refprop 9.0 (NIST, Gaithersburg, MD, USA). The heat exchangers models were used in two modes: sizing and simulation. These are represented as counter-flow heat exchanger, as shown in Figure 4.3. In order to consider the property variations of the working fluid and the secondary fluid (geofluid), the entire length of the heat exchangers was divided into three zones with variable lengths of each zone: liquid zone (Liq), two-phase zone (TP), and vapor zone (Vap), with respect to the working fluid.

The heat exchangers were modeled using two energy balance equations. One is the the geofluid heat flow rate. The example following is used for the overall evaporator:

$$\dot{m}_{wf}(h_3 - h_4) = \dot{m}_g c_{p,g}(h_{g,in} - h_{g,out}) . \quad (4.1)$$

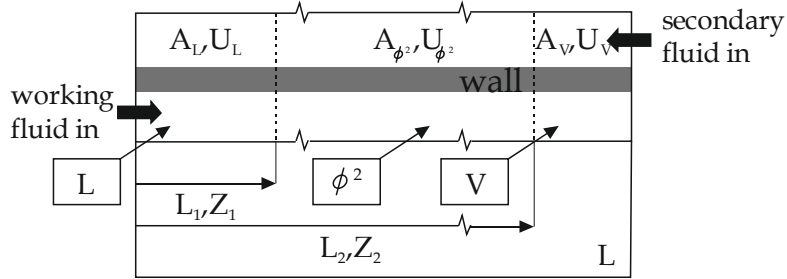


Figure 4. 3: Three-zone heat exchanger model (evaporator).

The other equation is the heat transfer equation, which uses the weighted temperature difference and an overall heat transfer coefficient. The example following is also shown for the evaporator:

$$\dot{m}_{wf}(h_3 - h_4) = U_{WTD} A_{tot} \Delta T_{WTD} . \quad (4.2)$$

The weighted temperature difference,  $\Delta T_{WTD}$  is calculated based on heat transfer coefficients and areas of each zone of the exchanger. It is represented by the following equation:

$$\Delta T_{WTD} = \frac{\dot{Q}}{U_L A_L + U_{\phi^2} A_{\phi^2} + U_V A_V} . \quad (4.3)$$

Being the partial heat transfer coefficient, for example at the liquid zone, given by:

$$U_L = \left[ \left( \frac{1}{\alpha_{i,L}} + R_{fouling} \right) \frac{AR \cdot d_o}{d_i} + \frac{\ln(d_o/d_i)}{2\pi L \cdot \lambda_w} + \frac{1}{\alpha_{o,L}} \right]^{-1} , \quad (4.4)$$

where AR is the area ratio of outer to inner heat transfer area, which is unity for shell/tube heat exchangers. R fouling is the thermal resistance associated with fouling in the heat exchanger tubes ( $R_{fouling} = 1.3 \times 10^{-4} \text{ m}^2\text{-K/W}$ , experiment data for geothermal brine [Hernandez-Galan and Alberto Plauchu, 1989]). For the evaporator, the heat transfer area dedicated to liquid zone,  $A_L$  is computed as the similar equation form is applied for the two-phase and vapor zone. The inner

tube was assumed to be a standard stainless-steel with the geometry described in Table 4. 1. Simplified layouts of the heat exchangers are illustrated in Figure 4. 4.

$$A_L = \dot{m}_{wf} \frac{h_{l,sat} - h_3}{U_l \frac{(T_{g,L} - T_{wf,sat}) - (T_{g,out} - T_3)}{\ln((T_{g,L} - T_{wf,sat}) / (T_{g,out} - T_3))}} = A_{tot} - (A_{\phi^2} - A_V) . \quad (4.5)$$

| component          | $d_o$<br>[mm] | $t$<br>[mm] | $P_T$<br>[mm] | $N_{tube}$<br>[-] | $N_{pass}$<br>[-] | $L$<br>[m] | $W$<br>[m] | $h$<br>[mm] |
|--------------------|---------------|-------------|---------------|-------------------|-------------------|------------|------------|-------------|
| evaporator         | 15.875        | 1.651       | 20.64         | variable          | 1                 | variable   | -          | -           |
| recuperator        | 31.75         | 2.11        | 39.69         | variable          | 1                 | variable   | -          | -           |
| condenser (1 cell) | 25.4          | 3.3         | 63.5          | 192               | 3                 | 9.14       | 3.05       | 15.9        |

Table 4. 1: Geometrical dimensions of heat exchangers.

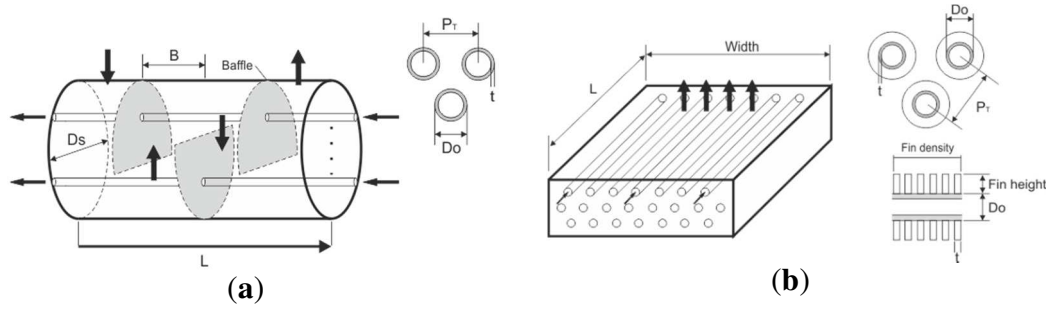


Figure 4. 4: (a) Layout of shell/tube exchanger (evaporator and recuperator); (b) Layout of fin/tube exchanger cell (air-cooled condenser).

The geometrical dimensions are listed in Table 4. 1. The cooling-system consisted of parallel air-cooled condenser cells that were modeled as a three-zone fin/tube heat exchanger. The fin density was assumed with 393 fins per meter, the fin height was 15.9 mm, and each cell contained 3 induced-draft fans. The dimensions of the heat exchanger model are summarized in Table 4. 1. The variables for the condenser were the cell numbers and fan capacity.

#### *Evaporator and recuperator heat transfer coefficients and pressure drops*

Forced convection heat transfer coefficients for single-phase fluid (liquid/vapor) are evaluated by means of the generic correlation:

$$\alpha_{L,V} = c \cdot \text{Re}^m \cdot \text{Pr}^n \cdot (\lambda/d_h) , \quad (4.6)$$

where the influence of temperature-dependent viscosity-effects was neglected. The constant,  $c$ , and exponents  $m$  and  $n$  were identified according to the Sieder-Tate correlation [Serth, 2007].

The overall boiling heat transfer coefficient was estimated by the Mostinski, and Palen correlations for enhanced heat transfer, due to convection around the bundles, and established for boiling in horizontal tubes without dependency on surface roughness. This heat exchange coefficient is considered to be constant during the whole evaporation process and is calculated by:

$$\alpha_{ev} = 1.167 \times 10^{-8} \cdot p_{crit}^{2.3} \Delta T_{sat}^{2.333} F_p^{3.333} \times F_{bundle} + 250 \left[ \frac{W}{m^2 K} \right] . \quad (4.7)$$

Parameters  $F_p$  (-) and  $F_{bundle}$  (-) were calculated using equations found in the literature [Serth, 2007], with  $p$  and  $T$  in kPa and K, respectively. The pressure drops are calculated using the Prandtl-Karman equation as follows

$$\Delta p = f \frac{G^2 L}{2 \rho d_h} \times \phi^2 , \quad (4.8)$$

where  $f$  is dependent on flow velocity and tube/shell roughness. For flow inside the tube,  $f$  is calculated using the explicit Swamee-Jain correlation [Serth, 2007]. The two-phase multiplier  $\phi^2$  is approximated with the Grant correlation, for two-phase flow crossing tube-bundles [Doo, 2005].

#### *Air condenser*

The single phase working-fluid heat transfer coefficient was calculated in the same manner as in eq. (4.6). The condensation heat transfer coefficient is estimated using the Dobson-Chato correlation [Dobson, M.K. Chato, J.C., 1998], developed for the case of smooth of horizontal tubes.

$$\alpha = 0.023 \text{Re}_L^{0.8} \text{Pr}_L^{0.4} \left[ 1 + \frac{2.22}{X_{tt}^{2.22}} \right] \times (\lambda_L/d_h) . \quad (4.9)$$

The partial heat transfer coefficient was computed using eq. (4.4) with AR = 21.4, the Gas Processors and Suppliers Association (GPSA) standard. The fouling thermal resistance was assumed with  $R_{fouling} = 1.7 \times 10^{-4}$  (GPSA assumption). Heat

transfer and pressure drop on the air-side are also approximated based on a GPSA correlation [Gas Processors Suppliers Association, 2004]

$$\alpha_a = 0.019G_a^{0.54} \text{ [W/m}^2\text{K]} \quad (4.10)$$

$$\Delta p_a = \frac{1.175 \cdot 10^{-10}}{(\rho_{a,av}/\rho_{21^\circ\text{C}})} + \left( \frac{\dot{V}_{a,out}}{10d_F^2} \right)^2 (\rho_{a,out}/\rho_{21^\circ\text{C}}) ,$$

with  $G_a$  and  $\dot{V}_a$  are in  $\text{kg/m}^2\text{-s}$  and  $\text{m}^3/\text{s}$ , respectively. For the calculation of the consumed fan power, a fan efficiency of 70%, and an electrical motor efficiency of 92% were assumed.

#### 4.3.2 Feed pump

The feed-pump and its characteristics are approximated by using the affinity law and the second-order pump characteristics, which can be expressed in the following equations:

$$\Delta p = \Delta p_{\dot{V}=0} \left[ \left( \frac{n}{n_{DP}} \right)^2 - \left( \frac{\dot{V}}{\dot{V}_{\Delta p=0}} \right)^2 \right] . \quad (4.11)$$

The efficiency is calculated from the volumetric flow and rotational speed at the design-point and operating-point, assuming  $\eta_0 = 0.8$ :

$$\eta_P = \eta_{P,DP} \left\{ 1 - \exp \left( - \frac{1 - \left( \left| \frac{\dot{V} \cdot n_{DP}}{\dot{V}_{P,DP} \cdot n} - 1 \right| \right)^a}{c \left( \left| \frac{\dot{V} \cdot n_{DP}}{\dot{V}_{P,DP} \cdot n} - 1 \right| \right)^b} \right) \right\} , \quad (4.12)$$

where constants  $a$ ,  $b$ , and  $c$  are defined as 1.8, 0.58, and 0.68, respectively [Shekun, 2007].

#### 4.3.3 Turbine

A radial turbine was used because it has a better efficiency for small ORC applications compared to axial turbines due to the smaller tip-clearance [17]. In order to calculate the mass flow rate in the ORC during operation, the empirical Stodola steam cone rule is applied in the form of

$$\dot{m} = \mu_T \cdot c_T \sqrt{p_i \cdot \rho_{in}} \sqrt{1 - 1/\pi} , \quad (4.13)$$

where  $\pi = p_{in}/p_{out}$  is the pressure ratio and  $\mu_T$  is the turbine nozzle position. The turbine constant  $c_T$  can be thought of as an equivalent area and has the unit square meters. In off-design operation, the equivalent area was adapted by varying  $\mu_T$  using variable inlet nozzle guide-vane. The guide vanes are moved in such a way that the flow area between the vanes changes. Thus, the inlet flow area is changed. In high-pressure ratio operation, where the turbine is choking, the pressure ratio factor  $\sqrt{1 - 1/\pi}$  is near unity and, therefore, can be neglected. These equations have been widely used to describe the relation between flow and pressure. Efficiency of the turbine under off-design condition is calculated as

$$\eta_T = \eta_{T,DP} \cdot F_{u/c_0} \cdot F_{\dot{V}_5} \quad (4.14)$$

The designed turbine efficiency was 0.75. The first correction factor was related to the variation of  $u/c_0$ , ratio of radial velocity to spouting velocity. Spouting velocity, is  $c_0 = \sqrt{2\Delta h_{is}}$ , is defined as that velocity has an associated kinetic energy equal to isentropic enthalpy drop. At the best efficiency point the value of  $u/c_0$  is found at 0.7 [Dixon, 2002]. The second correction factor was associated with the variation of the volumetric flow rate from the design value. The two correction factors were then observed in Figure 4. 5b, which is typical for radial turbine characteristics. The design point was pointed at a velocity ratio of 0.7 and volumetric flow rate of 100%.

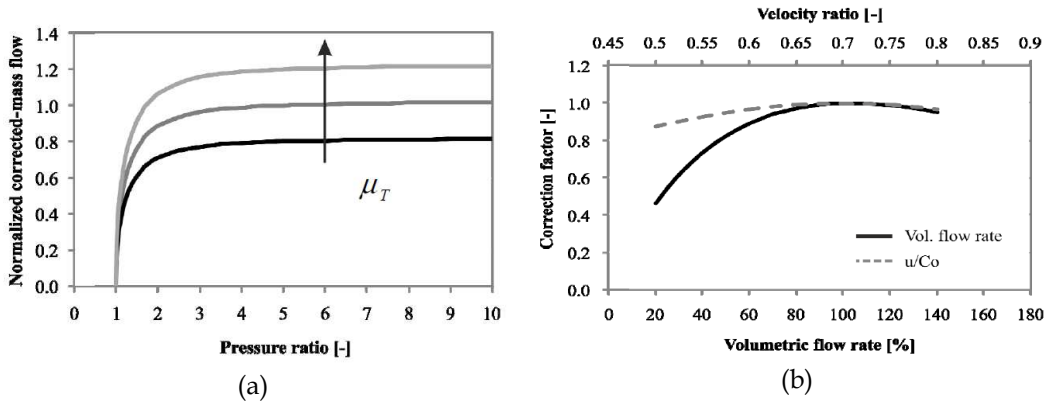


Figure 4. 5: (a) Stodola's cone rule as a function of nozzle position; (b) Typical turbine efficiency characteristics [Ghasemi *et al.*, 2013].

#### 4.4 RESULTS

Small, modular, subcritical ORCs should deliver good performance under a wide range of operating conditions. Consequently, the optimal component size of the plant needs to be determined. The optimum design-point was found using numerical simulation for operating conditions as follows:

$$\begin{aligned} 120 &\leq T_{g,in} (^{\circ}C) \leq 170 \\ -10 &\leq T_{a,in} (^{\circ}C) \leq 40 \\ 70 &\leq T_{g,out} (^{\circ}C) \end{aligned} \quad (4.15)$$

Considering the main component characteristics described in the previous section, there were 11 design variables to be optimized:

1.  $d_{shell,ev}, d_{shell,re}, L_{ev}, L_{re}$ : diameter and length of the shell-and-tube heat exchangers (i.e., evaporator and recuperator).
2.  $N_{cell}, PF$ : cell numbers and fan capacity for air-cooled condensers. These parameters are a function of the condenser load and the air-outlet temperatures.
3.  $c_T, \Delta h_{is0}, \dot{V}_{5,design}$ : inlet area constant, isentropic enthalpy drop, and outlet-volumetric flow rate at the design-point. The two latter parameters were used to define the pitch diameter.
4.  $\Delta p_{\dot{V}=0}, \dot{V}_{p=0}$ : the shut-off pressure head when the flow is zero which is typically 1.25 times of the design-head, design volumetric flow rate.

The objective of the modularization was to find the optimal configuration of these design variables. Conventional power-plants, such as gas turbines and diesel engines are designed to deliver a specific power output at specific heat source and heat sink temperatures, such as flame and ambient temperatures. Inspired by this approach, two-dimensional optimization was introduced; these are normal (design) wellhead temperature ( $T_{g,DP}$ ) and ambient temperature ( $T_{a,DP}$ ). The 11 design variables then were a product of the sizing for the design-point ( $T_{g,DP} - T_{a,DP}$ ).

#### 4.4.1 Component sizing for normal-design: thermodynamic optimization

In order to size the components, the thermodynamic cycle must be determined first. Thus, a thermodynamic optimization was carried out to maximize the net power output. The normal (design) condensation temperature is defined as

$$T_{1,design} = T_{a,DP} + ITD \quad (4.16)$$

In low temperature power-plants, lowering condensation temperature benefits power output [Frick *et al.*, 2012]. An initial temperature difference (ITD) of 14 K was selected as the lower bounding value for practical application [EPRI, 2005].

Isobutane can be categorized as a dry fluid (i.e., negative slope of saturated vapor line); hence, at design condition, saturated vapor is the best turbine inlet parameter [He *et al.*, 2012]. The optimal evaporation temperature (OET) as normal (design) evaporation temperature is obtained by solving:

$$\frac{\partial}{\partial T_{4,design}} \left\{ \begin{array}{l} \frac{T_{g0} - T_{4,design} - \Delta T_{pp,ev}}{T_{4,design}} (T_{4,design} - T_{1,design}) \\ \left[ 1 + \frac{c_{p,wf} T_{4,design}}{2\gamma} \ln \left( \frac{T_{4,design}}{T_{1,design}} \right) \right] \end{array} \right\} = 0 \quad (4.17)$$

The analytical OET results had an accuracy of 2.3%, compared to the numerical OET [He *et al.*, 2012]. The design pinch-point was 5 K for both the evaporator and recuperator. The normal wellhead temperature varied from 120 °C to 170 °C, and the normal ambient temperature varied from -10–40 °C, with a step of 10 °C, and 12 random points (6 × 6 grid + 12). The sizing results for each normal (design) wellhead temperature are listed in Table 4. 2. The net efficiency is defined as ratio of net power (gross power deducted by feed-pump and fan power) to the heat input.

| $T_{g0}$                                       | 120       | 130       | 140       | 150       | 160       | 170       |
|--|-----------|-----------|-----------|-----------|-----------|-----------|
| Evaporation temperature (sat.) (°C)            | 80–87     | 85–93     | 91–101    | 99–111    | 111–122   | 115–121 * |
| Condensation temperature (°C)                  | 4–54      | 4–54      | 4–54      | 4–54      | 4–54      | 4–54      |
| Geofluid mass flow rate (kg s <sup>-1</sup> )  | 31.3–95.7 | 24.8–68.8 | 20.2–51.1 | 16.7–38.7 | 12.9–28.1 | 10.3–21.8 |
| Isobutane mass flow rate (kg s <sup>-1</sup> ) | 15.6–50.2 | 14.8–43   | 13.9–37.4 | 13–32.8   | 12.5–27.1 | 12.8–27.1 |
| Gross power (kW)                               | 1,000     | 1,000     | 1,000     | 1,000     | 1,000     | 1,000     |
| Net efficiency (%)                             | 5.1–13.9  | 5.9–14.5  | 6.7–15.2  | 7.6–16    | 8.8–18.1  | 8.8–20.6  |

Table 4. 2: Thermodynamic design of ORC cycles, showing range of optimal sizing results.

After determining the optimum thermodynamic cycle conditions, the components were sized. The size of the rotating components (*i.e.*, feed-pump, turbine) was derived using the thermodynamic parameters. The heat exchangers were sized as follows.

1. Evaporator: Evaporation was realized using two parallel evaporators, with one shell/one tube pass configuration. During very low load (<50%) operation, one of the evaporators was fully closed. Both evaporators were sized by determining the shell diameter, and the number of tubes was calculated using “tube counts” based on standardized design parameters described in Table 4. 1. The baffle-spacing was constrained below the shell diameter and maximum-spacing in order to avoid instability caused by vibration. After calculating overall heat transfer coefficients and the total heat transfer area, tube length was computed. By setting the allowable pressure drop on the shell side, the optimum design (or equivalently, shell diameter) with smallest area was selected. This design procedure was also applied to the recuperator.
2. Condenser: An important preliminary step in the condenser design process is outlet air temperature. This parameter has a major effect on exchanger economics [Serth, 2007]. Increasing the outlet air temperature reduces the amount of air required, which reduces the fan power and, therefore, operating cost. However, it also reduces the air-side heat-transfer coefficient and the mean temperature difference in the exchanger, which increases the size of the unit and, therefore, the capital cost. Consequently, optimization with respect to outlet air temperature (or equivalently, air flow rate) was considered an important aspect of air-cooled condenser design.

The optimum condenser air-outlet temperature (or equivalently, pinch-point) was calculated by minimizing the annual cost function. First derivative of this function with respect to air-outlet temperature determines the minimum annual cost. It can be written as follows

$$\frac{\partial}{\partial T_{a0,out}} [CRF(C_{cd} + C_F) + (0.01C_{cd} + 0.03C_F) + CF \cdot P_F \cdot C_{el}] = 0 \quad (4.18)$$

Air-cooled heat exchanger investment cost  $C_{cd}$  and fan investment cost  $C_F$  are described in Table 4. 3. The annualization factor,  $CRF$  (Capital Recovery Factor) is defined as:

$$CRF = \frac{r(1+r)^y}{(1+r)^y - 1} \quad (4.19)$$

Heat transfer coefficient and pressure drop were computed from the ratio of design mass flow rate to the reference, which was mass flow rate at air velocity of 3.5 m/s, as recommended in the literature [Serth, 2007]. The maintenance cost was assumed to be 1% of the fin/tube heat exchangers cost and 3% of fan-motor cost [Taal *et al.*, 2003].  $CF$  (capacity Factor) of 0.7,  $y$  of 30 years,  $r$  of 12%, and electricity price  $C_{el}$  of 0.15 \$·kWh<sup>-1</sup> were assumed. Increasing the outlet air temperature increases heat transfer area required and conversely, reduces fan power consumption, as shown in Figure 4. 6a. This trade-off resulted in an optimum annual cost of 130-20 ( $T_{g0} - T_{a0}$ ) at air-outlet temperature of 30.4 °C, approximately 10 K above the inlet air temperature (Figure 4. 6b). Once the optimum air-outlet temperature was established, the heat transfer area (or equivalently, number of cells) and fan capacity were determined.

| component   | cost correlation  | reference                      |
|-------------|---|--------------------------------|
| evaporator  | $13,668 + 658 \cdot A^{0.85}$ (carbon-shell/stainless-steel)                                | [Taal <i>et al.</i> , 2003]    |
| recuperator | $11,256 + 579 \cdot A^8$ (carbon-shell/carbon-tube)   | [Taal <i>et al.</i> , 2003]    |
| condenser   | $5.6A$  | [Kashani <i>et al.</i> , 2013] |
| fans        | $(1887.5 + 159.95d_F^2 + 3.53d_F + 281.25P_F) \cdot N_F$                                    | [Kashani <i>et al.</i> , 2013] |
| feed-pump   | $4,900(P_P/30)^{0.7}$   | [Quoilin <i>et al.</i> , 2011] |
| turbine     | $(91,200d_{pitch}^{2.1} + 50,800d_{pitch}^3 + 62,700d_{pitch}^2) + 680,900(P_T/10^4)^{0.7}$ | [Milora and Tester, 1976]      |
| labor       | 0.3 x total component cost  | -                              |

Table 4. 3: Component cost as function of size.

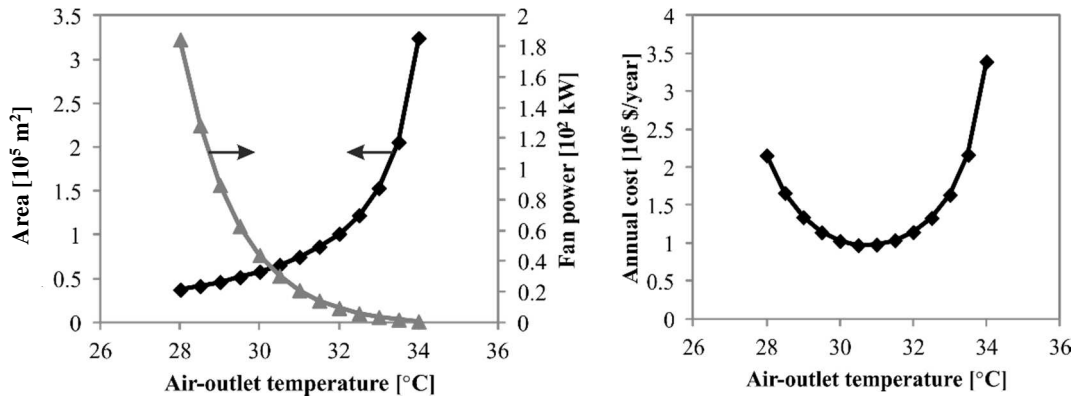


Figure 4. 6: Size optimization based on annual cost of condensers at 130-20 ( $T_{g,DP} - T_{a,DP}$ ) design-point.

#### 4.4.2 Off-design mapping

The off-design performance of the plant may be assessed using the Second Law of thermodynamics by comparing the actual net-power output to the maximum theoretical power that could be produced (energy) from the given geothermal fluid. This involves determining the energy-rate carried into the plant with the incoming geofluid [DiPippo, 2008]. In order to proportionally evaluate the off-design performance of each design-point, the geofluid mass flow rate at off-design conditions is computed using constant energy rate of 2,000 kW at ISO standard ambient temperature of 15 °C,

$$\dot{m}_{g,in-off} = \frac{2,000 \text{ [kW]}}{(h_{g,in} - h_{70^\circ C}) - 288.15[\text{K}](s_{g,in} - s_{70^\circ C})} \text{ (off - design)} \quad (4.20)$$

In order to obtain optimal operating point under off-design conditions, a three-variable control strategy was used. First, evaporation pressure was controlled by the turbine nozzle-opening  $\mu_T$ . Second, superheating/turbine inlet temperature was controlled by pump-speed  $n_p$  (isobutane mass flow rate), and third, condensation temperature by the fan-speed  $n_F$  (air volumetric flow rate). Constant sub-cooling was imposed by making use of the static pressure head between the pump and the liquid hot-well (Figure 4. 1). Using this control strategy for a modular ORC system, the net power output was maximized while keeping the injection temperature above scaling temperature to avoid scaling, which is described as

$$\max_{T_{g,out} \geq 70^\circ C} (\dot{W}_T - \dot{W}_P - \dot{W}_F) . \quad (4.21)$$

Scaling temperature is a site-specific problem. It depends on the chemical composition of the geothermal fluid most commonly silica and calcite, and temperature and pressure of the fluid. If the injection temperature of the geofluid falls below this temperature, there is the risk that scales might form in the heat exchanger or the piping system. A minimum bound of 70 °C was selected for this study, based on several works for mid-enthalpy geothermal resources [Aneke *et al.*, 2011; Bäumer *et al.*, 1990; Astolfi *et al.*, 2014]. The off-design simulation procedure was realized using a set of three heat balance equations, which were solved by using the Trust-Dogleg Region solver. The heat balance equations are

$$\begin{aligned} f_1 &= \dot{Q}_{re} - \dot{Q}_{re,new}(\text{function of } \dot{m}_{wf}, p_2, h_2, T_3, T_5, p_5) \\ f_2 &= \dot{Q}_{re} - \dot{Q}_{re,new}(\text{function of } \dot{m}_{g,in}, T_{g,in}, \dot{m}_{wf}, T_3, p_3, h_4) \end{aligned} \quad (4.22)$$

$$f_3 = \dot{Q}_{re} - \dot{Q}_{re,new}(\text{function of } n_F, T_{a,in}, \dot{m}_{wf}, T_1, T_6, p_6) ,$$

where  $f_1$  was determined using the three-zone recuperator model,  $f_2$  the evaporator model, and  $f_3$  the condenser model. Pressure drop in the evaporator was minimized to maintain evaporation temperature drop below 5 K. The equations were solved for given operation parameters to simulate the power-cycle. In order to find the optimum operation parameters for each operating condition, CMA-ES was implemented [Hansen, 2006]. After sizing the components for a design-point, the control variables turbine nozzle, pump and fan rotational speed are optimized to achieve maximum net power output during off-design operating conditions (Figure 4. 7a). The system is assumed to be steady-state for the cycle simulation. The net power output of the plant at 36 off-design wellhead and ambient temperatures (Figure 4. 7c) was evaluated. Gridfit algorithm [Daniel A. Keim Annemarie Herrmann, 1998] was then used to interpolate the profiles to produce a 2-D net power output surface contour, as shown in Figure 4. 8. Both design points had constant exergy input, which translated to higher geofluid mass flow rate at lower wellhead temperatures, as previously described in Equation (4. 20). The maximum net power output (978 kW) occurred at  $T_{g,in} = 120 \text{ }^\circ\text{C}$ ,  $T_{a,in} = -10 \text{ }^\circ\text{C}$  for 130-20 (Point A, Figure 4. 7b). While maximum net power output (1025 kW) occurred at  $T_{g,in} = 160 \text{ }^\circ\text{C}$ ,  $T_{a,in} = -10 \text{ }^\circ\text{C}$  for 160-20 (Point B, Figure 4. 7b). It can be observed contradictory net power-output trend between the two design points. For 130-20, by increase of geofluid temperature, the net power output decreases, especially at lower ambient temperature. In contrary, for 160-20, the net power output showed an opposite trend. This was affected mainly on the turbine isentropic efficiency characteristic at off-design. The nominal (design) isentropic enthalpy drop was lower and the nominal volumetric flow rate was higher for 130-20. Hence, if the plant was operated at higher wellhead temperature which has higher enthalpy drop and lower flow rate, the turbine isentropic efficiency would steeply deteriorated (see Figure 4. 5b). It is also important to note the different net-power dependencies on ambient temperature. When investigating at a constant  $T_{g,in}$  at the optimum point, the net power output decreased by 65.1% for 130-20 and 44.5% for 160-20 between  $-10 \text{ }^\circ\text{C}$  and  $40 \text{ }^\circ\text{C}$ .

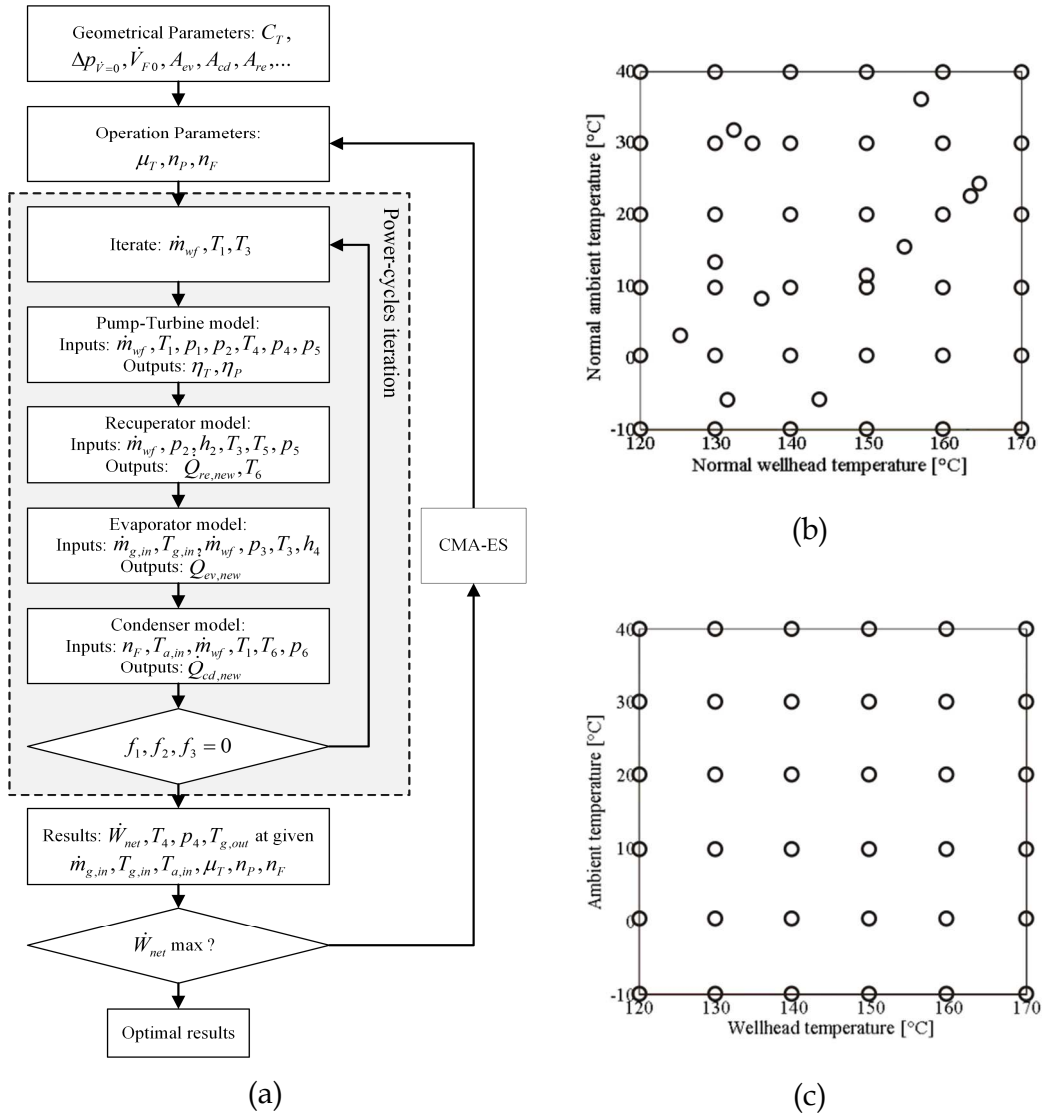


Figure 4. 7: (a) Off-design optimization procedure for a design-point ( $T_{g0} - T_{a0}$ ) and operating condition ( $\dot{m}_g, T_{g,in}, T_{a,in}$ ); (b) Design-point grid; and (c) Off-design grid.

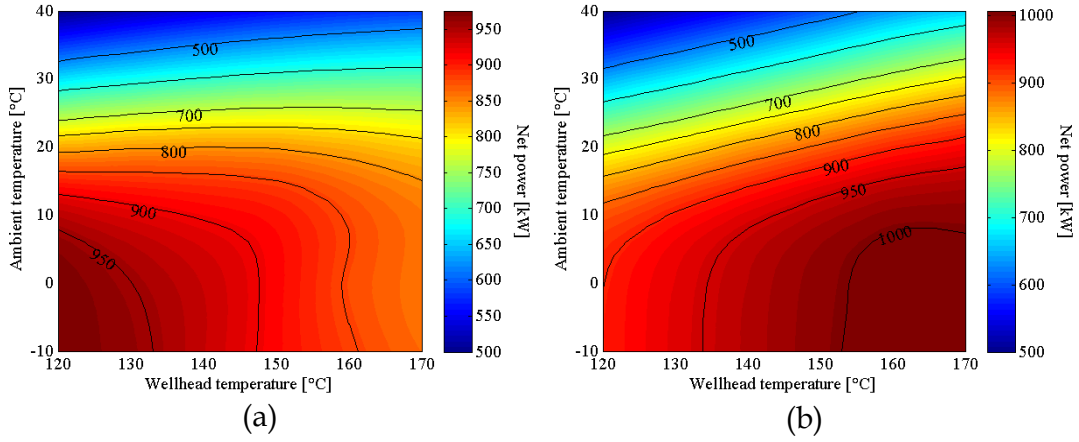


Figure 4. 8: Off-design maps of net power output for (a) 130-20; (b) 160-20.

#### 4.4.3 Annual simulation and thermo-economic selection

The system is assumed to be at steady-state for the annual simulations, and the heat loss in each component is neglected. The cycle performance is calculated in each time step of 1 h. The steady-state approximation is considered to be reasonably accurate since ambient temperature change is slower than the heat exchanger dynamics in the system. Thermal-economic optimization then was conducted to measure the trade-off between annual energy utilization and cost. Specific component costs are described in Table 4. 4; however, the cost correlations listed are not the exact economic values, since cost can vary strongly depending on market. Nonetheless, the values presented here used as a means to convert geometric design parameters into economic value, and correlations are taken from actual literatures [Taal *et al.*, 2003; Kashani *et al.*, 2013; Quoilin *et al.*, 2011]. The turbine cost was taken from a model developed by Barber-Nichols [Milora and Tester, 1976]. The correlations are corrected to current cost by using the Chemical Engineering Plant Cost Index (CEPCI) [Bernhard Spang and Roetzel, 2010]. The parameters,  $A$ ,  $d_F$ ,  $N_F$ ,  $P_F$ ,  $P_T$ , and  $P_P$  in Table 4. 4 were determined directly from the sizing results.

The turbine pitch (average wheel) diameter,  $d_{pitch}$ , was derived from a universal functional relationship, for optimum stage efficiency [Balje, 1962] as

$$\dot{V}_{5,design} = 0.177d_{pitch}\sqrt{\Delta h_{is,DP}} \quad (4. 23)$$

Two economic criteria were computed: specific investment cost (SIC) and mean cash flow (MCF). SIC is a typical parameter used in thermal-economic optimization, and is defined as

$$SIC[\$/kW] = \frac{\text{Component cost} + \text{Labor cost}}{\text{Averaged annual capacity } (\bar{P}_{net})} \quad (4.24)$$

where net P is mean annual net power output calculated as the averaged sum of annual energy production for each wellhead temperature (in kWh) divided by 7008 h. MCF measures the productivity of the power-plant, and is computed as

$$MCF[\$/year] = \text{Revenue} - CRF(\text{Component cost} + \text{Labor cost}) - C_{O\&M} - \text{Well cost} \quad (4.25)$$

where  $\text{Revenue} = P_{net} \times C_{el}$  and the three later terms are particularly annualized cost of electricity, i.e., investment cost, annual operation and maintenance costs of the overall plant which are assumed to be 4% of the investment cost [Entingh *et al.*, 1994], and well cost. Well cost accounted for the geofluid-pumping and drilling costs, which are arbitrary values dependent on site-specific characteristics. It was assumed a well cost equal to zero since it will only shift the MCF to a lower value, and result in an unchanged optimum design-point. The three climates temperate, tropical and dry – chosen for annual simulation were sampled from existing geothermal sites: Upper-Rhine Graben, Germany (temperate climate), Kamojang, Indonesia (tropical climate), and Birdsville, Australia (dry climate). The temperature distributions of each climate are shown in Table 4. 4.

| temperature<br>[°C] | temperate climate<br>( $T_{av} = 11.6$ °C) |            | tropical climate<br>( $T_{av} = 19.9$ °C) |            | dry climate<br>( $T_{av} = 25.1$ °C) |            |
|---------------------|--|------------|---|------------|--------------------------------------|------------|
|                     | number of<br>hours                         | %<br>hours | number of<br>hours                        | %<br>hours | number of<br>hours                   | %<br>hours |
| -10                 | 266  | 3.0        | 0   | 0          | 0                                    | 0          |
| 0                   | 2438                                       | 27.8       | 0   | 0          | 17                                   | 0.2        |
| 10                  | 2926                                       | 33.4       | 351                                       | 4.0        | 1195                                 | 13.6       |
| 20                  | 2159                                       | 24.6       | 7934                                      | 90.6       | 3139                                 | 35.8       |
| 30                  | 726  | 8.3        | 475                                       | 5.4        | 3154                                 | 36.0       |
| 40                  | 245  | 2.8        | 0   | 0          | 1254                                 | 14.3       |

Table 4. 4: Ambient temperature distribution of three climates during generic year.

The annual energy production was calculated using the hourly variation of  $T_{a,in}$  at each site. This calculation only includes cost, which varies significantly according to the component size. The remaining costs, such as piping, instrumentation and working fluid, were excluded. Under the conditions assumed for the temperate climate, the optimum points of SIC and MCF optimization was different

(Figure 4. 9). SIC minimization yielded 160-6, with a cost value of 1133 \$/kW, while MCF maximization yielded 153-10, with a cost value of 761,350 \$/year. The SIC and MCF showed large variation, ranging from 1133 \$/kW to 5296 \$/kW, and 92,224 \$/kW to 761,350 \$/kW, respectively.

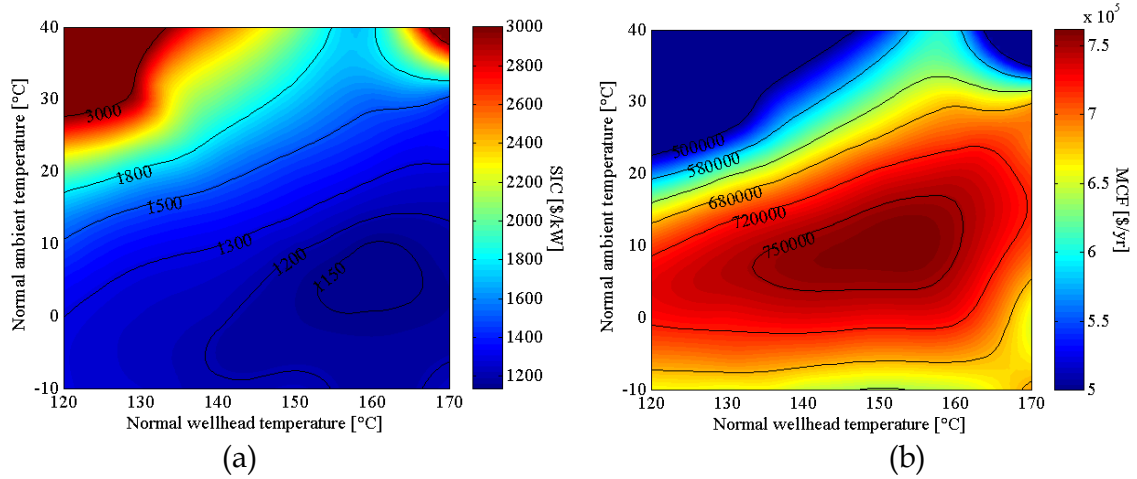


Figure 4. 9: Design-point based on minimizing SIC (a) and maximizing MCF (b) in temperate climate.

Comparing the two objective functions, SIC minimization resulted in values 5.1%–7.1% lower, relative to plants based on maximizing MCF. By maximizing MCF, values were 2.1%–10.8% higher compared to when SIC was minimized. The temperate climate had the lowest SIC minimum and highest MCF maximum, followed by the tropical and then the dry climate. The optimization results are reported in Table 4. 5. Using SIC minimization, the optimum normal wellhead temperature was constant at  $T_{g,DP}$  of 160 °C across the three climates, and optimum  $T_{a,DP}$  followed lower temperatures of 6 °C, 10 °C and 10 °C. While in MCF maximization, optimum  $T_{g,DP}$  was 153 °C, 163 °C and 163 °C, and  $T_{a,DP}$  followed average temperatures of 10 °C, 22 °C and 23 °C, respectively. Figure 4. 10 shows relative component costs among the three climates.

| sizing                   | design-point [°C] |            | SIC [\$/kW] | MCF [\$/year] |
|--------------------------|-------------------|------------|-------------|---------------|
|                          | $T_{g,DP}$        | $T_{a,DP}$ |             |               |
| <b>temperate climate</b> |                   |            |             |               |
| SIC minimization         | 160               | 6          | 1,133       | 745,770       |
| MCF maximization         | 153               | 10         | 1,198       | 761,350       |
| <b>tropical climate</b>  |                   |            |             |               |
| SIC minimization         | 160               | 10         | 1,303       | 642,070       |
| MCF maximization         | 163               | 22         | 1,403       | 683,120       |
| <b>dry climate</b>       |                   |            |             |               |
| SIC minimization         | 161               | 10         | 1,520       | 524,230       |
| MCF maximization         | 163               | 23         | 1,601       | 580,800       |

Table 4. 5: SIC and MCF for each optimal design-point and climate type.

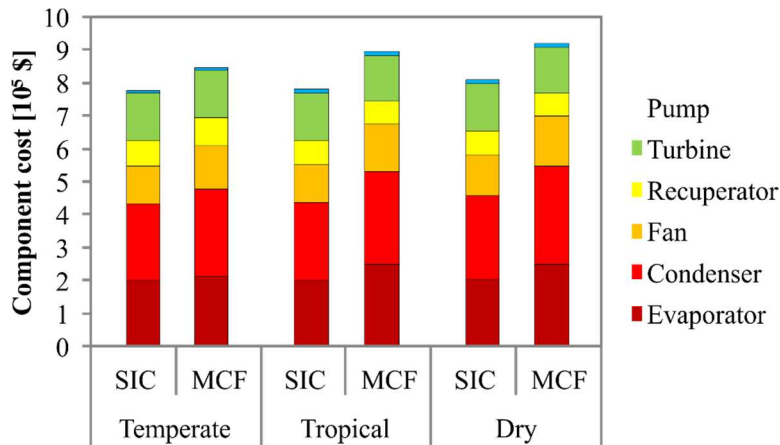


Figure 4. 10: Relative component cost comparison between SIC and MCF optimization under three different climate types.

SIC minimization resulted in a investment cost that was 8.2%–13% lower than plants designed using maximized MCF. The cooling-system cost (condenser heat exchangers, fans) dominated the total investment cost. For plants with minimized SIC, the cooling-system cost was 12.5%–16.7% lower than those designed using maximized MCF. In contrast, MCF maximization resulted in a higher mean annual net-power 3.4%–12.7%. This improvement was based on the optimal number of cells and fan capacity, which maintain low condensation pressure and, in turn, result in higher power.

## 4.5 CONCLUSIONS

The main conclusions of this work are as follows:

1. Using the modularization technique described in this paper, design optimization under three different climates (temperate, tropical, and dry) was derived. Using SIC minimization, the normal ambient temperatures were driven by the lower temperature. Using MCF maximization, the normal ambient temperatures were driven by average temperature in each climate region.
2. When SIC minimization and MCF maximization were compared, average net-power based on MCF maximization was higher. Although investment cost was slightly higher, the revenue or equivalently, the energy utilization was considerably improved. Consequently, MCF maximization is proposed as an optimization function.
3. Concerning the various components analyzed here, the condenser and fan size had the greatest influence on average net power output. The main feature in MCF maximization design was increased size of the cooling-system, which helped maintain low condensation pressure. Using isobutane, the condenser cost amounted to 35%–38% of the investment cost. Enhancing the heat transfer of cooling system technology will reduce the condenser size and, most importantly, the ORC investment cost.

# 5

## gEOSkit - AN EQUATION OF STATE ASSEMBLED FOR TWO-PHASE MULTI- COMPONENT GEOTHERMAL FLUIDS

submitted as

Nusiaputra, Y. Y., Dimier, A., Francke, H., Schröder, E., Herfurth, S., Kohl, T.,  
*gEOSkit - An Equation of State Assembled for Two-Phase Multicomponent Geo-  
thermal Fluids* in *Computers and Geosciences*

### ABSTRACT

Thermophysical properties of geothermal fluids play an important role for designing energy conversion systems. A geothermal fluid is a multiphase, multicomponent brine, which can be generalized as the system  $\text{H}_2\text{O}$  – salt ( $\text{Na-Ca-K-Mg-Cl-HCO}_3$ ) – gas ( $\text{CO}_2\text{-N}_2\text{-CH}_4\text{-H}_2\text{S}$ ). We developed an equation-of-state (EOS) solver for geothermal fluids using pressure and enthalpy as independent variables. The goal is to provide an efficient tool for two-phase geochemical transport simulation in geothermal reservoirs, wellbores, and heat exchangers. This tool employs improved gas activity coefficients obtained by the extension of neutral interactions for dissolved gases. The solver was developed in the object-oriented manner to facilitate extension to cover other salt and gas components. The validity of the solver presented here was evaluated using experimental data from literature and online field measurements in pressure, temperature, and ionic strength ranges of 0.5 – 50 MPa, 32 – 177 °C, and 0 – 8.1 mol/kgw, respectively. As shown by the validation, the solver can properly reproduce mutual gas solubility of ternary and quaternary mixtures as well as the density, specific heat capacity, and dynamic viscosity of mixtures. The source code for the algorithms is provided in the appendix.

### 5.1 INTRODUCTION

Geothermal systems often exhibit high salt content combined with presence of non-condensable gases (NCGs). As such examples Salton Sea [Williams and McKibben, 1989], Soultz-sous-Fôrets [Sanjuan *et al.*, 2010], and Groß-Buchholz [Hesshaus *et al.*, 2013]. Salt content and mineral composition is known to strongly affect technical infrastructure of these power plants, especially implication to corrosion and scaling [Nitschke *et al.*, 2014; Mundhenk *et al.*, 2013]. One method to

evaluate such processes is to use numerical models, including reactive (i.e. Bächler and Kohl [2005], Rabemanana [2003]), two-phase, multicomponent geothermal fluids. Reactive transport simulation of these system have to account for accurate thermodynamic properties (enthalpy, specific heat capacity, density, viscosity) of geothermal fluids over range of pressure and temperature in a corresponding application. Hasan and Kabir [2010] showed consideration of salts and NCGs may also be obligatory to compute accurate pressure and temperature profile along geothermal wells. Schröder et al. [2015] reported that the area required heat exchangers are can be reduced by 30%, if heat capacity is assumed to be 15% lower than the pure water values. Consequently, more realistic representations of geothermal fluids must include salts and non-condensable gases (NCGs).

The commonly used primary variables of the properties of salts-water or NCGs-brine mixtures are pressure and temperature ( $p - T$ ). Complexity increases when water evaporation or boiling occurs: within a specified pressure, temperature gradient is small (almost zero for lower salt content). Hence, primary variables of  $p - T$  cannot be used in this region. The thermodynamic state of two-phase fluids has to be defined by specifying another combination of two primary variables, e.g. pressure and specific enthalpy ( $p - h$ ). The gEOSkit, equation of state (EOS) described in this study, will be based on these variables. gEOSkit mainly consists of two models: (1) Vapor-liquid equilibrium (VLE) of liquid (aqueous) and gas (non- aqueous) phases, (2) thermophysical properties, i.e. density, isobaric heat capacity/enthalpy, dynamic viscosity, and thermal conductivity.

To develop a VLE or gas solubility model, two approaches are generally used, i.e. fugacity-fugacity ( $\phi - \phi$ ) and fugacity-activity ( $\phi - \gamma$ ). The first approach ( $\phi - \phi$ ) uses one EOS to compute fugacity of all phases in equilibrium, and the equations are solved by fugacity equality of different phases. The fugacity-activity approach ( $\phi - \gamma$ ) assumes a partition of fluid into gas-like (non-aqueous) and liquid-like (aqueous) phases by implementing ideal gas equations, virial, or cubic, e.g. Peng-Robinson (PR) or Soave Redlich Kwong (SRK), to compute the non-aqueous phase fugacity. An activity model is used for the calculation of the activity coefficient of the aqueous phase. The fugacity and the activity are then used to calculate chemical potentials. Equality of chemical potentials in both phases yields a system of equations, which is solved to determine the VLE. The  $\phi - \gamma$  approach, while much less computationally intensive, is also more convenient for integration with speciation and chemical equilibrium calculations [Springer *et al.*, 2015]. Thus, the  $\phi - \gamma$  method is more appropriate here.

A recent work based on  $\phi - \gamma$  approach was presented by Springer et al. (2015). It was based on the extension of a speciation-based model for mixed-solvent electrolyte systems [Wang *et al.*, 2002] to comprise the CO<sub>2</sub>-H<sub>2</sub>S-NaCl-CaCl<sub>2</sub>-water system. Unfortunately, not all details of the EOS have been released in this model and in some other publications, all of which are proprietary software. Hence, they are not easily available or reproducible for broader academic investigations in the geothermal energy sector. Appelo et al. [2014] used the Peng-Robinson equation for the computation of gas-phase fugacities with Henry constants to model the solubility of NCGs. This equation is embedded in PHREEQC, a geochemical speciation solver. However, the upper limit of the validity range was below 200 °C and validity of H<sub>2</sub>S solubility remained unclear. Other studies were conducted by Ziabakhsh-Ganji and Kooi [2012], Zirrahi et al. [2012] and Lei et al. [2016] for modeling the CO<sub>2</sub>-CH<sub>4</sub>-H<sub>2</sub>S-brine equilibrium. Still, in the first two studies, the pressure and temperature validity ranges (lower than 60 MPa and 110 °C) do not cover practically relevant geothermal applications. EOS7Cm established by Lei et al. [2016] covers wider pressure and temperature ranges, but has discrepancy in solubility compared to measured data. The Duan Research Group published comprehensive measurement studies for the solubility of a single gas component in pure water or brine of CO<sub>2</sub>, N<sub>2</sub>, CH<sub>4</sub>, and H<sub>2</sub>S [Duan and Mao, 2006; Duan and Sun, 2003; Duan *et al.*, 2007; Duan *et al.*, 2006; Mao and Duan, 2006; Mao *et al.*, 2013]. But their work does not consider the solubility of gas mixtures, which is of higher practical significance in field applications. Francke et al. [2013] unified these Duan's single-gas solubility functions to model the solubility of the CO<sub>2</sub>-N<sub>2</sub>-CH<sub>4</sub> mixture. However, the model still considers the gas phase as an ideal gas (fugacity coefficients equal to unity), which tends to be incorrect at higher pressures and for gas with strong intermolecular forces, i.e. water-vapor. In addition, gas solubility equation was used improperly: fugacity calculated from single gas function with the sum of water-vapor and the gases' partial pressures as input for the ion-molecular interaction functions.

With the goal to overcome the aforementioned limitations, the gEOSkit solver was devised and assembled for geothermal conditions. gEOSkit also includes VLE model which has been designed in the  $\phi - \gamma$  framework. The model is based on the EOS for NaCl-KCl-CaCl<sub>2</sub>-N<sub>2</sub>-CO<sub>2</sub>-CH<sub>4</sub>-H<sub>2</sub>O systems presented in the Modelica-based solver BrineProp solver [Francke *et al.*, 2013]. We extend a Peng-Robinson real-gas equation for fugacity calculation, including Duan and Sun (D-S) activity functions for each NCG-salt-water system to calculate gas mixture solubility. The total instead of the partial pressure which corresponds to realistic aqueous-phase pressure, is applied as input for the ion-molecular interaction parameters. Special emphasis on improvement of gas mixture solubility accuracy is presented by expressing neutral interaction parameters for dissolved gases.

Francke et al. [2013] described in detail a model of thermophysical properties of a geothermal fluid, which is limited to NaCl, CaCl<sub>2</sub>, and KCl. Parameters for other salts, such as MgCl<sub>2</sub> and NaHCO<sub>3</sub> were added by us. Extensions of the explicit model for enthalpy and the properties of dissolved gas and the non-aqueous phase were also implemented. gEOSkit solver inhere covers the mixture of water, salt (Na-Ca-K-Mg-Cl-HCO<sub>3</sub>) and gas (CO<sub>2</sub>-N<sub>2</sub>-CH<sub>4</sub>-H<sub>2</sub>S). For the advantage of other researches, the source code is provided in Python. It provides an accurate geothermal fluid properties that can be coupled with other geochemical code, i.e. PHREEQC, to cover geochemical processes.

## 5.2 CHEMICAL CHARACTERIZATION OF GEOTHERMAL FLUIDS

Geothermal fluids can be classified as Na-Cl and Na-Ca-Cl [Bozau *et al.*, 2015], Na-K-Cl, Na-HCO<sub>3</sub>, and Na-Cl-HCO<sub>3</sub> types. Sulfates (SO<sub>4</sub>)<sup>2-</sup> is also main component of geothermal fluids particularly in high-enthalpy systems. Nonetheless, the effects of salt associated with (SO<sub>4</sub>)<sup>2-</sup> on thermophysical properties are small. We assembled multicomponent geothermal fluid properties using an object-oriented scheme by decomposing the geofluid into classes of binary systems, i.e. binary salt systems: NaCl-H<sub>2</sub>O, CaCl<sub>2</sub>-H<sub>2</sub>O, KCl-H<sub>2</sub>O, MgCl<sub>2</sub>-H<sub>2</sub>O, and NCGs binary systems: CO<sub>2</sub>-brine, N<sub>2</sub>-brine, CH<sub>4</sub>-brine, and H<sub>2</sub>S-brine, as can be seen in Figure 5. 1. By using this scheme, the EOS can be extended easily to other salts and NCGs.

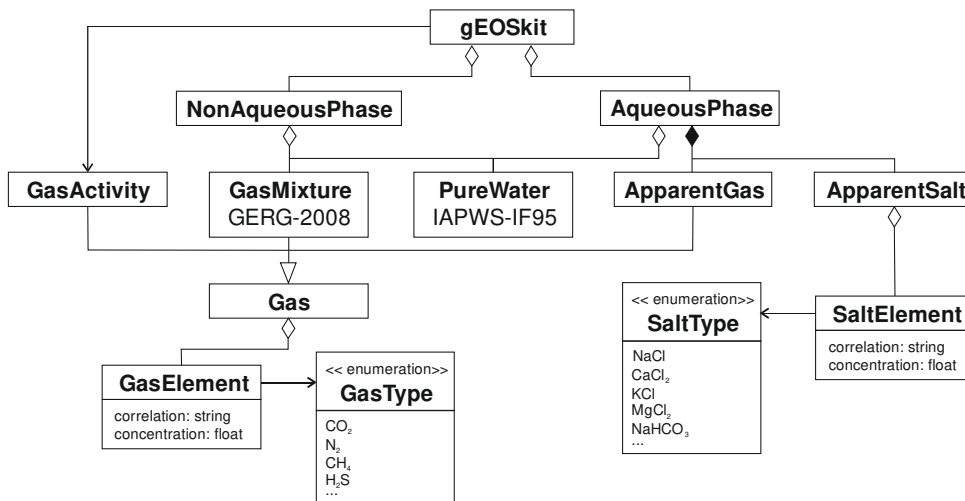


Figure 5. 1: Unified Modeling Language (UML) class diagram of the geothermal fluid's equations of state

The EOS comprises the independent classes of `AqueousPhase` and `NonAqueousPhase` of a `TwoPhaseGeofluid`. The third layer contains the ready-to-use medium models of `PureWater` and `GasMixture` from `CoolProp` (Bell et al. 2014), which can be replaced by other medium codes or tables. `TheGasActivity`, `ApparentGas`, and `ApparentSalt` packages are generic packages and define the correlations used to compute gas activity and apparent molar properties for use in the second layer.

### 5.3 EVALUATION OF THE VAPOR-LIQUID EQUILIBRIUM

#### 5.3.1 Theoretical background

In this study, a vapor-liquid equilibrium model was designed by fusing and improving the gas solubility models from the Duan Research Group (D-S). This model combines the Peng-Robinson (PR) equation of state with D-S semi-empirical equations for the dimensionless standard chemical potential, second-, and third-order (salts-gas) interaction parameters of  $\text{CO}_2$ ,  $\text{N}_2$ ,  $\text{CH}_4$ , and  $\text{H}_2\text{S}$ . The PR equation is used to iteratively calculate the mole fractions and fugacity coefficient of the gas, with the extended D-S equations being used to calculate gas solubility. The solubility of the gases  $K_j$  (mol/kgw) as a function of pressure, temperature, and ionic strength is expressed as

$$\begin{aligned} \ln(K_j) = & \ln(y_j \cdot \phi_j \cdot p) - \mu_j^{1(0)}/RT - 2\lambda_{j-\text{Na}}(b_{\text{Na}^+} + b_{\text{K}^+} + 2b_{\text{Ca}^{2+}} + 2b_{\text{Mg}^{2+}}) \\ & - \xi_{j-\text{Na-Cl}}(b_{\text{Na}^+} + b_{\text{K}^+} + c \cdot b_{\text{Ca}^{2+}} + c \cdot b_{\text{Mg}^{2+}})(b_{\text{Cl}^-} + b_{\text{HCO}_3^-}) \\ & - \sum_{j'} \chi_{j-j'} \cdot b_{j'} \end{aligned} \quad (5.1)$$

where  $\mu_j^{1(0)}/RT$  is the dimensionless standard chemical potential.  $\lambda_{j-\text{Na}}$  and  $\xi_{j-\text{Na-Cl}}$  are the second- and third-order gas-salts interaction parameters.  $c$  is 1 for  $\text{CO}_2$ ,  $\text{H}_2\text{S}$ ; and 2 for  $\text{N}_2$ ,  $\text{CH}_4$ . These three terms are ion-molecular interaction parameters depending on total pressure and temperature. The term  $\chi_{j-j'}$  represents an extension of the D-S model to include short-range interactions between neutral dissolved gas molecules. The values are determined by a best fit of available solubility data for mixtures containing  $\text{CO}_2$ ,  $\text{CH}_4$ ,  $\text{H}_2\text{S}$ , water, and  $\text{NaCl}$  [Qin *et al.*, 2008; Bachu and Bennion, 2009; Huang *et al.*, 1985]. These parameters are given in Table 5. 1.

| Gas $j$          | Gas $j'$         | $\chi_{j-j'}$                 |
|------------------|------------------|-------------------------------|
| CO <sub>2</sub>  | CH <sub>4</sub>  | -0.5529                       |
| CH <sub>4</sub>  | CO <sub>2</sub>  | -0.1111                       |
| CO <sub>2</sub>  | H <sub>2</sub> S | -0.2681                       |
| H <sub>2</sub> S | CO <sub>2</sub>  | -0.0222                       |
| CH <sub>4</sub>  | H <sub>2</sub> S | -0.1488                       |
| H <sub>2</sub> S | CH <sub>4</sub>  | $4.9119 \ln(T)$<br>$- 16.225$ |

Table 5. 1: Binary parameters used in the short-range interaction term of eq. (5. 1).

At a given pressure, temperature and salinity, the mole fraction of gases  $y_j$  is an iterative variable of eq. (5. 1). After evaluating the solubility, interphase mass balance is applied: If the actual gas concentration is smaller than the calculated solubility, the gas remain dissolved in the aqueous phase, the non-aqueous phase component is zero and no iteration is then needed. If the actual gas concentration is bigger than the calculated solubility, the difference between actual and calculated solubility is added to the non-aqueous phase component. Thus, we obtain the new mole fractions of gases  $y_{j,new}$ . This procedure is repeated until  $y_j = y_{j,new}$  is fulfilled.

The solubility functions are valid for (1) CO<sub>2</sub>: 0 - 150 MPa, 0 - 460 °C, and 0 - 4.5 mol/kgw ionic strength, (2) N<sub>2</sub>: 0 - 60 MPa, 0 - 317 °C, and 0 - 6 mol/kgw ionic strength, (3) CH<sub>4</sub>: 0 - 200 MPa, 0 - 300 °C, and 0 - 6 mol/kgw ionic strength, and (4) H<sub>2</sub>S: 0 - 100 MPa, 0 - 227 °C, and 0 - 6 mol/kgw ionic strength. The validity can be extended by fitting parameters to new experimental solubility data of a single gas in water/brine. For instance, the original Duan's function of H<sub>2</sub>S is only valid up to 21 MPa. To cover pressure of practical interest, however, we extended the function of standard chemical potential by fitting the parameters to the simulation results from Springer et al. [2015]. The fitted parameters are listed in Table 5. 2.

| $\mu_{\text{H}_2\text{S}}^{1(0)}/RT$ |           | $\mu_{\text{H}_2\text{S}}^{1(0)}/RT$ |           |
|--------------------------------------|-----------|--------------------------------------|-----------|
| c <sub>1</sub>                       | -5.81     | c <sub>5</sub>                       | 5.692E+3  |
| c <sub>2</sub>                       | -9.877E-4 | c <sub>6</sub>                       | 2.366E-3  |
| c <sub>3</sub>                       | -2.165E+1 | c <sub>7</sub>                       | -0.7343   |
| c <sub>4</sub>                       | -6.75E-5  | c <sub>8</sub>                       | -9.744E-6 |

Table 5. 2: Parameters for the H<sub>2</sub>S standard chemical potential equation of Duan et al. (2007) fitted for 21 MPa < p ≤ 100 MPa.

By using the mass balance, the main output of the VLE model is the ratio between the non-aqueous phase mass and the total mass,  $x = (m_{\text{H}_2\text{O}}^{\text{NA}} + \sum m_j^{\text{NA}}) / (m_{\text{H}_2\text{O}} + \sum m_i + \sum m_j^{\text{AQ}} + \sum m_j^{\text{NA}})$ .

In order to evaluate the solubility, eq. (5. 1), the PR cubic equation for real-gas mixtures is solved to determine the fugacity coefficients  $\phi_j$  of each gas component at a given pressure and temperature [Peng and Robinson, 1976]. It can be written as

$$p = \frac{RT}{V_m - b_m^*} - \frac{a\alpha_m}{V_m(V_m + b_m^*) + b_m^*(V_m - b_m^*)}, \quad (5. 2)$$

where  $a\alpha_m = \sum_j \left( \sum_{j'} (y_j y_{j'} (a_j \alpha_j \cdot a_{j'} \alpha_{j'})^{0.5}) \right) (1 - k_{jj'})$ ,  $b_m^* = \sum y_j b_j^*$ ,  $a_j = 0.45724 \cdot (RT_c)^2 / p_c$ ,  $b_j^* = 0.0778 \cdot RT_c / p_c$  with unknown variable of molar volume of the gas mixtures  $V_m$ . Here,  $p_c$  and  $T_c$  are the critical pressure and critical temperature of gas  $j$ , respectively,  $y_j$  is the mole fraction of gas  $j$  in the non-aqueous mixture, and  $y_j$  are binary interaction parameters for gas pairs taken from [Soreide and Whitson, 1992]. The  $\alpha_j$  is a temperature-dependent function which takes into account the attractive forces between the gas molecules.

Being a cubic equation, the PR equation has three roots. For the gas phase, the maximum root is taken as the molar volume of the mixture. By using the real-gas equation, the compressibility factor can be computed as  $Z = PV_m / RT$ . Hence, the fugacity coefficient of gas  $\phi_j$  can be calculated by

$$\ln(\phi_j) = B_r(Z - 1) - \ln(Z - B) + \frac{A}{2.828B} \left( \frac{B_r - 2a\alpha_{m,j}}{a\alpha_m} \right) \ln \left( \frac{Z + 2.414B}{Z - 0.414B} \right), \quad (5. 3)$$

where  $B_r = b_j^*/b_m^*$ ,  $A = a\alpha_m/(RT)^2$ ,  $B = p \cdot b_m^*/RT$ . In order to reduce computational cost, the mole fraction of water vapor is not included in the iterative process of gas solubility calculation, since it was assumed to be  $y_{\text{H}_2\text{O}} = p_{\text{sat,H}_2\text{O}}/p$ . For an ionic strength below the salt saturation, modified Raoult's law can be sufficiently applied to predict the saturation pressure of water  $p_{s,\text{H}_2\text{O}}$ ,

$$p_{\text{sat,H}_2\text{O}} = p_{\text{sat,H}_2\text{O}}^{\circ} \cdot \left( \frac{w_{\text{H}_2\text{O}}^{\text{AQ}}}{M_{\text{H}_2\text{O}}} - \sum_{N_i} n_{h,i} \frac{w_i^{\text{AQ}}}{M_i} \right) \cdot \left( \frac{w_{\text{H}_2\text{O}}^{\text{AQ}}}{M_{\text{H}_2\text{O}}} + \sum_{N_i} (z_i - n_{h,i}) \frac{w_i^{\text{AQ}}}{M_i} \right)^{-1}, \quad (5.4)$$

where  $p_{\text{sat,H}_2\text{O}}^{\circ}$  is the saturation pressure of pure water.  $w$ ,  $M$ ,  $z_j$ ,  $n_{h,j}$  are mass fraction, molar mass, the Van't Hoff factor (sum of the ion valence numbers), and temperature-dependent hydration number of each salt, respectively. By implementing temperature-dependent hydration number, the saturation-temperature accuracy is within 1.14 Kelvin up to (near critical temperature of water) 373 °C, corresponds to saturation pressure of 14 MPa and molality of 13.24 mol/kgw compared to SoWat [Driesner and Heinrich, 2007].

The critical pressure and temperature of saline water depend on its bulk composition, i.e. the mole fraction of salts and gases. Hence, the saturation pressure/temperature of saline water may exceed the critical pressure/temperature of pure water. In this region, a hypothetical  $p - T$  relation of pure water was devised to model the saline water saturation pressure. This hypothetical saturation pressure-temperature can be approximated by the quadratic relation

$$p_{\text{sat,H}_2\text{O}}^{\circ} = \sum_{n=1}^3 c_n T^{n-1}, \text{ for } T > 374 \text{ }^{\circ}\text{C} \quad (5.5)$$

$$T_{\text{sat,H}_2\text{O}}^{\circ} = \frac{-c_2 + \sqrt{c_2^2 - 4c_3(c_1 - p)}}{2c_3}, \text{ for } p > 22 \text{ MPa}$$

with  $c_1, c_2, c_3$  being 68.19, -0.4156, 5.291E-4, respectively. This saturation  $p - T$  relation was fitted using eq. (5.5) to SoWat, with zero hydration number assumption up to 28 MPa and 400 °C.

### 5.3.2 Solver algorithm

The algorithm used in this study calculates the thermodynamic properties of brine (aqueous salt), water vapor, and non-condensable gases using the correlations presented in the previous section. It covers a wide range of pressure and enthalpy, which is why the p-h domain is divided into three regions: (1) Gas exsolution (single-phase liquid, non-boiling two-phase system of NCG-water) in the supercritical region, (2) water vapor-dominated (boiling two-phase system, with most of the NCG exsolved), (3) superheated (water vapor and NCG). The regions are numerically partitioned by

$$\text{Region (1)} : h \leq h_{\text{exs}} ,$$

$$\text{Region (2)} : h_{\text{exs}} < h \leq h_{\text{dry}} ,$$

$$\text{Region (3)} : h > h_{\text{dry}} .$$

A boundary function of  $h_{\text{exs}}$  is enthalpy at  $T_{\text{sat},\text{H}_2\text{O}}$ , where the NCGs have been exsolved and  $h_{\text{dry}}$  is enthalpy at  $x = 1$ . The boundary enthalpies are computed in the initialization phase. Three different solvers based on mass balances were implemented to compute geothermal fluid properties in these regions. These properties are presented in the following subchapters. The algorithm is outlined in Figure 5. 2.

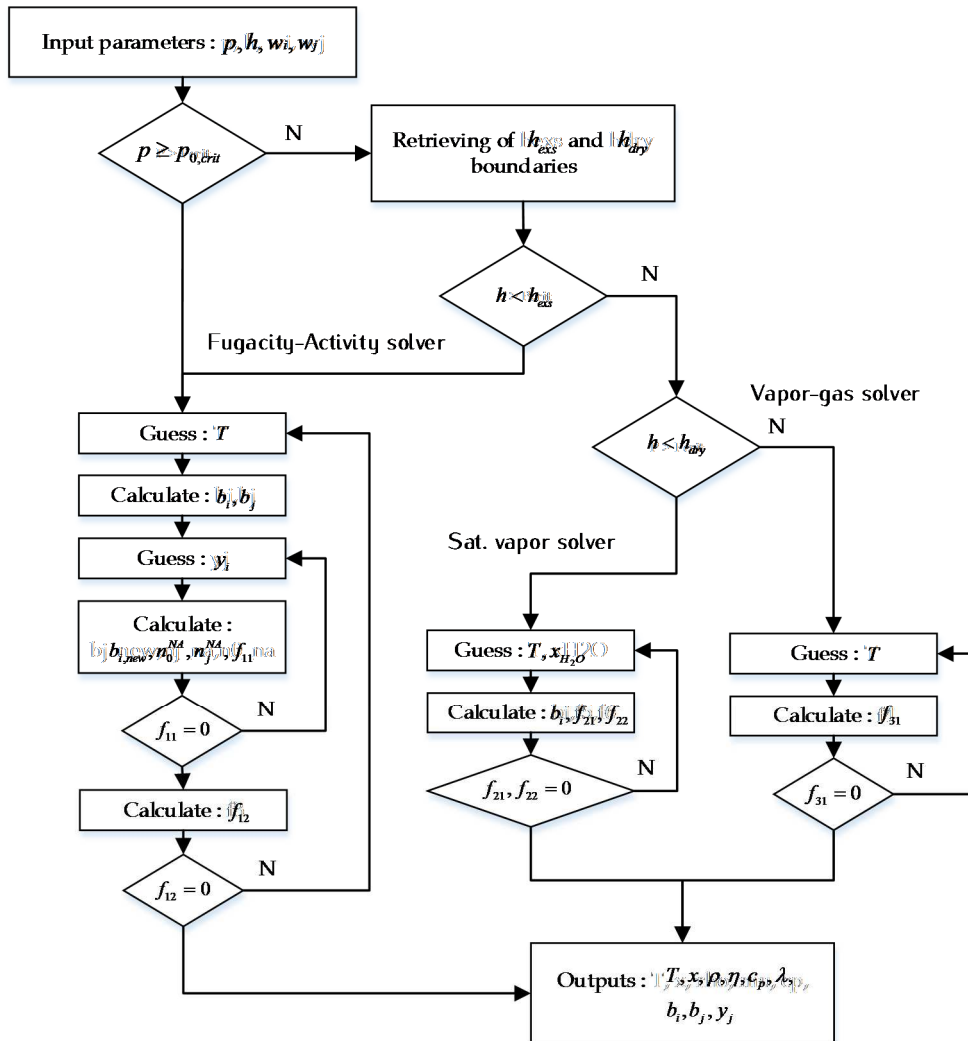


Figure 5. 2: Flow diagram of the procedure to calculate two-phase properties.

### *Fugacity-activity solver*

The fugacity-activity solver is used for region 1. The number of unknown variables is reduced to two, which are  $h_{dry}$  and  $T$ . Accordingly, a set of two functions, eq. (5. 6), is solved in sequence by using the iterative method. In this work, the functions are solved by means of the hybrid-Powell algorithm in Python.

$$f_{11} = y_j - y_{j,\text{new}}, \text{ inner loop,} \quad (5.6)$$

$$f_{12} = \left[ \frac{(h-h^{\text{AQ}})}{(h^{\text{NA}}-h^{\text{AQ}})} - x \right] \text{ (as function of } T\text{), outer loop.}$$

The procedure to execute the core routine of the “fugacity-activity solver” (inner loop in Figure 5. 2) comprises four steps:

1. Determine the input composition (mass fraction) of salts and gases. We need to compute the mole fraction of each gas (in aqueous and non-aqueous phases) under the given condition, i.e. pressure, temperature, salt, and gas mass fraction  $(p, T, w_i, w_j)$ .
2. Initial estimate of the mole fraction in the gas phase,  $y_j$ . In this step, the water-vapor quality  $x_{\text{H}_2\text{O}} = m_{\text{H}_2\text{O}}^{\text{NA}}/m_{\text{H}_2\text{O}}$  is necessary to update the molality of the salts.
3. Solve the Peng-Robinson cubic equation, eq. (5. 2), to compute the compressibility factor,  $Z$ , and, thus, the fugacity of the gases with eq. (5. 4).
4. Calculate molality of each gas in the aqueous phase  $b_{i,\text{new}}$  and (in case of actual gas concentration is smaller than the calculated solubility) its mole fraction in the non-aqueous phase  $y_{i,\text{new}}$ . Update the new value until convergence of  $y_j = y_{j,\text{new}}$  is achieved by solving  $f_{11}$ .

#### *Vapor-saturated solver*

The water vapor solver is used for region 2, where water vapor dominates the non-aqueous phase. Two variables need to be solved, namely, temperature  $T$  and water vapor quality  $x_{\text{H}_2\text{O}}$ . Both variables have to be solved simultaneously, since  $x_{\text{H}_2\text{O}}$  affects salt molality which depends on the amount of evaporation determined by the temperature of the saline water. This problem is defined in the functions below.

$$f_{21} = T - T_{\text{sat},\text{H}_2\text{O}} ,$$

$$f_{22} = x_{\text{H}_2\text{O}} - \frac{(h - h^{\text{AQ}})/(h^{\text{NA}} - h^{\text{AQ}}) \cdot (m_{\text{H}_2\text{O}} + \sum m_i + \sum m_j) - \sum m_j}{m_{\text{H}_2\text{O}}} , \quad (5.7)$$

with  $T_{s,\text{H}_2\text{O}}$  denoting the saturation temperature of water,  $m$  the mass;  $i$  the index for salt components, and  $j$  for NCG components.

### Vapor-gas solver

The vapor-gas solver is used for region 3, where water has evaporated completely. One variable has to be solved for region 3, which is temperature  $T$ . The function is defined by

$$f_{31} = h - h^{NA}(T) . \quad (5.8)$$

After solving the VLE, which yields temperature  $T$  and the non-aqueous phase quality  $x$ , the effective thermophysical properties of the geofluid can be evaluated, i.e. density  $\rho$ , specific heat capacity  $c_p$ , viscosity  $\eta$ , and thermal conductivity  $\lambda$ .

#### 5.3.3 VLE validation

The fugacity-activity solver results were compared with various experimental data taken from literature and covering a wide range of pressure, temperature, and composition, in complex systems with CO<sub>2</sub>-H<sub>2</sub>S, CO<sub>2</sub>-CH<sub>4</sub>, and CO<sub>2</sub>-CH<sub>4</sub>-H<sub>2</sub>S mixture in brine, respectively. A comparative analysis with existing codes, e.g. PHREEQC 3.2 [Appelo *et al.*, 2014] was plotted as well.

Figure 5. 3 shows that in a CO<sub>2</sub>-H<sub>2</sub>S-brine system the predicted solubility values exhibit an absolute average relative deviation (AARD) of around 5.7% compared to gEOSkit. Simulation of PHREEQC 3.2 produces an AARD of 33.38% with large deviations of H<sub>2</sub>S solubility. In a CO<sub>2</sub>-CH<sub>4</sub>-brine system (Figure 5. 4), for both CH<sub>4</sub> and CO<sub>2</sub> at 71 °C, the solubility increases with an increase in pressure. Moreover, it is found that the more CO<sub>2</sub> or CH<sub>4</sub> is contained in the dry non-aqueous mixture, the larger amount of corresponding gas is dissolved in water. In general, gEOSkit is able to accurately predict the CO<sub>2</sub> mole fraction in the aqueous phase of the ternary mixture with CH<sub>4</sub>. For both mixtures, the AARD of gEOSkit is approximately 3.65% compared to 8.84% of PHREEQC 3.2. In the second experiment (Figure 5. 5), a similar trend is observed. CO<sub>2</sub> solubility decreases with the CH<sub>4</sub> content and increases with pressure. Agreement between the measurement and the prediction by gEOSkit is very good for CO<sub>2</sub> and CH<sub>4</sub> at 103 °C (the AARD is around 3.8%). Both CO<sub>2</sub> and CH<sub>4</sub> solubilities are in good agreement at 52 °C, with an AARD of approx. 2.8%. These predictions are more accurate than the results of PHREEQC 3.2 (with AARD at 103 °C and 52 °C of 14.96% and 33.7%, respectively) and Lei *et al.* [2016], which confirms the reliability of the model when it is implemented in the CO<sub>2</sub>-CH<sub>4</sub>-brine systems.

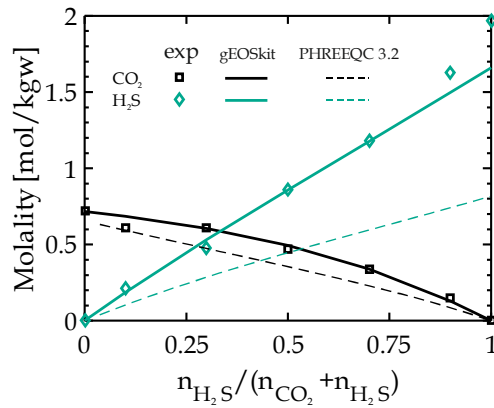


Figure 5. 3: Molality of CO<sub>2</sub> and H<sub>2</sub>S in the aqueous phase as a function of the H<sub>2</sub>S mole fraction in the dry non-aqueous phase: Dots are calculated results from Bachu and Bennion [2009] (unfilled squares - CO<sub>2</sub>; unfilled diamonds - H<sub>2</sub>S) and values predicted by gEOSkit (solid lines) and PHREEQC 3.2 (dashed lines). The experiment was conducted at p = 13.5 MPa and T = 61 °C with an NaCl concentration of 11.9 wt.%.

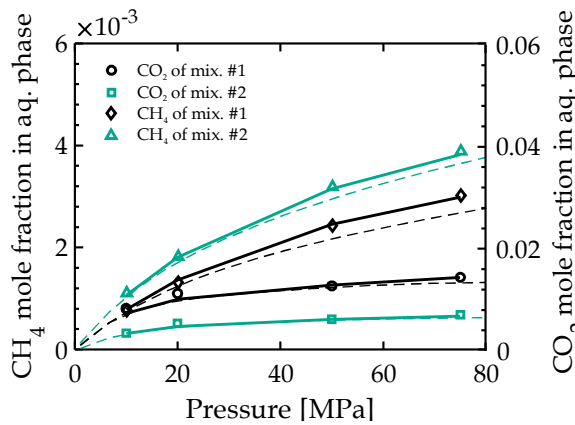


Figure 5. 4: Aqueous mole fraction of CO<sub>2</sub> and CH<sub>4</sub> as a function of pressure: Measured values from Dhima et al. [1998] (unfilled circles - CO<sub>2</sub> mix#1; unfilled squares - CO<sub>2</sub> mix#2; unfilled diamonds - CH<sub>4</sub> mix#2; unfilled triangles - CH<sub>4</sub> mix#2) and values predicted by gEOSkit (solid lines) and PHREEQC 3.2 (dashed lines). The experiment was conducted at T = 71 °C.

In Figure 5. 6, simulation results of (N<sub>2</sub> + CH<sub>4</sub>) solubility are in good agreement with the measured ones in the range of CH<sub>4</sub> mole fraction between 0 and 1. The AARD is approximately 4.5%. The calibrated (stars) and experimental data for the pure N<sub>2</sub>/CH<sub>4</sub> - brine mixture are observed to differ considerably, which may be due to the reliability of the experimental data. However, the qualitative trend of total solubility is predicted well by gEOSkit and PHREEQC 3.2 in the 0 - 1 CH<sub>4</sub>

mole fraction range. Finally, the thermodynamic model is tested in a  $\text{CO}_2\text{-H}_2\text{S-CH}_4\text{-H}_2\text{O}$  system in Figure 5. 7. gEOSkit, however, seems to slightly overestimate the  $\text{CO}_2$  solubility at 38 °C and 177 °C. The AARD is about 7%, while PHREEQC 3.2 has an AARD of 14.71%. The higher AARD of the quaternary mixture may indicate a strong influence of the short-range interactions,  $\chi_{j-j'}$  (see eq. (5. 1)), on neutral molecules, e.g. dissolved gases (Abrams, Prausnitz 1975).

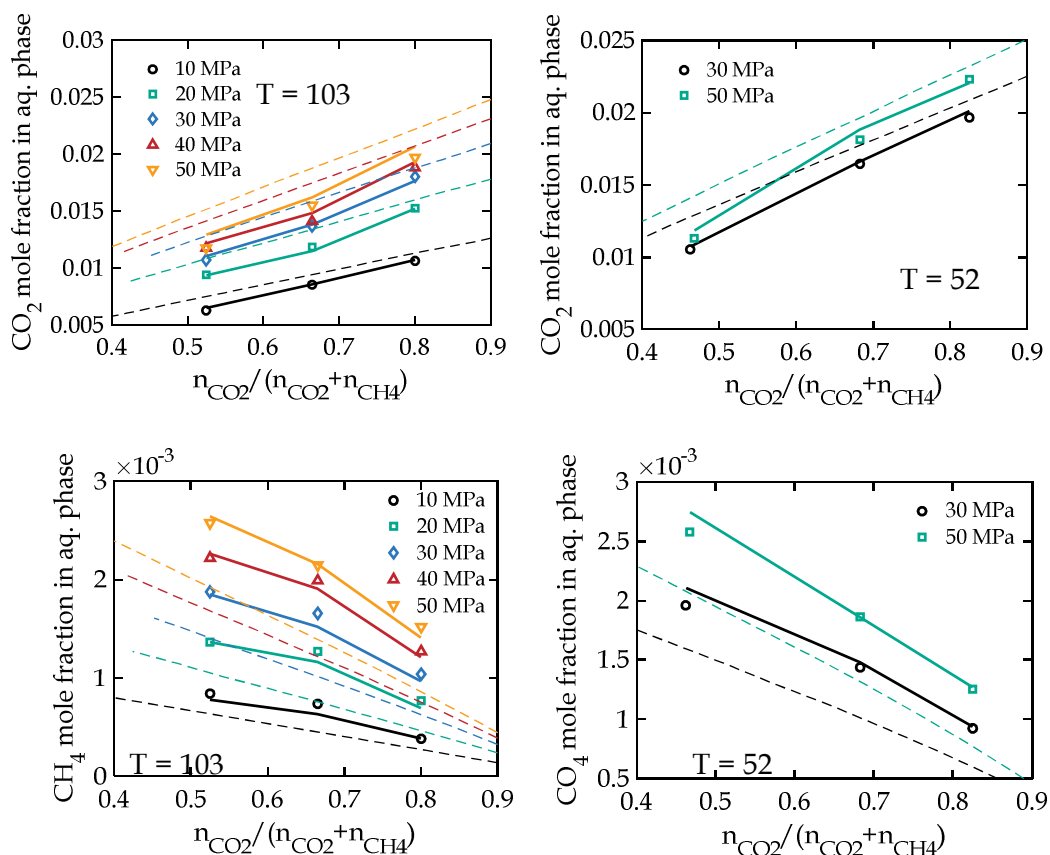


Figure 5. 5: Aqueous mole fraction of  $\text{CO}_2$  and  $\text{CH}_4$  versus the  $\text{CO}_2$  mole fraction in the dry non-aqueous phase: Experimental data from Qin et al. [2008] (unfilled circles 10 MPa; unfilled squares 20 MPa; unfilled diamonds 30 MPa; unfilled upward triangles 40 MPa; unfilled downward triangles 50 MPa) are compared with calculated values from gEOSkit (solid lines) and PHREEQC 3.2 results (dashed lines). The PHREEQC 3.2 results at 103 °C were adapted from Appelo et al. [2014].

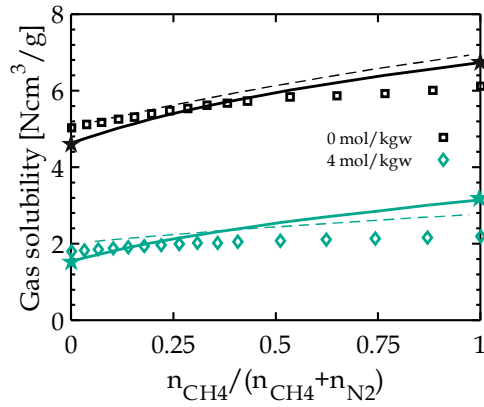


Figure 5. 6: Dry non-aqueous phase mole fractions of N<sub>2</sub> and CH<sub>4</sub>: Measurements results from Harting [1982] and calculated total solubility values of N<sub>2</sub> and CH<sub>4</sub> are compared with calculated values from gEOSkit (solid lines) and PHREEQC 3.2 (dashed lines). Stars mark points which were calibrated by results from Mao and Duan [2006], Duan and Mao [2006]. The experiments were conducted at  $p = 50.7$  MPa,  $T = 150$  °C.

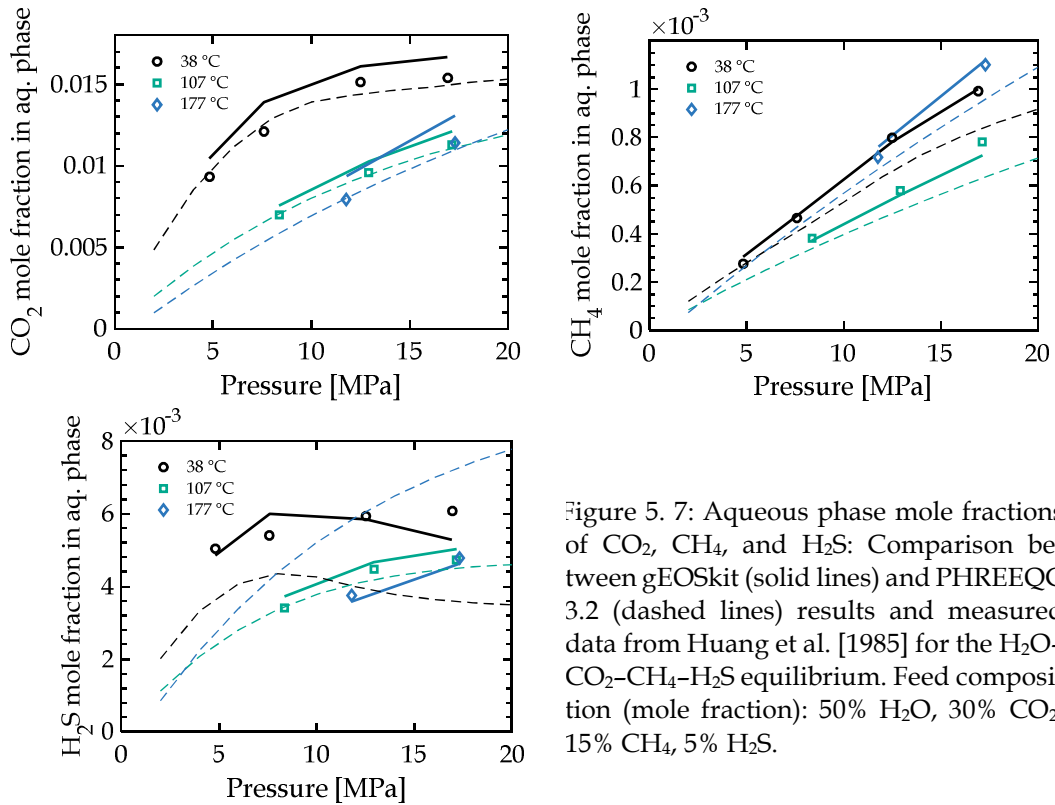


Figure 5. 7: Aqueous phase mole fractions of CO<sub>2</sub>, CH<sub>4</sub>, and H<sub>2</sub>S: Comparison between gEOSkit (solid lines) and PHREEQC 3.2 (dashed lines) results and measured data from Huang et al. [1985] for the H<sub>2</sub>O-CO<sub>2</sub>-CH<sub>4</sub>-H<sub>2</sub>S equilibrium. Feed composition (mole fraction): 50% H<sub>2</sub>O, 30% CO<sub>2</sub>, 15% CH<sub>4</sub>, 5% H<sub>2</sub>S.

## 5.4 THERMOPHYSICAL PROPERTIES

Specific enthalpy value is needed to solve system of equations as outlined in Section 3.2. Likewise, thermohydraulic, nondimensional numbers like Darcy, Reynolds, Prandtl or Peclet numbers are strongly dependent on the fluid properties value, i.e. heat capacity, density, and viscosity. The following sections describe gEOSkit evaluation of those thermophysical properties on selected case studies, comparison with measurement results, as well as comparison to that of pure water as a function of pressure along a representative isenthalpic (Figure 5.8, Figure 5.9, and Figure 5.10). The measurements of URG were made on-site using mobile testing unit developed at Karlsruhe Institute of Technology. The GrSk data were also measured on-site by using FluMo, a mobile fluid-chemical monitoring system developed at GFZ Potsdam [Feldbusch *et al.*, 2013]. The brine's thermal conductivity was not analyzed, since the value is roughly equal to pure water, as observed by Yusufova *et al.* [1975]. Table 5.3 summarizes the chemical compositions of the geothermal brines (aqueous-phase) of the selected case studies.

|                    | URG<br>(95 °C) | GrSk.<br>(150 °C) | Soultz<br>(200 °C) | Salton Sea #11<br>(260 °C) |
|--------------------|----------------|-------------------|--------------------|----------------------------|
| NaCl               | 7.74           | 9.85              | 6.98               | 11.81                      |
| CaCl <sub>2</sub>  | 2.69           | 15.11             | 1.83               | 6.35                       |
| KCl                | 0.68           | 0.56              | 0.55               | 2.40                       |
| MgCl <sub>2</sub>  | 0.50           | 0.17              | 0.04               | 0.01                       |
| NaHCO <sub>3</sub> | ≅ 0            | ≅ 0               | ≅ 0                | ≅ 0                        |

Table 5.3: Aqueous geothermal fluid compositions (wt. %) used in this study. The reservoir temperature is given in brackets. Data were taken from Sanjuan *et al.* [2010], William and McKibben [1989] and our measurement results.

### 5.4.1 Isobaric heat capacity and enthalpy

The effective specific heat capacity of the two-phase geofluid  $c_p$  is evaluated using a mass-averaged, mixture-specific heat capacity,

$$c_p = (1 - x) \cdot c_p^{AQ} + x \cdot c_p^{NA} . \quad (5.9)$$

The specific heat capacity of the gas mixture  $c_p^{NA}$  is determined by using the GERG 2008 EOS with the mixing correlation by Kunz and Wagner [2012] via

CoolProp [Bell *et al.*, 2014]. The specific heat capacity of the aqueous phase  $c_p^{AQ}$  can be expressed by the specific heat capacity of water and the apparent molar heat capacities of the particular salts. It is written as

$$c_p^{AQ} = w_{\text{H}_2\text{O}}^{AQ} \cdot c_{p,\text{H}_2\text{O}}^{AQ} + \sum_{N_i} \frac{w_i^{AQ}}{M_i} \cdot c_{p,i}^{\phi} + \sum_{N_j} \frac{w_j^{AQ}}{M_j} \cdot c_{p,j}^{\phi}, \quad (5.10)$$

where the apparent molar heat capacity,  $c_p^{\phi}$ , is defined as the change of absolute heat capacity of an arbitrary amount of solution caused by the addition of a salt (index  $i$ ) and gas (index  $j$ ). Francke *et al.* [2013] provided equation eq. (B.5) (Appendix A) and the coefficients for the apparent heat capacities of  $\text{CaCl}_2$  and  $\text{KCl}$  valid for  $p = 2.1 - 17.8$  MPa,  $T = 34 - 329$  °C,  $b_{\text{NaCl}} = 0.1 - 3$  mol/kgw and  $p = 16.4 - 17.8$  MPa,  $T = 52 - 327$  °C,  $b_{\text{KCl}} = 0.1 - 3$  mol/kgw, respectively. The apparent heat capacity for  $\text{MgCl}_2$  is extended by fitting experimental data from (White *et al.*, 1988) (from the range:  $p = 2.3 - 17.9$  MPa,  $T = 76 - 325$  °C,  $b_{\text{MgCl}_2} = 0 - 2.3$  mol/kgw). The accuracy of the solver is within 2%.

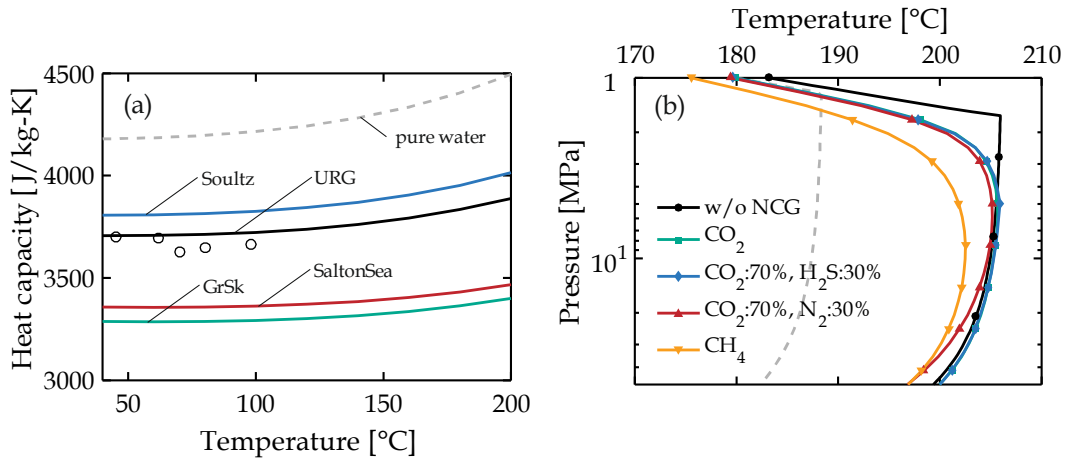


Figure 5. 8: Aqueous phase isobaric heat capacities of geofluids listed in Table 5. 3 and vapor-saturated NaCl (3 mol/kgw) solution: (a) Comparison of gEOSkit (solid lines), measurement data (unfilled circles - URG), and pure water (dashed line) and (b) temperature of URG brine for different gas compositions (1% wt. NCG) and pure water (dashed lines) at an enthalpy of 800 kJ/kg.

To calculate all the properties in the solver presented here, where pressure and enthalpy are the primary variables, an additional function for the enthalpy has to be included. It can be derived from the specific heat capacity. The specific enthalpy of the two-phase geothermal fluid  $h$  can be calculated in analogy to eq. (5.10) as

$$h = (1 - x) \cdot h^{AQ} + x \cdot h^{NA} , \quad (5.11)$$

where the enthalpy of the gas mixture in the non-aqueous phase  $h^{NA}$  is determined by GERG 2008 via CoolProp. To calculate the enthalpy in the aqueous phase  $h^{AQ}$ , the following formula is used

$$h^{AQ} = w_{\text{H}_2\text{O}}^{AQ} \cdot h_{\text{H}_2\text{O}}^{AQ} + \sum_{N_i} \frac{w_i^{AQ}}{M_i} \cdot h_i^\phi + \sum_{N_j} w_j^{AQ} \left( h_j + \frac{h_{\text{sol},j}^\phi}{M_j} \right) . \quad (5.12)$$

$h_{\text{H}_2\text{O}}^{AQ}$ ,  $h_i^\phi$  are the liquid pure-water enthalpy and the apparent molar enthalpy of salt  $i$ , respectively. Since we do not have any apparent molar enthalpy for dissolved gas, the enthalpy of dissolved gas is estimated by mixing two properties  $h_j$  and  $h_{\text{sol},j}^\phi$ , which are the enthalpy of gas  $j$  at the corresponding total pressure and the solution enthalpy of gas  $j$ , respectively. The experimental data for the enthalpy of salt solutions are very limited. However, by using the relation between specific heat capacity and enthalpy, the latter can be derived quickly based on the equation of specific heat capacity by Driesner [2007]. Driesner's equation scales the NaCl solution properties to the pure water properties by scaling the temperature:  $h^{NA}(T^*) = h_{\text{H}_2\text{O}}^{AQ}(T_h^*)$ , which leads to  $c_p^{AQ}(T) = q_2 \cdot c_{p,\text{H}_2\text{O}}^{AQ}(T_h^*)$ . By taking the temperature integral according to the reverse chain rule, it can be defined for any salt  $i$  that

$$\begin{aligned} h_{i,\text{Dr}}^{AQ}(p, T, m_i) &= \int c_{p,i}^{AQ}(p, T, m_i) \cdot dT \\ &= \int q_2 \cdot c_{p,\text{H}_2\text{O}}^{AQ}(T_h^*(p, T, m_i)) \cdot dT \\ &= h_{\text{H}_2\text{O}}^{AQ}(p, T_h^*) + c , \end{aligned} \quad (5.13)$$

with  $T_h^* = q_1 + q_2 \cdot T$ . By setting the integration constant  $c$  equal to zero, the equation follows the formulation of Driesner's model. The apparent temperature  $T_h^*$ , hence, can be derived by fitting the experimental data of specific heat capac-

ity of any salts  $c_{p,i}^{AQ}$  to Driesner's model of specific heat capacity  $c_{p,H_2O}^{AQ}(T_h^*)$ . Accordingly, after knowing  $T_h^*$ , we are able to calculate the enthalpy  $h_{i,Dr}^{AQ}$ . However, the experiments were conducted at constant pressure, while the parameters  $q_1$  and  $q_2$  are strongly pressure-dependent. In order to minimize the error, the apparent molar enthalpy  $h_i^\phi$  was derived from the calculated enthalpy  $h_{i,Dr}^{AQ}$ ,

$$h_i^\phi = c_{01} + c_{02} \cdot b_i + c_{03} \cdot (T + 273.15) + c_{04} \cdot (T + 273.15)^2 + (b_i^{c_1} + c_2) \cdot \left( c_3 \cdot (T + 273.15) - c_4 \cdot \ln \left( 1 - \frac{T + 273.15}{c_5} \right) \right), \quad (5.14)$$

which considers limited effect of pressure. The parameters of all salts,  $c_{01} - c_{04}$  and  $c_1 - c_5$ , are summarized in Table 5. 4. The fitted data ranges for the apparent molar enthalpies of  $\text{CaCl}_2$ ,  $\text{KCl}$ , and  $\text{MgCl}_2$  are similar to those used in fitting the apparent molar heat capacities. Aqueous  $\text{NaCl}$  enthalpy is directly derived from Driesner model.

|          | $\text{CaCl}_2$ | $\text{KCl}$ | $\text{MgCl}_2$ |
|----------|-----------------|--------------|-----------------|
| $c_{01}$ | 9.0590E+4       | 0            | 0               |
| $c_{02}$ | 0               | 3.9580E+3    | -4.4950E+4      |
| $c_{03}$ | 0               | -1.5990E+2   | 5.9170E+2       |
| $c_{04}$ | 0               | 2.1150E-1    | -7.9050E-1      |
| $c_1$    | 5.1170E-1       | 4.7190E-1    | 5.0200E-1       |
| $c_2$    | -2.2890E+0      | -2.7380E+0   | -1.5620E+0      |
| $c_3$    | 1.3030E+0       | -5.2720E+1   | 9.5460E+1       |
| $c_4$    | 1.9550E+4       | 2.1460E+4    | 9.1770E+3       |
| $c_5$    | 6.2030E+2       | 6.2710E+2    | 6.0230E+2       |

Table 5. 4: Apparent molar enthalpy parameters for Eq. (5. 14).

eq. (5. 12) also comprises the solution enthalpy  $h_{\text{sol},j}^\phi$  which is the enthalpy change associated with the dissolution of NCG in water at constant pressure resulting in infinite dilution. It can be computed by using the first derivative of the standard chemical potential in eq. (5. 1) with respect to temperature,

$$h_{\text{sol},j}^{\phi} = \frac{\partial}{\partial T} (\mu_j^{1(0)} / RT) . \quad (5.15)$$

#### 5.4.2 Density

The effective density of a two-phase mixture can be computed using void fraction or the ratio,  $\varepsilon$ , between the non-aqueous phase volume and the total volume,

$$\rho = (1 - \varepsilon) \cdot \rho^{AQ} + \varepsilon \cdot \rho^{NA} , \quad (5.16)$$

with  $\rho^{AQ}$  and  $\rho^{NA}$  denoting the density of the aqueous and non-aqueous phase, respectively. The density of the gas mixture in the non-aqueous phase  $\rho^{NA}$  is calculated using the PR cubic equation.

Driesner [2007] formalism is applied to compute NaCl apparent molar volume in a wide range of  $p - T - X$ . For other binary aqueous chlorides, Rowland and May [2013], Mao and Duan [2006] are used for pressures up to 100 MPa for temperatures ranging from 0 to 300 °C. The mixing rule that converts the apparent molar volume,  $V_{\phi}$ , into aqueous phase density,  $\rho^{AQ}$ , is provided by Laliberte' and Cooper [2007], as was recommended by Francke et al. [2013]. It is equivalent to the averaged apparent molar volume weighted by the mole number, called Young's rule [Young and Smith, 1954], which is suggested by Zezin et al. [2014]. In these methods, the salts' apparent molar volumes  $V_{\phi}$  for the total molality of the solute are combined to yield the density of the solution, which can be written as

$$\rho^{AQ} = \left( \frac{w_{\text{H}_2\text{O}}^{AQ}}{\rho_{\text{H}_2\text{O}}} + \sum_{N_i} \frac{w_i^{AQ}}{M_i} \cdot V_i^{\phi} + \sum_{N_j} \frac{w_j^{AQ}}{M_j} \cdot V_j^{\phi} \right)^{-1} , \quad (5.17)$$

where  $w$  is the mass fraction,  $i$  as the index for salt components, and  $j$  for NCG components. gEOSkit calculated density is in good agreement with the experimental data, as the predicted values differ by less than 1% from the measured ones. The gEOSkit and PHREEQC 3.2 results are in good agreement.

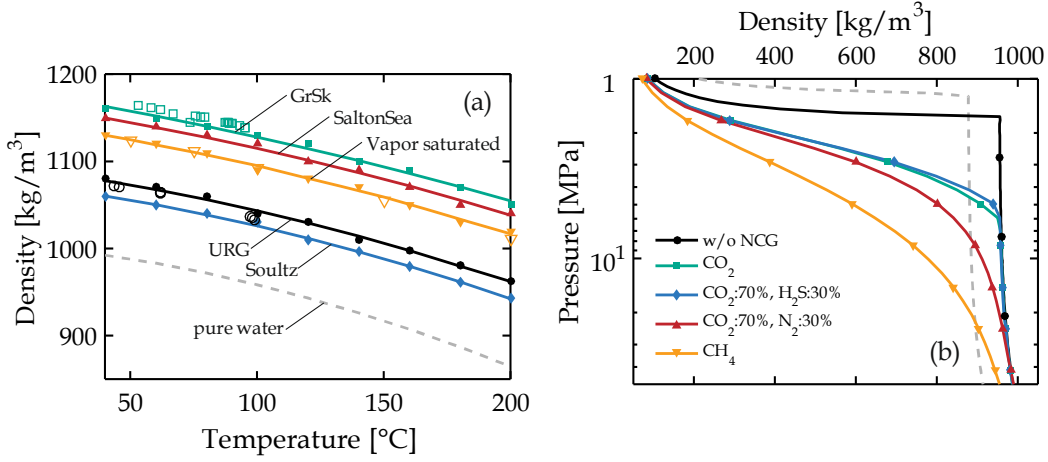


Figure 5. 9: Aqueous phase density of geofluids listed in Table 5. 3 and vapor-saturated NaCl (3 mol/kgw) solution: (a) Comparison of gEOSkit (solid lines), PHREEQC 3.2 (filled dots), and measurement data (unfilled circles URG; unfilled squares GrSk; unfilled triangles Vapor Sat.) and (b) effective two-phase density of URG brine with different gas compositions (1% wt. NCG) (solid lines) and pure water (dashed lines) at an enthalpy of 800 kJ/kg.

The influence of dissolved gases, if present, on brine density differs by roughly 2.5% at a mole fraction of 0.05. The correlation for the apparent volume of NCGs was based on experimental data from Hnedkovský et al. [1996a] (see Appendix B). The apparent molar volume is fitted by superposition

$$V_j^\phi = g_1 \cdot f_1 + g_2 \cdot (1 - f_1) + f_2 \quad (5. 18)$$

of two polynomial functions:  $g_1(T)$ ,  $g_2(T)$  (cm<sup>3</sup>/mol).

### 5.4.3 Viscosity

The effective dynamic viscosity of a two-phase mixture is derived using the arithmetic mean of the Maxwell-Eucken 1 and Maxwell-Eucken 2 models [Awad and Muzychka, 2008]. Estimation of the dynamic viscosity of the non-aqueous phase  $\eta^{NA}$  is based on the GERG-2008 transport property implemented in CoolProp. The dynamic viscosity of the aqueous phase  $\eta^{AQ}$  is computed by combining viscosities of binary solutions using a logarithmic mixing rule weighted by the molar fraction, as recommended by Francke et al. [2013],

$$\eta^{AQ} = \eta_{\text{H}_2\text{O}}^{AQ} \cdot \prod_{N_i} \eta_{r,i}^{\left(\frac{b_i}{\sum b_i}\right)}, \quad (5. 19)$$

where the viscosity of the binary solutions is expressed by relative viscosity  $\eta_{r,i}$  the viscosity ratio of solution and pure water. It was taken from correlations available in literature for NaCl, KCl [Mao and Duan, 2009] ( $p = 0.1 - 100$  MPa,  $T = 0 - 350$  °C,  $b_{\text{NaCl}} = 0 - 6$  mol/kgw,  $b_{\text{KCl}} = 0 - 4.5$  mol/kgw), CaCl<sub>2</sub>, and MgCl<sub>2</sub>. The CaCl<sub>2</sub> correlation from Zhang et al. [1997] is based on molarity which is density-dependent, which was converted into a form following Mao and Duan [2009], eq. (B.8) (fitted data range:  $p = 0.1 - 30$  MPa,  $T = 25 - 300$  °C,  $b_{\text{CaCl}_2} = 0.2 - 2.2$  mol/kgw). Additionally, a correlation for MgCl<sub>2</sub> was derived by fitting experimental data from Azizov [1999] to the eq. (B.8) (fitted data range:  $p = 10 - 30$  MPa,  $T = 25 - 300$  °C,  $b_{\text{MgCl}_2} = 0.2 - 0.9$  mol/kgw). The difference between predicted and measured values is within 2%.

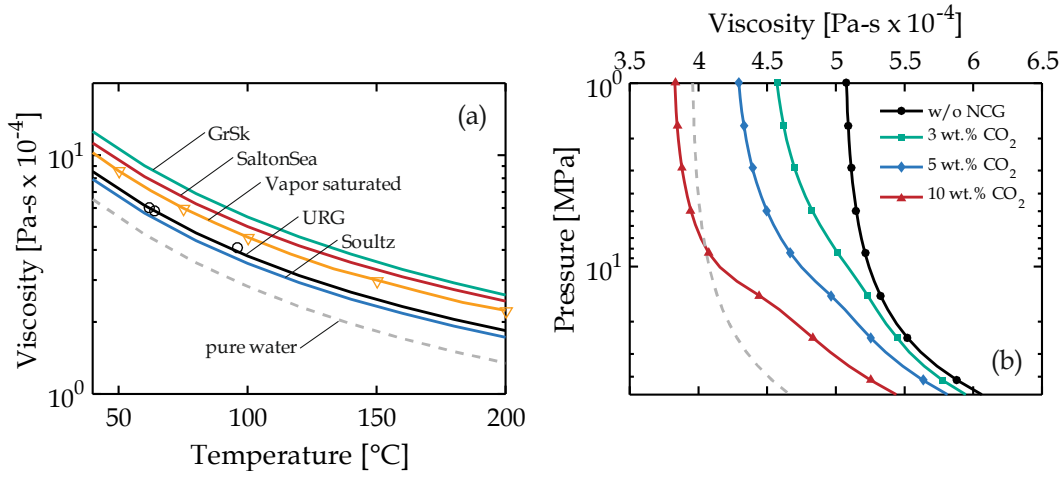


Figure 5.10: Aqueous phase viscosity of geofluids listed in Table 5.3 and vapor-saturated NaCl (3 mol/kgw) solution: (a) Comparison between gEOSkit (solid lines) and measurement data (unfilled circles URG; unfilled triangles Vapor Sat.) and (b) effective two-phase viscosity of URG brine with different gas compositions (solid lines) and pure water (dashed lines) at an enthalpy of 800 kJ/kg.

## 5.5 CONCLUSIONS

In geothermal fluid processes: reservoir management, wellbore and heat exchanger operation and design, accurate estimation of two-phase multicomponent fluid properties is of great importance. We developed gEOSkit, a pressure-enthalpy based equation of state (EOS) for geothermal fluids by merging H<sub>2</sub>O-salts (NaCl, KCl, MgCl<sub>2</sub>, CaCl<sub>2</sub>, NaHCO<sub>3</sub>) binary, and brine-NCG (CO<sub>2</sub>, N<sub>2</sub>, CH<sub>4</sub>, H<sub>2</sub>S) systems. By using an object-oriented scheme, we presented an easily extendable or adaptable EOS. The solver validity is directly linked to the validity range of classes of the binary systems. For instance, the solver is valid in the pressure,

temperature, and total salt molality ranges of up to 60 MPa, 227 °C, 4.5 mol/kgw, respectively, for the CO<sub>2</sub>-N<sub>2</sub>-CH<sub>4</sub>-H<sub>2</sub>S-brine system; 100 MPa, 227 °C, 4.5 mol/kgw for the CO<sub>2</sub>-H<sub>2</sub>S-brine system; and 150 MPa, 300 °C, 4.5 mol/kgw for the CO<sub>2</sub>-CH<sub>4</sub>-brine system. These validity ranges are adequate for the simulation of mid-enthalpy geothermal reservoirs, wellbores, and heat exchangers. For a basic mixture of the system CO<sub>2</sub>-H<sub>2</sub>O-NaCl, the solver is valid up to 150 MPa, 300 °C, 8 mol/kgw (halite). In the current version, the temperature is limited to 300 °C due to restriction on apparent molar properties correlations.

The gEOSkit was validated using a complete dataset of the VLE and thermophysical properties of geothermal fluids in the temperature range of 32 - 177 °C under total pressures of 0.5 - 50 MPa. For the Vapor Liquid Equilibrium (VLE) between the aqueous and the non-aqueous phases, the Absolute Average Relative Deviation (AARD) of the calculated and the measured solubility ranges between about 3% and 6%. This accuracy was reached by an improvement relating to the short-range interaction between neutral, dissolved gas molecules. In fact, the solver is more accurate than results of any other available code, e.g. PHREEQC 3.2 [Appelo *et al.*, 2014] and EOS7Cm [Lei *et al.*, 2016].

The evaluation of thermophysical properties of water, salts, NCGs, and the mixing rules were based on a comprehensive literature review for selection of the most widely accepted procedures and methods. The AARD of the resulting prediction of thermophysical properties of the aqueous phase was 1 - 2%. These comparisons indicated that the calculated results are in good quantitative and qualitative agreement with experimental data, which confirms the validity of gEOSkit solver.

The algorithm also needs to be enhanced to allow more efficient computation. To improve calculation speed, the state properties can be preevaluated for the given fluid composition from gEOSkit on a  $p - h$  grid and then be interpolated as necessary during a simulation. In a  $p - T$  based simulation (without boiling water), a stand-alone fugacity-activity (region 1) solver can be used directly to evaluate the properties, avoiding temperature root-finding as using enthalpy. The solver is useful for accurately simulating thermohydraulic problems of geothermal fluids in practice. Integration of speciation and chemical equilibrium codes also is feasible. This is particularly important for modeling the interactions between minerals and fluid phases bearing gas mixtures, which is the major objective of reactive thermohydraulic simulations.

# 6

## THERMOHYDRO-CHEMICAL MODELING OF GEOTHERMAL WELL FLOW WITH TWO-PHASE MULTICOMPONENT FLUIDS

in preparation as

Nusiaputra, Y. Y., Dimier, A., Nitschke, F., Kohl, T., *Thermohydro-Chemical Modeling of Geothermal Well Flow with Two-Phase Multicomponent Fluids*

### ABSTRACT

In geothermal wellbore flow with high salt and non-condensable gas content applications, pressure, temperature, non-aqueous phase fraction, pH, and mineral saturation indices (scaling) will interplay. A simulation model that allows quantitative predictions under different scenarios will be an interesting tool. In this paper, WellboreKit, a sequential coupling between transport, geochemical reaction, (de-)pressurization, and fluid-rock heat transfer of two-phase multi-component geothermal fluid is performed. The thermodynamical and transport properties for an H<sub>2</sub>O - salt (Na-Ca-K-Mg-Cl-HCO<sub>3</sub>) - gas (CO<sub>2</sub>-N<sub>2</sub>-CH<sub>4</sub>-H<sub>2</sub>S) mixture are calculated using the fugacity-activity, three-region equation of state solver. The fluid flow is described by a heterogeneous model, which is solved by means the Elmer FEM. An operator splitting algorithm is applied to include PHREEQC for calculating chemical reaction. Major scales deposition in the geothermal industry, such as barite, calcite, and silica were investigated. Numerical results are shown, indicating the impact of mixture composition, constitutive correlations, operating parameters, and the feasibility of the approach. The total scale thickness formed after ten days of production is quantified, indicating that poor operating parameters lead a problem to the initial stage of wellbore life.

## 6.1 INTRODUCTION

An important factor in geothermal energy is the transport between the bottom hole and the wellhead or vice-versa at the wellbore. The transport in wellbores will take place at high pressures down to low pressure or vice-versa, where the geothermal fluids in aqueous (liquid-like) and non-aqueous (gas-like, supercritical) states. Due to ascending flow, the fluid is depressurized. The pressure decrease will arise a phase change in the geothermal fluid, resulting in a strong cooling of the geothermal fluid. If the temperature becomes low enough, the mineral may become precipitated, causing a clog and much damage, i.e. Nitschke, F. et al.[2017]. Therefore, for a proper wellbore design, it is necessary to be able to estimate the fluid state changes during production or injection.

A further illustration to consider is complexities that may occur along the deep geothermal wellbore due to the geothermal fluid-mixture composition. The recent development of EGS at greater depth tends to have non-negligible fluid salinity and non-condensable gas (NCG). For instance, the solubility of gasses in water decreases with decreasing pressure and increasing temperature. Hence, if NCG is present, an aqueous-NCG phase may form at some points in the wellbore. Dissolved acid gasses, i.e.  $\text{CO}_2$  and  $\text{H}_2\text{S}$  is unwanted, since it may cause corrosion. A multi-phase multi-component flow model, including heat transfer to the surrounding formations and geochemical reaction, is needed to predict the occurrence of such phenomena.

Such estimations involve comprehensive thermodynamical, fluid dynamical and geochemical considerations. First, information is needed about the thermodynamic and transport properties, such as phase equilibrium, density, viscosity, surface tension, etc. As a real geothermal fluid stream involves several major components, e.g. salts and gasses, reliable thermodynamical models for multi-component geothermal fluid mixtures are required. Next, it is required to have a transient two-phase flow model including for several components. Finally, an accurate, efficient, and robust numerical method is required.

This paper covers two main points: First, a numerical framework is presented for handling the modeling mentioned above issues in a robust and unique way. The thermodynamical and transport properties are modeled using the fugacity-activity, gEOSkit, equation of state. The wellbore flow is described by a heterogeneous two-phase multicomponent model.

Herein, each chemical component is tracked explicitly. The heterogeneous model is a system of coupled nonlinear hyperbolic differential equations. The mass, energy, pressure, and chemical species inherent in the model are resolved numerically by using the operator-splitting method.

Second, example computations are performed which indicate that the proposed model, embedded with constitutive relations, has the prospective of describing the (de-)pressurization of multicomponent geothermal fluid mixtures in wellbores. Further, it is indicated that geothermal fluid-mixture composition can significantly affect the behavior during (de-)pressurization.

With the goal to handle the two points above, an Elmer-PHREEQC coupling platform is used to develop the wellbore model. Elmer [CSC, 2016] is a computer program for the resolution of multi-physical problems. It is used to solve fluid dynamics and heat transfer equations. Then, Elmer normally works for the thermal-hydraulic simulation, but as chemical reactions need to be calculated, the PHREEQC results must be integrated. PHREEQC [Parkhurst, 1999] is a computer program for speciation, batch-reaction, one-dimensional transport and inverse geochemical calculations. PHREEQC solves chemical equilibrium and transport equations. COMSOL multiphysics and PHREEQC (geochemistry) coupling has been early performed by through iCP [Nardi *et al.*, 2014]. Nonetheless, COMSOL is a proprietary software which delivers lower level of abstraction. Elmer is an open-source solver that can handle thermal-hydraulic behaviors and transport of the species. It allows wider modification by its high level of abstraction.

The rest of the paper is structured as following. Section 2 describes an outline of the applied fluid dynamical and thermodynamical models, while Section 3 summarizes the numerical method. Section 4 presents example calculations establishing the feasibility of the devised approach, and Section 5 concludes the work.

## 6.2 THE TWO-PHASE ONE-DIMENSIONAL WELLBORE PROBLEM

In the derivation of models here describing two-phase flow in wellbores, the governing equations are written for one fluid. A one-dimensional one-fluid model can then be found by averaging the governing equations across a pipe cross-section, and can even be used to simulate condensation induced water hammer (CIWH), see Milivojevic *et al.* [2014]. For several flow patterns, particularly when the non-aqueous (NA) and aqueous (AQ) motion is strongly coupled, it is possible to correlate the velocity ratio between the non-aqueous and aqueous phases, the slip, as a function of the flow variables (e.g. Zuber and Findlay [1965], Hasan-

Kabir, [2010]). This a priori knowledge of the flow can be employed to reduce the number of transport equations to be solved, and the result is called the heterogeneous two-phase model. A heterogeneous model similar to the one described in the following was also described by Schmidt et al. [2010].

The scope of this work is limited to practical situations that fit the following simplifying assumptions: a slow-transient is performed; axial conduction, radiative heat transfer, and ambient temperature effects are negligibly small. The general modeling for the evolution of the streams is based on one-dimensional mass, momentum and energy balances for each string. Then, the problem is governed by eqs. (6. 1) - (6. 5) for one string, which represents momentum and energy balances for fluid and rock. For mass balance,

$$A \frac{\partial \rho_H}{\partial t} + \sin\theta \frac{\partial \dot{m}}{\partial z} = 0 . \quad (6. 1)$$

with  $z$  is axial distance based on true vertical depth (TVD). The derivation of homogeneous density  $\rho_H$  (see Table 6. 1) about time is expanded by using chain rule of partial derivatives, as explained by Thorade and Saadat [2013]. Time step in geothermal wellbore operation typically has a larger value ( $t > 1$  min.). When reaction occurs, the reactive transport equation is applied

$$\begin{aligned} & \frac{\partial}{\partial t} (\rho^{AQ} w_{H_2O} C_a) + U_m \frac{\partial}{\partial t} (\rho_s C_m) \\ & = U_a \left( -\frac{\partial}{\partial z} (\rho^{AQ} w_{H_2O} v_a C_a) + D_a \frac{\partial^2}{\partial z^2} (\rho^{AQ} w_{H_2O} C_a) + S \right) , \end{aligned} \quad (6. 2)$$

where  $w_{H_2O}$ ,  $U$ ,  $C$ ,  $D$ ,  $S$  are water mass fraction, component matrices (e.g. ), concentration (mol/kgw), diffusivity, and species source term, correspondingly. Subscript  $a$  and  $m$  denote aqueous and mineral. The simulation assumes the following thermal transport mechanisms, namely transient change of heat content, advection and heat transfer which are partial equilibrium. These may be written as follows

$$\begin{aligned} & A \frac{\partial}{\partial t} (\varepsilon \rho^{NA} h^{NA} + (1 - \varepsilon) \rho^{AQ} h^{AQ}) + \frac{(m \cdot c_p)_{tubular} \cdot F}{A} \frac{\partial h}{\partial t} + \\ & \sin\theta \frac{\partial}{\partial z} \left[ \dot{m} \left( h + \frac{\dot{m}^2}{2A^2 \rho_E^2} \right) \right] = A \frac{\partial p}{\partial t} + \pi d_h \dot{q}_w + \frac{\dot{m}}{\rho_H} \Delta p_f + \dot{m} g \sin\theta , \end{aligned} \quad (6. 3)$$

where  $\varepsilon$ ,  $(m \cdot c_p)_{tubular}$ ,  $F$  are void fraction, mass-averaged tubular mass- $c_p$  and enthalpy fraction (0 - 1), respectively. The enthalpy fraction is employed to model the heat storage effect of tubular structures like tubing, annulus, casing and cement. The mixed enthalpy is defined as

$$h = xh^{NA} + (1 - x)h^{AQ} , \quad (6.4)$$

and in the formation matrix, diffusion with the transient term is using H-K dimensionless time [Hasan and Kabir, 2010]. A mechanistic flow pattern to correlate the relative velocity between the phases, the slip velocity, as a function of the flow variables, was also adapted from H-K model. Due to complex rules of H-K void fraction model, it is not trivial to derive the void fraction with regard to time. Therefore, to remedy this issue, the transient void fraction term was approached by using the homogenous form for annular flow and improved Dix correlation from Woldesemayat and Ghajar [2007] for non-annular flow (see Appendix D).

Momentum balance is written as Navier-Stokes equation for 1D problem which could be closed with empirical equations for the shear stress, i.e. frictional pressure drop as follows.

$$\frac{1}{A} \frac{\partial \dot{m}}{\partial t} + \sin\theta \frac{\partial p}{\partial z} = -\rho_H g \sin\theta - \Delta p_f - \frac{\sin\theta}{A^2} \frac{\partial}{\partial z} \left( \frac{\dot{m}^2}{\rho_I} \right) + \Delta p_P \quad (6.5)$$

The time derivative of the momentum of the control volume is assumed to be zero which is reasonable as long as fast dynamic processes (e.g., sound propagation) are not considered (see Casella and Leva [2006]). The coupling between enthalpy and mainly the density make the system non-linear and thus the iterative solution is required.

| Parameter           | Definition   |
|---------------------|--|
| Homogeneous density | $\rho_H = \varepsilon \rho^{NA} + (1 - \varepsilon) \rho^{AQ} \quad (6.6)$   |
| Impulse density     | $\frac{1}{\rho_I} = \frac{x^2}{\rho^{NA} \varepsilon} + \frac{(1-x)^2}{\rho^{AQ} (1-\varepsilon)} \quad (6.7)$               |
| Energy density      | $\frac{1}{\rho_E^2} = \frac{x^3}{(\rho^{NA})^2 \varepsilon^2} + \frac{(1-x)^3}{(\rho^{AQ})^2 (1-\varepsilon)^2} \quad (6.8)$ |

Table 6. 1: Density definitions used in the modeling.

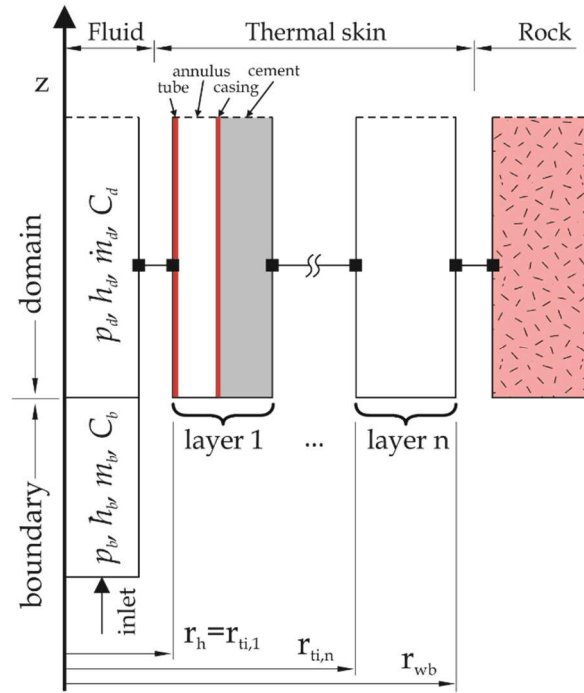


Figure 6. 2: Schematic of the one-dimensional wellbore and formation system considered.

By using this schematic approach, we can model complex geometry of the wellbore that significantly changes about depth. Likewise, stratigraphy variation over the depth.

The gas-liquid mixture properties are modeled using mechanistic two-phase flow model from Hasan-Kabir [2010], which also include slip between gas-liquid velocities which determines the flow pattern: bubbly, slug, churn or annular flow. The constitutive equations of hydraulic, thermal, and chemical to close all the equation systems above are described below in detail.

### 6.2.1 Heat transfer models

Energy or thermal exchange is driven by the temperature difference between fluid and rock/formation:

$$\dot{q}_w = \left( \frac{T_D \cdot r_{wb}}{\lambda_e} + \frac{1}{U_{wb}} \right)^{-1} \frac{r_{wb}}{r_h} (T_e - T_{wf}) \Big|_{r=r_h}, \quad (6.9)$$

where  $T_D$  is dimensionless time function to represent the transient heat transfer to the formation.  $U_{wb}$  is the overall heat transfer coefficient between a rock at wellbore skin and geothermal fluid stream. In a steady-state analysis, it can be computed on the base of thermal resistances [Incropera and DeWitt, 1996], which also can be used for transient analysis [Richter, 2008]. eq. (6. 10) applies for the geometry shown in Figure 6. 2.

$$\frac{1}{U_{wb}} = \frac{1}{\alpha_f} \frac{r_{wb}}{r_h} + r_{wb} \sum_{layer=1}^n \left[ \frac{\ln(r_{to,n}/r_{ti,n})}{\lambda_{t,n}} + \frac{1}{r_{to,n} h_a} + \frac{\ln(r_{co,n}/r_{ci,n})}{\lambda_{c,n}} + \frac{\ln(r_{ti,n+1}/r_{co,n})}{\lambda_{cem,n}} \right]. \quad (6. 10)$$

with  $U$  is overall heat transfer coefficient,  $r$  is radius,  $\alpha$  is convection heat transfer coefficient, and  $\lambda$  is thermal conductivity. Subscripts  $t$ ,  $c$ ,  $cem$  denote tube, casing, and cement. While  $i$  and  $o$  represent the inner and outer part.  $n$  is thermal layer (e.g. fluid stream, tubing, annulus, casing, cement) index number, see Figure 6. 2.

Single phase, supercritical,  $\alpha^{AQ}$  is computed using correlation from traditional Sieder-Tate [1936] correlation as

$$\frac{\alpha^{AQ} \cdot d_h}{k} = \begin{cases} 1.86 \left( Re Pr \frac{d_h}{L} \right)^{0.33}, & Re \leq 2300 \\ 0.027 Re^{0.8} Pr^{0.33}, & Re > 2300 \end{cases}. \quad (6. 11)$$

The reinforcement of the two-phase convective heat transfer coefficient is due to the increase of gas phase, which is defined as  $\alpha^{\phi^2}/\alpha^{AQ}$ . The non-boiling two-phase correlation was used as recommended by Ghajar et al. [2010] for oil-gas applications and regardless of flow regime and Nusselt number. It can be written as

$$\frac{\alpha^{\phi^2}}{\alpha^{AQ}} = \begin{cases} F_p \left[ 1 + 0.55 \left( \frac{x}{1-x} \right)^{0.1} \left( \frac{1-F_p}{F_p} \right)^{0.4} \times \left( \frac{Pr^{NA}}{Pr^{AQ}} \right)^{0.25} \left( \frac{\mu^{NA}}{\mu^{AQ}} \right)^{0.25} (I^*)^{0.25} \right], & \text{non-boiling} \\ (1-\varepsilon)^{-0.9}, & \text{bubbly and slug} \\ \left( 1 + \frac{x}{1-x} \right)^{0.33}, & \text{dispersed} \end{cases}. \quad (6. 12)$$

$F_p$  and  $I^*$  denote flow pattern and inclination factors, respectively. For boiling two-phase, the relationship is chosen by the flow regime, i.e. the Rezkallah and Sims equation for bubble and slug flow, and the Knott et al. equation for dispersed flow, and the Ravipudi and Godbold equation for annular flow, as suggested by Zhou-Zheng [2015]. The value increases rapidly in bubble flow and intermission flow, and slowly in annular flow.

The natural convection in the annuli caused by the density difference between the bulk fluid and the fluid near tube surfaces, which, in turn, enhances the heat transfer is modeled by using correlation from Dropkin-Sommerscales [1965] [Hasan and Kabir, 2010], as

$$\alpha_{ac} = \frac{0.049Gr^{0.333}Pr^{0.407}\lambda_a}{r_{to}\ln(r_{ci}/r_{to})}, \quad (6.13)$$

where with  $\lambda_a$  is thermal conductivity of the annuli fluid,  $r_{ia}$  and  $r_{oa}$  are the inner and outer diameter of the annuli, and the Grashof number is defined as

$$Gr = (r_{oa} - r_{ia})^3 g \rho_a^2 \beta (T_{ia} - T_{oa}) / \mu_a^2, \quad (6.14)$$

with  $\mu_a$  is the annuli viscosity and isobaric thermal expansion coefficient is  $\beta = 1/T$  for ideal gas; for liquid, it is computed from the density. This heat transfer relationship reflects the extent of motion of the annular fluid caused by natural convection. Depending on size and temperature in the annulus, radiation can significantly affect the heat transfer. The radiative heat transfer inside annulus can be expressed as Stefan-Boltzmann Law

$$\alpha_{ar} = \frac{\sigma(T_{to}^2 + T_{ci}^2)(T_{to} + T_{ci})}{\frac{1}{E_{to}} + \frac{r_{to}}{r_{ci}} \left( \frac{1}{E_{ci}} - 1 \right)}, \quad (6.15)$$

where  $E, T$  are emissivity and absolute temperature [K], in turn. Thus, the total equivalent heat transfer coefficient of the annulus can be calculated as  $\alpha_a = \alpha_{ac} + \alpha_{ar}$ .

### 6.2.3 Pressure drop models

Hydrostatic pressure holds the main role of the hydraulic system with density variation as the variable. This part is already included as a term in the momentum balance equation above related to wellbore deviation angle.

Flow inside tubes is imposed by the pressure drop in the same direction of the mass flow rate due to shear stress with the tube surface. The shear stress is modeled on the base of a two-phase multiplier. Of the following is the application of equations for the frictional pressure drop of two-phase tube flow. The frictional term is a part of momentum balance equation

$$\Delta p_f = f_H \frac{\dot{m}^2}{2A^2 \rho_H d_h}, \quad (6.16)$$

where  $f$  is Darcy friction factor and  $\rho_H$  is mixture average density as a function of fluid properties and flow conditions.

Investigations of the hydraulic behavior in pipes from the early century. Schlichting [2000] described the boundary layer theory to compute frictional pressure drop. In this study, an empirical correlation from Fang [2011] is taken to take into account scaling and corrosion effect to the friction factor.

$$f_H = 1.613 \left[ \ln \left( 0.234(\epsilon/d_h)^{1.1007} - \frac{60.525}{Re_H^{1.1105}} + \frac{56.291}{Re_H^{1.0712}} \right) \right]^{-2}, \quad (6.17)$$

with the Reynolds number is defined as

$$Re_H = \frac{\dot{m} d_h}{A \mu_H}. \quad (6.18)$$

Productivity index is modeled by the correlation by McGuinness [2014] for two-phase reservoir conditions.

### 6.2.4 Geochemical reaction models

For aqueous phase, the mass balance kinetics of  $n$  species per volume of medium may be defined as [Yeh-Tripathi, 1989]

$$w_{H_2O} \frac{\partial C_a}{\partial t} = L(C) + w_{H_2O} \cdot r_{kin} , \quad (6.19)$$

$w_{H_2O}$  is the water mass fraction,  $t$  is the time,  $L$  is advection-diffusion operator, see eq. (6. 2);  $C$  is the total dissolved concentration.

It is beyond the scope of this paper to describe all the equations that PHREEQC uses to represent chemical reactions. The complete formulation can be found in the PHREEQC manual [Parkhurst and Appelo, 1999]. In general, a geochemical PHREEQC batch problem used in this study can be formulated as an ordinary differential equations (ODE) of the following form

$$U_m \frac{\partial}{\partial t} (\rho_s C_m) = w_{H_2O} \cdot r_{kin} . \quad (6.20)$$

The system describes the solid mineral dissolve/precipitated about time due to reaction rate. The reaction rate  $r_{kin}$  is assumed to be  $\Delta C_a$  (equilibrium) as a reference in this study to simplify the model. However, some minerals often do not react to equilibrium during the predefined time. We recommend to model the reaction kinetic when the situation demands, as investigated in Chapter 6.4.3.

To model geothermal fluid at high temperature and pressure, “gebo” database was attached. It includes Pitzer additional solution master species, which are Fe, Fe(+2), Fe(+3), S(-2), N, N(+5), N(+3), N(0), N(-3), C(-4), Si, Zn, Pb, and Al [Bozau, 2013]. According to this solution master species, associated solution species, solid phases, and gasses, as well as temperature dependences of the appropriate mass action law constants are implemented. Pitzer parameters for the calculation of Ba, Na, Cl, SO<sub>4</sub>(-2) activity coefficients in aqueous solutions of high ionic strength are extended based on Appelo et al. [2015]. As opposed to the conventional “pitzer.dat” database, the extended version allows computing several additional hydrogeochemical equilibrium reactions that are necessary.

### 6.2.5 Thermodynamics

Liquid-like (aqueous), that may include dissolved noncondensable gasses in addition to water and dissolved solids and gas-like (non-aqueous), basically a multicomponent mixture that can be in gas, supercritical or condensed conditions phases partitioning. We implemented our in-house equation of state for two-phase multicomponent geothermal fluids, gEOSkit. The EOS does not include solid/minerals as a separate phase. PHREEQC handles this part.

## 6.3 NUMERICAL APPROACH

## 6.3.1 Technical description of Elmer-PHREEQC coupling

For a specified time step, Elmer calculates the progression of the system during this time step and gives the result. PHREEQC calculates the chemical reaction at this step, based on the initial chemical state and Elmer's result, and writes the result. Elmer now knows the new chemical state of each cell and can re-calculate physical changes, such as the flow and dispersion during the time step. Again, PHREEQC will calculate the chemical equilibrium at this point, and this will continue until the end of the simulation. The smaller the time step, the greater the precision.

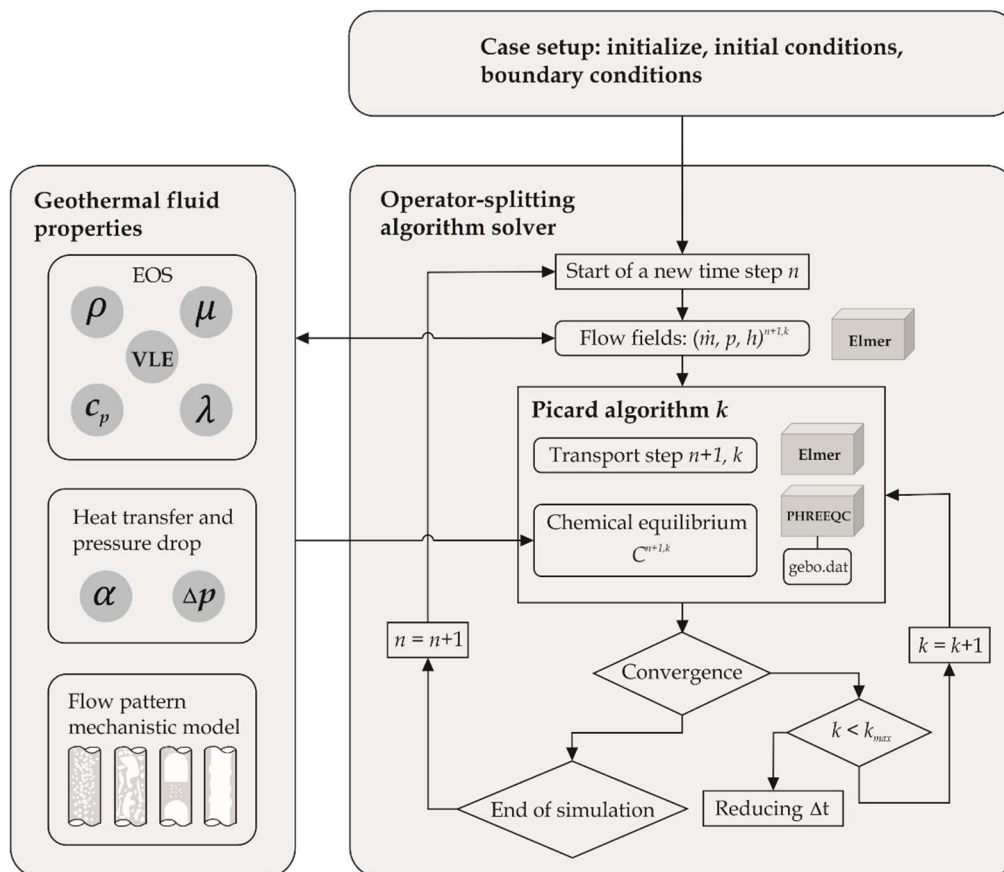


Figure 6. 3: Calculation procedure of WellboreKit.

Once the boundary conditions have been set, each solver step for a specified time step, consists of the following major sub-steps:

1. For definite salt and gas concentrations at each cell, chemical equilibrium is solved in PHREEQC to obtain the saturation index of minerals according to eqs. (6. 19) - (6. 20) to , which is then used to determine mineral scaling and to calculate the dissolved salt concentration in the aqueous phase.
2. Thermodynamic properties, i.e., aqueous and non-aqueous enthalpy  $h^{AQ}, h^{NA}$ ; density  $\rho^{AQ}, \rho^{NA}$ ; viscosity  $\mu^{AQ}, \mu^{NA}$ ; thermal conductivity  $\lambda^{AQ}, \lambda^{NA}$ ; gas fugacity  $\phi_j$ , and quality  $x$ , are determined using the equation of state described in section 6.4 as a function of the pressure  $p(z)$ , enthalpy  $h(z)$ , and the salt  $b_i(z)$  and gas molality  $b_j(z)$ , and gas mole fraction  $y_j(z)$ .
3. The void fraction with constitutive relations, i.e. heat transfer coefficient  $a$ , wall shear  $(dp/dz)_f$ , and hydrostatic pressure gradient  $(dp/dz)_h$  are determined by eqs. (6. 6) to (6. 18), based on the flow pattern map, mechanistic flow H-K model, which is the used to calculate the effective two-phase thermodynamic properties. Pressure drop is then evaluated step wisely along the wellbore path using eq. (6. 5).
4. Geothermal fluid heat and mass transfer, and species transport are solved in Elmer using eqs. (6. 1) to (6. 4) with transient terms eqs. (D.1) to (D.12).

From Elmer calculation, we retrieve new pressure, temperature, species concentration, and gas fugacity fields, which are sent to PHREEQC for the equilibrium at the next time step, see Figure 6. 3.

### 6.3.2 Model validation

To test the validity of the fluid-casing-cement-formation heat transfer, a validation case has been carried out using WellboreKit, and the results have been compared with those obtained using analytical solutions from Ramey [1962] and Wu-Pruess [1990]. They are here used to solve bottom-hole temperature (BHT) during cold injection of pure water. A boundary water is injected at the inlet of the domain, progressively displacing the initial water. Likewise, for the advection-diffusion with reaction, “computational” tracer test has been done with a benchmark to the analytical solution of Lapidus and Amundson [1952]. The simulated results are in good agreement with the analytical solutions confirming the reliability of the mass-energy and advection-diffusion-reaction solvers. More details of the problem setup and are included in Table 6. 2 and 6.3.

| parameters          | values                 | parameters       | values     |
|---------------------|------------------------|------------------|------------|
| $\nabla T_g$        | 0.0385 m               | $\lambda_f$      | 0.63 W/m-K |
| $T_{inj}$ (ambient) | 15 °C                  | $\mu_f$          | 8E-4 Pa-s  |
| $T_{res}$           | 250 °C                 | d                | 0.21 m     |
| $\dot{m}$           | 30 kg/s                | tube thickness   | 0.017 m    |
| $\rho_f$            | 1008 kg/m <sup>3</sup> | cement thickness | 0.033 m    |
| $c_{p,f}$           | 4106 J/kg-K            | depth            | 6096 m     |

Table 6. 2: Simulation parameters for validation of fluid-casing-formation heat transfer.

Finally, the mechanistic two-phase model is validated. A comparison between WellboreKit results and reference is presented. The aim of this comparison is not primarily the validation of the physical models but rather the elimination of input errors and the avoidance of incorrect implementation of the correlations. The numerical solution is validated with the production scenario of well KE1-22 [Garg, 2004]. The comparison shows very good agreement between the present solution and the measured pressure data. Throughout this investigation, the accuracy of the results was maintained at least to the third digit. This accuracy is believed to be sufficient for most engineering applications.

| bottom of<br>(TVD) [m] | layer | lambda<br>[W/m-K] | $c_p$<br>[J/kg-K] | rho<br>[kg/m <sup>3</sup> ] |
|------------------------|-------|-------------------|-------------------|-----------------------------|
| -1981                  | L1    | 2.5               | 920               | 2350                        |
| -2438                  | L2    | 1.43              | 1100              | 2520                        |
| -6096                  | L3    | 4                 | 790               | 2630                        |

Table 6. 3: Lithology of case thermal parameters, layer definition adapted from Eppelbaum [2014], Rybach [1982] and Clauser-Huenges [1995]

## 6.4 GEOTHERMAL FLUID PRODUCTION/INJECTION EXAMPLE

Sandia, working with ThermaSource Inc, a geothermal drilling contractor, developed tasks, time-, and cost descriptions of the construction process for a geothermal well [Polsky et al., 2008; Yost et al., 2015]. The well is designed to generate 5 MWe from 80 kg/s of 200 °C wellhead fluid produced from a depth of 20,000 ft. (note that we are using the foot, inches units since this was used in the Sandia Case). To reach the designed depth of 20,000 ft, Sandia's well design (see Figure 6. 4) calls for five casing strings – a Surface Casing, an Intermediate Casing, and three production liners, labeled Production 1, Production 2, and Production 3.

Each casing string overlaps the previous casing string by 200 ft. A tieback liner rests on top of the Intermediate Casing and fits within the Surface Casing to create a sealed, smooth conduit for injection of a working fluid.

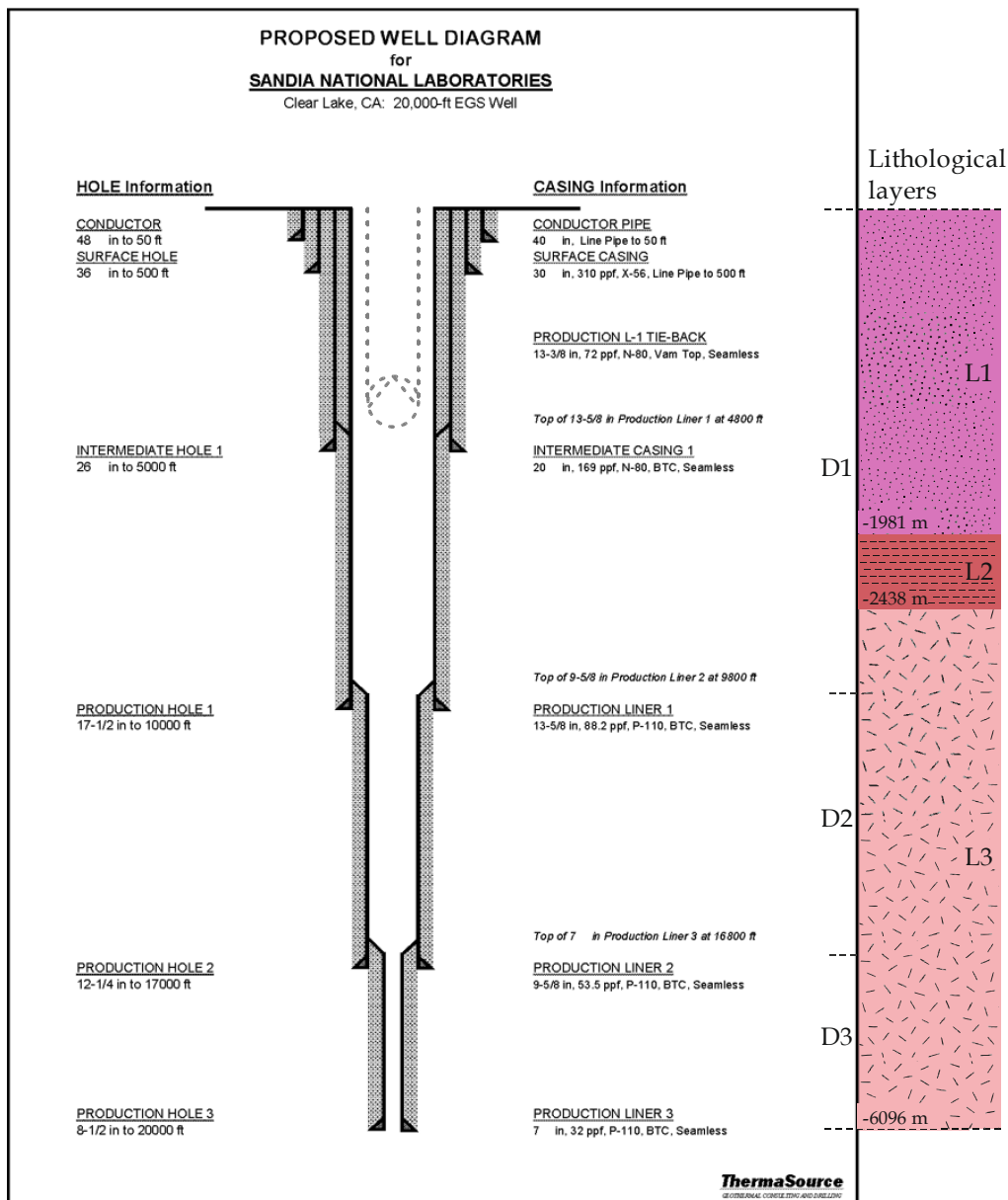


Figure 6. 4: The proposed well diagram from Sandia National Laboratories modified from Polsky [2008]. The dashed lines indicates pump installation at 1,200 m depth for some production examples.

A one-dimensional element can be used for the calculation of transport in tube structures that are exchanging with the surrounding formation. Since the annual temperature variations affect only the topmost 15 m, negligible on the total wellbore depth range, a constant surface temperature of 15 °C (annual mean) was taken as an upper boundary condition. The few borehole temperature measurements available prevent us from reaching a detailed definition of the subsurface and allowed only to perform homogeneous considerations.

The geometry of the wellbore system allows us to assume axial symmetry around the center of the system so that we can perform 2D simulations by 1D geometry (depth  $z$ ). According to Eskilson [1987], axial effects start to be significant after a period of  $a \cdot t \leq H^2/90$ . With the depth of typical geothermal wellbore of 0.5 – 5 km, the time limit of axial (3D) effect can be calculated as 176 – 17,616 years (rock thermal diffusivity  $a$  is assumed as  $0.5 \times 10^{-6}$  m<sup>2</sup>/s). Hence, axial heat transfer effect can be neglected.

Heat transfer in the inclined borehole is also a three-dimensional problem. Therefore, the temperature responses on the inclined wellbore wall perimeter of any cross-section perpendicular to its axis are unequal and vary with the borehole depth. It can be concluded from Ping [2006] that the variation of the temperature on the inclined borehole wall along its depth was almost similar to that on the vertical borehole. This illustrates that inclined borehole can be modeled as vertical borehole for simplicity of one-dimensional problem.

The two-phase multicomponent geothermal fluid flow was simulated by 1D elements, which is capable of calculating accurately thermal advection at high fluid flow rates and accounting exactly for flow velocity changes at different diameters. Table 6. 4 summarized hypersaline water compositions (0.9 and 3.4 mol/kgw NaCl) used in this study, as a reference mixtures, adapted from Demir et al. [2014], with pH of 6.5 at the reservoir condition. The reservoir pressure is assumed to be hydrostatic, with productivity and injectivity indices (PI and II) of 1 kg/s/bar.

| species | concentration<br>[mol/kgw] | species               | concentration<br>[mol/kgw] |
|---------|----------------------------|-----------------------|----------------------------|
| Na      | 0.9 (3.4)                  | Ba                    | 1.57E-5                    |
| K       | 4.9E-5                     | Si                    | 6.2E-3 (4.3E-3)            |
| Mg      | 4.6E-3                     | SO <sub>4</sub>       | 1.83E-3                    |
| Ca      | 2.1E-4                     | CO <sub>2</sub> (aq)  | 2100 mg/kg                 |
| Cl      | 0.9 (3.4)                  | H <sub>2</sub> S (aq) | 900 mg/kg                  |

Table 6. 4: Reference mixture composition used in the examples.

As the multicomponent geothermal fluid flows through the wellbore path, the system undergoes some dissolution/precipitation reactions that change the chemical composition. In geothermal industry, the main four grouping of scales can be summarized as the following.

- Silica and siliceous materials, which include quartz, gibbsite, and amorphous silica
- Carbonates, which include calcite, dolomite, siderite and strontianite
- Sulfates, which include anhydrite, barite, gypsum and celestite

As a reference, one major mineral scale of each group was taken, namely amorphous silica, calcite, and barite. The modified gebo.dat database [Bozau, 2013] established for PHREEQC was used in the simulation. The modification includes amorphous silica log K database. The mineral deposition is modeled as volume reduction at each cell, as shown in Figure 6. 5.

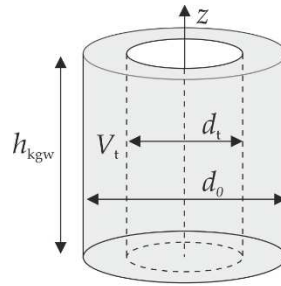


Figure 6. 5: Scheme of a precipitated mineral volume (in 1 kg of water) calculation and its impact to reduced inner diameter.

From Figure 6.5, the inner diameter reduction ( $d = 2r$ ) due to mineral precipitation can be computed by using

$$d_t = \left[ \left( 1 - \frac{V_t \cdot w_{H_2O} \cdot \rho^{AQ}}{8} \right) d_0^2 \right]^{0.5}, \quad (6.21)$$

where  $h_{kgw}$  is height of 1 kg water column.  $V_t$  is the volume of the total precipitated minerals at time  $t$  in 1 kg of water, and is computed as

$$V_t = \sum_i \left( c_{t,i} \frac{M_i}{x_{H_2O} \cdot \rho_i} \right), \quad (6.22)$$

with  $c$ ,  $w_{H_2O}$ ,  $x_{H_2O}$  are precipitated mineral in mol/kgw, water mass fraction, and steam quality, respectively.  $M_i$  and  $\rho_i$  are molar mass and density of mineral  $i$ .

All the calculations presented in the following have been performed using the operator-splitting scheme. A similar wellbore parameters were taken as the one in model validation (see Table 6. 2), except wellbore geometry and flow parameters (e.g. thermophysical properties, flow rate, injection temperature). In the examples, a perfectly vertical wellbore with reference mixture composition, mass flow rate of 60 kg/s is considered and the plotted data are from  $t = 10$  days.

### 6.3.3 Impact of chemical composition

To show the impact of the mixture composition, two different scenarios have been considered, one with chloride salt (electrolyte) and the other with non-condensable gas content variation.

#### *Salts*

For deep, Na-Cl water type geothermal formation water, maximum TDS value is approximately 250 g/l [Bozau *et al.*, 2015]. Thus, to study the influence of electrolyte concentration, we updated the NaCl concentration value to 200 g/l or equivalent to 3.42 mol/kgw. Figure 6. 6 displays results calculated at  $t = 10$  days. The left-hand plot depicts the pressure-temperature profile. It can be seen that the wellhead temperature is higher for the mixture with higher NaCl concentration (3.42 mol/kgw). For given higher NaCl concentration, pumping is needed since the assumed hydrostatic reservoir pressure is not sufficient to up-lift the hot fluid.

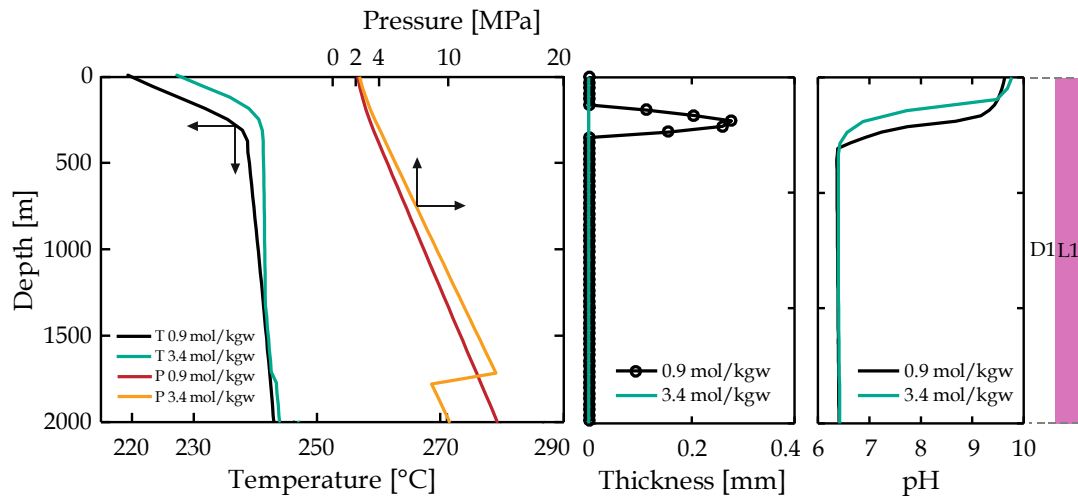


Figure 6. 6: Depressurization of the salty mixtures: Comparison of water with different NaCl salinity (0.9 and 3.4 mol/kgw). Pressure-temperature (left), calcite thickness (middle), and pH value (right).

The middle and left-hand plot of Figure 6. 6 shows the calcite deposition with corresponding pH value. The scale suppression effect of higher NaCl concentration is shown by no observed calcite deposition, even with the slightly higher pH value. In addition, no barite deposition is observed for mixture with 3.42 mol/kgw of NaCl, showing “salting in” effect on barite solubility.

#### *Non-condensable gases*

Some non-condensable vary from 10 wt.% in some dry steam wells to almost zero in others. Liquid brine resources contain a percentage of  $\text{CO}_2$ , of less than 2 wt.%, which is released when the pressure of the system is lowered in the well or the flashing chamber [Michaelides, 1982]. Garg et al. [2004] show non-condensable gas content of most of the wells in the data set (37 wells) are less than 1% (mass fraction of the produced fluid). Here, we assumed total non-condensable content of 0.3 wt.% (3000 mg/kg) for each NCG variation below.

- 70% of  $\text{CO}_2$  and 30% of  $\text{H}_2\text{S}$  (Table 6. 4)
- 100% of  $\text{CO}_2$
- 70% of  $\text{CO}_2$  and 30% of  $\text{N}_2$
- 100% of  $\text{CH}_4$

In Figure 6. 7, the left-hand plot shows the pressure-temperature profile. Different degassing-point depth can be observed. One can also note that the mixture with less soluble gas like  $N_2$  and  $CH_4$  tends to degas earlier. While,  $CO_2$  and  $H_2S$  mixture degas later with almost similar thermohydraulic behavior. As results, wellhead pressure for the mixture with  $N_2$  or  $CH_4$  is higher.

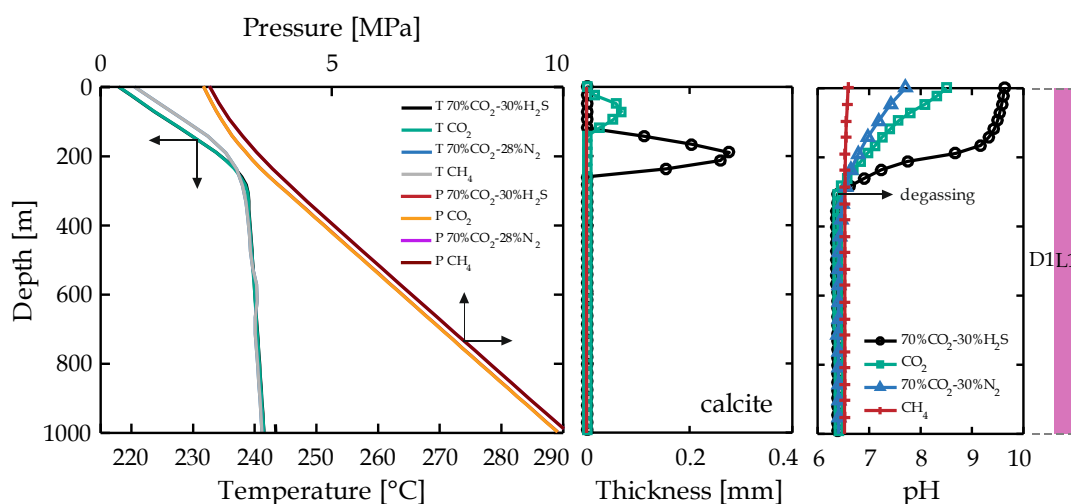


Figure 6. 7: Depressurization of the gassy mixtures: comparison of water with different gas compositions. Pressure-temperature (left), calcite thickness (middle), and pH value (right).

Barite solubility is not affected by the gas composition. However, the calcite solubility is. The pH increase for the mixture without  $H_2S$  is somewhat 1 unit lower. For the mixture with only  $CO_2$ , the pH increases up to 8.5 inducing some calcite precipitation quite far from its degassing point.  $N_2$  existence shifted the pH value to 7.8. This lower pH is not sufficient to precipitate the given Ca with  $HCO_3(-)$  dissolved in the water. For the mixture with abundant  $CH_4$ , no  $HCO_3(-)$  exists. Thus the pH is relatively neutral, only affected by water evaporation.

#### 6.4.1 Impact of slip correlation

An assumption of no slip between the aqueous and non-aqueous phases is likely to be a slightly rough simplification. Nonetheless, to establish which slip relation is better matched for geothermal fluid wellbore depressurizations is outside the scope of the present study. However, as an illustration of the effect that the slip relation may have, calculations have been performed employing the Hasan-Kabir correlation [2010].

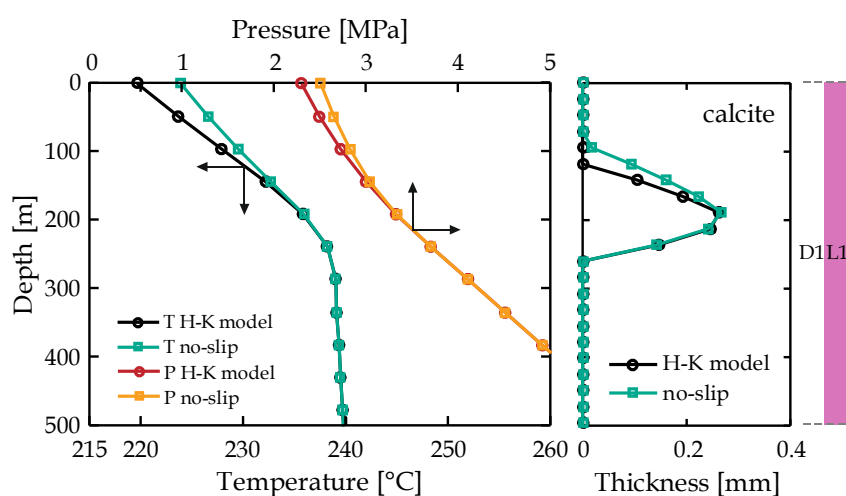


Figure 6. 8: Depressurization of the reference mixture: Comparison of no slip and the Hasan-Kabir correlation. Pressure-temperature (left) and calcite thickness (right).

Figure 6. 8 shows the effect of employing the Hasan-Kabir correlation compared to using the no-slip assumption. This case is for the reference mixture (Table 6. 4). The right-hand plot shows the calcite thickness. Interestingly, both the cases result in quite similar thickness. Nonetheless, for the no-slip example, the deposition is more spread-out at the upper part the wellbore due to higher temperature and void fraction (or equivalently Ca concentration). The pressure profile is also affected by the slip relation, as shown by the left-hand plot.

#### 6.4.2 Impact of wall friction

In this section, we will investigate the effect of applying average mixture friction, eq. (6. 16) from Hasan-Kabir [2010] for the wall-friction force in the momentum balance, eq. (6. 5). The reference mixture is considered, and Figure 6. 9 displays a plot of the pressure-temperature (left), barite thickness (middle), and calcite thickness (right). As expected, the exclusion of the wall-friction increases the pressure, shifts degassing point upward and results in postponed calcite deposition to far location. Remarkably, somewhere in the bottom of the wellbore, no-friction assumption lower the barite deposition, while at the end of the wellbore, the barite deposition is higher for the no-friction one.

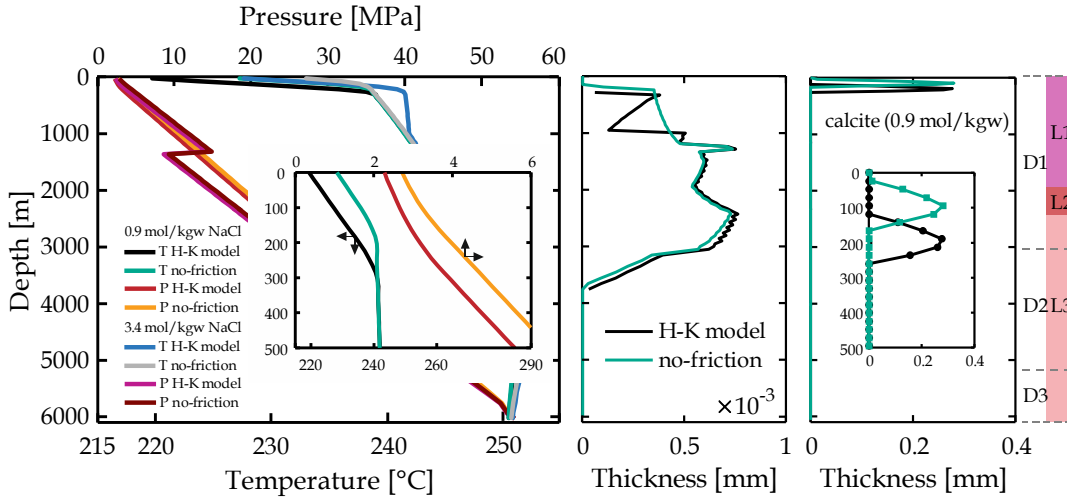


Figure 6. 9: Depressurization of the reference mixture: Impact of wall-friction. Pressure-temperature (left), barite thickness (middle), and calcite thickness (right).

### 6.4.3 Impact of reaction kinetic

The rate law uncertainties have been studied in detail in another publication (see [Zhang *et al.*, 2016]). In the present study, we employed the traditional linear rate law below to explore the effect of rate law uncertainties on salt composition effect:

$$r = \pm \left\{ k_{25}^{nu} \exp \left[ \frac{-E_a^{nu}}{R} \left( \frac{1}{T} - \frac{1}{298.15} \right) \right] + k_{25}^H \exp \left[ \frac{-E_a^{nu}}{R} \left( \frac{1}{T} - \frac{1}{298.15} \right) \right] a_H \right\} \cdot S \left| 1 - \left( \frac{IAP}{K} \right)^p \right|^q, \quad (6.23)$$

where  $r$ ,  $S$ ,  $k_{25}$ ,  $E_a$ , and  $a_H$  are precipitation rate (mol/kgw/s), reactive surface area (m<sup>2</sup>/kgw), rate constant at 25 °C (mol/m<sup>2</sup>/s), activation energy (kJ/mol), and H(+) (hydrogen ion) activity (mol/kgw), respectively. Transition State Theory (TST) or traditional linear rate law,  $q = 1$ , LIN law [Delany *et al.*, 1986] is used. The coefficient  $p$  is related to the stoichiometry of the reaction when an activated complex is formed. Often,  $p$  is equal to 1 as used in this study. Here we represent the uncertainty in term of the surface area  $S$  (m<sup>2</sup>/kgw). The chemical reactions and related parameters are listed in Table x from Xu [2004], Palandri, J.L. and Kharaka, Y.K. [2004], Xu [2006], TOUGHREACT database. For the kinetic examples, all minerals treated as kinetic reactions, except for calcite.

| mineral     | type of reaction | $\log k_{25}^H(E_a)$<br>(acid) | $\log k_{25}^{nu}(E_a)$<br>(neutral) | reactive surf.<br>[m <sup>2</sup> /kgw] |
|-------------|------------------|--------------------------------|--------------------------------------|---|
| silica (am) | kinetics         | -                              | -9.42 (49.8)                         | 1                                       |
| calcite     | equilibrium      | -                              | -                                    | -                                       |
| barite      | kinetics         | -6.63 (43.54)                  | -                                    | 1.29                                    |

Table 6. 5: Simulated minerals and the adopted kinetic parameters.

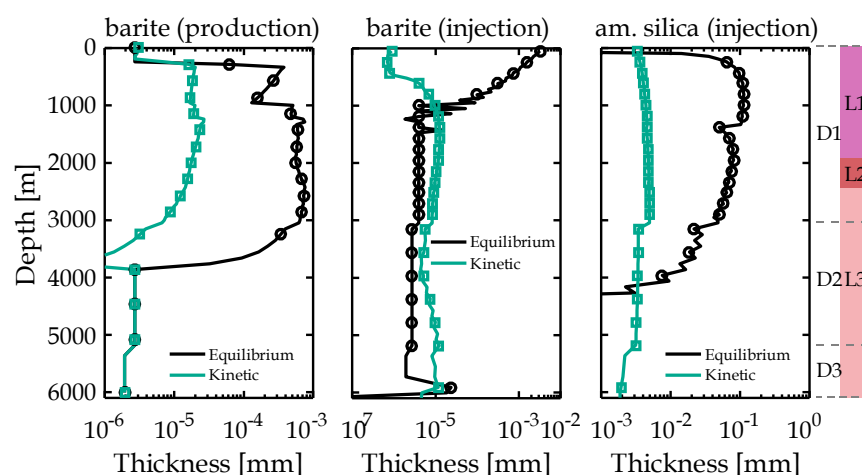
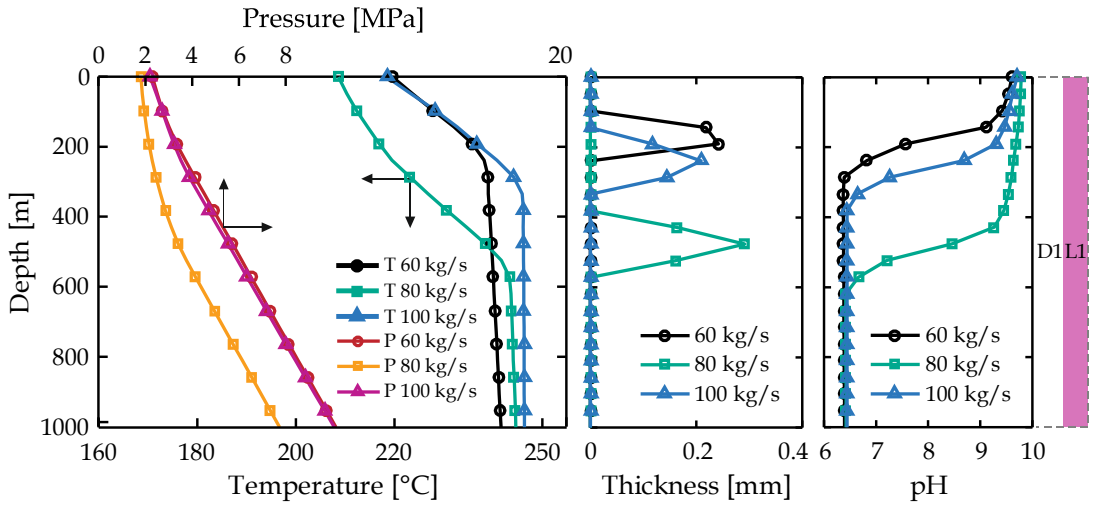


Figure 6. 10: (De-)pressurization of the mixture with 3.4 mol/kgw NaCl (in logarithmic scale): Impact of reaction kinetic to mineral deposition. Barite thickness at production (left), barite and amorphous silica at injection (middle and right, respectively).

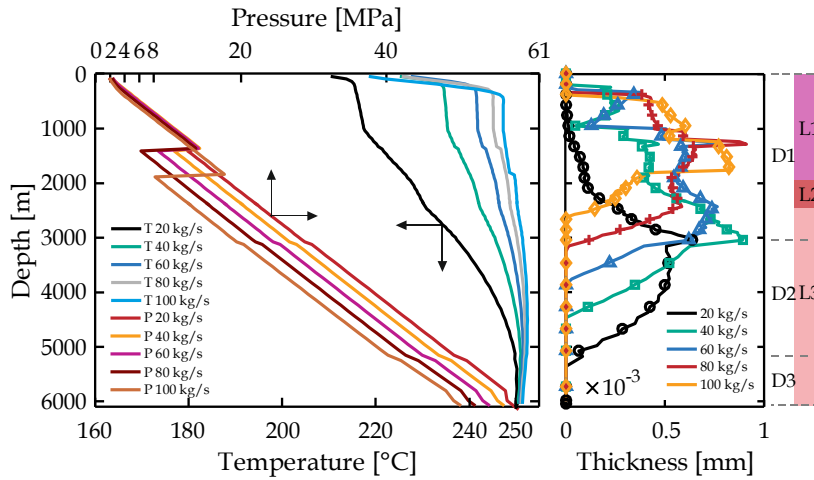
In Figure 6. 10, it is shown that the uncertainty related to reaction kinetic is greatly significant. For production example, we found that implementing reaction rate to the barite precipitation reduces barite thickness about one-tenth to 1/100 compared to equilibrium one. In the injection example, barite deposition is about half to 1/6 compared to the equilibrium one. At the same injection example, we found that amorphous silica thickness reduction due to kinetic effect is also reduces the thickness to about 1/30 times. It is interesting to note that in injection example, kinetic doesn't only change the amount, but also postpones the mineral deposition to far location. Based on the results, it can be concluded that to produce an accurate mineral deposition prediction, kinetic grain mechanics correlation for each mineral must be determined first.

6.4.5 Impact of operation parameter

In order to examine the effect of flow and injection temperature parameters on the pressure, temperature, and mineral deposition profile along the wellbore, the following simulations have been performed.



(a) Production (0.8 mol/kgw NaCl) with calcite precipitation



(b) Production (3.42 mol/kgw NaCl) with barite precipitation

Figure 6. 11: Depressurization of the reference mixture during productions: Impact of production mass flow rate. Pressure-temperature (left), calcite thickness (middle), and pH (right) for production with 0.8 mol/kgw NaCl (a). Pressure-temperature (left), barite thickness (right) for production with 3.42 mol/kgw (b).

### Flowrate

The production mass flow rates of 40 - 100 kg/s are imposed to the reference case mixture. For the injection examples, the flow rate and thus species concentration is adjusted by factor of 0.8 hot-brine flow, and 0.7 two-phase, mid-enthalpy flow, as mass loss factor [Kaya *et al.*, 2011]. For 0.9 mol/kgw NaCl mixture, it is found that higher flow rate causes deeper degassing point. This condition leads to exponentially increase calcite deposition thickness. Thicker calcite for the 100 kg/s scenario was induced also due to smaller diameter, as pump installation consequence. For 3.4 mol/kgw NaCl mixture, higher flow rate pushes the deposition peak upward, and linearly increase the maximum thickness.

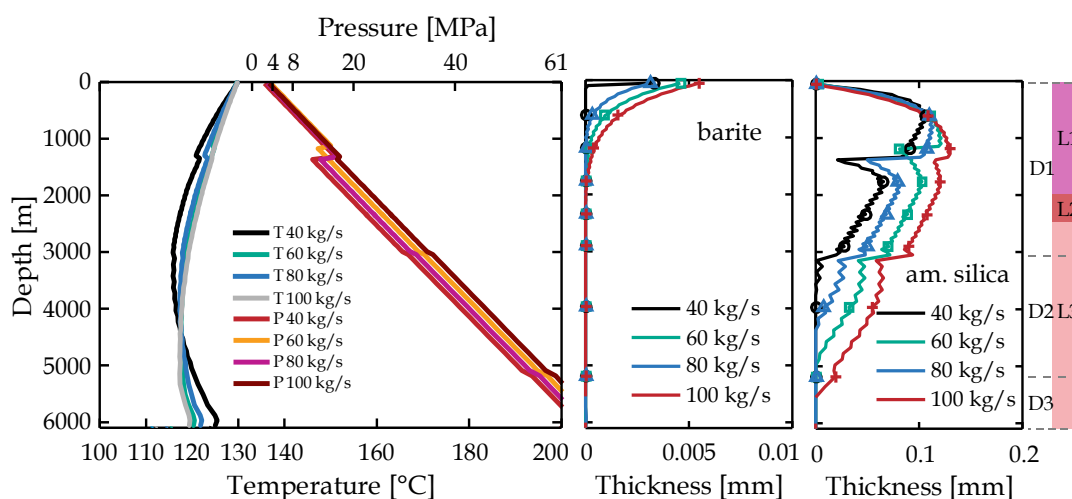


Figure 6. 12: Depressurization of the reference mixture during productions: Impact of production mass flow rate of fluid injection with 3.4 mol/kgw NaCl at 130 °C well-head temperature.

Emission of some of these gases, particularly CO<sub>2</sub> and H<sub>2</sub>S, remains one of the main environmental concerns associated with high-enthalpy geothermal energy utilization [Aradóttir *et al.*, 2015]. Therefore for the injection examples, it is assumed that all the non-condensable gases, i.e. CO<sub>2</sub> and H<sub>2</sub>S are captured and injected back to the reservoir. It is interesting to note that H<sub>2</sub>S that are dissolved in the geothermal fluid will supply S(-6) which emulates barite precipitation. In Figure 6. 12, it is shown that barite is already over saturated at the wellhead condition. While, amorphous silica is somewhat at equilibrium. It can be seen that increasing flow rate distributes the precipitation location to far location and monotonic increase of precipitated mineral amount was observed.

### Injection temperature

By using similar assumption as above,  $\pm 10$  °C range of injection temperature (120 °C and 140°C) was simulated. The results are plotted and compared to reference example of 130 °C, in Figure 6. 13 below.

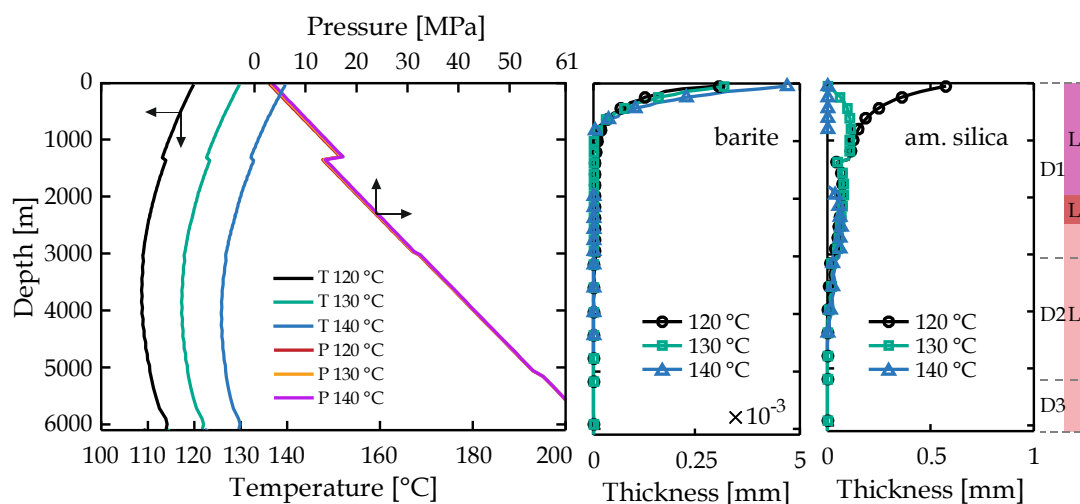


Figure 6. 13: Injection of the mixture with 3.4 mol/kgw NaCl: Impact of injection temperature. Pressure-temperature (left), barite thickness (middle), and amorphous silica thickness (right).

Obviously, the amount and location of barite deposition are somewhat similar in the three scenarios. The location of mineral depositions of amorphous silica are shifted to deeper location at injection temperature of 140 °C, where the temperature is colder. At 120 °C the deposition occurs directly at the wellhead (over saturated). While at 130 °C, the amorphous silica is at equilibrium and start to precipitate at deeper location where the temperature is colder. Nevertheless, at the bottom hole, no precipitation is observed due to Ba and Si concentration reduction after scaling at the shallower depth.

## 6.6 CONCLUSIONS

WellboreKit, a two-phase multi-component heterogeneous model for the reactive transport and depressurization of geothermal fluid mixtures, has been developed. Calculations have been performed for a geothermal fluid mixture using the gE-OSkit equation of state to compute the mixture properties. The operator-splitting scheme was employed for the numerical solution of the heterogeneous model. It should be noted, nonetheless, that the accuracy of the model itself, depends on constitutive correlations like the slip correlation, scaling-corrosion related wall-friction model, and deposition kinetics and flow mechanics which need to be further studied for geothermal wellbore applications. The present results confirm that the mixture composition and operation parameter impact the pressure-temperature profile and the amount of mineral deposition exerted by heat loss and depressurization. These issues should be considered for the design and operation of geothermal wellbore installations. The application of this model could be used to evaluate the amount of mineral deposited in realistic conditions during geothermal heat and electricity production, and should be a valuable tool for flow assurance risk assessment studies to minimize scale formation.

# 7

## SUMMARY AND CONCLUSIONS

Geothermal technical installations (e.g. wellbore and power block) cost is a major factor in determining the economic feasibility of binary geothermal projects. It holds a major share of 65 to 80% of total project cost [Borealis GeoPower, 2016; Sabo, 2013; Verkis consulting, 2014; Astolfi et al., 2013; Chatenay et al., 2014]. As such, their design and operational efficiency could lead to a significant cost reduction. The purpose of this research was to study the various factors to improve the economic and technical feasibility of geothermal systems, with a special emphasis on wellbore simulator. The objectives of this thesis were twofold: to enhance the economics of geothermally fueled Organic Rankine Cycle (ORC) using modularity through advanced control strategy, and to improve understanding of thermohydro-chemical (THC) characteristics of geothermal fluid flow in geothermal wellbores by development of a numerical tool.

Geothermal, small scale energy provision in remote areas requires a holistic approach to addressing challenges in geothermal exploration, reservoir, wellbore, and power plant engineering. At many locations in Indonesia, medium enthalpy resources can be found at depths of about several hundred meters. For instance at 300-500 meters at Blok Langkoan, Lahendong geothermal field, North Sulawesi [Azimudin et al., 2001] or about 600-800 meters at Atadei, East Nusa Tenggara [Nanlohy et al., 2003]. These resources could be utilized using flexible small scale binary power modules. Also, power plant engineering and operation could be simplified significantly for such sites. Flexible plant sizes applicable at different geothermal sites can be realized based on modular setup and enable reliable operation and low maintenance. A 60 kWel prototype of such an adaptable small scale binary unit has been developed and installed at Groß-Schönebeck (GrSk), Germany, to be tested and optimized. This pilot project could be the base for a large-scale deployment of small-scale power plants for remote areas of Indonesia [Erbas, 2015].

By feeding the heat to the power plant, wellbore exhibits strong multicomponent fluid flow state changes that induced scaling and corrosion problem. As examples, the Mataloko field, Indonesia, produces geothermal fluid containing clay particles and chemicals that might be harmful for the surface installation [PLN, 2015]. In Dieng field, Indonesia, sulfides scaling has been observed in the wellbore and pipelines [Harijoko *et al.*, 2015]. Furthermore, the recent development

of enhanced geothermal system (EGS) at greater depth is most likely expected to result in the presence of non-negligible salt and gas content. All these issues require the application of a reactive wellbore simulator. Backed by the necessity for a valid, computationally efficient geothermal ORC and wellbore simulation models suitable for the herein study purposes, thermohydro(-chemical) simulation models were established.

## 7.1 MAJOR RESULTS

Mid-enthalpy geothermal fields can be exploited by using state-of-the-art Organic Rankine Cycles. Standardization is a key point to reduce the surface cost related to the power plant. However, to standardize a geothermal ORC is a non-trivial task, as explained in this thesis.

In Chapter 3, improvements to modular geothermal ORC performance are presented. The optimal turbine inlet temperature and pressure (TITP) of sub- and supercritical geothermal ORC is often found by brute force method. Empirical correlations were devised to solve this problem. The correlations can be used to predict TITP, improving computational time in the design process. Another improvement includes advance in component technology, such as turbines with variable nozzle-vanes, speed pumps and fans which allow the cycle to adapt to a wide range of operating conditions by modifying evaporation pressure, superheating, and condensation temperature.

Model for heat exchangers was developed to simulate the steady-state, off-design performance at these ranging conditions. Discrete parameter approach, i.e. three zones model, was used and compared to stream evolution approach using Aspen Plus exchangers design and rating (EDR). The EDR results can be predicted accurately by the developed model with an absolute average relative difference (AARD) of 2 - 4% and temperature accuracy of 0.5 - 2 °C. The models have also been used to determine the set points for multivariable or multiple-input-multiple-output (MIMO) control strategy.

Dynamic load change and ambient temperature are supposed to be the main challenge occurring in the insular operation. Therefore, one of the main parts of the present work has been devoted to the detailed examination of the dynamic behavior of 60 kWel GrSk and Chapter four's modular 1,000 kWel ORC. The MIMO control strategy showed an advantage over traditional control strategies, e.g. constant and sliding pressure. It is found that hysteresis phenomena are occurred during ramp-up/down. The fast ramp-down in load has been revealed

to result in isobutane mass moving from the cold-side of the ORC and accumulating on the hot-side, which eventually results in decreases in turbine inlet pressure and thus net power output. The contrary has been shown to occur during fast ramp-up in electrical load: fast ramp-up improves net power output and thermal efficiency.

In Chapter 4, the modularization technique for geothermal ORC has been devised and a thermoeconomic tool has been developed. By using the tool, we designed a modular 1,000 kWel ORC to adapt variable boundary conditions through off-design mapping. Thermoeconomic optimization was carried out in annual basis simulation. It can be concluded that minimizing SIC did not yield significant benefits, but MCF proved to be a much better optimization function.

Simulations on varying geothermal and ambient temperature suggest that the design ambient temperature is primarily laid at an average temperature of one year: 10 °C for temperate, 22 °C for tropical, and 23 °C (which is likely a maximum limit) for a dry climate. Also, the design geothermal (wellhead) temperature should be slightly higher than the average, e.g. about 155 to 165 °C.

The objective of the second part of the thesis was the development of numerical THC numerical tool for two-phase, multicomponent geothermal well flow. In Chapter 5, the equation of state for two-phase multisalt, multigas geothermal fluids has been programmed in gEOSkit. Novel neutral dissolved gas interaction parameters have been applied to improve the mutual gas solubility prediction accuracy (AARD of 3% to 6%). The results show reasonable agreement with the measurement data and better than any other available codes, e.g. PHREEQC 3.2 [Appelo *et al.*, 2014], EOS7Cm [Lei *et al.*, 2016]. Nonetheless, water-CH<sub>4</sub>-H<sub>2</sub>S experimental data is still needed to complete the validation.

Explicit enthalpy correlations for other salts than NaCl was added by derivation of Drisner [2007] model. As results, the thermophysical properties, e.g. heat capacity, density, and viscosity models are capable of accurately predicting the online and literature measurement data with AARD of 1 - 2%. Hypothetical saturation  $p - T$  relation has also been formulated to estimate at pressure and temperature higher than of critical states of pure water. Due to limitation of apparent properties relations, the solver is generally valid up to 300 °C.

In Chapter 6, Two-phase multicomponent EOS described above has been implemented to compute the fluid properties in WellboreKit, a THC wellbore flow simulator. Elmer-PHREEQC coupling platform has been extended to model slow-transient THC behavior of geothermal fluid flowing in wellbores. Mechanistic-based one-dimensional model for two-phase flow [Hasan and Kabir, 2010] was

used. The mechanism takes account of Taylor bubble velocity to determine the flow pattern, while for the transient term, an improved drift-flux correlation was employed. The impact of mixture composition, slip, friction, and operating parameters to temperature, pressure, and mineral (e.g. barite, calcite, and silica) saturation was investigated.

## 7.2 FURTHER IMPROVEMENT AND DIRECTION

Further research and experimentation will be required in the field of modular geothermal ORCs optimization, namely:

- The experiment of 60 kWel GrSk ORC to fitting the model, validation, and further optimization, including dynamic test to examine the heat mass transfer dynamic characteristics.
- Analysis of flow-induced vibration on the evaporator: fluid-induced vibration (FIV) in shell-and-tube heat exchangers. FIV can be handled by using Dimpled Tube Support (DTS™) and Saddled Tube Support (STS™) to enable wider and flexible operating conditions.

WellboreKit, the THC wellbore flow simulator can still be further improved by parallelization of the gEOSkit code. Conversion to C++ code using solver derived from root-finding solver embedded in Coolprop [Bell *et al.*, 2014] is also desirable. So that, the gEOSkit solver is also amenable for application in reservoir simulator.

In the future, more effort should be focused on the development of mineral scale prediction and fast-transient modeling:

- A multiscale approach for scaling in the wellbore, i.e. in tube diameter transition using microstructure simulation (phase-field modeling) should be performed.
- Development of mechanistic models and experiment for the prediction of the rate of mineral deposit formation under forced convective conditions.
- As contribution to DEEPEGS project, several studies can be carried out, such as condensation induced water hammer (CIWH) in supercritical well killing; slugging and geysering in geothermal wellbore flow. Pseudo one-fluid two-phase flow models can be developed herewith.
- Geochemistry in supercritical geothermal fluid and solubility of minerals in high-temperature steam has not been completely understood. Improvement of this geochemical processes is also necessary.
- Coupled with mechanics, this model can be further used to investigate the effect of corrosion to the structural integrity of the wellbores.

## APPENDIX A

## ORC DYNAMIC SIMULATION MODEL

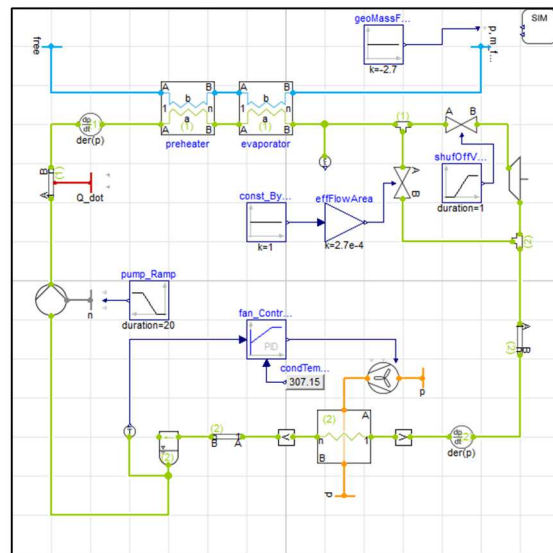


Figure A.1: Dynamic model of 60 kWel GrSk.

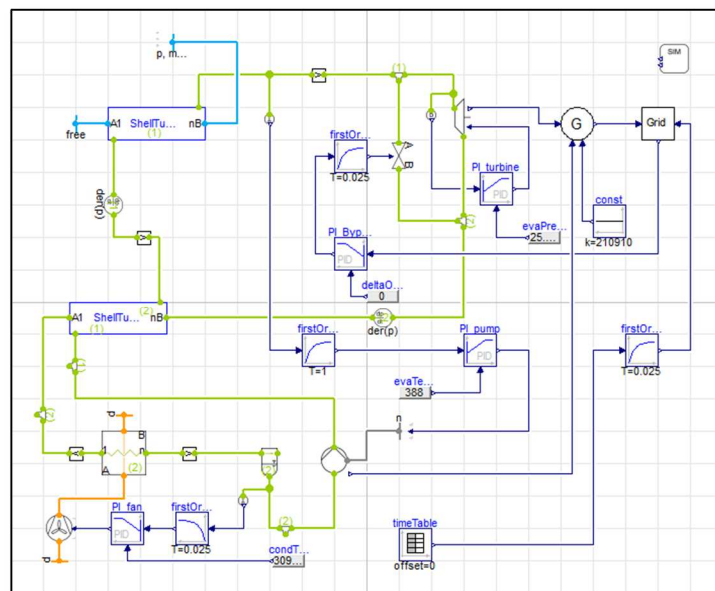


Figure A. 2: Dynamic model of modular 1,000 kWel ORC.

## APPENDIX B

## gEOSkit CORRELATION FORMULAE

*Density*

For the subcritical region  $g_1(T \leq 330^\circ\text{C})$ , we take the formulation by Garcia [2001]

$$g_1(T) = \sum_{n=1}^4 c_{0n} \cdot T^{(n-1)}, \quad (\text{B.1})$$

while  $g_2(412^\circ\text{C} < T \leq 432^\circ\text{C})$  is defined as a linear function of temperature in the supercritical region.

$$g_2(T) = V_1^\phi + \frac{(V_2^\phi - V_1^\phi)}{(T_2 - T_1)} (T - T_1), \quad (\text{B.2})$$

with the two points,  $(T_1, V_1^\phi)$  and  $(T_2, V_2^\phi)$ , being chosen accordingly to minimize error. In this study, the latter two datasets in the function were implemented, i.e.  $T_1 = 412^\circ\text{C}$ ,  $T_2 = 432^\circ\text{C}$ . In order to represent the pseudocritical region, both functions  $g_1(T)$  and  $g_2(T)$  were blended by using a transition function

$$f_1(T) = (1 + \exp((T - T_{\text{ps}})/(c_1 T_{\text{ps}})))^{-1}, \quad (\text{B.3})$$

where  $T_{\text{ps}}$  denotes the pseudocritical temperature ( $T_{\text{ps}} = 395^\circ\text{C}$ ) and  $c_1$  is a parameter which is gas-dependent (TableS), indicating the width of the exponential region. In addition, the exponential function,  $f_2(T)$ , represents the peak of the apparent molar volume at the pseudocritical temperature.

$$f_2(T) = c_{21} \exp(c_{22} \cdot |(T - T_{\text{ps}})/T_{\text{ps}}|^{c_{23}}), \quad (\text{B.4})$$

with the parameters  $c$  to adjust the height and shape of the peak of the apparent molar volume in the pseudocritical region. Those values of each gas and parameters  $c_{01} - c_{23}$  are listed in Table B.1.

|                 | CO <sub>2</sub> | CH <sub>4</sub> | H <sub>2</sub> S |
|-----------------|-----------------|-----------------|------------------|
| $V_1^\phi$      | 607             | 742             | 479              |
| $V_2^\phi$      | 409             | 476             | 338              |
| c <sub>01</sub> | 37.51           | 32.98           | 32.19            |
| c <sub>02</sub> | -9.585E-2       | 1.648E-1        | 1.13E-1          |
| c <sub>03</sub> | 8.74E-4         | -1.278E-3       | -6.901E-4        |
| c <sub>04</sub> | -5.044E-7       | 4.62E-6         | 2.679E-6         |
| c <sub>1</sub>  | 7.516E+0        | 7.4670E+0       | 7.1700E+0        |
| c <sub>21</sub> | 9.611E+2        | 1.2480E+3       | 7.5470E+2        |
| c <sub>22</sub> | -6.7980E-2      | -6.2020E-2      | -7.5430E-2       |
| c <sub>23</sub> | 1.271E+0        | 1.3510E+0       | 1.2680E+0        |

Table B.1 Parameters for the apparent molar volume of dissolved gas.

Comparison between experimental data and the apparent volume, calculated using the equation developed here is given in Figure B. 1. Parameters for other gases, such as N<sub>2</sub>, can simply be adapted to the model when the experimental data are available.

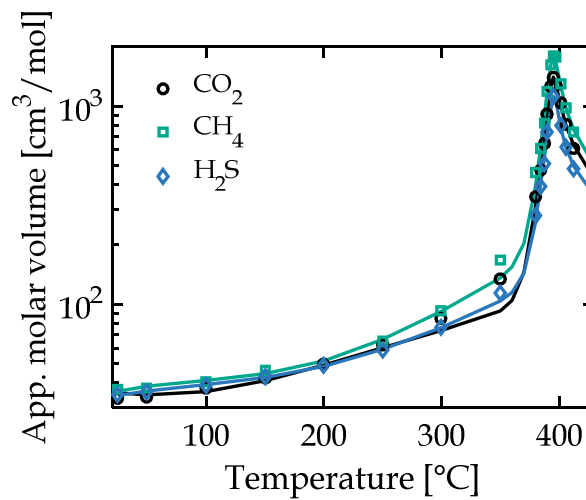


Figure B. 1: Apparent molar volume of dissolved gases: Comparison of experimental data from Hnědkovský et al. [1996b].

### Specific heat capacity

Following Francke [2013], the apparent specific heat capacity can be evaluated as a function of temperature and molality

$$c_{p,i}^{\phi} = (b_i^{c_1} + c_2) \cdot (c_3 - c_4 \cdot (c_5 - T + 273.15)^{-1}), \quad (\text{B.5})$$

with the parameters,  $c_1 - c_5$ , listed in Table 2S. In case of NaCl, the apparent molar heat capacity is directly derived from the equation by Driesner [2007] (validity:  $p = 0.1 - 500$  MPa,  $T = 0 - 1000$  °C, NaCl mole fraction of 0 - 1).

| Par.  | MgCl <sub>2</sub> | CaCl <sub>2</sub> | KCl       |
|-------|-------------------|-------------------|-----------|
| $c_1$ | -3.339E-3         | 0.982E-1          | -0.198E-2 |
| $c_2$ | -9.909E-1         | -0.124E-1         | -9.960E-1 |
| $c_3$ | -1.693E+3         | -0.328E+3         | 1.373E+3  |
| $c_4$ | 3.355E+6          | -1.310E+5         | 6.740E+6  |
| $c_5$ | 6.280E+2          | 6.288E+3          | 6.280E+3  |

Table B.2: Apparent molar heat capacity parameters for MgCl<sub>2</sub>. Parameters for CaCl<sub>2</sub> and KCl were taken from Francke [2013].

Eq. (5. 10) also includes the apparent heat capacities of dissolved gases in water. In this study, they are derived from experimental data reported by Hnědkovský et al. [1997]. These data are used to fit equations for the dissolved gas apparent volume. Two exponential curves in the supercritical region are shown in Figure B. 2. Hence, the apparent specific heat capacity is defined by using three blended functions

$$c_{p,j}^{\phi} = \begin{cases} g_1 \cdot f_1 + g_2 \cdot (1 - f_1) + f_2, & \text{for } T \leq 396 \text{ } ^\circ\text{C} \text{ with } T_{\text{ps}} = 389 \text{ } ^\circ\text{C} \\ g_2 \cdot f_1 + g_3 \cdot (1 - f_1) + f_2, & \text{for } T > 396 \text{ } ^\circ\text{C} \text{ with } T_{\text{ps}} = 398 \text{ } ^\circ\text{C} \end{cases}, \quad (\text{B.6})$$

with  $g_1$  (in J/K-mol) being analogous to eq. (B.1), with the two linear functions,  $g_2(T)$ ,  $g_3(T)$

$$g_2(T) = c_{p,1}^\phi + \frac{(c_{p,2}^\phi - c_{p,1}^\phi)}{(T_2 - T_1)} \cdot (T - T_1) ,$$

$$g_3(T) = c_{p,3}^\phi + \frac{(c_{p,4}^\phi - c_{p,3}^\phi)}{(T_4 - T_3)} \cdot (T - T_3) .$$
(B.7)

$f_1(T)$  and  $f_2(T)$  (eqs. (B.3) – (B.4)) with different parameters  $T_{ps}$ ,  $c_1 - c_{23}$  were used to blend  $g_1(T \leq 327 \text{ }^\circ\text{C})$  ,  $g_2(393 \text{ }^\circ\text{C} (T_1) < T \leq 396 \text{ }^\circ\text{C} (T_2))$  , and  $g_3(416 \text{ }^\circ\text{C} (T_3) < T \leq 431 \text{ }^\circ\text{C} (T_4))$ . The parameters used in eq. (B.6) are summarized in Table B.3.

|                | CO <sub>2</sub> |             | CH <sub>4</sub> |             | H <sub>2</sub> S |             |
|----------------|-----------------|-------------|-----------------|-------------|------------------|-------------|
| $c_{p,1}^\phi$ | 7710            |             | 9320            |             | 4210             |             |
| $c_{p,2}^\phi$ | -15670          |             | -19000          |             | -11220           |             |
| $c_{p,3}^\phi$ | -2347           |             | -2960           |             | -1731            |             |
| $c_{p,4}^\phi$ | -789            |             | -1035           |             | -582             |             |
| $c_{01}$       | 214.3           |             | 236.4           |             | 177.5            |             |
| $c_{02}$       | -1.683E-1       |             | 5.124E-1        |             | -1.556E-1        |             |
| $c_{03}$       | -2.972E-3       |             | -1.059E-2       |             | -3.378E-3        |             |
| $c_{04}$       | 1.494E-5        |             | 3.423E-5        |             | 1.478E-5         |             |
|                | $g_1 - g_2$     | $g_2 - g_3$ | $g_1 - g_2$     | $g_2 - g_3$ | $g_1 - g_2$      | $g_2 - g_3$ |
| $c_1$          | 9.044E-03       | 4.399E-03   | 9.072E-03       | 4.716E-03   | 9.360E-03        | 5.319E-03   |
| $c_{21}$       | 1.716E+3        | -1360       | 1.234E+3        | -2865       | 7.836E+2         | -1597       |
| $c_{22}$       | 8.784E+12       | 1.275E+09   | 8.784E+12       | 3.520E+10   | 8.784E+12        | 5.461E+27   |
| $c_{23}$       | 5.5             | 6.248       | 5.5             | 5           | 5.5              | 12.67       |

Table B.3: Coefficients for the apparent molar heat capacity of dissolved gas, eqs. (B.6) – (B.7).

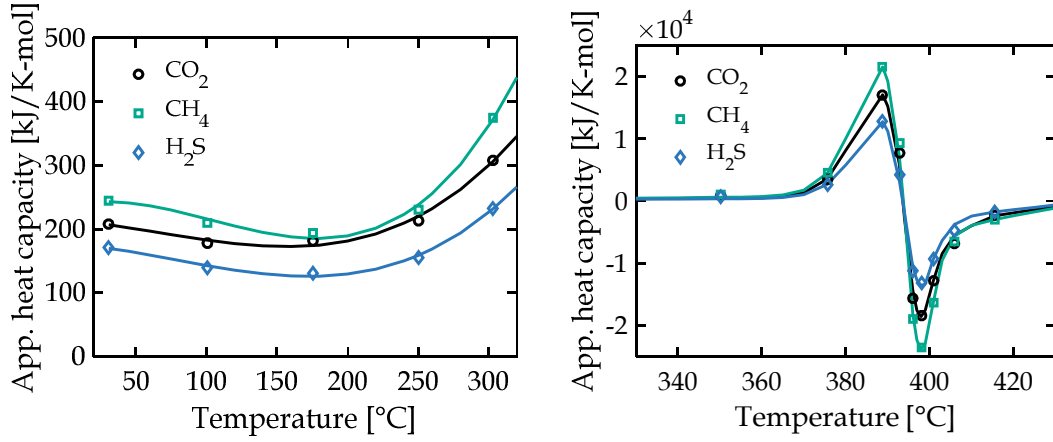


Figure B. 2: Apparent molar heat capacities of dissolved gases: Comparison between experimental data from Hnědkovský et al. [1997] and fitted equations in the subcritical region (left) and in the supercritical region (right).

### Viscosity

The (apparent molar) viscosity ratio introduced for the aqueous phase in eq. (5.19) is described as

$$\ln(\eta_{r,i}) = (c_{10} + c_{11} + c_{12}^2) \cdot \sum_{N_i} b_i + (c_{20} + c_{21} + c_{22}^2) \cdot \left( \sum_{N_i} b_i \right)^2 + (c_{30} + c_{31}) \cdot \left( \sum_{N_i} b_i \right)^3, \quad (\text{B.8})$$

with  $b_i$  denoting the molality of salt  $i$ . The parameters,  $c_{10} - c_{31}$ , for  $\text{CaCl}_2$  and  $\text{MgCl}_2$  are listed in Table B.4.

|          | $\text{CaCl}_2$ | $\text{MgCl}_2$ |          | $\text{CaCl}_2$ | $\text{MgCl}_2$ |
|----------|-----------------|-----------------|----------|-----------------|-----------------|
| $c_{10}$ | 2.7850E-1       | 3.9600E-1       | $c_{21}$ | 1.8100E-4       | -8.2870E-4      |
| $c_{11}$ | 2.8830E-4       | 9.4200E-4       | $c_{22}$ | -1.7130E-7      | 2.2080E-6       |
| $c_{12}$ | -6.4450E-7      | -1.9410E-6      | $c_{30}$ | 1.4060E-2       | 2.7550E-1       |
| $c_{20}$ | -6.9290E-2      | -1.4840E-1      | $c_{31}$ | -1.0530E-5      | -6.0010E-4      |

Table B.4: Viscosity ratio parameters for  $\text{CaCl}_2$  and  $\text{MgCl}_2$

## APPENDIX C

TECHNICAL DESCRIPTION OF WellboreKit -  
AN ELMER-PHREEQC COUPLING

By using a Finite Element Method (FEM) solver like Elmer, multi-physical problems can be modeled. Developed by CSC-IT, a Finnish Institute, it is a software based on finite element technologies; written mainly in fortran90, it also uses C and C++. Elmer, in its 6.1 version, is distributed under the GNU license (GPL 2.). The use of Elmer gives access for direct methods, Lapack or Umfpack libraries are made accessible; and for iterative methods, preconditioned Krylov subspace or, multilevel methods are made available. It can also be run parallel using the MPI tool. It uses domain decomposition to distribute the load to multiple processes that are being run either on different cores or CPU's. Here, mesh partitioning can be made using Metis. It is used to solve fluid dynamics and heat transfer equations. Elmer is organized in distinct modules, such as Advection-Reaction for the advection-reaction equations, and Stat Elec Solve for the electrostatic equations, which can be loaded. Some of them, like the heat equation solver, are directly included in the solver. Elmer has its mesh generator, but as it is not very easy to use, particularly for unusual geometry, the use of Gmsh was preferable. Then, all the physics is written to a file, with a .sif extension. Solver options are defined as the Linear System Solver, and some informatics tolerances are also defined, as it is easier for the user to control approximations. Then, Elmer normally works for the whole simulation period, but as chemical reactions need to be calculated, the PHREEQC results must be integrated.

PHREEQC is a computer program for speciation, batch-reaction, one-dimensional transport and inverse geochemical calculations. It enables to simulate chemical reactions in natural or polluted water. The tool is based on equilibrium chemistry of aqueous solutions interacting with minerals, gasses, solid solutions, exchangers, and sorption-surfaces. It also enables to handle kinetically controlled reactions. The choice of PHREEQC was primarily determined, among potential open source software's, by its ability to make a mass balance on involved gaseous components, that point being mandatory when considering unsaturated hydrogeochemical modeling. It is to note that, within the coupling, we only employ its batch reactions capacities. To deal with the flow, ion transport, temperature, and mechanics, we used Elmer.

## C.1 STATE OF THE ELMER-PHREEQC COUPLING AT THE BEGINNING OF THE THESIS: Etumos

To setup a coupling between PHREEQC, as geochemical tool, and Elmer as multi-physic and Elmer as multiphysics model, we used a high-level programming language as glue to tie components together to enrich the physics to be handled [Dimier, 2011]. An interpreted language, like Python, enabling code readability and maintainability appeared as the best solution.

Regarding the chemical transport algorithm, the main requirement is to “wrap” the legacy codes in Python, these becoming Python extensions modules, so-called shared objects on Linux (analogous to DLLs on Windows). The wrapping code process could be to some extent automated via the use of SWIG, the Simple Wrapper Interface Generator. Nevertheless, most of the necessary methods being developed from scratch, we decided to avoid SWIG to improve the readability of that wrapping. That way, we have to create C wrapping functions; these functions will enable data manipulation between the tool itself and the Python interpreter. These functions have specific structures of each tool.

The first method to be created concerns the initialization. Once the specific data files have been created via Python, this method will enable to launch the soft, read the data file and generate the suitable structures. As an example, for Elmer, we have a function bounded to initialization. `c_elmer_initialise` is a C function enabling to wrap the Fortran subroutine ensuring Elmer initialization. The `elmer_initialise.f90` subroutine is part of the `ElmerSolver.f90` standard one. The time stepping is managed by Python, Elmer methods being called sequentially over time stepping for each managed phenomenology to be involved, eventually with various time stepping.

PHREEQC is managed in a similar manner. Exchange of concentration fields is made at a memory level through the set and get methods. We won't detail here all necessary methods for the coupling algorithm.

## C.2 WellboreKit COUPLING INTERFACES

WellboreKit is a slow-transient, one-dimensional, two-phase multicomponent THC wellbore flow simulator. The simulator is an extension of Etumos, the Elmer-PHREEQC coupling platform. The following sections describe fortran90 solver and python modules used in the extended programming.

### C.2.1 Overview of the wellbore simulator routines

The structure of WellboreKit can be seen in Unified Modeling Diagram in Figure C. 1. New classes comprise mass-energy solver for heterogeneous two-phase flow problem; flowMechanic\_2p; and wellUtility\_2p.

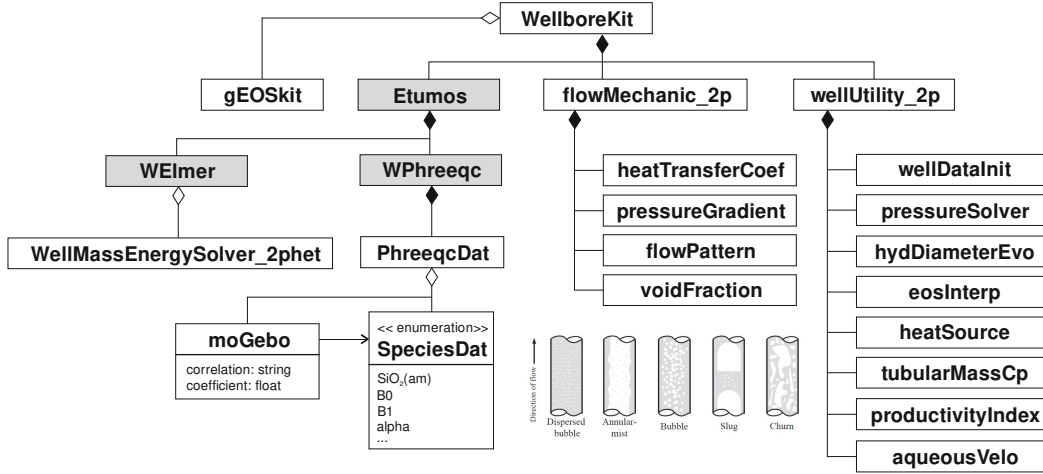


Figure C. 1: Unified Modeling Language diagram of WellboreKit: The gray blocks are classes that are developed at the beginning of the thesis as an Elmer-PHREEQC coupling platform.

### C.2.2 Detailed description of the solver

Detailed derivation of the mass-energy coupled equations applied to the Well-MassEnergySolver\_2phet.f90. Mass and energy balances.

Transient density change is written as

$$A \left[ (\rho^{NA} - \rho^{AQ}) \left( \frac{\partial x}{\partial h} \right)_p \frac{\partial \varepsilon}{\partial x} + c_{11} \left( \frac{\partial \rho^{AQ}}{\partial h} \right)_p + c_{12} \left( \frac{\partial \rho^{NA}}{\partial h} \right)_p \right] \frac{\partial h}{\partial t} \quad (C. 1)$$

The mass balance about spatial discretization is

$$\sin\theta \frac{\partial \dot{m}}{\partial z}, \quad (C. 2)$$

with the mass source term

$$S_M = - \left\{ (\rho^{NA} - \rho^{AQ}) \left( \frac{\partial x}{\partial p} \right)_h \frac{\partial \varepsilon}{\partial x} + c_{11} \left( \frac{\partial \rho^{AQ}}{\partial p} \right)_h + c_{12} \left( \frac{\partial \rho^{NA}}{\partial p} \right)_h + \frac{\partial \varepsilon}{\partial p} \right\} \frac{\partial p}{\partial t}. \quad (\text{C. 3})$$

For the thermal damping

$$A(\rho^{NA} h^{NA} - \rho^{AQ} h^{AQ}) \frac{\partial \varepsilon}{\partial \dot{m}} \frac{\partial \dot{m}}{\partial t}, \quad (\text{C. 4})$$

and

$$A \left[ c_{21} \left( \frac{\partial \rho^{AQ}}{\partial h} \right)_p + c_{22} \left( \frac{\partial \rho^{NA}}{\partial h} \right)_p + \varepsilon \frac{\rho^{NA}}{c_{23}} + (1 - \varepsilon) \frac{\rho^{AQ}}{c_{24}} - c_{25} \left( \frac{\partial x}{\partial h} \right)_p + \frac{(m \cdot c_p)_{tub} \cdot \psi}{A \cdot F_h} \right] \frac{\partial h}{\partial t}. \quad (\text{C. 5})$$

For thermal advection

$$\left( \frac{3\dot{m}^2}{2A^2 \rho_E^2} \right) \sin\theta \frac{\partial \dot{m}}{\partial z}, \quad (\text{C. 6})$$

and enthalpy balance about spatial discretization

$$\dot{m} \cdot \sin\theta \frac{\partial h}{\partial z}. \quad (\text{C. 7})$$

The heat source term is summed as

$$S_E = P\dot{q}_w + \frac{\dot{m}}{\rho_H} \Delta p_f + \dot{m}g \cdot \sin\theta + \left\{ A + c_{21} \left( \frac{\partial \rho^{AQ}}{\partial p} \right)_h + c_{22} \left( \frac{\partial \rho^{NA}}{\partial p} \right)_h - \left[ (\rho^{NA} - \rho^{AQ}) \frac{\partial \varepsilon}{\partial x} - c_{25} \right] \left( \frac{\partial x}{\partial p} \right)_h + \frac{\partial \varepsilon}{\partial p} \right\} \frac{\partial p}{\partial t}, \quad (\text{C. 8})$$

where

$$c_{11} = (\rho^{NA} - \rho^{AQ}) \frac{\partial \varepsilon}{\partial \rho^{AQ}} + (1 - \varepsilon) \quad (\text{C. 9})$$

$$c_{12} = (\rho^{NA} - \rho^{AQ}) \frac{\partial \varepsilon}{\partial \rho^{NA}} + \varepsilon \quad (\text{C. 10})$$

$$c_{21} = (\rho^{NA} h^{NA} - \rho^{AQ} h^{AQ}) \frac{\partial \varepsilon}{\partial \rho^{AQ}} + (1 - \varepsilon) h^{AQ} \quad (\text{C. 11})$$

$$c_{22} = (\rho^{NA} h^{NA} - \rho^{AQ} h^{AQ}) \frac{\partial \varepsilon}{\partial \rho^{NA}} + \varepsilon h^{NA} \quad (\text{C. 12})$$

$$c_{23} = x + (1 - x) \frac{c_p^{AQ}}{c_p^{NA}} \quad (\text{C. 13})$$

$$c_{24} = 1 + x \left( \frac{c_p^{NA}}{c_p^{AQ}} - 1 \right) \quad (\text{C. 14})$$

$$c_{25} = (\rho^{NA} - \rho^{AQ}) \left[ \frac{\varepsilon}{c_{23}} + \frac{(1 - \varepsilon)}{c_{24}} \right] \quad (\text{C. 15})$$

The momentum balance is solved in a separate solver. The pressure gradient is calculated via `flowMechanic_2p.py`. Integration of the pressure gradient was done in the `wellUtility_2p.py`, for each cell. A loop is implemented to calculate pressure along the wellbore path sequentially.

The aqueous transport of species is computed through standard advection-diffusion solver implemented already in Elmer.

### C.2.3 Detailed description of function classes

There are three major classes as foundations of WellboreKit, namely `gEOSkit`, `flowMechanic_2p`, and `wellUtility_2p`. Each class has a specific purpose and comprises lower level classes, i.e. functions.

#### *gEOSkit*

The class is coded in `gEOSkit.py`. It solves vapor-liquid equilibrium and thermo-physical properties of the two-phase multisalt, multigas geothermal fluid (see Chapter 5 for a detailed description of this class).

*flowMechanic\_2p*

`flowMechanic_2p.py` delivers `flowPattern` based on mechanistic model (Hasan-Kabir, 2002) which determines void fraction, heat transfer, and pressure gradient.

*wellUtility\_2p*

The main class of `wellUtility_2p.py` is `pressureSolver`. This solver step-wisely (bottom-top or top-down) solve the pressure-traverse along the wellbore path. The governing equation is finite difference form of eq. (6. 5).

$$p_z = p_{z-\Delta z} - \rho_{HG}\Delta z - \Delta p_f \frac{\Delta z}{\sin\theta} - \frac{1}{A^2} \left[ \left( \frac{\dot{m}^2}{\rho_I} \right)_z - \left( \frac{\dot{m}^2}{\rho_I} \right)_{z-\Delta z} \right] - \frac{\Delta z}{A \sin\theta} \frac{\Delta \dot{m}}{\Delta t} + \Delta p_p, \quad (\text{C. 16})$$

where  $\Delta p_f, \Delta p_p$  is frictional pressure gradient, pump pressure-increase as flux-boundary term, respectively. `hydraulicDiameterEvolution`, see Chapter 6.

`heatSource`. H-K dimensionless time function is defined as

$$T_D = \begin{cases} 1.1281\sqrt{t_D}(1 - 0.3\sqrt{t_D}), & \text{for } t_D \leq 1.5 \\ (0.4063 + 0.5\ln(t_D))(1 + 0.6/t_D), & \text{for } t_D > 1.5 \end{cases}, \quad (\text{C. 17})$$

with dimensionless time  $t_D = \lambda_e t / \rho_e c_{p,e} r_{wb}^2$ .

`tubularMassCp`. It computes averaged product of mass and  $c_p$  to include thermal storage effect. Thermal skin layer comprises tube, annulus, casing and cement, see Figure 6. 2.

$$(m \cdot c_p)_{tub} = \sum_{layer} (m \cdot c_p) / \sum_{layer} m \quad (\text{C. 18})$$

`productivityIndex` is calculated by implementing feed-point viscosity from McGuinness [McGuinness, 2014].

`aqueousVelo` calculates aqueous velocity to compute the species advection as

$$v^{AQ} = \frac{4 \cdot \dot{m}(1 - x)}{\pi d_h^2 \cdot \rho^{AQ}(1 - \varepsilon)} \quad (\text{C. 19})$$

*moGebo*

Modified gebo database includes amorphous silica and Pitzer parameters for PbS.

### C.3 WellboreKit FEATURES

Table C.1 summarizes the capabilities of the wellbore simulators, with reference to the following features:

- *Thermohydraulic (TH)*: All simulators can be used to compute thermohydraulic variables (temperature and pressure) to some level; TOUGH2 embedded wellbore model only calculates hydrostatic pressure gradient without thermal energy balance.
- *Mineral deposition/dissolution (C)*: Reactive chemical transport in geothermal wellbore is a major topic, particularly if typical chemical species are included, e.g. barium, calcium, silica, and lead. This feature is desirable to predict mineral scales within wellbore lifetime. It should be noted that the “C” feature set in OLGA<sup>a</sup> [Schlumberger, 2014] is applied for oil and gas wax problem; its geothermic application is not available.
- *Two-phase flow*: The two-phase effect can be modeled by several approaches, namely homogenous, heterogeneous, drift-flux and two-fluid or even three-fluid model. The accuracy is dependent to mass flux, gas phase quality and phenomena to be modeled. For instance, to model geysering, at the minimum, a two-fluid mass equation is prerequisite.
- *Transient*: Solving transient term of the mass and energy equations to model heat storage (dampening) effect. This feature is needed when the wellbore is operated on time-varying working conditions (e.g. enthalpy, pressure, flow rate). Some solvers implement quasi steady-state, e.g. YAWS<sup>b</sup> [Francke *et al.*, 2013], PROFILI<sup>c</sup> [Battistelli, 2010].
- *Gas-liquid slip*: This feature includes ratio between gas and liquid velocity ( $S$ ) into the governing equations. In the homogenous approach, the gas and liquid velocities are similar, thus  $S = 1$ . It is however experimentally observed, the ratio can be significantly different, depending on the flow pattern (e.g. bubbly, slug, churn, and annular).
- *Multicomponent equation of state (EOS)*: Obtaining sufficient accurate thermodynamic properties of multisalt and multigas geothermal fluids to minimize thermohydraulic error propagation. The major component can be generalized as Na-Ca-K-Mg-Cl (salt) and CO<sub>2</sub>-N<sub>2</sub>-CH<sub>4</sub>-H<sub>2</sub>S (gas).
- *Multifeed*: Geothermal reservoirs especially the high-enthalpy one often has more than one feeding layers.

| capability                            | WellboreKit  | T2Well<br>[Pan and OI-<br>denburg, 2014] | HEX-B2<br>[Mégel <i>et al.</i> ,<br>2005] | YAWS<br>[Francke <i>et al.</i> , 2013]           |
|---------------------------------------|--|--|---|--|
| Thermohydraulic (TH)                  | ●  | ●  | ●   | ●  |
| Mineral deposition (C)                | ●  |  |   |  |
| Two-phase flow<br>(modeling approach) | ●<br>(het.)  | ●<br>(dflux)                             |   | ●<br>(hom.)                                      |
| Transient                             | ●  | ●  | ●   | <i>b</i>   |
| Gas-liquid slip                       | ●  | ●  |   |  |
| Mult. equation of state               | ●  | ●  | ●   | ●  |
| Salt                                  | Na-Ca-K-Mg-Cl-<br>HCO <sub>3</sub>                                 | Na-Cl                                    | Na-Cl                                     | Na-Ca-K-Cl                                       |
| Gas                                   | CO <sub>2</sub> -N <sub>2</sub> -CH <sub>4</sub> -H <sub>2</sub> S | CO <sub>2</sub>                          |   | CO <sub>2</sub> -N <sub>2</sub> -CH <sub>4</sub> |
| Multifeed                             | ●  | ●  | ●   | ●  |

| capability                            | OLGA <sup>a</sup><br>[Schlumberger, 2014] | PROFILI<br>[Battistelli,<br>2010]                                  | SwelFlo<br>[McGuinness, 2014] | WellSim<br>[GSDS, 2016] |
|---------------------------------------|---|--|-------------------------------|-------------------------|
| Thermohydraulic (TH)                  | ●   | ●  | ●                             | ●                       |
| Mineral deposition (C)                | ●   |  |                               |                         |
| Two-phase flow<br>(modeling approach) | ●<br>(two-fluid)                          | ●<br>(n/a)   | ●<br>(het.)                   | ●<br>(het.)             |
| Transient                             | ●   | <i>c</i>   |                               |                         |
| Gas-liquid slip                       | ●   | ●  | ●                             | ●                       |
| Mult. equation of state               | ●   | ●  |                               | ●                       |
| Salt                                  | n/a                                       | Na-Cl  |                               | Na-Cl                   |
| Gas                                   | n/a                                       | CO <sub>2</sub> -N <sub>2</sub> -CH <sub>4</sub> -H <sub>2</sub> S |                               | CO <sub>2</sub>         |
| Multifeed                             | ●   | ●  | ●                             | ●                       |

Table C. 1: Features of WellboreKit, in comparison with other wellbore simulators.

## APPENDIX D

## TRANSIENT TERMS OF WellboreKit

For a simplified treatment of the void fraction derivation with regard to time, the Dix void-fraction approximation is used for non-annular flow pattern. While, for annular flow, homogenous void-fraction is applied. With slip between aqueous and non-aqueous phase, transient energy term for bubbly, dispersed-bubbly, slug, and churn can be written as

$$\begin{aligned} \frac{\partial}{\partial t} (\varepsilon \rho^{NA} h^{NA} + (1 - \varepsilon) \rho^{AQ} h^{AQ}) &= (\rho^{NA} h^{NA} - \rho^{AQ} h^{AQ}) \frac{\partial \varepsilon}{\partial t} + \varepsilon \cdot \\ & \left( \rho^{NA} \frac{\partial h^{NA}}{\partial t} + h^{NA} \frac{\partial \rho^{NA}}{\partial t} \right) + (1 - \varepsilon) \cdot \left( \rho^{AQ} \frac{\partial h^{AQ}}{\partial t} + h^{AQ} \frac{\partial \rho^{AQ}}{\partial t} \right) \end{aligned} \quad (D.1)$$

where the void fraction derivation with regard to time can be written as

$$\frac{\partial \varepsilon(p, \dot{m}, x, \rho^{AQ}, \rho^{NA})}{\partial t} = \frac{\partial \varepsilon}{\partial p} \frac{\partial p}{\partial t} + \frac{\partial \varepsilon}{\partial \dot{m}} \frac{\partial \dot{m}}{\partial t} + \frac{\partial \varepsilon}{\partial x} \frac{\partial x}{\partial t} + \frac{\partial \varepsilon}{\partial \rho^{AQ}} \frac{\partial \rho^{AQ}}{\partial t} + \frac{\partial \varepsilon}{\partial \rho^{NA}} \frac{\partial \rho^{NA}}{\partial t} \quad (D.2)$$

with repeated parameters is listed in Table D. 1.

| Parameter       | Definition   |
|-----------------|--|
| $\underline{U}$ | $(1 - x)/x$  |
| $\underline{V}$ | $\rho^{NA}/\rho^{AQ}$  |
| $\underline{W}$ | $gD_h\sigma(1 + \cos\theta)$                                     |
| $\Omega_a$      | $1 + (\underline{UV})^{0.1}$                                     |
| $\Omega_b$      | $\frac{2.9A\rho^{NA}}{x\dot{m}}$                                 |
| $\Omega_c$      | $\frac{W \cdot (\rho^{AQ} - \rho^{NA})}{(\rho^{AQ})^2}$          |
| $\Omega_d$      | $1.22 + 1.22\sin\theta$  |
| $\Lambda$       | $\Omega_a + \Omega_b\Omega_c^{0.25}\Omega_d^{\frac{p_{atm}}{p}}$ |

Table D. 1: Parameters used in transient terms.

For pressure

$$\frac{\partial \varepsilon}{\partial p} = \frac{-1}{\Lambda^2} \Omega_b \Omega_c^{0.25} \Omega_d^{\frac{p_{atm}}{p}} \ln(\Omega_d) \left( \frac{-p_{atm}}{p^2} \right) \quad (D.3)$$

For mass flow

$$\frac{\partial \varepsilon}{\partial \dot{m}} = \frac{1}{\Lambda^2 \dot{m}} \Omega_b \Omega_c^{0.25} \Omega_d^{\frac{p_{atm}}{p}} \quad (D.4)$$

For steam quality

$$\frac{\partial \varepsilon}{\partial x} = \frac{1}{(\Lambda \cdot x)^2} \left( \underline{V}^{(0.1+V^{0.1})} \underline{U}^{(V^{0.1}-1)} + x \cdot \Omega_b \Omega_c^{0.25} \Omega_d^{\frac{p_{atm}}{p}} \right) \quad (D.5)$$

For aqueous density

$$\frac{\partial \varepsilon}{\partial \rho^{AQ}} = \frac{-1}{\Lambda^2} \frac{\partial \Lambda}{\partial \rho^{AQ}} = \frac{-1}{\Lambda^2} \left[ \frac{\partial \Omega_a}{\partial \rho^{AQ}} + \frac{\partial \left( \Omega_b \Omega_c^{0.25} \Omega_d^{\frac{p_{atm}}{p}} \right)}{\partial \rho^{AQ}} \right]$$

with

$$\frac{\partial \Omega_a}{\partial \rho^{AQ}} = -\underline{V}^{0.1} (\underline{UV})^{V^{0.1}-1} \frac{\underline{U} \rho^{NA}}{(\rho^{AQ})^2} + (\Omega_a - 1) \cdot \ln(\underline{UV}) [-0.1(\rho^{NA})^{0.1}(\rho^{AQ})^{-1.1}] \quad (D.6)$$

and

$$\frac{\partial \left( \Omega_b \Omega_c^{0.25} \Omega_d^{\frac{p_{atm}}{p}} \right)}{\partial \rho^{AQ}} = 0.25 \Omega_b \Omega_c^{-0.75} \Omega_d^{\frac{p_{atm}}{p}} \left[ -2 \frac{\Omega_c}{\rho^{AQ}} + \frac{W}{(\rho^{AQ})^2} \right]$$

For non-aqueous density

$$\frac{\partial \varepsilon}{\partial \rho^{NA}} = \frac{-1}{\Lambda^2} \left[ \frac{\partial \Omega_a}{\partial \rho^{NA}} + \frac{\partial \left( \Omega_b \Omega_c^{0.25} \Omega_d^{\frac{p_{atm}}{p}} \right)}{\partial \rho^{NA}} \right] \quad (D.7)$$

with

$$\frac{\partial \Omega_a}{\partial \rho^{NA}} = \underline{V}^{0.1} (\underline{UV})^{V^{0.1}-1} \frac{\underline{U}}{\rho^{AQ}} + (\Omega_a - 1) \cdot \ln(\underline{UV}) [0.1(\rho^{NA})^{-0.9}(\rho^{AQ})^{-0.1}] \quad (\text{D.8})$$

and

$$\frac{\partial \left( \Omega_b \Omega_c^{0.25} \Omega_d^{\frac{p_{atm}}{p}} \right)}{\partial \rho^{NA}} = \frac{\Omega_b}{\rho^{NA}} \Omega_c^{0.25} \Omega_d^{\frac{p_{atm}}{p}} - \Omega_b \left[ 0.25 \Omega_c^{-0.75} \frac{W}{(\rho^{AQ})^2} \right] \quad (\text{D.9})$$

For annular flow, homogenous non-slip model is used; for quality

$$\frac{\partial \varepsilon}{\partial x} = \frac{\underline{V}}{[(\underline{UV} + 1) \cdot x]^2} \quad (\text{D.10})$$

For aqueous density

$$\frac{\partial \varepsilon}{\partial \rho^{AQ}} = \frac{\underline{UV}}{(\underline{UV} + 1)^2 \rho^{AQ}} \quad (\text{D.11})$$

For non-aqueous density

$$\frac{\partial \varepsilon}{\partial \rho^{NA}} = \frac{-\underline{U}}{(\underline{UV} + 1)^2 \rho^{AQ}} \quad (\text{D.12})$$

## APPENDIX E

## PARTIAL VALIDATION OF WellboreKit

WellboreKit was validated partially by separated it into classes of models, namely energy balance and its heat source: fluid-formation heat transfer (T), advection-diffusion with reaction (C) and two-phase flow pattern, heat-loss and pressure-traverse (TH) models. First, T model were validated using a synthetic case and compared with analytical solutions. Three different layers of rock are applied as in Chapter 6. Second, C model was validated by means of analytical solution. The comparison between simulation results and analytical solutions are shown in Figure E. 1.

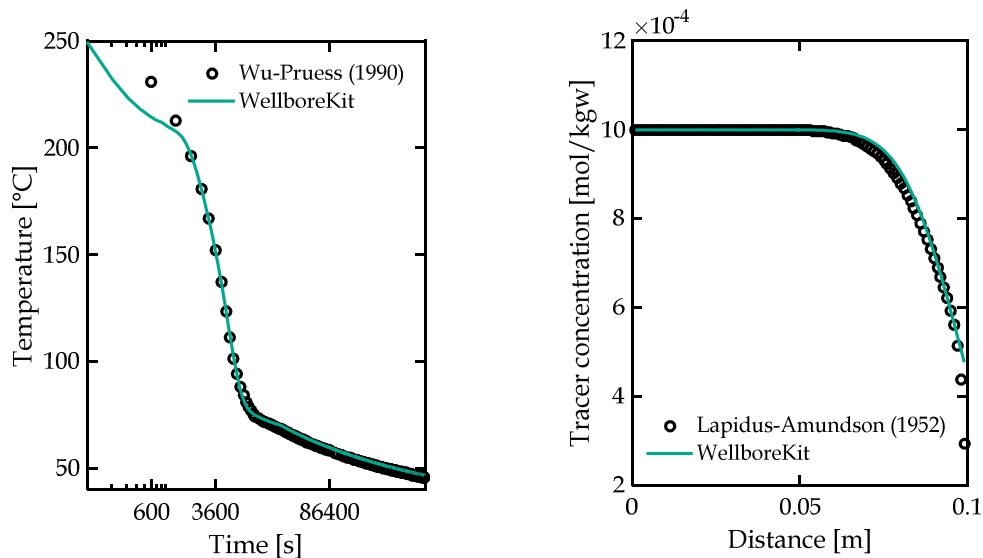


Figure E. 1: Analytical validation of WellboreKit: Energy balance and fluid-formation heat transfer (a); advection-diffusion validation using tracer test (b).

Finally, after confirming the validity of the T solver, TH model were validated using flow-test data of well KE1-22, Kirishima, Japan.

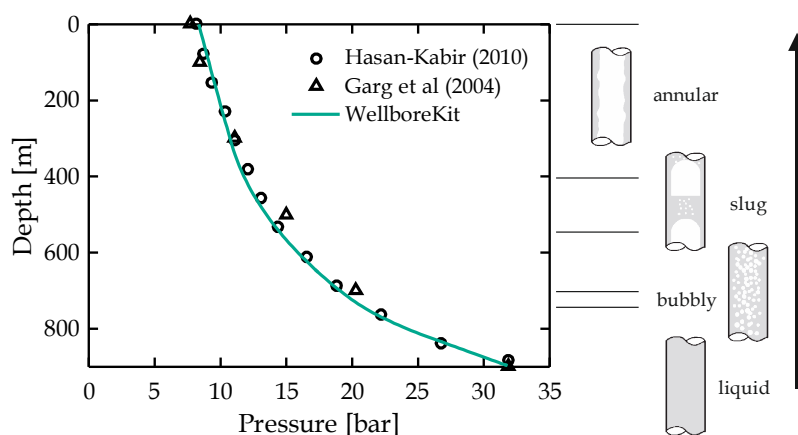


Figure E. 2: Two-phase flow pattern and pressure-traverse validation, KE1-22 well.

Figure E.2 shows the pressure profile calculated by the WellboreKit for the KE1-22 well. This particular example was chosen because it exhibited multiple flow regimes, starting with single-phase water flow at the bottomhole and ending with annular two-phase flow at the wellhead. Therefore, the homogeneous (no-slip) model was not expected to perform well in estimating pressures in the entire wellbore. Stepwise calculations for this well are calculated in `wellUtility_2p.pressureSolver` by implementing pressure gradient from `flowMechanic_2p.pressureGradient`. The pressure-traverse was calculated bottom-up. A cumulative effect of slight difference at certain depth results in a significant difference in the estimated well head pressure (WHP). The comparison is in good agreement between calculated and measured pressure confirming reliability of WellboreKit's thermohydraulic solver.

Other (C) solver, e.g. speciation solver was validated separately within PHREEQC software platform [Parkhurst, 1999].

---

## REFERENCES

---

- Aleksander Dhima, Jean-Charles de Hemptinne, Gerard Moracchini (1998), Solubility of light hydrocarbons and their mixtures in pure water under high pressure, *Fluid Phase Equilibria*, 145, 129–150.
- Alekseyev, V. A., L. S. Medvedeva, N. I. Prisyagina, S. S. Meshalkin, and A. I. Balabin (1997), Change in the dissolution rates of alkali feldspars as a result of secondary mineral precipitation and approach to equilibrium, *Geochimica et Cosmochimica Acta*, 61(6), 1125–1142, doi:10.1016/S0016-7037(96)00405-X.
- Alvarez, R. R., and R. C. Fra-Olahem (2011), Use of wellbore simulation as a tool to evaluate well issues in mature geothermal fields, *GRC Transactions*.
- Anderko, A., and K. S. Pitzer (1993), Equation-of-state representation of phase equilibria and volumetric properties of the system NaCl-H<sub>2</sub>O above 573 K, *Geochimica et Cosmochimica Acta*, 57(8), 1657–1680, doi:10.1016/0016-7037(93)90105-6.
- Aneke, M., B. Agnew, and C. Underwood (2011), Performance analysis of the Chena binary geothermal power plant, *Applied Thermal Engineering*, 31(10), 1825–1832, doi:10.1016/j.applthermaleng.2011.02.028.
- Antonia Olivia Sabo (2013), Wirtschaftlichkeitsaspekte einer geothermischen energieverorgungsanlage (mit 2 MW) für industriestandorte Indonesien: Vergleichende betrachtung zu konventionellen energieerzeugungsalternativen, diesel-generatoren, Bachelorarbeit, Hochschule Konstanz, Konstanz, Germany.
- Appelo, C. (2015), Principles, caveats and improvements in databases for calculating hydrogeochemical reactions in saline waters from 0 to 200°C and 1 to 1000atm, *Applied Geochemistry*, 55, 62–71, doi:10.1016/j.apgeochem.2014.11.007.
- Appelo, C. A. J., D. L. Parkhurst, and V. E. A. Post (2014), Equations for calculating hydrogeochemical reactions of minerals and gases such as CO<sub>2</sub> at high pressures and temperatures, *Geochimica et Cosmochimica Acta*, 125, 49–67, doi:10.1016/j.gca.2013.10.003.
- Appelo, C. A. J., and D. Postma (2005), *Geochemistry, groundwater and pollution*, 2nd ed., xviii, 649, Balkema, Leiden, New York.
- Aradóttir, E. S. P., I. Gunnarsson, B. Sigfússon, G. Gunnarsson, B. M. Júlíusson, E. Gunnlaugsson, H. Sigurdardóttir, M. T. Arnarson, and E. Sonnenthal (2015), Toward Cleaner Geothermal Energy Utilization: Capturing and Sequestering CO<sub>2</sub> and H<sub>2</sub>S Emissions from Geothermal Power Plants, *Transp Porous Med*, 108(1), 61–84, doi:10.1007/s11242-014-0316-5.
- Ashat, A., and F. Adriansyah (2012), Igniting the ring of fire, 110 pp., World Wild Fund.
- Astolfi, M., M. C. Romano, P. Bombarda, and E. Macchi (2014), Binary ORC (Organic Rankine Cycles) power plants for the exploitation of medium–low temperature geothermal sources – Part B: Techno-economic optimization, *Energy*,

- 66(0), 435–446, doi:10.1016/j.energy.2013.11.057.
- Augustine, C. (2009), Hydrothermal Spallation Drilling and Advanced Energy Conversion Technologies for Engineered Geothermal Systems, PhD Thesis, Chemical Engineering, Massachusetts Institute of Technology.
- Awad, M. M., and Y. S. Muzychka (2008), Effective property models for homogeneous two-phase flows, *Experimental Thermal and Fluid Science*, 33(1), 106–113, doi:10.1016/j.expthermflusci.2008.07.006.
- Azizov, N. D. (1999), The main results of investigation of the viscosity of aqueous solutions of electrolytes, *TVT*, 37(3), 404–410.
- Bächler, D., and T. Kohl (2005), Coupled thermal-hydraulic-chemical modelling of enhanced geothermal systems, *Geophysical Journal International*, 161(2), 533–548, doi:10.1111/j.1365-246X.2005.02497.x.
- Bachu, S., and D. B. Bennion (2009), Chromatographic partitioning of impurities contained in a CO<sub>2</sub> stream injected into a deep saline aquifer: Part 1. Effects of gas composition and in situ conditions, *International Journal of Greenhouse Gas Control*, 3(4), 458–467, doi:10.1016/j.ijggc.2009.01.001.
- Balje, O. E. (1962), A Study on Design Criteria and Matching of Turbomachines, *J. Eng. for Power, Trans. ASME*: 83-102.
- Battistelli, A. (2010), PROFILI wellbore flow simulator: from geothermal wells to GHG and acid gas injection wells, Geotherm Expo, Ferrara.
- Bäumer, R., I. Kalinowski, E. Röhler, J. Schöning, and W. Wachholz (1990), Construction and operating experience with the 300-MW THTR nuclear power plant, *Nuclear Engineering and Design*, 121(2), 155–166, doi:10.1016/0029-5493(90)90100-C.
- Bell, I. H., J. Wronski, S. Quoilin, and V. Lemort (2014), Pure and Pseudo-pure Fluid Thermophysical Property Evaluation and the Open-Source Thermophysical Property Library CoolProp, *Industrial & Engineering Chemistry Research*, 53(6), 2498–2508, doi:10.1021/ie4033999.
- Bernhard Spang, and W. Roetzel (2010), Costs and Economy of Heat Exchangers, in *VDI Heat Atlas*, Verein Deutscher Ingenieure.
- Borealis GeoPower (2016), Geothermal industrial park and direct-heat use workshop, <http://borealisgeopower.com/our-projects/>.
- Bozau, E. (2013), Prozessmodellierung hochsalinärer Wässer mit einem erweiterten PHREEQC-Datensatz, *Grundwasser*, 18(2), 93–98, doi:10.1007/s00767-013-0222-8.
- Bozau, E., C.-D. Sattler, and W. van Berk (2015), Hydrogeochemical classification of deep formation waters, *Applied Geochemistry*, 52, 23–30, doi:10.1016/j.apgeochem.2014.10.018.
- Burton, W. K., N. Cabrera, and F. C. Frank (1951), The Growth of Crystals and the Equilibrium Structure of their Surfaces, *Philosophical Transactions of the Royal Society A: Mathematical, Physical and Engineering Sciences*, 243(866), 299–358, doi:10.1098/rsta.1951.0006.
- Casella, F., and A. Leva (2006), Modelling of thermo-hydraulic power generation processes using Modelica, *Mathematical and Computer Modelling of Dynamical Systems*, 12(1), 19–33, doi:10.1080/13873950500071082.
- Chatenay, C., and T. Johannesson (2014), How do financial aspects of geothermal compare with other energy

- sources?: Short Course VI on Utilization of Low- and Medium-Enthalpy Geothermal Resources and Financial Aspects of Utilization.
- Claesson, J. (2004), Thermal and Hydraulic Performance of Compact Brazed Plate Heat Exchangers Operating as Evaporators in domestic Heat Pumps, Doctoral thesis, Stockholm, Sweden.
- Dahlgren, E., C. Göçmen, K. Lackner, and G. van Ryzin (2013), Small Modular Infrastructure, *The Engineering Economist*, 58(4), 231–264, doi:10.1080/0013791X.2013.825038.
- Dahmus, J. B. (2001), Modular Product Architecture, *Design Studies*, 22, 409–424.
- Daniel A. Keim Annemarie Herrmann (1998), The Gridfit Algorithm: An Efficient and Effective Approach to Visualizing Large Amounts of Spatial Data, pp. 181–188, IEEE.
- Debye, P., and E. Hückel (1923), Zur Theorie der Elektrolyte. I. Gefrierpunktserniedrigung und verwandte Erscheinungen, *Physikalische Zeitschrift*, 24(9), 185–206.
- Demir, M. M., A. Baba, V. Atilla, and M. İnanlı (2014), Types of the scaling in hyper saline geothermal system in north-west Turkey, *Geothermics*, 50, 1–9, doi:10.1016/j.geothermics.2013.08.003.
- DiPippo, R. (2008), *Geothermal power plants: principles, applications, case studies, and environmental impact*, Butterworth-Heinemann, Massachusetts.
- Dittus, F. W., and L. Boelter (1930), Heat transfer in automobile radiators of the tubular type, *Publications in Engineering*, 2, 443.
- Dixon, S. L. (2002), *Fluid mechanics and thermodynamics turbomachinery*, Elsevier Butterworth-Heinemann.
- Dobson, M.K. Chato, J.C. (1998), Condensation in Smooth Horizontal Tubes, *Journal of Heat Transfer*, 120(1), 193, doi:10.1115/1.2830043.
- Doo, G. H. (2005), A Modeling and Experimental Study of Evaporating Two-Phase Flow on the Shellside of Shell-and-Tube Heat Exchangers, PhD Thesis, Mechanical Engineering, U. o. Strathclyde.
- Driesner, T. (2007), The system H<sub>2</sub>O–NaCl. Part II: Correlations for molar volume, enthalpy, and isobaric heat capacity from 0 to 1000°C, 1 to 5000bar, and 0 to 1 XNaCl, *Geochimica et Cosmochimica Acta*, 71(20), 4902–4919, doi:10.1016/j.gca.2007.05.026.
- Driesner, T., and C. A. Heinrich (2007), The system H<sub>2</sub>O–NaCl. Part I: Correlation formulae for phase relations in temperature–pressure–composition space from 0 to 1000°C, 0 to 5000bar, and 0 to 1 XNaCl, *Geochimica et Cosmochimica Acta*, 71(20), 4880–4901, doi:10.1016/j.gca.2006.01.033.
- Duan, Z., and S. Mao (2006), A thermodynamic model for calculating methane solubility, density and gas phase composition of methane-bearing aqueous fluids from 273 to 523K and from 1 to 2000bar, *Geochimica et Cosmochimica Acta*, 70(13), 3369–3386, doi:10.1016/j.gca.2006.03.018.
- Duan, Z., and R. Sun (2003), An improved model calculating CO<sub>2</sub> solubility in pure water and aqueous NaCl solutions from 273 to 533 K and from 0 to 2000 bar, *Chemical Geology*, 193, 257–271.
- Duan, Z., R. Sun, R. Liu, and C. Zhu (2007), Accurate Thermodynamic Model for the Calculation of H<sub>2</sub>S Solubility in Pure Water and Brines, *Energy & Fuels*, 21, 2056–2065.
- Duan, Z., R. Sun, C. Zhu, and I. M. Chou (2006), An improved model for the calculation of CO<sub>2</sub> solubility in aqueous solutions containing Na<sup>+</sup>, K<sup>+</sup>, Ca<sup>2+</sup>,

- Mg<sup>2+</sup>, Cl<sup>-</sup>, and SO<sub>4</sub><sup>2-</sup>, *Marine Chemistry*, 98(2-4), 131-139, doi:10.1016/j.marchem.2005.09.001.
- Dwivedi, A. K., and S. K. Das (2007), Dynamics of plate heat exchangers subject to flow variations, *International Journal of Heat and Mass Transfer*, 50(13-14), 2733-2743, doi:10.1016/j.ijheatmasstransfer.2006.11.029.
- Entingh, D., E. J. Easwaran, and L. McLarty (1994), Small Geothermal Electric Systems for Remote Powering 10, G. R. Council, Davis, CA.
- EPRI (2005), Air-Cooled Condenser Design, Specification, and Operation Guidelines 1007688, Electric Power Research Institute, Palo Alto, CA.
- Fang, X., Y. Xu, and Z. Zhou (2011), New correlations of single-phase friction factor for turbulent pipe flow and evaluation of existing single-phase friction factor correlations, *Nuclear Engineering and Design*, 241(3), 897-902, doi:10.1016/j.nucengdes.2010.12.019.
- Fauzi, A. (2015), Geothermal resources and reserves in Indonesia: An updated revision, *Geoth. Energ. Sci.*, 3(1), 1-6, doi:10.5194/gtes-3-1-2015.
- Feldbusch, E., S. Regenspurg, J. Banks, H. Milsch, and A. Saadat (2013), Alteration of fluid properties during the initial operation of a geothermal plant: results from in situ measurements in Groß Schönebeck, *Environmental Earth Sciences*, 70(8), 3447-3458, doi:10.1007/s12665-013-2409-9.
- Francke, H., M. Kraume, and A. Saadat (2013), Thermal-hydraulic measurements and modelling of the brine circuit in a geothermal well, *Environmental Earth Sciences*, 70(8), 3481-3495, doi:10.1007/s12665-013-2612-8.
- Franco, A., and M. Vaccaro (2012), An integrated "Reservoir-Plant" strategy for a sustainable and efficient use of geothermal resources, *Energy*, 37(1), 299-310, doi:10.1016/j.energy.2011.11.029.
- Frick, S., A. Saadat, and S. Kranz (Eds.) (2012), *Cooling of low-temperature power plants: challenges for the example of geothermal binary power plants*, 6th International Symposium on Cooling Towers - ISCT 2012, Cologne.
- Gabbrielli, R. (2012), A novel design approach for small scale low enthalpy binary geothermal power plants, *Energy Conversion and Management*, 64(0), 263-272, doi:10.1016/j.enconman.2012.04.017.
- Garcia, A. S. (2009), Reactive solute transport in variable density fluid flow, Master thesis, Department of Geotechnical Engineering and Geosciences, Technical University of Catalonia, Barcelona.
- Garcia, J. E. (2001), Density of aqueous solutions of CO<sub>2</sub>, *Lawrence Berkeley National Laboratory*.
- García-Cascales, J. R., F. Vera-García, J. M. Corberán-Salvador, and J. González-Maciá (2007), Assessment of boiling and condensation heat transfer correlations in the modelling of plate heat exchangers, *International Journal of Refrigeration*, 30(6), 1029-1041, doi:10.1016/j.ijrefrig.2007.01.004.
- Gas Processors Suppliers Association (2004), *Engineering Data Book*, 12th ed., Gas Processor Suppliers Association (GPSA), Tulsa, OK.
- Ghajar, A. J., and C. C. Tang (2010), Importance of Non-Boiling Two-Phase Flow Heat Transfer in Pipes for Industrial Applications, *Heat Transfer Engineering*, 31(9), 711-732, doi:10.1080/01457630903500833.
- Ghasemi, H., M. Paci, A. Tizzanini, and A. Mitsos (2013), Modeling and optimization of a binary geothermal power

- plant, *Energy*, 50(0), 412–428, doi:10.1016/j.energy.2012.10.039.
- Grant, I. D. R. (1977), Pressure Drop on the Shell-Side of Shell-and-Tube Heat Exchangers in Single and Two-Phase Flows, *HTFS Design Report*, 16.
- GSDS (2016), WellSim, <http://www.gsds.co.nz/wellsim/>.
- Haaf, S. von, F. (. Steimle, and K. (. Stephan (1988), *Handbuch der Klimatechnik: Sechster Band / Teil B: Wärmeaustauscher:Wärmeübertragung in Kluftkühlern*, Springer, Berlin.
- Hansen, N. (2006), Towards a New Evolutionary Computation, in *Studies in Fuzziness and Soft Computing*, vol. 192, pp. 75–102, Springer Berlin Heidelberg.
- Harjoko, A., K. Hapsari, and Y. T. Wibowo (Eds.) (2015), *The Sulfide Minerals Deposit in the Geothermal Pipes of Dieng Geothermal Field, Indonesia, World Geothermal Congress 2015*, Melbourne.
- Harting, P., May, F., Schütze, H. (1982), *Tabellen und Diagramme zur Löslichkeit von Methan-Stickstoff-Gemischen in wäßrigen Natriumchloridlösung*, Akademie der Wissenschaften der DDR, Zentralinst. für Isotopen- u. Strahlenforschung, Leipzig.
- Hasan, A. R., and C. S. Kabir (2010), Modeling two-phase fluid and heat flows in geothermal wells, *Journal of Petroleum Science and Engineering*, 71(1-2), 77–86, doi:10.1016/j.petrol.2010.01.008.
- He, C., C. Liu, H. Gao, H. Xie, Y. Li, S. Wu, and J. Xu (2012), The optimal evaporation temperature and working fluids for subcritical organic Rankine cycle, *Energy*, 38(1), 136–143, doi:10.1016/j.energy.2011.12.022.
- Hernandez-Galan, J. L., and L. Alberto Plauchu (1989), Determination of fouling factors for shell-and-tube type heat exchangers exposed to los azufres geothermal fluids, *Geothermics*, 18(1-2), 121–128, doi:10.1016/0375-6505(89)90018-7.
- Hesshaus, A., G. Houben, and R. Kringel (2013), Halite clogging in a deep geothermal well – Geochemical and isotopic characterisation of salt origin, *Physics and Chemistry of the Earth, Parts A/B/C*, 64, 127–139, doi:10.1016/j.pce.2013.06.002.
- Hnědkovský, L., R. H. Wood, and V. Majer (1996a), Volumes of aqueous solutions of CH<sub>4</sub>, CO<sub>2</sub>, H<sub>2</sub>S and NH<sub>3</sub> at temperatures from 298.15 K to 705 K and pressures to 35 MPa, *J. Chem Thermodynamics*, 28, 125–142.
- Hnědkovský, L., R. H. Wood, and V. Majer (1996b), Volumes of aqueous solutions of CH<sub>4</sub>, CO<sub>2</sub>, H<sub>2</sub>S and NH<sub>3</sub> at temperatures from 298.15 K to 705 K and pressures to 35 MPa, *J. Chem Thermodynamics*, 28, 125–142.
- Hnědkovský, L., R. H. Wood, and V. Majer (1997), Apparent molar heat capacities of aqueous solutions of CH<sub>4</sub>, CO<sub>2</sub>, H<sub>2</sub>S, and NH<sub>3</sub> at temperatures from 304 K to 704 K at a pressure of 28 MPa, *J. Chem Thermodynamics*, 29, 731–747.
- Hochstein, M. P., and S. Sudarman (2008), History of geothermal exploration in Indonesia from 1970 to 2000, *Geothermics*, 37(3), 220–266, doi:10.1016/j.geothermics.2008.01.001.
- Hsieh, Y. Y., and T. F. Lin (2002), Saturated flow boiling heat transfer and pressure drop of refrigerant R-410A in a vertical plate heat exchanger, *International Journal of Heat and Mass Transfer*, 45(5), 1033–1044, doi:10.1016/S0017-9310(01)00219-8.
- Huang, S. S. S., A. D. Leu, H. J. Ng, and D. B. Robinson (1985), The phase behavior of two mixtures of methane, carbon dioxide, hydrogen sulfide, and water, *Fluid Phase Equilibria*, 19(1), 21–32, doi:10.1016/0378-3812(85)85033-0.

- IEA (2011), Technology Roadmap: Geothermal Heat and Power.
- Kashani, A., A. Hesam, A. Maddahi, and H. Hajabdollahi (2013), Thermal-economic optimization of an air-cooled heat exchanger unit, *Applied Thermal Engineering*, 54(1), 43–55, doi:10.1016/j.applthermaleng.2013.01.014.
- Kaya, E., S. J. Zarrouk, and M. J. O'Sullivan (2011), Reinjection in geothermal fields: A review of worldwide experience, *Renewable and Sustainable Energy Reviews*, 15(1), 47–68, doi:10.1016/j.rser.2010.07.032.
- Kunz, O., and W. Wagner (2012), The GERG-2008 Wide-Range Equation of State for Natural Gases and Other Mixtures: An Expansion of GERG-2004, *Journal of Chemical & Engineering Data*, 57(11), 3032–3091, doi:10.1021/jc300655b.
- Laliberté, M., and W. E. Cooper (2007), Model for calculating the viscosity of aqueous solutions, *J. Chem. Eng. Data*, 52(2), 321–335.
- Lapidus, L., and N. R. Amundson (1952), Mathematics of Adsorption in Beds. VI. The Effect of Longitudinal Diffusion in Ion Exchange and Chromatographic Columns, *J. Phys. Chem.*, 56(8), 984–988, doi:10.1021/j150500a014.
- Lei, H., J. Li, X. Li, and Z. Jiang (2016), EOS7Cm: An improved TOUGH2 module for simulating non-isothermal multiphase and multicomponent flow in CO<sub>2</sub>-H<sub>2</sub>S-CH<sub>4</sub>-brine systems with high pressure, temperature and salinity, *Computers & Geosciences*, 94, 150–161, doi:10.1016/j.cageo.2016.06.011.
- Manente, G., A. Toffolo, A. Lazzaretto, and M. Paci (2013), An Organic Rankine Cycle off-design model for the search of the optimal control strategy, *Energy*, 58(0), 97–106, doi:10.1016/j.energy.2012.12.035.
- Mao, S., and Z. Duan (2006), A thermodynamic model for calculating nitrogen solubility, gas phase composition and density of the N<sub>2</sub>-H<sub>2</sub>O-NaCl system, *Fluid Phase Equilibria*, 248(2), 103–114, doi:10.1016/j.fluid.2006.07.020.
- Mao, S., and Z. Duan (2009), The Viscosity of Aqueous Alkali-Chloride Solutions up to 623 K, 1,000 bar, and High Ionic Strength, *International Journal of Thermophysics*, 30(5), 1510–1523, doi:10.1007/s10765-009-0646-7.
- Mao, S., D. Zhang, Y. Li, and N. Liu (2013), An improved model for calculating CO<sub>2</sub> solubility in aqueous NaCl solutions and the application to CO<sub>2</sub>-H<sub>2</sub>O-NaCl fluid inclusions, *Chemical Geology*, 347, 43–58, doi:10.1016/j.chemgeo.2013.03.010.
- Martin, H. (1996), A theoretical approach to predict the performance of chevron-type plate heat exchangers, *Chemical Engineering and Processing: Process Intensification*, 35(4), 301–310, doi:10.1016/0255-2701(95)04129-X.
- McGuinness, M. J. (2014), Feedpoint viscosity in geothermal wellbore simulation, *Geothermics*, 50, 24–29, doi:10.1016/j.geothermics.2013.07.007.
- Mégel, T., T. Kohl, A. Gérard, L. Rybach, and R. Hopkirk (Eds.) (2005), *Downhole Pressures Derived from Wellhead Measurements during Hydraulic Experiments*, 6 pp.
- Michaelides, E. E. (1982), The influence of non-condensable gases on the net work produced by the geothermal steam power plants, *Geothermics*, 11(3), 163–174, doi:10.1016/0375-6505(82)90025-6.
- Milivojevic, S., V. D. Stevanovic, and B. Maslovaric (2014), Condensation induced water hammer: Numerical prediction, *Journal of Fluids and Structures*,

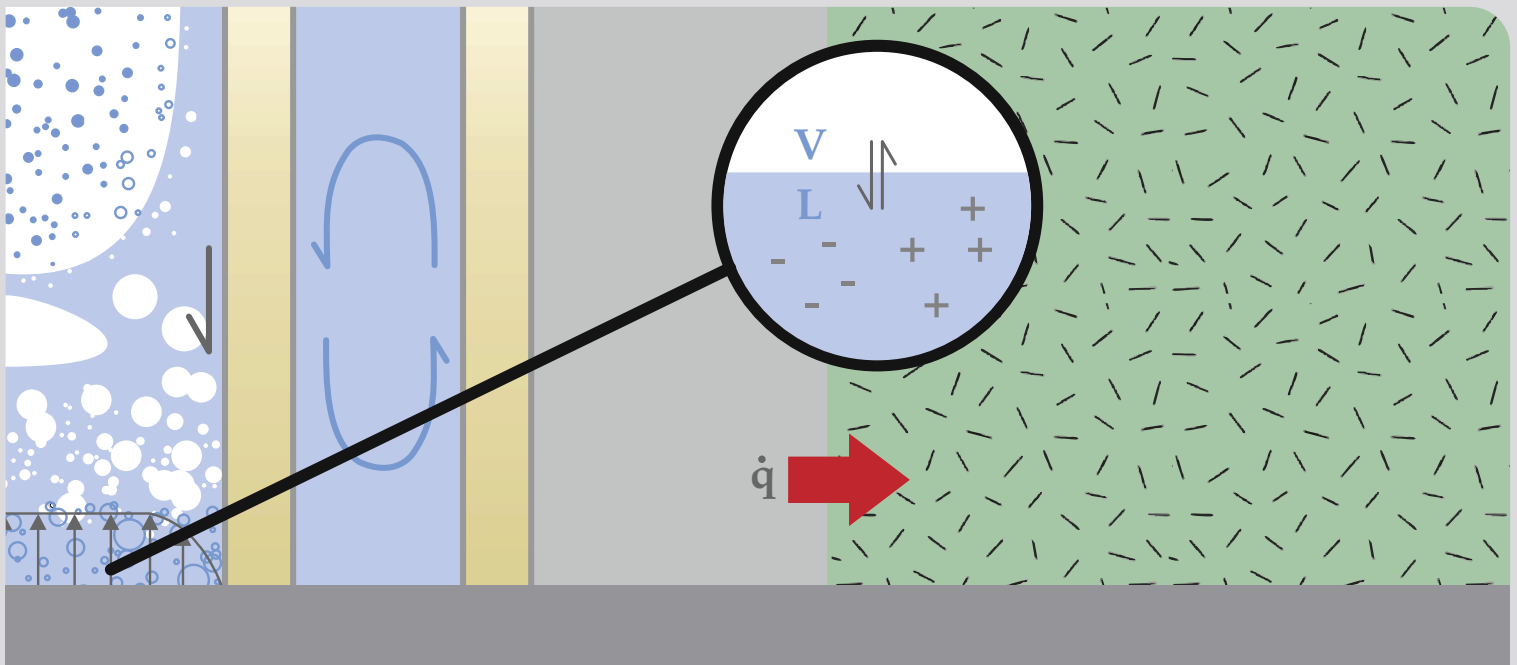
- 50, 416–436, doi:10.1016/j.jfluidstructs.2014.07.003.
- Milora, S. L., and J. W. Tester (1976), *Geothermal Energy as a Source of Electric Power*, The MIT Press, Cambridge, Massachusetts.
- Muley, A., and R. M. Manglik (1999), Experimental Study of Turbulent Flow Heat Transfer and Pressure Drop in a Plate Heat Exchanger With Chevron Plates, *J. Heat Transfer*, 121(1), 110, doi:10.1115/1.2825923.
- Mundhenk, N., P. Huttenloch, T. Kohl, H. Steger, and R. Zorn (2013), Metal corrosion in geothermal brine environments of the Upper Rhine graben - Laboratory and on-site studies, *Geothermics*, 46, 14–21, doi:10.1016/j.geothermics.2012.10.006.
- Nardi, A., A. Idiart, P. Trinchero, L. M. de Vries, and J. Molinero (2014), Interface COMSOL-PHREEQC (iCP), an efficient numerical framework for the solution of coupled multiphysics and geochemistry, *Computers & Geosciences*, 69, 10–21, doi:10.1016/j.cageo.2014.04.011.
- Nitschke, F., S. Held, T. Himmelsbach, and T. Kohl (2017), THC simulation of halite scaling in deep geothermal single well production, *Geothermics*, 65, 234–243, doi:10.1016/j.geothermics.2016.09.009.
- Nitschke, F., J. Scheiber, U. Kramar, and T. Neumann (2014), Formation of alternating layered Ba-Sr-sulfate and Pb-sulfide scaling in the geothermal plant of Soultz-sous-Forêts, *N. Jb. Miner. Abh.*, 191(2), 145–156, doi:10.1127/0077-7757/2014/0253.
- Pan, L., and C. M. Oldenburg (2014), T2Well—An integrated wellbore–reservoir simulator, *Computers & Geosciences*, 65, 46–55, doi:10.1016/j.cageo.2013.06.005.
- Parkhurst, D. L., and C. Appelo (1999), User's guide to PHREEQC (Version 2): A computer program for speciation, batch-reaction, one-dimensional transport, and inverse geochemical calculations, *Water-Resources Investigations Report 99-4259*, U.S. Geological Survey.
- Peng, D.-Y., and D. B. Robinson (1976), A New Two-Constant Equation of State, *Industrial & Engineering Chemistry Fundamentals*, 15(1), 59–64, doi:10.1021/i160057a011.
- Pitzer, K. S., and G. Mayorga (1973), Thermodynamics of electrolytes. II. Activity and osmotic coefficients for strong electrolytes with one or both ions univalent, *J. Phys. Chem.*, 77(19), 2300–2308, doi:10.1021/j100638a009.
- Qin, J., R. J. Rosenbauer, and Z. Duan (2008), Experimental Measurements of Vapor–Liquid Equilibria of the H<sub>2</sub>O + CO<sub>2</sub> + CH<sub>4</sub> Ternary System, *J. Chem. Eng. Data*, 53, 1246–1249.
- Quoilin, S., S. Declaye, B. F. Tchanche, and V. Lemort (2011), Thermo-economic optimization of waste heat recovery Organic Rankine Cycles, *Applied Thermal Engineering*, 31(14–15), 2885–2893, doi:10.1016/j.applthermaleng.2011.05.014.
- Quoilin, S., V. Lemort, and J. Lebrun (2010), Experimental study and modeling of an Organic Rankine Cycle using scroll expander, *Applied Energy*, 87(4), 1260–1268, doi:10.1016/j.apenergy.2009.06.026.
- Quoilin, S., M. D. van Broek, S. Declaye, P. Dewallef, and V. Lemort (2013), Techno-economic survey of Organic Rankine Cycle (ORC) systems, *Renewable and Sustainable Energy Reviews*, 22(0), 168–186, doi:10.1016/j.rser.2013.01.028.
- Råback, P., M. Malinen, Ruokolainen Juha, A. Pursula, and T. Zwinger (2016),

- Elmer models manual, CSC - IT Center for Science.
- Rabemanana, V., P. Durst, D. Bächler, F.-D. Vuataz, and T. Kohl (2003), Geochemical modelling of the Soultz-sous-Forêts Hot Fractured Rock system, *Geothermics*, 32(4-6), 645-653, doi:10.1016/S0375-6505(03)00069-5.
- Richter, C. (2008), Proposal of New Object-Oriented Equation-Based Model Libraries for Thermodynamic Systems, Fakultät für Maschinenbau, Technischen Universität at Carolo-Wilhelmina zu Braunschweig, Braunschweig, Germany.
- Rowland, D., and P. M. May (2013), A Pitzer-based characterization of aqueous magnesium chloride, calcium chloride and potassium iodide solution densities to high temperature and pressure, *Fluid Phase Equilibria*, 338, 54-62, doi:10.1016/j.fluid.2012.10.021.
- Rybach, L. (2014), Geothermal Power Growth 1995-2013 - A Comparison with Other Renewables, *Energies*, 7(8), 4802-4812, doi:10.3390/en7084802.
- Saaltink, M. W., C. Ayora, and J. Carrera (1998), A mathematical formulation for reactive transport that eliminates mineral concentrations, *Water Resour. Res.*, 34(7), 1649-1656, doi:10.1029/98WR00552.
- Sanjuan, B., R. Millot, C. Dezayes, and M. Brach (2010), Main characteristics of the deep geothermal brine (5km) at Soultz-sous-Forêts (France) determined using geochemical and tracer test data, *Comptes Rendus Geoscience*, 342(7-8), 546-559, doi:10.1016/j.crte.2009.10.009.
- Sanyal, S. K. (Ed.) (2005), *Classification of Geothermal Systems - A Possible Scheme, Thirtieth Workshop on Geothermal Reservoir Engineering*, Stanford.
- Schlichting, H., and K. Gersten (2000), *Boundary-layer theory*, 8th ed., xxiii, 799, Springer, Berlin, New York.
- Schlumberger (2014), *OLGA Dynamic Multiphase Flow Simulator*.
- Schmidt, H. (2010), *VDI heat atlas: Two-Phase Gas-Liquid Flow*, 2nd ed., 1 online resource (xxii, 1586, *VDI-buch*, Springer, Berlin, London.
- Schröder, E., K. Thomauske, J. Schmalzbauer, S. Herberger, C. Gebert, and M. Velevska (2015), Design and test of a new flow calorimeter for online detection of geothermal water heat capacity, *Geothermics*, 53, 202-212, doi:10.1016/j.geothermics.2014.06.001.
- Serth, R. W. (2007), *Process Heat Transfer: Principles and Applications*, Elsevier.
- Shekun, G. D. (2007), Approximating the efficiency characteristics of blade pumps, *Thermal Engineering*, 54, 886-891.
- Sieder, E. N., and G. E. Tate (1936), Heat Transfer and Pressure Drop of Liquids in Tubes, *Ind. Eng. Chem.*, 28(12), 1429-1435, doi:10.1021/ie50324a027.
- Soreide, I., and C. H. Whitson (1992), Peng-Robinson predictions for hydrocarbons, CO<sub>2</sub>, N<sub>2</sub>, and H<sub>2</sub>S with pure water and NaCl brine, *Fluid Phase Equilibria*, 77, 217-240.
- Springer, R. D., P. Wang, and A. Anderko (2015), Modeling the Properties of H<sub>2</sub>S/CO<sub>2</sub>/Salt/Water Systems in Wide Ranges of Temperature and Pressure, *SPE-173902-PA*, doi:10.2118/173902-pa.
- Springer, R. D., Z. Wang, A. Anderko, P. Wang, and A. R. Felmy (2012), A thermodynamic model for predicting mineral reactivity in supercritical carbon dioxide: I. Phase behavior of carbon dioxide-water-chloride salt systems

- across the H<sub>2</sub>O-rich to the CO<sub>2</sub>-rich regions, *Chemical Geology*, 322-323, 151-171, doi:10.1016/j.chemgeo.2012.07.008.
- Stefansson, V. (Ed.) (2005), *World Geothermal Assessment, World Geothermal Congress 2005*, Antalya, Turkey.
- Taal, M., I. Bulatov, J. Klemeš, and P. Stehlík (2003), Cost estimation and energy price forecasts for economic evaluation of retrofit projects, *Applied Thermal Engineering*, 23(14), 1819-1835, doi:10.1016/S1359-4311(03)00136-4.
- Thorade, M., and A. Saadat (2013), Partial derivatives of thermodynamic state properties for dynamic simulation, *Environ Earth Sci*, 70(8), 3497-3503, doi:10.1007/s12665-013-2394-z.
- Valdez, B., M. Schorr, M. Quintero, M. Carrillo, R. Zlatev, M. Stoytcheva, and J. de Dios Ocampo (2009), Corrosion and scaling at Cerro Prieto geothermal field, *Anti-Corrosion Meth & Material*, 56(1), 28-34, doi:10.1108/00035590910923437.
- Valdimarsson, P. (2014), New Development in the ORC Technology, UNU-GTP and LaGeo, Santa Tecla, El Salvador.
- (2010), *VDI Heat Atlas*, Verein Deutscher Ingenieure.
- Verkis Consulting (2014), Geothermal Binary Power Plants: Preliminary study of low temperature utilization, cost estimates and energy cost.
- Vetter, C. (2014), Thermodynamische Auslegung und transiente Simulation eines überkritischen Organic Rankine Cycles für einen leistungsoptimierten Betrieb, Dissertation, Fakultät für Maschinenbau, Karlsruhe Institute of Technology, Karlsruhe.
- Vetter, C., H.-J. Wiemer, and D. Kuhn (2013), Comparison of sub- and supercritical Organic Rankine Cycles for power generation from low-temperature/low-enthalpy geothermal wells, considering specific net power output and efficiency, *Applied Thermal Engineering*, 51(1-2), 871-879, doi:10.1016/j.applthermaleng.2012.10.042.
- Wang, P., A. Anderko, and R. D. Young (2002), A speciation-based model for mixed-solvent electrolyte systems, *Fluid Phase Equilibria*, 203, 141-176.
- Wei, D., X. Lu, Z. Lu, and J. Gu (2007), Performance analysis and optimization of organic Rankine cycle (ORC) for waste heat recovery, *Energy Conversion and Management*, 48(4), 1113-1119, doi:10.1016/j.enconman.2006.10.020.
- Williams, A. E., and M. A. McKibben (1989), A brine interface in the Salton Sea Geothermal System, California: Fluid geochemical and isotopic characteristics, *Geochimica et Cosmochimica Acta*, 53, 1905-1920.
- Woldesemayat, M. A., and A. J. Ghajar (2007), Comparison of void fraction correlations for different flow patterns in horizontal and upward inclined pipes, *International Journal of Multiphase Flow*, 33(4), 347-370, doi:10.1016/j.ijmultiphaseflow.2006.09.004.
- Young, T. F., and M. B. Smith (1954), Thermodynamic Properties of Mixtures of Electrolytes in Aqueous Solutions, *The Journal of Physical Chemistry*, 58(9), 716-724, doi:10.1021/j150519a009.
- Yu, J., and S. Koyama (Eds.) (1998), *Condensation Heat Transfer of Pure Refrigerants in Microfin Tubes*.
- Yusufova, V. D., R. I. Pepinov, V. A. Nikolaev, and G. M. Guseinov (1975), Thermal conductivity of aqueous solutions of NaCl, *Journal of engineering physics*, 29(4), 1225-1229.

- Zein, D., T. Driesner, S. Scott, C. Sanchez-Valle, and T. Wagner (2014), Volumetric Properties of Mixed Electrolyte Aqueous Solutions at Elevated Temperatures and Pressures. The Systems CaCl<sub>2</sub>-NaCl-H<sub>2</sub>O and MgCl<sub>2</sub>-NaCl-H<sub>2</sub>O to 523.15 K, 70 MPa, and Ionic Strength from (0.1 to 18) mol·kg<sup>-1</sup>, *Journal of Chemical & Engineering Data*, 59(8), 2570–2588, doi:10.1021/je500371u.
- Zhang, G., P. Lu, X. Wei, and C. Zhu (2016), Impacts of Mineral Reaction Kinetics and Regional Groundwater Flow on Long-Term CO<sub>2</sub> Fate at Sleipner, *Energy Fuels*, 30(5), 4159–4180, doi:10.1021/acs.energyfuels.5b02556.
- Zhang, H.-L., G.-H. Chen, and S.-J. Han (1997), Viscosity and Density of H<sub>2</sub>O + NaCl + CaCl<sub>2</sub> and H<sub>2</sub>O + KCl + CaCl<sub>2</sub> at 298.15 K, *J. Chem. Eng. Data*, 42, 526–530.
- Zhou, F., and X. Zheng (2015), Heat transfer in tubing-casing annulus during production process of geothermal systems, *J. Earth Sci.*, 26(1), 116–123, doi:10.1007/s12583-015-0511-5.
- Ziabakhsh-Ganji, Z., and H. Kooi (2012), An Equation of State for thermodynamic equilibrium of gas mixtures and brines to allow simulation of the effects of impurities in subsurface CO<sub>2</sub> storage, *International Journal of Greenhouse Gas Control*, 11, S21-S34, doi:10.1016/j.ijggc.2012.07.025.
- Zirrahi, M., R. Azin, H. Hassanzadeh, and M. Moshfeghian (2012), Mutual solubility of CH<sub>4</sub>, CO<sub>2</sub>, H<sub>2</sub>S, and their mixtures in brine under subsurface disposal conditions, *Fluid Phase Equilibria*, 324, 80–93, doi:10.1016/j.fluid.2012.03.017.
- Zuber, N., and J. A. Findlay (1965), Average Volumetric Concentration in Two-Phase Flow Systems, *J. Heat Transfer*, 87(4), 453, doi:10.1115/1.3689137.





Geothermal technical installations (e.g. wellbore and power block) cost is a major factor determining commercial feasibility of binary geothermal power plant projects. This thesis presents thermohydro-chemical simulations of the technical systems that allow cost efficiency during it's design and operation. In the first part of the thesis, two studies are devoted in modularization technique of geothermal Organic Rankine Cycles and the dynamic simulations for insular operation. In the second part, we develop WellboreKit - a reactive wellbore flow simulator based on Elmer-PHREEQC coupling. gEOSkit - an equation of state for two-phase multisalt, multigas geothermal fluids - is embedded inside. The tool provides slow-transient analyses that predicting wellbore system dynamics such as time-varying flow rate, temperature, pressure, fluid composition, and tendency to corrosion and mineral deposition.